UNIVERSITY OF OTTAWA

DOCTOR OF PHILOSOPHY THESIS

Engineered Photonic Structures for Enhanced Light–Matter Interaction and Telecom-Band DFB Lasers

Author:
Sina AGHILI

Supervisor:
Prof. Ksenia DOLGALEVA

A thesis submitted to the University of Ottawa in partial fulfillment of the requirements for the Doctorate of Philosophy in Electrical Engineering

Department of Electrical Engineering
Faculty of Engineering
University of Ottawa

Declaration of Authorship

I, Sina AGHILI, declare that this thesis, titled “Engineered Photonic Structures for Enhanced Light–Matter Interaction and Telecom-Band DFB Lasers”, and the work presented in it are my own. I confirm that except where specific reference is made to the work of others, the contents of this dissertation are original and have not been submitted in whole or in part for consideration for any other degree or qualification in this, or any other university. This dissertation is my own work and contains nothing which is the outcome of work done in collaboration with others, except as specified in the text and Acknowledgments.

Sina Aghili
June, 2026
Ottawa, Canada

To my parents,

Anoushirvan & Pourandokht

Abstract

High performance photonic devices increasingly rely on resonant micro- and nanoscale structures to shape electromagnetic fields within compact footprints. As two important classes of such resonant devices, this thesis investigates metasurfaces and waveguide Bragg gratings (WBGs) as periodically structured photonic components that enable precise control of light propagation and emission.

In the first part, we studied metasurfaces as ultrathin resonant devices that manipulate free space radiation through engineered scattering from sub-wavelength meta-atoms. We employed established numerical and semi-numerical tools to analyze linear and nonlinear responses, including multipolar contributions to the scattering response of linear resonant metamaterials and nonlinear scattering theory for second-harmonic generation (SHG). In the terahertz (THz) regime, we demonstrated an indium antimonide (InSb)-based plasmonic metasurface that supports a spectrally narrow surface lattice resonance (SLR) in a periodic meta-molecule array, and we investigated its potential for sensing and tweezing applications. We further investigated emission engineering in coupled emitter–antenna systems using InSb-based resonant antennae, showing that magnetization and multipolar resonances provide a practical route to dynamically control the spontaneous emission of a quantum emitter.

We then focused on nonlinear plasmonic metasurfaces motivated by SHG microscopy applications. We studied a structurally disordered metasurface composed of asymmetrical L- and V-shaped gold meta-atoms and clarified how the SH response is governed by polarization- and orientation-dependent emission channels in the metasurface. To achieve both second-harmonic (SH) signal strength and near-field resolution simultaneously, we proposed a bi-layered stack metasurface design that combines a passive linear metasurface supporting an SLR with an upper nonlinear antenna layer supporting localized surface plasmon resonances (LSPRs), enabling

enhanced forward SH emission while maintaining improved near-field resolution.

In the second part, we investigated higher-order WBGs as wavelength-selective feedback components for distributed feedback (DFB) semiconductor lasers. We implemented a coupled wave analysis for higher-order gratings with arbitrary profiles and accounted for the effect of radiative waves, which enabled longitudinal mode discrimination for single-mode operation. By extending this analysis into a threshold-oriented framework for modeling lasing onset, we optimized and experimentally characterized a compact third-order surface-etched grating DFB laser on the vertical integration platform, and we demonstrated good agreement between the modeling approach and measured device performance.

Overall, this thesis provides practical designs and analysis approaches for THz metasurfaces, THz resonant metamaterials, nonlinear SHG metasurface platforms, and higher-order grating DFB lasers as promising building blocks for sensing, emission control, nonlinear microscopy, and telecom photonic integrated circuits (PICs), respectively.

Acknowledgments

I am grateful to the people who supported me throughout my PhD and helped shape this thesis. First of all, I would like to thank Prof. Ksenia Dolgaleva for her continuous support and for respecting my preferences throughout this long period.

I also thank our postdoctoral researchers Dr. Rasoul Alaee, Dr. Daniel H. Espinosa, Dr. Boris Rosenstein, and Dr. Lais Fujii dos Santos for their valuable contributions across different research directions.

Finally, I would like to thank my colleagues Soheil Zibod, Ozan W. Oner, Athulya Thulaseedharan, Mohammadreza Mohammadpour, and Shayan Saeidi for their collaborations.

Contents

List of Figures

List of Tables

Abbreviations

InSb	**I**ndium **A**ntimonide
QSA	**Q**uasi **S**tatic **A**pproximation
LSPRs	**L**ocalized **S**urface **P**lasmon **R**esonances
SLR	**S**urface **L**attice **R**esonance
ENZ	**E**psilon **N**ear **Z**ero
SCS	**S**cattering **C**ross **S**ection
ACS	**A**bsorption **C**ross **S**ection
ED	**E**lectric **D**ipole
MD	**M**agnetic **D**ipole
EQ	**E**lectric **Q**uadrupole
MQ	**M**agnetic **Q**uadrupole
EO	**E**lectric **O**ctupole
MO	**M**agnetic **O**ctupole
SE	**S**pontaneous **E**mission
LDOS	**L**ocal **D**ensity **O**f **O**ptical **S**tates
NLST	**N**onlinear **S**cattering **T**heory
SHG	**S**econd **H**armonic **G**eneration
WBG	**W**aveguide **B**ragg **G**ratings
DFB	**D**istributed **F**eed**B**ack
LCGs	**L**aterally **C**oupled **G**ratings
VC-SEGs	**V**ertically **C**oupled - **S**urafce **E**tched **G**ratings

Publications

1. **Aghili, Sina**, Ozan W. Oner, Tuhin Paul, M.R Mohammadpour, Kushal Jayarathna, Lisa Fischer, Boris Rosenstein, Daniel H. Espinosa, Gabriel A. Flizikowski, and Ksenia Dolgaleva,"Short-cavity single-mode on-chip DFBL source for monolithic PICs in the telecom range," *Journal of Physics D: Applied Physics* (2026).

2. **Aghili, Sina**, M.R Mohammadpour, Athulya Thulaseedharan, Lais Fujii dos Santos, Lora Ramunno, and Ksenia Dolgaleva, "Bi-layered stack plasmonic metasurface for high-resolution near-field SHG microscopy applications," *Journal of the Optical Society of America B* **43**, no. 5 (2026): 1024–1033.

3. **Aghili, Sina**, Rasoul Alaee, Amirreza Ahmadnejad, Ehsan Mobini, Mohammadreza Mohammadpour, Carsten Rockstuhl, and Ksenia Dolgaleva, "Dynamic control of spontaneous emission using magnetized InSb higher-order-mode antennas," *Journal of Physics: Photonics* **6**, no. 3 (2024): 035011.

4. **Aghili, Sina**, Aydin Amini, Leyla Shirafkan Dizaj, and Ksenia Dolgaleva, "THz plasmonic metasurface based on a periodic array of InSb metamolecules with narrow resonances," *Optics Communications* **508** (2022): 127805.

5. Saeidi, Shayan, **Sina Aghili**, Tuhin Paul, Boris Rosenstein, Valery Tolstikhin, Pierre Berini, and Ksenia Dolgaleva, "Finite-difference coupled-mode analysis of waveguide gratings and their optimization for single-mode DFB lasers," *Journal of the Optical Society of America B* **42**, no. 2 (2025): 438–445.

6. Thulaseedharan, A., L. Fujii dos Santos, **S. Aghili**, M. R. Mohammadpour, O. W. Oner, and K. Dolgaleva, "Tuning

proximity effect correction for plasmonic metasurfaces," *Journal of the Optical Society of America B* **43**, no. 3 (2026): A132–A136.

7. Enhanced SHG Microscopy via Near-Field Engineering in a Random Plasmonic Metasurface **(manuscript in preparation)**.

Chapter 1

Introduction

1.1 Introduction

Engineering electromagnetic waves with devices that are simultaneously compact, efficient, and compatible with a straightforward fabrication process is a main goal of modern photonics. Recent advances in fabrication technologies and numerical electromagnetic modeling have enabled micro- and nanoscale structures that reshape light propagation, accelerating the transition from bulky free space optics toward flat [1] and integrated photonic components [2]. In this context, periodic optical structures provide a powerful design framework [3] by enabling control over diffracted waves, spectral response, and light-matter interaction, and therefore support applications ranging from spectroscopy and imaging to optical communications and on-chip signal processing.

An optical grating component is a structure with a periodic spatial modulation of geometry or material properties such as the refractive index. This periodicity introduces additional spatial momentum components, enabling engineered coupling between incident or guided optical fields and new propagation channels [4]. Traditionally, gratings have been bulk optical elements, such as ruled [5], blazed [6], or holographic diffraction gratings [7], and have been widely used in spectrometers [8] and pulse compressors [9]. The advent of nanofabrication has further miniaturized and transformed the concept of classical diffraction gratings, leading to compact photonic components that form the core of this thesis, including metasurfaces and waveguide Bragg gratings (WBGs). Although these platforms rely on different physical mechanisms, namely scattering for metasurfaces [10] and guided wave interference for WBGs [11], both are governed by engineered grating arrays at micro- and nanoscales to achieve unprecedented control over light.

Metasurfaces primarily control free space radiation through engineered scattering and interference across a planar surface, enabling flat optics for beam shaping [12], holography [13], and lensing [14]. In contrast, WBGs control guided fields through distributed coupling and coherent interference between forward and backward propagating waves, which is essential for lasing [15], coupling [16], and filtering applications [17].

In this chapter, we briefly describe the fundamental concepts that provide the general background for the research presented in the subsequent chapters. Each research chapter then includes its own specific introduction and statement of purpose, in which the motivation, relevant context, and objectives of the corresponding project are discussed in more detail.

1.2 Metasurfaces

Metasurfaces represent a paradigm shift in optical engineering by transforming bulky refractive and diffractive elements into planar components with sub-wavelength thicknesses, often referred to as thin grating layers. By engineering the geometry, composition, and spatial arrangement of their constituent elements, metasurfaces overcome the limitations of traditional optics by exploiting both localized resonant responses and collective lattice interactions. Their ability to impart local phase discontinuities and control scattering amplitude enables compact implementations of functionalities including metalenses [18], beam steering [19], holography [13], polarization conversion [20], and spectral filtering [21]. Furthermore, metasurfaces provide a powerful platform for tailoring and enhancing light–matter interactions, which is central to applications in sensing, emission control, and nonlinear optical processes [22].

As discussed in Section 1.1, a key link between metasurfaces and classical grating physics is that a periodic array of resonant particles can support not only localized resonances, but also collective surface lattice resonances (SLRs), as illustrated in Fig. 1.1. In metasurfaces, the grating concept appears as a two-dimensional arrangement of sub-wavelength scatterers, often referred to as meta-atoms, that collectively tailor the amplitude, phase, and polarization of the transmitted or reflected field at a sub-wavelength structured interface [10]. Metasurfaces can scatter light over a wide range of angles, and they allow us to control which diffraction orders propagate and which ones decay rapidly.

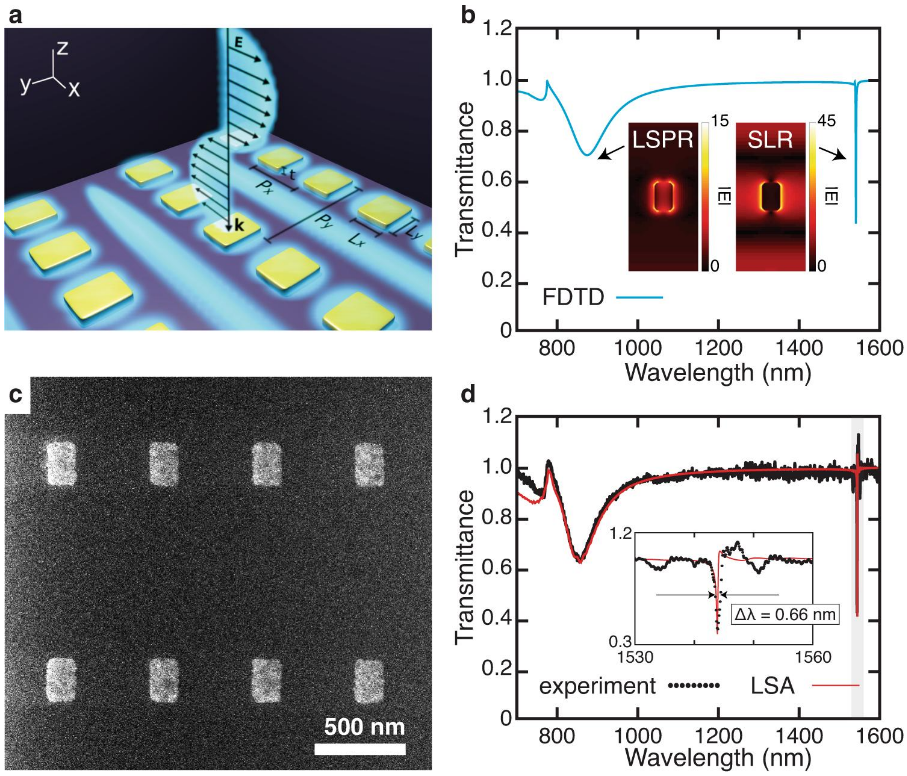

FIGURE 1.1: (a) Schematic of a gold nanobar metasurface, where the in-plane diffraction order $(1, 0)$ couples the LSPRs of the meta-atoms and forms a SLR across the metasurface plane. (b) Simulated transmission spectrum highlighting the broad linewidth of the LSPR and the narrow linewidth of the SLR. Insets show the corresponding electric field distributions. (c) SEM image of the periodic metasurface designed to support an SLR in the x–y plane. (d) Comparison of simulated and measured transmission spectra, emphasizing the narrow linewidth of SLR with an ultra-high Q factor of 2400. Adopted from M. S. Bin-Alam *et al.* [23] under the Creative Commons Attribution 4.0 International License.

By engineering the geometry and arrangement of meta-atoms across the surface, metasurfaces can support anomalous scattering responses. According to grating theory, a square metasurface, as a general case, with periodicity D placed at the interface of two materials with refractive indices n_1 and n_2, can support in-plane diffraction orders (m, p), whose spectral positions are described by [24]

$$\lambda_{m,p} = D\,\frac{\sqrt{n_2^2(m^2+p^2) - n_1^2 p^2 \sin^2\theta} \pm m n_1 \sin\theta}{m^2+p^2}, \tag{1.1}$$

where θ is the angle of incidence, and m and p are integers indicating diffraction orders along the x- and y-directions, respectively. Accordingly, the metasurface can support in-plane diffraction orders such as $(1, 0)$, $(0, 1)$, and $(1, 1)$, enabling resonant field confinement across the entire structured surface and thereby dramatically strengthening light–matter interactions. When the array period satisfies in-plane diffraction conditions associated with Rayleigh anomalies [25], scattered fields from individual resonators couple through diffraction channels, suppressing radiative loss and giving rise to resonances with linewidths that are significantly narrower than those of isolated particles. Metasurfaces can be broadly categorized according to their resonant mechanisms into plasmonic and dielectric platforms, each supporting distinct modes and therefore enabling different performance characteristics and applications.

These properties have motivated metasurface platforms for sensing [26] and spectral filtering [27], as well as for enhancing nonlinear optical processes [28] and controlling emission from nearby coupled dipole sources [29], which are central applications of the first part of this thesis.

1.2.1 Plasmonic Metasurfaces

Plasmonic metasurfaces typically utilize noble metals, such as gold and silver, at optical frequencies, or highly doped semiconductors at infrared and terahertz (THz) frequencies. They operate by exciting localized surface plasmon resonances (LSPRs), where incident electromagnetic fields couple coherently to collective oscillations of free carriers [30].

The main advantage of plasmonic metasurfaces is their ability to confine electromagnetic energy into deeply sub-wavelength regions and generate strong near-field enhancement. This feature significantly strengthens light–matter interactions and makes plasmonic metasurfaces particularly important for applications in which the interaction strength is the main limiting factor. Accordingly, they have been widely explored for refractive-index and biochemical sensing [31, 32], surface-enhanced spectroscopy [33], emission enhancement of quantum emitters [29, 34], and nonlinear nanophotonics [28, 35], where the enhanced local field increases the induced nonlinear current sources [36].

However, these advantages are accompanied by important limitations. Ohmic losses associated with free-carrier absorption dissipate optical energy as heat, broaden plasmonic resonances, and reduce the resonance quality factor, which can limit device efficiency, especially in wavefront-shaping or nonlinear applications that require high transmission, strong radiation efficiency, or narrow spectral response. Therefore, a central design challenge in plasmonic metasurfaces is to preserve strong near-field localization while reducing radiative and non-radiative losses.

1.2.2 Dielectric Metasurfaces

Dielectric metasurfaces are composed of high-index, low-loss materials such as silicon, germanium, or III–V semiconductors [37]. Unlike plasmonic structures, they support electric and magnetic Mie resonances driven by induced displacement currents within the dielectric volume.

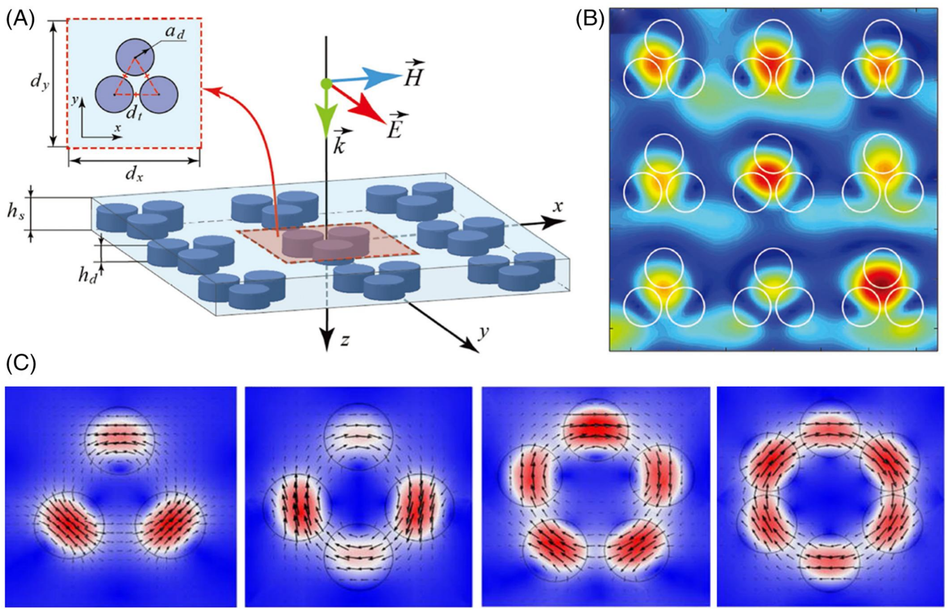

FIGURE 1.2: (A) Periodic array of high-index dielectric disk clusters. (B) Near-field map of the E_z component at the toroidal resonance, arising from the cross-coupling of electric and magnetic resonant modes. (C) Simulated magnetic field distributions for dielectric metasurfaces with different oligomer configurations, including trimer, quadrumer, pentamer, and hexamer, respectively. Panels (A,B) reproduced with permission from Xu *et al.* [38]. Copyright © 2018 Wiley-VCH. Panel (C) reproduced with permission Zhang *et al.* [39]. Copyright © 2019 Wiley-VCH.

By tailoring the geometry and spatial arrangement of their constituent elements, dielectric metasurfaces enable precise control of optical wavefront for efficient beam shaping [40]. The simultaneous excitation of electric and magnetic resonances facilitates highly directional scattering and enables control over the emission directivity of quantum emitters [41]. As shown in Fig. 1.2, a main limitation of dielectric metasurfaces is that their resonant features are typically confined to the resonator volume and governed by the refractive index contrast with the background medium. As a result, their near-field localization is generally weaker than in plasmonic structures, which can make them less suitable for applications that rely on sub-wavelength electromagnetic hotspots.

1.2.3 THz Plasmonics

The THz spectral region, approximately extending from 0.1 to 10 THz, is of significant interest for non-destructive imaging, security screening, molecular fingerprint spectroscopy, and biomedical diagnostics [42]. THz waves can penetrate many non-conducting materials and can directly probe low energy excitations, such as molecular rotations and lattice vibrational modes in solids [43].

For the further development of THz application systems, there is a strong demand for efficient devices capable of guiding, modulating, and manipulating THz waves in amplitude, phase, and polarization. However, low power and bulky THz sources, together with weak detection sensitivity, remain two major challenges of conventional THz technologies, motivating the development of engineered structures that can address these limitations.

THz plasmonics aims to confine and enhance electromagnetic fields at subwavelength scales, enabling miniaturized devices that mitigate the limitations of traditional THz components by providing strong local electric field intensities [44]. In addition to metals and graphene, which are commonly used plasmonic materials in the THz range [45], III–V semiconductors provide an attractive route toward active and tunable THz plasmonics, since their carrier density and transport properties can be modulated over a wide range using doping, electrical gating, optical pumping, and temperature control [46].

Among these materials, indium antimonide (InSb) is particularly promising due to its narrow bandgap, small electron effective mass, high electron mobility, and strong tunability of its optical response under external stimuli [47, 48]. Compared to passive structured metallic devices operating in the THz

TABLE 1.1: Drude–Lorentz parameters used to model the plasmonic response of III–V semiconductors in the THz regime [46].

	GaAs n-doped	GaAs p-doped	InP n-doped	InSb n-doped	InSb p-doped	InSb undoped
ω_p (10^{14} rad/s)	3.33 ± 0.01	4.44 ± 0.02	4.70 ± 0.01	2.82 ± 0.01	0.63 ± 0.01	0.57 ± 0.01
ω_p (cm^{-1})	1769.2 ± 1.9	2356.4 ± 9.1	2494.1 ± 1.8	1495.20 ± 1.83	332.60 ± 1.49	302.40 ± 0.33
τ_p (10^{-1} ps)	0.71 ± 0.01	0.09 ± 0.01	0.71 ± 0.01	2.65 ± 0.04	0.75 ± 0.01	5.16 ± 0.06
ω_L (10^{13} rad/s)	5.06 ± 0.01	5.06 ± 0.01	5.73 ± 0.01	3.38 ± 0.01	3.38 ± 0.01	3.38 ± 0.01
ω_L (cm^{-1})	268.4 ± 0.1	268.5 ± 0.2	303.9 ± 0.1	179.40 ± 0.13	179.40 ± 0.06	179.50 ± 0.06
τ_L (ps)	2.79 ± 0.27	1.95 ± 0.29	3.01 ± 0.24	1.81 ± 0.13	1.90 ± 0.04	1.99 ± 0.04
A_L	2.13 ± 0.03	2.15 ± 0.09	2.89 ± 0.04	2.02 ± 0.07	2.00 ± 0.01	2.02 ± 0.01
ε_∞	11.58 ± 0.01	11.34 ± 0.02	10.01 ± 0.01	15.68 ± 0.03	15.74 ± 0.01	15.86 ± 0.01
σ_0 (kS/m)	69.46 ± 0.54	16.54 ± 0.22	139.06 ± 0.77	186.35 ± 2.63	2.51 ± 0.04	14.83 ± 0.17

range, InSb-based plasmonic structures offer a versatile platform for THz metasurfaces requiring both strong field enhancement and dynamic control of spectral response.

A further and distinct advantage of THz plasmonic devices based on III–V semiconductors is their pronounced magneto-optical properties [49, 50]. Owing to the small effective mass and high mobility of charge carriers in InSb, the application of a relatively weak static magnetic field can induce strong gyrotropy and corresponding anisotropy in the complex permittivity. This enables magnetoplasmonic effects, in which plasmonic resonances can be dynamically tuned or spectrally split using an external magnetic bias, supporting functionalities such as polarization control [51], tunable filtering [52], enhanced scattering [53], and bright THz sources within compact platforms [54]. Table 1.1 summarizes the fitted parameters for III–V semiconductors exhibiting strong plasmonic response at low THz frequencies.

The complex permittivity of III–V semiconductors can be described by the Drude–Lorentz model as [46]

$$\varepsilon_r = \varepsilon_\infty - \frac{\omega_p^2}{\omega^2 + \mathrm{i}\omega/\tau_p} + \frac{A_L\omega_L^2}{\omega_L^2 - \omega^2 - \mathrm{i}\omega/\tau_L}, \tag{1.2}$$

where ε_∞ is the constant background permittivity, ω_p is the plasma frequency, and τ_p is the carrier scattering time, which is inversely proportional to the Drude damping rate γ_p. The last term in Eq. (1.2) represents the Lorentz contribution, where ω_L is the Lorentz frequency associated with lattice vibrations in the semiconductor crystal, $\tau_L = 1/\gamma_L$ is the scattering time of the Lorentz term, and A_L is an empirical amplitude determined by the difference between the permittivity below and above the Lorentz resonance [46].

By combining the resonant response of individual meta-atoms with the collective behavior of a periodic array, they provide a platform in which local field enhancement, linewidth control, radiation channels, and material tunability can be engineered together. This capability is especially important for optical and THz processes that are intrinsically weak or difficult to access in compact structures, where increasing the local electromagnetic field and controlling the emitted or scattered radiation are both essential.

The plasmonic metamaterial platforms investigated in this thesis target applications in which enhanced light–matter interaction is the key requirement. Narrow resonances and strong field confinement can improve refractive-index sensing and medium perturbation detection, while large field gradients can support plasmonic tweezing and manipulation of nanoscale objects. Resonant plasmonic structures can modify the electromagnetic environment of nearby dipole sources and enhance radiative decay channels, providing a route toward brighter and more directional THz emitters. In nonlinear optics, the same local field enhancement can increase the nonlinear current sources and strengthen second-harmonic generation (SHG), which is important for near-field microscopy and label-free imaging.

Therefore, plasmonic metamaterials provide the physical basis for several application directions considered in this dissertation, while their intrinsic losses motivate the use of semiconductor plasmonics, collective resonances, and hybrid metasurface designs to improve spectral selectivity, tunability, and efficiency.

1.3 Waveguide Bragg Gratings

While metasurfaces manipulate free space radiation through engineered scattering at a sub-wavelength interface, WBGs operate within guided wave structures, shaping light through distributed coupling and phase-sensitive interference.

Periodic structures play a complementary role in guided wave devices through WBGs, where a periodic perturbation of the effective refractive index, introduced by an embedded grating layer, provides the phase matching required to couple a forward propagating wave to its backward counterpart. This distributed coupling produces a spectrally narrow reflection band around the Bragg wavelength, and therefore such waveguides can function as wavelength-selective reflectors and filters within a compact footprint [55]. Waveguide Bragg gratings also serve as efficient sensing tools, since even small perturbations in the effective index or the grating period can significantly shift the Bragg resonance wavelength [56]. Most importantly, when a grating layer is implemented along a waveguide containing a gain region, it forms the feedback mechanism of a distributed feedback (DFB) semiconductor laser, providing strong modal discrimination and enabling stable single-mode operation required for coherent optical sources in telecommunications and photonic integrated circuits (PICs) [57].

According to grating theory, the diffraction angle θ_d of the waves generated by a WBG can be described by [58]

$$\sin\theta_d = \frac{2m}{M} - 1, \tag{1.3}$$

where m is a positive or negative integer indicating the diffraction order, and M is the grating order defined as

$$M = \frac{2\Lambda N_{\text{eff}}}{\lambda}, \tag{1.4}$$

with Λ the grating period, N_{eff} the effective refractive index of the fundamental guided mode confined within the waveguide, and λ the operating wavelength satisfying the Bragg condition. In the ideal case of a first-order grating $(M = 1)$, corresponding to $\theta_d = \pm\pi/2$, the forward wave propagating along the longitudinal direction of the WBG couples directly to a backward propagating wave. In this case, the WBG supports two diffraction orders, $m = 0$ and $m = 1$, where coupling of light to the zeroth-order diffraction corresponds to the feed-forward effect along the waveguide, while coupling of light to the first-order diffraction generates the backward propagating wave that forms the feedback effect [58]. As a result, the WBG enables the forward and backward waves to couple to each other continuously as they propagate through the periodically perturbed structure along the longitudinal direction of the waveguide.

For higher-order WBGs with $M > 1$, the grating can support additional diffraction orders that couple propagating waves to radiative waves. These radiative waves scatter out of the waveguide, primarily perpendicular to the longitudinal direction, and escape from the WBG cavity, resulting in additional optical loss. Importantly, they also introduce additional coupling channels between the contra-directional propagating waves and therefore must be taken into account in the design of higher-order WBGs, particularly those employed in DFB laser sources operating in the telecom windows, which are the focus of the second part of this thesis.

1.3.1 Higher-Order Grating DFB Lasers

Selective feedback mechanism is particularly critical for semiconductor laser sources, where stimulated emission gain must be combined with precise spectral selection inside a cavity. Modern semiconductor lasers achieve this functionality through epitaxially grown heterostructures that simultaneously confine injected charge carriers and the optical mode. The evolution from single heterostructures [59] to double heterostructures [60], and subsequently to separate confinement heterostructures (SCHs) incorporating quantum well active regions [61], has enabled significantly lower threshold currents by optimizing both carrier confinement and waveguiding region. In these structures, the active region composition, typically based on III–V alloys such as InGaAsP or AlGaInAs, is engineered to provide optical gain at telecommunications wavelengths with minimal absorption loss [62]. The surrounding waveguide layers ensure strong transverse confinement, promote single-mode operation, and harness carrier diffusion and modal leakage into unwanted regions.

Early semiconductor lasers relied on Fabry–Perot cavities formed by cleaved facets, which provide broadband optical feedback and therefore support multiple longitudinal modes within the material gain bandwidth [63]. This multi-mode operation results in reduced spectral purity and wavelength stability, which is impractical for dense wavelength division multiplexing (DWDM) systems.

Distributed feedback lasers overcome this limitation by incorporating a periodic grating structure along the propagation direction of the waveguide [64]. The WBG provides distributed and wavelength-selective optical feedback by coupling counter-propagating guided waves at the Bragg wavelength. The resulting cavity exhibits strong modal discrimination, enabling stable single-mode operation with narrow linewidth and a high side-mode suppression ratio (SMSR), which is essential for coherent optical sources in modern optical communication infrastructures [65].

The performance, fabrication complexity, and efficiency of DFB lasers depend critically on how the Bragg grating is integrated with the active waveguide. Conventional high performance designs often employ buried gratings, in which the periodic corrugation is defined within or adjacent to the active region and requires an epitaxial regrowth process [66], as shown in Fig. 1.3(a). This approach maximizes the overlap between the optical mode and the grating region, resulting in high coupling coefficients and allowing for short cavity lengths [67].

However, the regrowth process significantly increases fabrication complexity and reduces manufacturing throughput. For telecommunications wavelengths, first-order gratings require small periods that challenge standard fabrication processes and often necessitate high-resolution patterning methods, such as electron-beam or deep-UV lithography [68]. Higher-order gratings relax this constraint by using larger periods that are more compatible with standard optical lithography, thereby improving fabrication tolerance and yield. However, higher-order designs introduce additional complexities, including contributions from radiative waves and higher-order partial modes, which can increase optical loss and threshold current. These limitations have motivated the development of regrowth-free grating implementations, which can be categorized into several platforms.

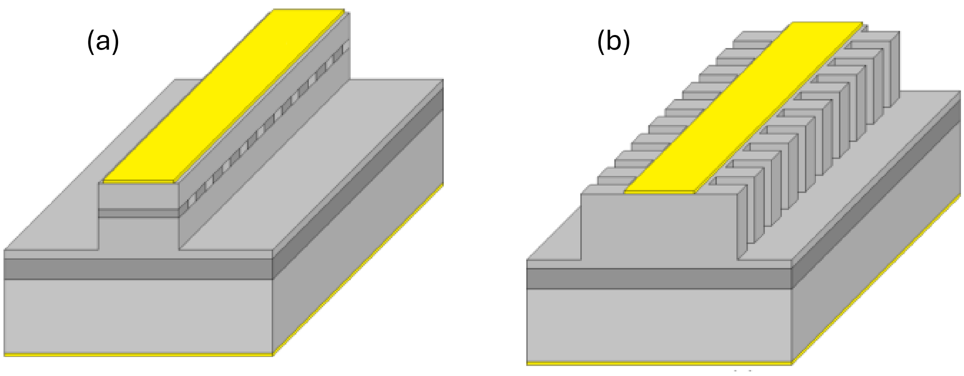

FIGURE 1.3: Representative implementations of WBGs for DFB laser cavities, including (a) a buried grating and (b) a laterally coupled etched grating formed along the ridge sidewalls. Reproduced from Lei [55] under the Creative Commons Attribution-NonCommercial-NoDerivs 2.5 License.

Surface-etched gratings are formed by etching a periodic trench pattern into the upper waveguide or cladding layers above the active region [69], as shown in Fig. 1.3(b) and Fig. 1.4. This approach eliminates epitaxial regrowth and can provide substantial refractive index contrast between etched and unetched regions, enabling a high coupling coefficient. However, it requires precise control over the etch depth to balance coupling strength against scattering loss while maintaining sufficient optical confinement. Therefore, the separation between the grating bottom and the upper boundary of the waveguiding part must be optimized to ensure adequate overlap between the guided mode and the grating perturbation, while keeping modal scattering losses minimized.

Laterally coupled gratings implement the periodic perturbation using grooves etched on both sides of a ridge waveguide [70], as shown in Fig. 1.3(b). In this configuration, the guided mode interacts with the grating through its evanescent field, leading to weaker coupling compared to buried gratings but offering a simplified fabrication process. The grating can be patterned concurrently with ridge definition in a single etch step, eliminating additional epitaxial processes. The resulting coupling coefficient is highly sensitive to geometric parameters, particularly the ridge waveguide dimensions and the grating geometry. A ridge with a larger height generally provides stronger lateral confinement and reduces the evanescent overlap between the guided mode and the grating region, which decreases the coupling strength. In contrast, a shallower ridge increases the interaction of the guided mode with the lateral grating grooves and can enhance the coupling coefficient. The ridge width introduces additional trade-offs. A narrow ridge increases fabrication difficulty and electrical resistance, whereas a wider ridge spreads the current distribution in the active region and increases the mode size, which can reduce the optical confinement. From the grating side, increasing the groove depth can increase modal overlap with the grating region and strengthen coupling, whereas shallow gratings can bring the guided mode closer to the metal contacts, which can increase absorption loss. Accordingly, a laterally coupled grating design requires an optimized groove depth and high-quality vertical corrugations, together with a balanced ridge width and height, to maximize the coupling coefficient while maintaining low modal loss [58].

Metal-assisted gratings incorporate periodic metallic features positioned on the waveguide surface or along ridge sidewalls [71]. While attractive due to their compatibility with regrowth-free fabrication, these designs introduce additional optical absorption that can degrade laser efficiency and increase threshold current. Design strategies typically involve thick cladding layers for the waveguiding parts [72] to isolate the guided mode from metallic contacts and careful optimization of ridge dimensions [71] to balance modal overlap with absorption losses.

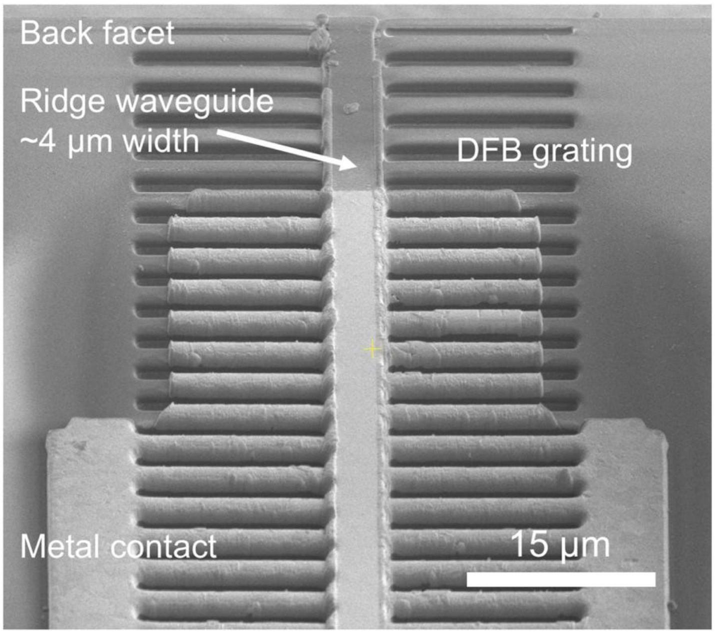

FIGURE 1.4: Scanning electron micrograph (SEM) of a high-order DFB surface grating fabricated by focused ion beam (FIB) etching on an InGaN/GaN green ridge-waveguide laser diode. Adapted from Holguín-Lerma *et al.* [73] under the Creative Commons Attribution 4.0 License.

The recent shift toward photonic integrated circuits (PICs) in optical communication networks further constrains DFB laser design, since the semiconductor laser must function as a coherent on-chip source monolithically integrated with modulators, multiplexers, detectors, and passive routing waveguides. Regrowth-free integration strategies are particularly important in this context. Vertical integration approaches address a key bottleneck by enabling multiple waveguide layers within a single epitaxial stack, allowing efficient coupling between active and passive components through tapered vertical transitions [74]. In such architectures, the grating must provide sufficient optical feedback without disrupting vertical mode transfer or requiring complex regrowth processes. Consequently, surface-etched and laterally coupled higher-order gratings have emerged as promising solutions, offering a viable pathway toward compact and efficient DFB lasers compatible with advanced PIC platforms [75].

Accurate electromagnetic modeling methods that account for the interaction between guided and radiative waves are therefore essential for designing efficient higher-order DFB lasers with high SMSR and narrow-linewidth operation [76, 77]. To analyze these structures, coupled-wave theory provides a practical framework for relating the physical grating geometry and optoelectronic parameters of a DFB cavity to its threshold response. Starting from the classical coupled-wave description of DFB lasers, the forward and backward propagating fields can be solved under steady-state conditions with appropriate boundary conditions to obtain the threshold gain and detuning eigenvalues of the cavity [77, 78]. This threshold-oriented analysis, also discussed in the optoelectronic device modeling framework of Xun Li [79], allows important parameters such as optical loss, confinement factor, material gain, bias-induced refractive-index change, and facet reflectivity to be included directly in the coupled-wave equations. For higher-order gratings, the same formulation can be extended by incorporating direct and indirect coupling coefficients associated with radiative waves and partial modes, so that their influence on the eigenvalues, threshold response, and longitudinal mode discrimination can be evaluated at lasing onset. Therefore, a steady-state coupled-wave model provides an efficient route to assess the near-threshold behavior of practical higher-order DFB lasers without solving the full time-dependent carrier and photon rate equations, while still capturing the dominant mechanisms that determine stable single-mode operation.

By engineering the coupling-coefficient parameters within this framework, the threshold response and the required cavity length can be accurately estimated. This makes the modeling method a practical tool for optimizing the output characteristics of higher-order DFBLs toward narrow-band operation, high SMSR, and stable continuous wave (CW) output power.

1.4 Thesis Structure

This thesis is organized into two main parts. The first part investigates sub-wavelength metamaterials and metasurfaces as thin, periodically structured layers in which light–matter interactions are governed by scattering phenomena, and the resulting optical responses are emitted incoherently in all directions. Metasurfaces, as thin grating layers, enable unprecedented control over diffracted waves and inherently overcome the conventional limitations of bulky components, such as phase-matching, phase accumulation, and refractive-index contrast. This dissertation is presented in a paper-based format and includes four published journal articles and one manuscript in preparation.

Part One comprises five chapters. Chapter 2 establishes the fundamental physics of linear and nonlinear metamaterials and metasurfaces designed in this thesis. Chapter 3 presents a published study on III–V semiconductor metasurfaces exhibiting exceptional THz electromagnetic responses arising from collective lattice plasmonic resonances. Chapter 4 discusses a published paper focusing on emission enhancement in coupled emitter–antenna systems, achieved through III–V resonant metamaterials using a semi-numerical design framework. Chapters 5 and 6 are related to nonlinear plasmonic metasurfaces. Chapter 5 investigates the design and characterization of a UV–visible metasurface for second-harmonic generation (SHG) microscopy applications, while Chapter 6 introduces an optimized plasmonic metasurface design to improve near-field SHG microscopy performance.

The second part focuses on guided wave components, where optical responses arise from refractive index-based guiding principle and total internal reflection in wavelength-scale structures. In contrast to the scattering-based systems of Part One, these guided wave structures are highly sensitive to phase interference effects. Waveguides and grating waveguides are key components in this category, forming the foundation for the devices such as semiconductor lasers.

Chapter 7 presents the theoretical framework for light propagation in grating waveguides using modified coupled wave equations, with particular emphasis on DFB laser design. Chapter 8 is devoted to the study of a practical on-chip third-order grating waveguide DFB laser, which achieves a narrow-bandwidth response in the telecommunication band.

Chapter 9 concludes the thesis by outlining prospective research directions and future developments based on the studied photonic components.

Chapter 2

Linear and Nonlinear Metamaterials and Metasurfaces

2.1 Introduction

When light, as an electromagnetic wave, impinges upon an object, it will scatter in all directions. Depending on the object's geometrical and electromagnetic properties, the incident and scattered electromagnetic fields have distinct properties [80]. The object's features seem to be encoded in the scattered field, and one can extract these features by solving the scattering problems. The optimal method for solving the scattering problem is determined based on the effective size of the scatterer relative to the incident wavelength.

Quasi-Static Approximation (QSA) method [30] allows one to evaluate the scattering response of the sub-wavelength particles by treating them as spheres that only support electric dipole (ED) moments. By exciting the spherical particle in a homogeneous medium with a linearly polarized plane wave, the induced polarizability of the particle is defined as

$$\alpha\left(\omega\right) = 4\pi r^3 \frac{\varepsilon(\omega)\,\varepsilon_m}{\varepsilon(\omega) + 2\varepsilon_m}\,, \tag{2.1}$$

where r is the sphere radius, $\varepsilon(\omega)$, and ε_m are dielectric functions of the sphere's material and its surrounding medium, respectively. A Drude-Lorentz model is a conventional method to define the dielectric function of a material [81], described by

$$\varepsilon(\omega) = \varepsilon_\infty - \frac{\omega_p^2}{\omega^2 + i\gamma_D\omega} + \sum_{j=1} \frac{f_j}{\omega_j^2 - \omega^2 - i\gamma_j\omega}\,, \tag{2.2}$$

where ε_∞ is the high-frequency permittivity, ω_p is the plasma frequency of free electrons, and γ_D is the damping constant for free electron oscillations. The second summation term represents the contributions from bounded electron vibrations, each with a Lorentz frequency of ω_j, a damping constant of γ_j, and an oscillator strength of f_j.

The material's dispersive dielectric permittivity dictates how the particle responds to the incident light, and its real and imaginary parts describe the stored and dissipated energies by the particle, respectively. The sign and magnitude of the dielectric permittivity can also determine the optical behavior of the particle, categorized into plasmonic, epsilon-near-zero (ENZ), and dielectric responses. Knowing the dielectric permittivity and the polarizability enables us to calculate the scattering cross-section (SCS) and absorption cross-section (ACS) of the sub-wavelength particle, as follows [80]

$$C_{\text{sca}}(\omega) = \frac{8\pi}{3}\left(\frac{\omega^4}{c^4}\right)|\alpha(\omega)|^2, \tag{2.3}$$

$$C_{\text{abs}}(\omega) = \frac{4\pi\omega}{c}\text{Im}[\alpha(\omega)]. \tag{2.4}$$

In the following Section, we present the scattering responses of spherical particles using the QSA method to compare light-matter interactions for these three different optical behaviors.

2.2 Plasmonic Materials

Plasmonic materials exhibit distinctive optical properties when the real part of their permittivity becomes negative, caused by the interaction of incident light with free carriers at the particle's surface [30]. This interaction results in localized surface plasmon resonances (LSPRs) highly dependent on the particle's size, shape, and the surrounding medium's refractive index. The primary advantage of plasmonic materials is their ability to localize light at the nanoscale, beyond the diffraction limit, significantly enhancing local electromagnetic fields. This feature is critical to scaling down the optical components and improving the performance of imaging, sensing, and filtering applications [82].

Noble metals, such as gold, are widely used in plasmonic applications across a broad frequency range. Figure 2.1 shows the optical properties of a single gold sphere with three different radii. The complex permittivity of the

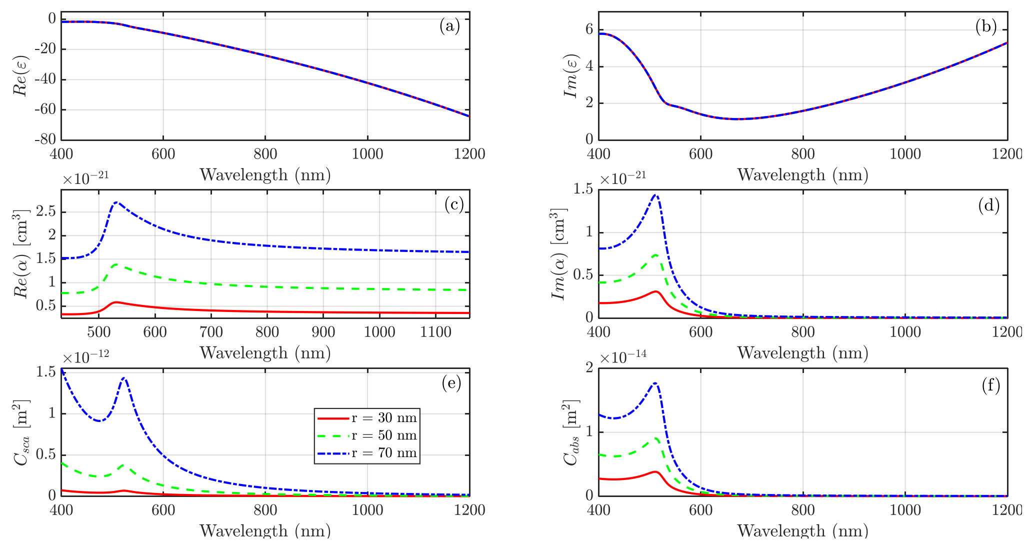

FIGURE 2.1: (a) Real and (b) imaginary parts of gold permittivity. (c) The real and (d) imaginary parts of polarizability for gold nanoparticles with three different radii. (e) The SCS and (f) the ACS of gold nanoparticles.

material was extracted from a database which is defined based on the Drude model [83]. As shown in Fig. 2.1(a) and (b), the nanoparticle exhibits a negative real part and a positive imaginary part of the permittivity at frequencies below the plasma frequency. The polarizability of nanoparticle, as mentioned in Eq. (2.1), goes to infinity at this specific wavelength range due to the Frohlich condition of $\varepsilon(\omega) \approx 2\varepsilon_m$ [30], corresponding to the LSPR phenomena (Fig. 2.1(c) and (d)). At the LSPR wavelength, the optical response of the plasmonic particle is governed by two main types of light–matter interaction channels. Radiative interaction is defined as the diffracted waves escaping into free space, and a non-radiative process involves light absorption by the plasmonic particle. The scattered and absorbed powers can be calculated from Eq. (2.3) and (2.4), respectively, as shown in Fig. 2.1(e) and 2.1(f). The pronounced maxima in these spectra highlight the strong impact of LSPRs. Furthermore, both SCS and ACS increase with the particle radius.

However, plasmonic materials show huge joule heating losses mainly due to the imaginary part of the permittivity, impairing the efficiency of plasmonic devices. Overcoming these losses is one of the main challenges in plasmonics, such that most recent research focuses on reducing heat generation while maintaining localized field enhancement [23].

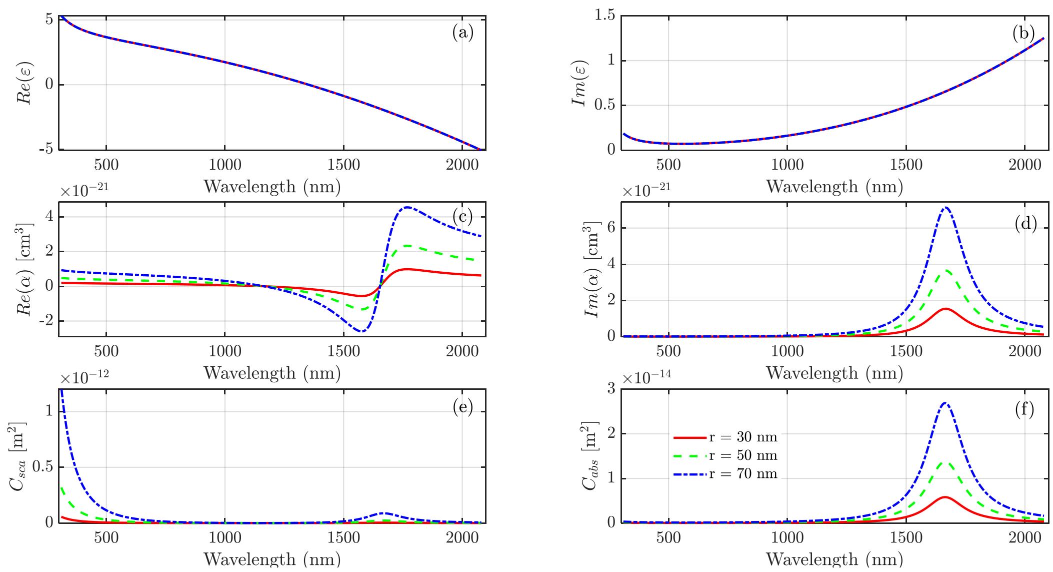

FIGURE 2.2: (a) Real and (b) imaginary parts of the permittivity of ITO. (c) Real and (d) imaginary parts of polarizability for ITO nanoparticles with three different radii. (e) The SCS and (f) ACS of ITO nanoparticles.

2.3 ENZ Materials

Epsilon-near-zero (ENZ) materials exhibit a real part of the permittivity close to zero over a finite spectral range, leading to very weak phase accumulation and an almost spatially uniform phase inside the medium [84]. The near-zero real permittivity also makes the refractive index highly sensitive to optical intensity, substantially enhancing nonlinear effects for all-optical phase modulation and beam steering applications [85].

The optical properties of Indium tin oxide (ITO) nanoparticles have been studied to demonstrate the light-matter interactions of ENZ materials. Figure 2.2 shows the optical response of an ITO sphere with different radii, such that the material's complex permittivity is extracted from experimental data [83], shown in Fig. 2.2(a) and (b). As shown in Fig.2.2(c), the nanoparticle exhibits very weak polarizability within the ENZ region (1050 nm $<\lambda<$ 1450 nm), where the imaginary part of polarization is also negligible (Fig.2.2(d)). Scattering and absorption responses are dependent on polarizability. When the real part of the polarizability goes to zero, the nanoparticle is transparent with a minimum interaction with light, rendering the particle invisible. Accordingly, the nanoparticle's interaction with light results in almost zero SCS within the ENZ region, as shown in Fig.2.2(e) and (f), respectively. The ITO nanoparticle demonstrates plasmonic behavior and

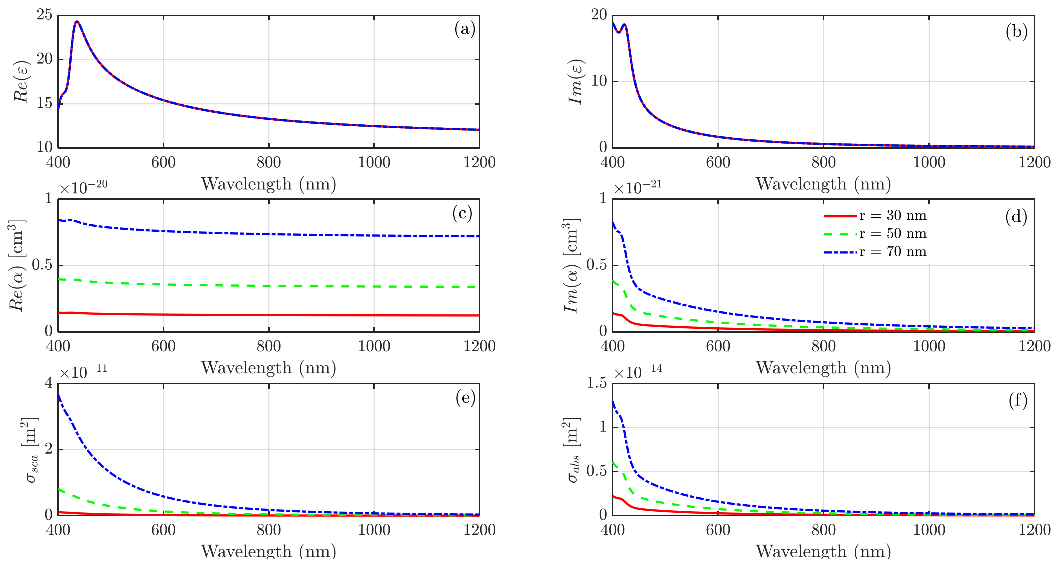

FIGURE 2.3: (a) Real and (b) imaginary parts of GaAs permittivity. (c) Real and (d) imaginary parts of polarizability for GaAs nanoparticles with three different radii. (e) and (f) show the SCS and ACS of GaAs nanoparticles, respectively.

experiences a transition from invisibility to the plasmonic region at longer wavelengths. However, utilizing ENZ materials presents challenges due to material losses, particularly at optical frequencies.

2.4 Dielectric Materials

High-index materials with low losses enable efficient light manipulation by exciting electrical displacement oscillating current within the nanoparticles [37]. Unlike plasmonic and ENZ particles, where conductive currents are excited at the surface, high-index nanoparticles are excited by resonant displacement currents inside their volume [86]. The low losses of these materials mitigate Joule heating and absorption losses that limit the efficiency of plasmonic and ENZ structures. High-index nanoparticles are particularly attractive for applications such as high-Q resonators and directional scattering with low energy dissipation [41, 87]. The permittivity of such materials can be described solely by the Lorentz term, since the negligible contribution of free carriers in high-index dielectrics and semiconductors removes dependence of their permittivity on the plasma frequency.

Figure 2.3 shows the optical properties of Gallium arsenide (GaAs) nanoparticles to clarify the light-matter interaction of high-index materials whose permittivity was extracted from the experimental database [83]. As shown in Fig. 2.3(a) and (b), GaAs nanoparticles exhibit two different types of optical response due to the band gap energy of GaAs, a typical III–V semiconductor. Below the band gap ($\lambda < 870\,\text{nm}$), the material experiences significant interband absorption, resulting in large non-radiative losses that strongly enhance the absorption process. Above the band gap ($\lambda > 870\,\text{nm}$), the permittivity becomes real with a trivial imaginary contribution, indicating that the scattering processes dominate. More generally, III–V semiconductors such as GaAs are recognized as efficient scatterers in the terahertz (THz) regime, where the free-carrier contribution described by the Drude model plays an important role [46].

Figure 2.3(c) and (d) show the real and imaginary parts of the polarizability, where its real part increases with nanoparticle size and the imaginary part remains significant at shorter wavelengths. At longer wavelengths, the imaginary part of the polarizability approaches zero. Hence, there is no room for non-radiative channels to dissipate the optical power. Figure 2.3(e) and (f) present the SCS and ACS of the GaAs nanoparticles, respectively, highlighting that GaAs nanoparticles achieve higher SCS and ACS compared to plasmonic and ENZ counterparts.

The QSA is a simple and fast tool to estimate the scattering behavior of deep sub-wavelength spherical objects. It simplifies the Maxwell equations by assuming a static electric field across the particle. However, this approach loses its validity when the particle dimensions become comparable to or exceed the incident light wavelength. To circumvent this limitation, the subsequent section is devoted to a semi-numerical framework that enables the precise calculation of the scattering problem for particles of arbitrary shapes and sizes at different wavelength ranges. By incorporating near-field and far-field interactions, this approach provides a comprehensive analysis of the scattering phenomena, allowing for efficient design of the sub-wavelength optical antennas.

2.5 Induced Linear Current Density Method

The interaction of an monochromatic electric field with an arbitrarily shaped object induces an oscillating electric current density, $\mathbf{J}(\mathbf{r}', \omega)$, which serves as the source of scattered or radiated electromagnetic field [80]. This current density arises from both free and bound charges within the material at each position of $\mathbf{r}'$ and is described by [88]

$$\mathbf{J}(\mathbf{r}',\omega) = -i\omega\varepsilon_0\big[\varepsilon(\omega) - \varepsilon_b(\omega)\big]\,\mathbf{E}(\mathbf{r}',\omega)\,, \tag{2.5}$$

where $\varepsilon(\omega)$ is the complex permittivity of the object, $\varepsilon_b(\omega)$ is the permittivity of surrounding background medium, ω is the angular frequency of the field, and $\mathbf{E}(\mathbf{r}',\omega)$ is the total electric field inside the object, often obtained numerically via full-wave simulations (e.g., using COMSOL Multiphysics [89]). The scattered electric field outside the object can be defined within the framework of Green's tensor formalism, as [90]

$$\mathbf{E}_{\text{sca}}(\mathbf{r}) = i\omega\mu_0 \int_{V_s} \hat{\mathbf{G}}(\mathbf{r},\mathbf{r}') \cdot \mathbf{J}(\mathbf{r}')\, d^3\mathbf{r}'\,, \tag{2.6}$$

where the dyadic Green's function acts as the propagator operator connecting localized current sources to the radiated or scattered field carrying multipole moments. Here, $\mathbf{r}$ denotes the observation point, V_s is the object volume, and k_d is the wavenumber in the homogeneous background medium. In the far-field regime, $r = |\mathbf{r}| \gg |\mathbf{r}'|$, the distance can be approximated as $|\mathbf{r}-\mathbf{r}'| \approx r - \mathbf{n}\cdot\mathbf{r}'$ with $\mathbf{n} = \mathbf{r}/r$ that denotes the unit vector of the propagation direction toward the observation point [90]. Dyadic Green's function of the homogeneous background medium can be defined by [80, 88]

$$\hat{\mathbf{G}}_{\text{s}}(\mathbf{r},\mathbf{r}') = \frac{e^{ik_d r}}{4\pi r}(\hat{I} - \mathbf{nn})\, e^{-ik_d(\mathbf{n}\cdot\mathbf{r}')}\,, \tag{2.7}$$

where $(\hat{I} - \mathbf{nn})$ is the transverse projection dyadic tensor that filters out the longitudinal component of the field along $\mathbf{n}$. By substituting Eq. (2.7) into Eq. (2.6), the far-field scattered field is determined by

$$\mathbf{E}_{\text{sca}}(\mathbf{r}) = i\omega\mu_0 \frac{e^{ik_d r}}{4\pi r}\,(\hat{I} - \mathbf{nn}) \int_{V_s} e^{-ik_d(\mathbf{n}\cdot\mathbf{r}')}\mathbf{J}(\mathbf{r}')\, d^3\mathbf{r}'. \tag{2.8}$$

The exponential factor $e^{-ik_d(\mathbf{n}\cdot\mathbf{r}')}$, which accounts for the accumulated phase delay from each source point $\mathbf{r}'$ inside the object, plays a central role in the decomposition of multipole moments [91]. An exact spherical multipole decomposition can be found from Eq. (2.8) in the Cartesian basis by employing the plane wave representation in terms of spherical harmonics [90], as below

$$e^{-ik_d(\mathbf{n}\cdot\mathbf{r}')} = 4\pi \sum_{l=0}^{\infty} \sum_{m=-l}^{l} (-i)^l j_l(k_d r') Y_{lm}^*(\theta,\phi) Y_{lm}(\theta',\phi'), \tag{2.9}$$

where $j_l(k_d r')$ denotes the l-order spherical Bessel function and Y_{lm} are the scalar spherical harmonics. Here, $\mathbf{r}' = (r',\theta',\phi')$ is the source point inside the object in spherical coordinates, $\mathbf{n} = (\theta,\phi)$ is the unit vector toward the observation point, that angles of θ and ϕ (θ' and ϕ') are the polar and azimuthal angles of $\mathbf{n}$ ($\mathbf{r}'$) in the spherical coordinate system [90]. By replacing this expansion into Eq. (2.8), the scattered field becomes

$$\begin{aligned} \mathbf{E}_{\mathrm{sca}}(\mathbf{r}) =& i\omega\mu_0 \frac{e^{ik_d r}}{4\pi r} \left(\hat{I} - \mathbf{nn}\right) \\ &\times \sum_{l,m} 4\pi(-i)^l Y_{lm}^*(\theta,\phi) \int_{V_s} j_l(k_d r') Y_{lm}(\theta',\phi') \mathbf{J}(\mathbf{r}') d^3\mathbf{r}'. \end{aligned} \tag{2.10}$$

At this step, by substituting the spherical harmonics with the l-order Legendre polynomial of P_l, the scattered field can be written as [90]

$$\begin{aligned} \mathbf{E}_{\mathrm{sca}}(\mathbf{r}) =& i\omega\mu_0 \frac{e^{ik_d r}}{4\pi r} \left(\hat{I} - \mathbf{nn}\right) \\ &\times \sum_{l=0}^{\infty} (-i)^l (2l+1) \int_{V_s} j_l(k_d r') P_l(\cos\gamma) \mathbf{J}(\mathbf{r}')\, d^3\mathbf{r}', \end{aligned} \tag{2.11}$$

where $\mathbf{n} = \mathbf{r}/r = (\sin\theta\cos\phi, \sin\theta\sin\phi, \cos\theta)$ is the unit vector pointing toward the observation direction, and $\mathbf{n}' = \mathbf{r}'/r' = (\sin\theta'\cos\phi', \sin\theta'\sin\phi', \cos\theta')$ is the source coordinate inside the object. The angle γ between $\mathbf{n}$ and $\mathbf{n}'$ is defined as $\cos\gamma = \mathbf{n}\cdot\mathbf{n}' = \cos\theta\cos\theta' + \sin\theta\sin\theta'\cos(\phi-\phi')$.

Equation (2.11) defines the scattered field as a multipole expansion where the angular dependence is governed by $P_l(\cos\gamma)$ [90]. The corresponding Cartesian multipole moments are systematically extracted through a transformation procedure consisting of symmetrization, which ensures full index symmetry of the Cartesian tensors, and detracing, which removes redundant trace components [92, 93]. This procedure yields the irreducible Cartesian multipole tensors that are consistent with the spherical representation and introduced in the following equations [94], as

$$p_\alpha = -\frac{1}{i\omega}\left[\int J_\alpha \, dv + \frac{k^2}{10}\int \left((\mathbf{J}\cdot\mathbf{r})r_\alpha - 2r^2 J_\alpha\right) dv \right. \\ \left. + \frac{k^4}{280}\int \left(3r^4 J_\alpha - 2r^2(\mathbf{r}\cdot\mathbf{J})r_\alpha\right) dv\right], \tag{2.12}$$

$$m_\alpha = \frac{1}{2}\left[\int (\mathbf{r}\times\mathbf{J})_\alpha \; dv \; - \frac{k^2}{10}\int r^2 \left(\mathbf{r}\times\mathbf{J}\right)_\alpha \; dv\right], \tag{2.13}$$

$$Q^e_{\alpha\beta} = -\frac{1}{i\omega}\left[\int \left(r_\alpha J_\beta + r_\beta J_\alpha - \frac{2}{3}(\mathbf{r}\cdot\mathbf{J})\delta_{\alpha\beta}\right) dv \right. \\ \left. + \frac{k^2}{42}\int \left(4(\mathbf{r}\cdot\mathbf{J})r_\alpha r_\beta + 2\delta_{\alpha\beta}(\mathbf{r}\cdot\mathbf{J})r^2 - 5r^2(r_\alpha J_\beta + r_\beta J_\alpha)\right) dv\right], \tag{2.14}$$

$$Q^m_{\alpha\beta} = \frac{1}{3}\left[\int \left(r_\alpha(\mathbf{r}\times\mathbf{J})_\beta + r_\beta(\mathbf{r}\times\mathbf{J})_\alpha\right) dv \right. \\ \left. - \frac{k^2}{4}\int r^2 \left(r_\alpha(\mathbf{r}\times\mathbf{J})_\beta + r_\beta(\mathbf{r}\times\mathbf{J})_\alpha\right) dv\right], \tag{2.15}$$

$$O^e_{\alpha\beta\gamma} = -\frac{1}{i\omega}[\int r_\alpha r_\beta J_\gamma + r_\beta r_\gamma J_\alpha + r_\gamma r_\alpha J_\beta - \frac{1}{5}\delta_{\alpha\beta}\left(r^2 J_\gamma + 2\left(\mathbf{r}.\mathbf{J}\right) r_\gamma\right) \\ -\frac{1}{5}\delta_{\beta\gamma}\left(r^2 J_\alpha + 2\left(\mathbf{r}.\mathbf{J}\right) r_\alpha\right) - \frac{1}{5}\delta_{\gamma\alpha}\left(r^2 J_\beta + 2\left(\mathbf{r}.\mathbf{J}\right) r_\beta\right) \; dv], \tag{2.16}$$

$$O^m_{\alpha\beta\gamma} = \frac{1}{24}[\int \left(r_\alpha r_\beta \left(\mathbf{r}\times\mathbf{J}\right)_\gamma + r_\beta r_\gamma \left(\mathbf{r}\times\mathbf{J}\right)_\alpha + r_\gamma r_\alpha \left(\mathbf{r}\times\mathbf{J}\right)_\beta\right) \\ -\frac{1}{5}\delta_{\alpha\beta} r^2 \left(\mathbf{r}\times\mathbf{J}\right)_\gamma - \frac{1}{5}\delta_{\beta\gamma} r^2 \left(\mathbf{r}\times\mathbf{J}\right)_\alpha - \frac{1}{5}\delta_{\gamma\alpha} r^2 \left(\mathbf{r}\times\mathbf{J}\right)_\beta \; dv], \tag{2.17}$$

and, hence the SCS from object can be defined in terms of multipole moments obtained by Eq. (2.12) to Eq. (2.17), as

$$
\begin{aligned}
C_{\text{sca}}^{\text{tot}} = &\frac{k^4}{6\pi\varepsilon_0^2|E_{\text{inc}}|^2}|p_\alpha|^2 + \frac{k^4}{6\pi c^2\varepsilon_0^2|E_{\text{inc}}|^2}|m_\alpha|^2 + \frac{k^6}{160\pi\varepsilon_0^2|E_{\text{inc}}|^2}\sum_{\alpha\beta}|Q^e_{\alpha\beta}|^2 \\
&+ \frac{k^6}{80\pi c^2\varepsilon_0^2|E_{\text{inc}}|^2}\sum_{\alpha\beta}|Q^m_{\alpha\beta}|^2 + \frac{k^8}{1890\pi\varepsilon_0^2|E_{\text{inc}}|^2}\sum_{\alpha\beta\gamma}|O^e_{\alpha\beta\gamma}|^2 \\
&+ \frac{k^8}{1890\pi c^2\varepsilon_0^2|E_{\text{inc}}|^2}\sum_{\alpha\beta\gamma}|O^m_{\alpha\beta\gamma}|^2.
\end{aligned}
\tag{2.18}
$$

Here p_α/m_α, $Q^e_{\alpha\beta}/Q^m_{\alpha\beta}$, and $O^e_{\alpha\beta\gamma}/O^m_{\alpha\beta\gamma}$ are electric/magnetic dipole moments, electric/magnetic quadrupole moments, and electric/magnetic octupole moments, respectively. c is the speed of light, E_0 represents the electric field magnitude of the incident light, and $\alpha, \beta, \gamma = x, y, z$.

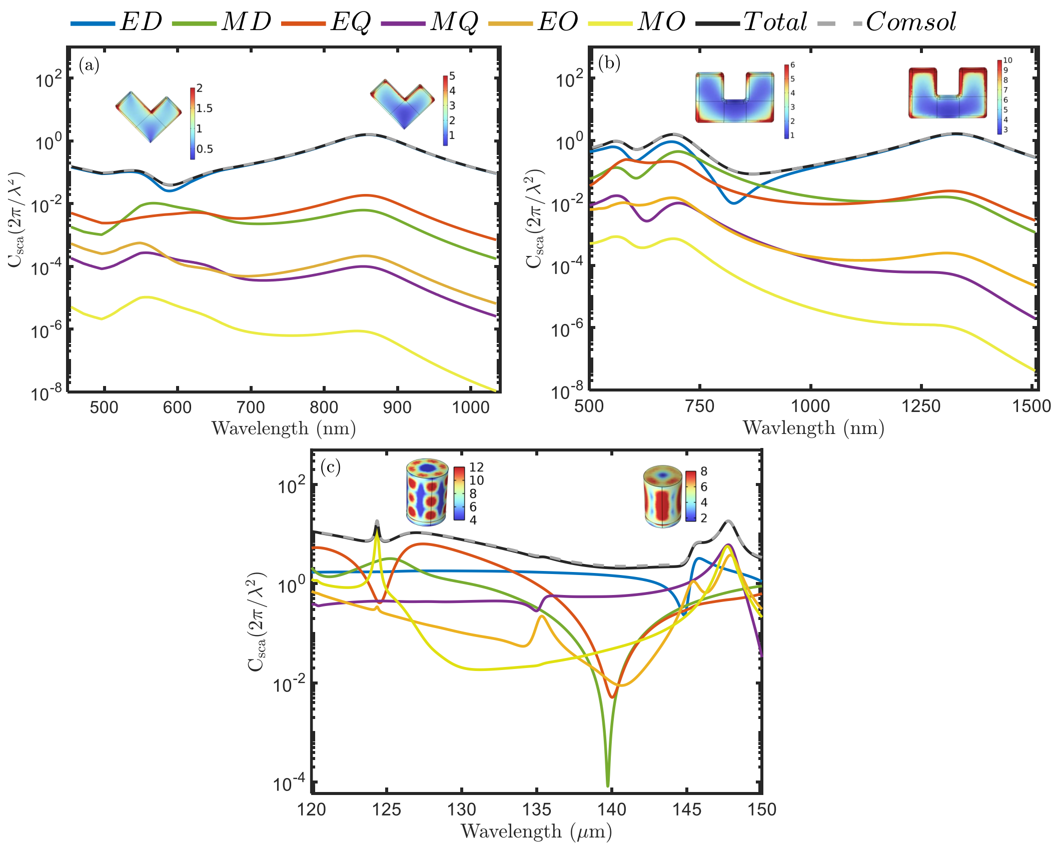

FIGURE 2.4: (a) Multipole contributions to the SCS spectral response of an L-shaped plasmonic particle, showing a zenith at the LSPR wavelength corresponding to an ED mode. (b) SCS of a U-shaped plasmonic particle, dominated by ED, EQ, and MD modes. (c) SCS of a cylindrical hybrid InSb–Si structure in the THz range, featuring an ultra-narrow MO mode.

At the end of this section, we study the scattering characteristics of objects varying in shape, size, material composition, and operating wavelength range. This investigation verifies the accuracy of the semi-numerical method compared to the direct simulation performed using Comsol software. Figure 2.4(a) demonstrates the SCS of an L-shaped gold nanoparticle, with an effective area of 5×10^{-15} m^2, subjected to a linearly $x-$polarized plane wave, with a propagation constant along the $z-$axis. The nanoparticle, composed of a conventional plasmonic material, demonstrates LSPRs characterized by high local field enhancement. The L-shaped particle mainly supports a dominant ED mode within the visible region due to its relatively small effective area. The second study focuses on the SCS of a U-shaped gold nanoparticle exhibiting plasmonic properties within the studied spectral range. With an effective area of 8×10^{-15}m^2, this nanoparticle supports LSPRs at the surface of its horizontal and vertical arms under the same illumination setup. ED resonances emerge primarily due to the LSPRs driven by surface-induced currents along its arms. A unique aspect of the U-shaped geometry is the support of circular induced currents in the gap between vertical arms, leading to contribution of EQ and MD resonances to the SCS response around the wavelength of 750 nm. As illustrated in Fig. 2.4(b), the SCS of U-shaped particle is notably higher than that of the L-shaped counterpart, primarily due to the involvement of higher-order multipole moments in the scattering response. As the next design, we consider a cylindrical hybrid structure composed of indium antimonide (InSb) at the bottom with a radius of 25 μm and a thickness of 7 μm, and silicon (Si) on top with a radius of 25 μm and a thickness of 70 μm. The structure is excited by a z-polarized plane wave with the wavevector along x- direction in the THz region, where the scatterer exhibits dielectric behavior. Figure 2.4(c) depicts the design's scattering spectral response based on the contribution of multipole moments. The electric displacement current induces high Q resonances, particularly a MO mode around the wavelength of 125 μm. The SCS magnitude of this dielectric structure exceeds that of its plasmonic counterparts due to the size dependency of scattered power. Furthermore, the linewidth of resonances is significantly narrower than that of plasmonic resonances due to the negligible losses in dielectric particles.

As shown in Fig. 2.4, the induced current method evaluates the scattering response of single particles as the smallest building blocks of photonic networks, referred to as meta-atoms in the visible region and meta-molecules in the THz. Engineering their SCS through induced multipole moments is central to designing optical antennas for field-enhanced spectroscopy [95] and surface-enhanced Raman scattering applications [96] at sub-wavelength scales. Such antennas can also amplify, direct, and reshape the spontaneous emission (SE) of nearby quantum emitters [41, 97], providing a versatile platform for controlling light–matter interaction beyond the diffraction limit [98, 99].

2.5.1 Optical Antennas

Spontaneous emission rate of a quantum emitter, such as an atom, molecule, or quantum dot, is not an intrinsic fixed property. Following Edward Purcell's pioneering work [100], the SE rate can be tailored by embedding the emitter in a structured electromagnetic environment. In such medium, the local density of optical states (LDOS), or the density of available electromagnetic modes for transitions in the emitter, can be strongly modified via radiative and non-radiative energy exchange between the emitter and its surroundings. Conventionally, the SE rate modification has been achieved using microcavities and photonic crystals, where the enhancement factor is estimated by the Purcell factor [98], as

$$F_{\mathrm{P}} = \frac{\Gamma_{\mathrm{rad}}}{\Gamma_0} \approx \frac{3}{4\pi^2}\left(\frac{\lambda}{n}\right)^3 \frac{Q}{V}, \tag{2.19}$$

where Q is the quality factor, V is the effective mode volume, λ is the cavity resonant wavelength, n is the refractive index of the surrounding medium, Γ_{rad} and Γ_0 are the radiative decay rates of the emitter in presence and absence of the closed cavity or surrounding medium, respectively. However, achieving a high Q factor in such bulky resonators often requires a long optical propagation length, which limits their compactness and suitability for applications requiring control at sub-wavelength scales.

Resonant optical antennas, such as the meta-atoms and meta-molecules introduced in Section 2.5, have been proposed as efficient alternatives to bulky closed cavities for sub-wavelength applications [101]. These antennas support induced multipole moments as resonant modes that can couple to the transition dipole moments of nearby quantum emitters in the near field region.

From a quantum mechanical perspective, placing a two-level emitter, or dipole source, in the near field of a resonant antenna modifies its relaxation lifetime of the excited carriers. In many cases, this results in an accelerated

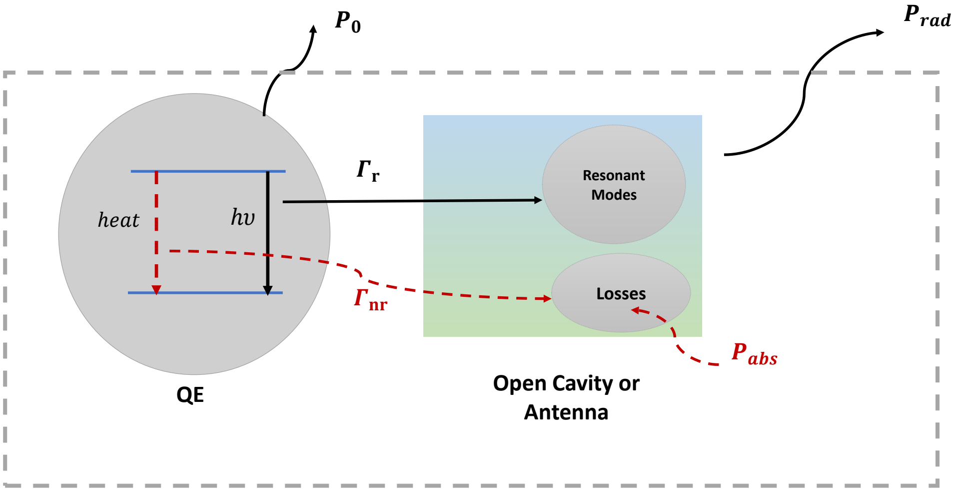

FIGURE 2.5: Schematic of radiative and non-radiative coupling channels in a coupled emitter–antenna system, leading to SE rate modification of the quantum emitter.

radiative decay and thus an enhanced SE rate. From the perspective of classical electrodynamics, which is consistent with quantum intuition, the coupled emitter–antenna system can be regarded as an open cavity, where the antenna's scattered waves determine the enhancement of photon production rate of the dipole source. As schematically presented in Fig. 2.5, the total decay rate of an emitter near the antenna is sum of radiative and non-radiative contributions as $\Gamma_{\text{tot}} = \Gamma_{\text{rad}} + \Gamma_{\text{nr}}$ that can be approximated by [41]

$$\begin{aligned} \frac{\Gamma_{\text{rad}}}{\Gamma_0} &= \frac{P_{\text{sca}}}{P_0}, \\ \frac{\Gamma_{\text{nr}}}{\Gamma_0} &= \frac{P_{\text{abs}}}{P_0}, \end{aligned} \tag{2.20}$$

where P_{sca} and P_{abs} are the scattered and absorbed powers by the antenna, respectively, and P_0 is the emitted power by the dipole source in the absence of antenna. The radiative channel corresponds to scattered power escaping into the far-field, while the non-radiative channel accounts for power dissipated within the antenna due to absorption. As highlighted in Eq. (2.20), engineering the SCS of individual antenna through multipole moments defines its resonant modes. This is critical for applications requiring enhanced directional emission and also the development of single-photon sources with ultra-high radiative decay rates [102, 103].

In the next section, we extend the discussion from single antenna to ensembles comprising millions of meta-atoms or meta-molecules that enable practical device fabrication and provide greater freedom in tailoring light–matter interactions.

2.6 Linear Metasurfaces

In photonics, recent decades have witnessed rapid progress driven by advances in micro- and nano-fabrication technologies, opening avenues to scaling down optical components. Metamaterials are artificially engineered media with electromagnetic properties unattainable in natural materials. Their fundamental building blocks are meta-atoms, introduced in Section 2.5, which can be tailored in geometry, composition, and arrangement to realize specific optical functionalities.

Metamaterials are generally classified into two categories according to their thickness [104]. The first generation, known as three-dimensional (3D) metamaterials, demonstrated unique optical properties such as negative refractive index, near-zero index, electromagnetic cloaking, and optical magnetism [53, 105, 106]. However, their high optical losses, strong dispersion, and complicated fabrication processes limited their practical functions. These challenges led to the emergence of semi-3D metamaterials, or metasurfaces, which are ultrathin designs with much simpler fabrication requirements [107]. Metasurfaces consist of deep sub-wavelength meta-atoms arranged either randomly or periodically in an array [108]. The optical response of a metasurface can be described as a scattering problem, similar to the case of individual meta-atoms. The structured surface scatters light into all directions, and this collective scattering determines the transmission and reflection spectra of the metasurface. By analyzing the mutual interactions between neighboring meta-atoms, one can design metasurfaces with tailored functionalities.

In design, a periodic unit cell containing a single meta-atom is modeled to evaluate the local electromagnetic fields inside the representative structure. Once the local field distribution is obtained, the induced-current method, as outlined in Section 2.5, can be applied to calculate the effective multipole moments of the meta-atom. These multipoles reproduce the collective response of the metasurface ensemble. Reflection and transmission spectra of the metasurface under normal incidence can be defined based on the induced multipole moments of the meta-atom in unit cell. For an x-polarized plane-wave excitation, they are expressed as

$$r = \frac{ik_b}{E_0 2S_L \varepsilon_0 \varepsilon_b}\left(p_x - \frac{m_y}{v_b} + \frac{ik_b}{6}Q_{xz} - \frac{ik_b}{2v_b}M_{yz} - \frac{k_b^2}{6}O^e_{xzz} + \frac{ik_b^2}{2v_b}O^m_{yzz}\right),$$
$$t = 1 + \frac{ik_b}{E_0 2S_L \varepsilon_0 \varepsilon_b}\left(p_x + \frac{m_y}{v_b} - \frac{ik_b}{6}Q_{xz} - \frac{ik_b}{2v_b}M_{yz} - \frac{k_b^2}{6}O^e_{xzz} - \frac{ik_b^2}{2v_b}O^m_{yzz}\right), \tag{2.21}$$

and for a y-polarized plane-wave excitation, becomes

$$r = \frac{ik_b}{E_0 2S_L \varepsilon_0 \varepsilon_b}\left(p_y - \frac{m_x}{v_b} + \frac{ik_b}{6}Q_{yz} - \frac{ik_b}{2v_b}M_{xz} - \frac{k_b^2}{6}O^e_{yzz} + \frac{ik_b^2}{2v_b}O^m_{xzz}\right),$$
$$t = 1 + \frac{ik_b}{E_0 2S_L \varepsilon_0 \varepsilon_b}\left(p_y + \frac{m_x}{v_b} - \frac{ik_b}{6}Q_{yz} - \frac{ik_b}{2v_b}M_{xz} - \frac{k_b^2}{6}O^e_{yzz} - \frac{ik_b^2}{2v_b}O^m_{xzz}\right), \tag{2.22}$$

with propagation along the z-direction [109]. Here, ε_b and k_b denote the background permittivity and wavenumber, v_b is the phase velocity in the background, S_L is the metasurface unit-cell area in the x–y plane, and E_0 is the incident electric field amplitude. Transmission and reflection coefficients are defined as $T = |t|^2$ and $R = |r|^2$, respectively. Throughout this thesis, Metasurfaces are defined in the x–y plane, while the z-axis represents the propagation direction normal to the array surface.

Besides tuning the induced multipole moments of individual meta-atoms, the periodic distance between them, known as the lattice constant, is another critical parameter that governs the scattering response of a metasurface. Metasurfaces can be regarded as thin grating arrays capable of modulating the phase and amplitude of incident light at the sub-wavelength scale. In this framework, the lattice constant tunes the diffraction directions [110], as

$$nP\left(\sin\theta_m + \sin\theta_i\right) = m\lambda\,, \tag{2.23}$$

where n is the refractive index of the background medium, P is the lattice constant in the x–y plane, θ_i is the incident angle, θ_m is the radiation angle of m^{th} order diffraction, and λ is the free space wavelength. For an array embedded in a homogeneous medium and illuminated perpendicularly to the plane ($\theta_i = 0°$), the condition $\theta_m = 90°$ corresponds to Rayleigh anomaly (RA) diffraction, yielding $P = \lambda/n$ [111]. In this regime, in-plane diffraction enables constructive coupling of the scattered fields across the lattice, giving rise to a narrow linewidth surface lattice resonance (SLR).

Plasmonic meta-atoms, such as noble metals in the visible regime or InSb in the THz range, naturally support LSPRs [23, 50]. These resonances strongly confine light but typically exhibit broad linewidths due to intrinsic absorption and radiative losses. When plasmonic meta-atoms are periodically arranged with lattice constants tuned near the RA diffraction condition, their scattered fields couple constructively while suppressing out-of-plane radiation channels. The resulting SLR features an ultra-narrow linewidth and a high Q-factor, Achieving strong near-field enhancement at the array surface with suppression of radiative losses. Such high-Q SLRs make plasmonic metasurfaces highly attractive for applications in sensing, imaging, lasing, and optical filtering at the sub-wavelength scale [112].

Figure 2.6 presents the optical response of a plasmonic metasurface characterized by a SLR in the low THz frequency range [48]. The proposed design consists of InSb meta-molecules embedded in a homogeneous medium with a refractive index of $n = 1.8$. The metasurface is illuminated by a linearly x-polarized plane wave with a wavevector k_z. The lattice constants along the x and y directions are $P_x = 167\,\mu$m and $P_y = 200\,\mu$m, satisfying the RA diffraction condition. The InSb meta-molecules, with dimensions $L_x = 25\,\mu$m, $L_y = 45\,\mu$m, and $L_z = 0.2\,\mu$m, support only ED modes due to their broad LSPRs. Constructive interactions of these individual ED-LSPR modes, through RA diffraction in the x–y plane, produce an ultra-narrow resonance at the SLR frequency.

Another strong route for designing resonant building blocks for metasurfaces is to use Mie resonant meta-atoms. A meta-atom supports its first Mie resonance when the optical size satisfies $\lambda/n_s \approx 2R_s$, where λ is the resonance wavelength, n_s is the particle refractive index, and R_s is its radius [113]. High-index dielectrics and undoped semiconductors with large n_s and low loss readily meet this condition (see Table 2.1), making them a strong counterpart to the plasmonic meta-atoms discussed above.

Unlike plasmonic resonances, which arise from surface conduction currents and are typically dominated by an ED response with large losses, Mie resonant meta-atoms are driven by displacement currents of bound charges and can concurrently support ED and MD modes with negligible radiative loss. At deep sub-wavelength scale, the response of meta-atoms is governed primarily by the ED and MD modes. When these meta-atoms are arranged in a two-dimensional periodic array within a homogeneous medium, the collective excitation of ED and MD modes leads to unique optical responses.

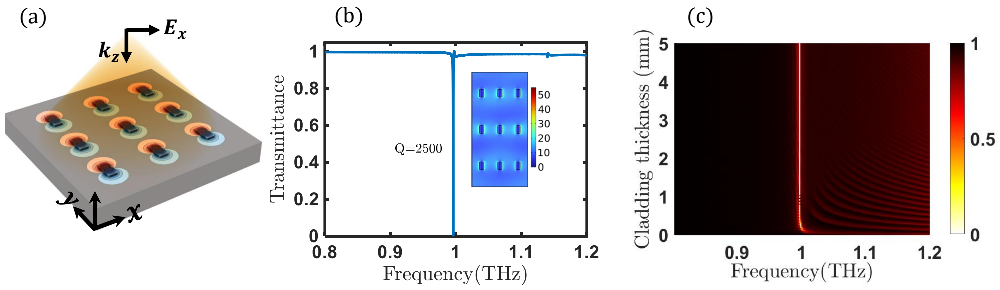

FIGURE 2.6: (a) Plasmonic metasurface based on InSb meta-molecules that numerically designed to achieve a high-Q SLR. (b) Transmission spectrum of the metasurface shows emergence of a narrow SLR due to coherent coupling of individual LSPRs. The inset depicts electric field distribution at the SLR frequency, extending across the entire surface with strong enhancement. (c) Effect of cladding thickness on the SLR linewidth. Increasing the cladding thickness suppresses out-of-plane diffraction channels, while thinner claddings allow coupling between LSPRs and photonic modes of the background medium, leading to multiple narrow resonances.

These collective interactions enable Mie-based metasurfaces to manipulate light's amplitude, phase, and polarization with high efficiency. One of the most important collective response of metasurfaces based on Mie resonant meta-atoms is described by Kerker's theory. By engineering the shape, material, and arrangement of a high-index meta-atom array, Kerker showed that a silicon metasurface can support a frequency region with near-unit transmission and no reflection, known as the first Kerker effect, and another frequency range with full reflection and zero transmission, so-called the second Kerker effect [114]. The Kerker condition depends on the phase and

TABLE 2.1: Refractive and absorption indices of high-index materials [37].

Materials	Refractive Index	Intrinsic Loss
Si	3.5 – 5	0 – 0.2
Ge	4 – 5.8	0.23 – 2.4
Te	4.8 – 6.3	0
GaAs	3.3 – 5.2	0.07 – 2
InAs	3.7 – 4.46	0 – 0.2
AlGaAs	3.66 – 5	0.06 – 2
InP	3.5 – 4.4	0 – 0.2
GaP	3.1 – 5.4	0 – 0.2

magnitude of ED and MD moments, and it can be described by

$$
\begin{aligned}
r_p &= \frac{ik_b}{E_0 2S_L \varepsilon_0 \varepsilon_b}\, p_x, \\
r_m &= \frac{ik_b}{E_0 2S_L \varepsilon_0 \varepsilon_b}\, \frac{m_y}{\nu_b},
\end{aligned}
\tag{2.24}
$$

where r_p and r_m are the reflection terms of ED and MD modes, respectively. The first Kerker effect is fulfilled when the magnitude and phase of r_p and r_m are equal. In this case, in-phase oscillations of ED and MD modes with equal magnitudes suppress reflected waves, and the transmission is near unity. On the other hand, out-of-phase oscillations of these modes with the same magnitudes result in a near-unity reflection design or a second Kerker metasurface. These uni-directional structures can be efficiently employed for wave mixing and beam steering applications, and all fields require high-directional antennas. Beyond the primary ED and MD multipoles, high-index meta-atoms can also support more exotic resonant modes through multipolar cross-coupling [37]. By asymmetrically arranging Mie resonant meta-atoms in a densely packed assembly, the enhanced near-field interactions of ED and MD moments result in circular displacement currents within the unit cell that excite high-Q non-radiating modes [115] known as toroidal resonances and are described by

$$
\begin{aligned}
p^t_\alpha &= \frac{1}{i\omega}\left[\frac{k^2}{10}\int (\mathbf{J}\cdot\mathbf{r})\, r_\alpha - 2r^2 J_\alpha \, dv\right], \\
m^t_\alpha &= \frac{k^2}{10}\int r^2 \left[\mathbf{r}\times\mathbf{J}\right]_\alpha dv\,.
\end{aligned}
\tag{2.25}
$$

Here, p^t_α and m^t_α are toroidal ED and MD moments, respectively. Interestingly, toroidal moments can interact with prime ED and MD moments, leading to another non-radiating mode, the so-called anapole mode [116]. The destructive near-field interaction of ED and MD moments suppresses the far-field radiation. Hence, the metasurfaces support high-Q resonances highly confined around meta-atoms and promising to detect local perturbations.

Figure 2.7 demonstrates the collective optical response of a Mie-based metasurface composed of pillar amorphous silicon (a-Si:H) meta-atoms to act as a label-free biosensor [117]. Silicon meta-atoms with radii of $A = 1.96$ μm, and $B = 0.96$ μm and the thickness of $H = 0.7$ μm are periodically deposited on a MgF_2 substrate such that the lattice constants of the unit cell are $P_x = 3.92\mu$m

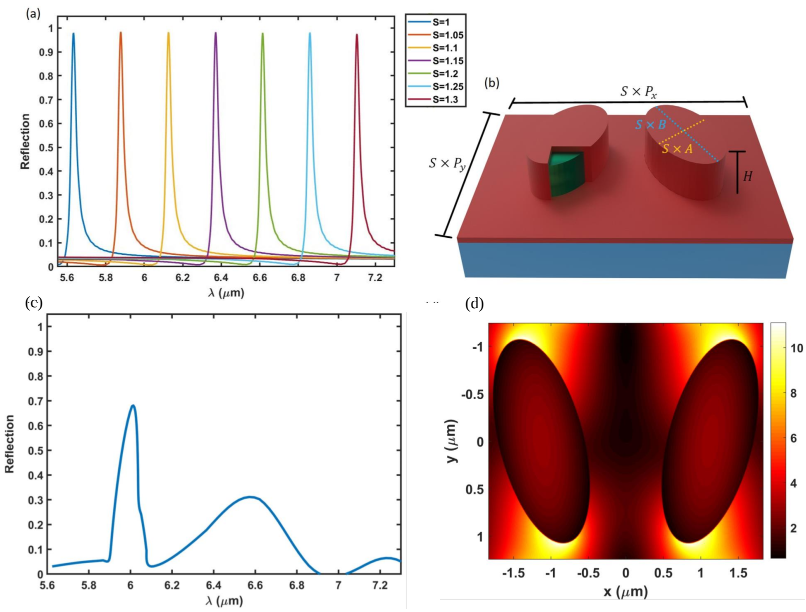

FIGURE 2.7: (a) Reflection coefficient of the bared metasurface. (b) The unit cell includes the pillar meta-atoms arrayed on the substrate with a refractive index of $n = 1.32$. (c) Reflection modulation of the metasurface covered by a thin protein later. (d) E-field profile of the metasurface in $x - y$ plane highlights the near-field interaction of ED moments at the outer surface along the y-direction. (Simulation results generated by the author using structures based on the designs reported in Ref. [117].

and $P_y = 2.26\ \mu$m. The high-index meta-atoms are arrayed with a tilting angle of $\theta = 20°$ to block MD moments when the array is illuminated by a linearly y-polarized plane wave with a wavevector of k_z. Hence, The near-field interactions of ED moments at the outer surface of meta-atoms realize a high-Q non-radiating mode that strictly localizes the electric field in the gap between adjacent meta-atoms along the y-direction. With a giant local field enhancement, this design is conformally covered by a thin protein layer to serve as a biosensor. Figure 2.7(a) shows the reflection coefficient of the bared metasurface with a high Q resonance, which is spectrally tuned by the scaling factor of S. The electric field profile of the unit cell demonstrates how the electric field blocks inside the meta-atoms and enhances at the outer surface (Fig. 2.7(d)). Figure 2.7(c) shows the reflection envelope when a thin protein layer targets the metasurface. Interaction of ED moments with the lattice vibrant resonances of the protein layer changes the ensemble's collective optical response and highlights the biosensor's efficiency.

2.7 Nonlinear Metasurface

The emergence of high-intensity semiconductor lasers has been pivotal in advancing photonics by enabling the study and application of nonlinear light-matter interactions. Under intense optical excitation, bound and free carriers are displaced beyond the linear regime, forming microscopic current sources that oscillate nonlinearly and radiate at frequencies different from the incident field. Coherent and in-phase oscillation of these induced currents leads to efficient frequency conversion processes. Total induced current density in a material can be expressed as

$$\mathbf{J}^{\mathrm{tot}}(\mathbf{r},\omega) = \mathbf{J}^{\mathrm{Lin}}(\mathbf{r},\omega) + \mathbf{J}^{\mathrm{NL}}(\mathbf{r},\omega)\,, \tag{2.26}$$

where the nonlinear term is given by

$$\mathbf{J}^{\mathrm{NL}}(\mathbf{r},\omega) = -i\omega\varepsilon_0\left[\chi^{(2)}(\omega)\mathbf{E}^2(\mathbf{r},\omega) + \chi^{(3)}(\omega)\mathbf{E}^3(\mathbf{r},\omega) + \cdots\right]. \tag{2.27}$$

Here, $\mathbf{E}(\mathbf{r},\omega)$ is the electric field inside the medium, and $\chi^{(n)}(\omega)$ denotes the n-th order optical susceptibility, which becomes significant under strong excitation. In this thesis, the focus resides on second-order nonlinearities, and the following expressions is aligned accordingly. Substituting the nonlinear current into Maxwell's equations yields the nonlinear wave equation [118], as

$$\nabla \times \nabla \times \mathbf{E}(\mathbf{r},\omega) - k_0^2\,\varepsilon(\omega)\,\mathbf{E}(\mathbf{r},\omega) = -i\omega\mu_0\,\mathbf{J}^{\mathrm{NL}}(\mathbf{r},\omega)\,, \tag{2.28}$$

where μ_0 is the free space permeability, k_0 is the free space wavenumber, and $\varepsilon(\omega)$ is complex dielectric function of the medium. In a conventional bulk material with sufficient second-order susceptibility $\chi^{(2)}(\omega)$, characterized by a refractive index $n(\omega) = n'(\omega) + i\,n''(\omega)$ and illuminated by an intense field $\mathbf{E}(\mathbf{r},\omega) = E_0\,e^{i(\mathbf{k}\cdot\mathbf{r}-\omega t)}$, the induced microscopic currents generate a second-harmonic (SH) response whose output intensity can be written as [119]

$$I_{\mathrm{SH}}(\omega) = \frac{\omega^2\,\left|\chi^{(2)}(\omega)\right|^2}{2c^3 n'(2\omega)\,\varepsilon_0\,[n'(\omega)]^2}\,\left|E'(\omega)\right|^4 L^2\,e^{-2k''(\omega)L-k''(2\omega)L}\,\left|\mathrm{sinc}\left(\tfrac{\Delta k L}{2}\right)\right|^2. \tag{2.29}$$

The efficiency of process depends on the uniform electric field amplitude $E'(\omega)$ within the bulk medium, phase-matching factor Δk, and the material length L. Constructive interference, ensured by phase-matching, typically requires long propagation distances [118]. Consequently, conventional bulk nonlinear crystals, while effective in macroscopic systems, become impractical for sub-wavelength applications where compact devices demand strong frequency conversion . This limitation has driven the development of resonant meta-atoms and metasurfaces designed to achieve enhanced nonlinear responses at sub-wavelength scales, enabling applications in nanolasers [120], near-field microscopy [121, 122], and ultrafast optical signal processing [123].

Metasurfaces, introduced in Section 2.5 as engineered arrays of resonant meta-atoms, provide a powerful platform for enhancing nonlinear optical processes. Unlike bulk crystals, they do not require long propagation lengths to fulfill phase-matching conditions [124]. Instead, nonlinear responses arise from local resonant interactions of meta-atoms acting as microscopic current sources under intense illumination [125]. Beyond this phase-matching free behavior, metasurfaces concentrate electromagnetic energy into the near-field regime, producing giant local field enhancements that directly amplify the intensity of nonlinear response [126]. Together, these features make metasurfaces promising for efficient nonlinear responses in sub-wavelength devices, offering opportunities for integrated all-optical processing.

In metasurfaces, the resonant properties of the constituent meta-atoms dictate the mechanism of nonlinear enhancement. Plasmonic metasurfaces exploit localized and lattice resonances to generate nanoscale hot spots with extreme field confinement, strongly boosting nonlinearities in surface-sensitive applications such as ultrafast microscopy [127]. In contrast, Mie-based metasurfaces sustain ED and MD resonances with negligible absorption, enabling efficient energy storage and prolonged light–matter interaction that improve wavelength conversion [128]. ENZ metasurfaces offer yet another distinct advantage, as they can induce abrupt phase shifts due to high index change in a sub-picosecond time scale, promising for beam steering applications [129, 130]. The geometry and symmetry of the resonant meta-atoms further govern the type of nonlinear response, such that symmetric meta-atoms typically enhance odd-order processes, whereas breaking inversion symmetry enables even-order processes. Interestingly, Mie resonant meta-atoms with symmetric geometries but supporting higher-order multipole modes can also excite even-order nonlinearities [131].

Although bulk nonlinear media can be macroscopically treated by Eq. (2.29), the design of nonlinear metasurfaces requires a framework that captures both local and non-local responses originating from resonant meta-atoms. The hydrodynamic model provides such a framework by describing the nonlinear optical behavior of plasmonic and ENZ metasurfaces through a fluid-like treatment of free electrons' clouds. This approach can also be extended to Mie-based metasurfaces, where the nonlinear response is governed by displacement current oscillations rather than free-carrier dynamics.

2.7.1 Hydrodynamic Model

The hydrodynamic model provides a rigorous framework for studying nonlinear optical processes in plasmonic and ENZ metasurfaces. Unlike conventional local response theories [132, 133], which treat free carriers as independent dipole oscillators, the hydrodynamic approach incorporates pressure and spatial dispersion terms due to collective interaction of the electron gas. This extension is essential when the spatial variation of the electromagnetic field approaches the electron mean free path, particularly for resonant sub-wavelength meta-atoms, where a purely local description fails to predict nonlinear light–matter interactions [121].

As introduced in Eq. (2.28), the NL current density governs the inhomogeneous wave equation as a source term, representing the acceleration of charges driven by intense optical fields. In plasmonic metasurfaces, where free electrons dominate the nonlinear response, an accurate expression for this current density is crucial for predicting nonlinear processes, such as SHG response. The classical Drude theory remains a reliable model for the linear optical response of plasmonic systems, yet it omits nonlocality, electron gas pressure, and quadratic driving terms from Coulomb interactions and the Lorentz force that generate harmonics. To include these effects, we employ the hydrodynamic model, which describes the collective motion of the electron fluid under electromagnetic excitation via the Euler equation, defined as [133]

$$\frac{\partial \mathbf{v}}{\partial t} + (\mathbf{v} \cdot \nabla)\mathbf{v} + \gamma\,\mathbf{v} = -\frac{e}{m^*}\mathbf{F} - \frac{\beta^2}{n}\,\nabla n, \tag{2.30}$$

where m^* is the effective carrier mass, $-e$ is the electron charge, γ is the phenomenological damping rate, and $\mathbf{v}(\mathbf{r},t)$ and $n(\mathbf{r},t)$ denote the velocity and density of the electron fluid, respectively. The first term on the left-hand side represents the local acceleration of the electron fluid, while $(\mathbf{v} \cdot \nabla)\mathbf{v}$ describes the convective acceleration associated with the spatial variation of the carrier velocity. The term $\gamma\mathbf{v}$ accounts for momentum relaxation arising from carrier scattering. On the right-hand side, the quantity $\mathbf{F}(\mathbf{r},t) = \mathbf{E}(\mathbf{r},t) + \mathbf{v}(\mathbf{r},t) \times \mathbf{B}(\mathbf{r},t)$ contains the electric and magnetic contributions to the Lorentz force, such that the total electromagnetic force acting on an electron is $-e\mathbf{F}$. The electric-field component drives the carrier motion, whereas the magnetic component couples the electron-fluid velocity to the local magnetic field and contributes to the nonlinear optical response.

The final term describes the pressure-gradient force within the electron gas and accounts for spatially nonlocal corrections that are absent from the conventional local Drude model. Within the low-frequency Thomas–Fermi approximation for a homogeneous and degenerate electron gas, the nonlocal parameter can be approximated as $\beta \approx v_F/\sqrt{3}$, where v_F is the Fermi velocity. In this approximation, β is evaluated at the equilibrium carrier density and is treated as a material constant. The pressure term becomes increasingly important for plasmonic particles with nanometre-scale dimensions, narrow gaps, sharp geometrical features, or strong carrier-density gradients, where the local optical response is no longer sufficient. Together with the continuity equation and the relation $\mathbf{J} = -en\mathbf{v}$, this hydrodynamic equation provides a self-consistent description of the linear and nonlinear current densities. In particular, the convective term, the magnetic contribution of the Lorentz force, and the density-dependent pressure response act as nonlinear sources that contribute to second-harmonic generation in plasmonic structures. Using $\mathbf{J} = -ne\,\mathbf{v}$, Eq. (2.30) can be rewritten in terms of the current density [134], as

$$\frac{\partial \mathbf{J}}{\partial t} - \frac{\mathbf{J}}{en}\nabla\cdot\mathbf{J} - \mathbf{J}\cdot\nabla\left(\frac{\mathbf{J}}{en}\right) - \gamma\,\mathbf{J} = \frac{ne^2}{m^*}\,\mathbf{E} - \frac{e}{m^*}\,\mathbf{J}\times\mathbf{B} - \frac{\beta^2}{n}\,\nabla n, \tag{2.31}$$

which presenting intrinsic sources of nonlocality and nonlinearity at deep sub-wavelength scales. Combining Eq. (2.31) with the continuity equation, $\nabla\cdot\mathbf{J} - e\,\partial n/\partial t = 0$, and performing a perturbative expansion for time-harmonic fields ($e^{-i\omega t}$), the induced current densities at the pump and second harmonic frequencies satisfy [135]

$$\begin{aligned}
&\beta^2\,\nabla(\nabla\cdot\mathbf{J}_1) + \left(\omega^2 + i\omega\gamma\right)\mathbf{J}_1 = -\,i\,\omega\,\frac{ne^2}{m^*}\,\mathbf{E}_1,\\
&\beta^2\,\nabla(\nabla\cdot\mathbf{J}_2) + \left((2\omega)^2 + i(2\omega)\gamma\right)\mathbf{J}_2 = -\,i\,2\omega\,\frac{ne^2}{m^*}\,\mathbf{E}_2 \;-\; i\,2\omega\,\mathbf{S}_{\mathrm{NL}}.
\end{aligned} \tag{2.32}$$

Here $\mathbf{J}_1 \equiv \mathbf{J}_{\mathbf{Lin}}(\mathbf{r},\omega)$ and $\mathbf{J}_2 \equiv \mathbf{J}_{\mathbf{Lin}}(\mathbf{r},2\omega)$, and the second-order nonlinear source term at 2ω is

$$\mathbf{S}_{\mathrm{NL}} = -\,\frac{e}{i\omega m^*}\,\mathbf{E}_1\,(\nabla\cdot\mathbf{J}_1) - \frac{e}{m^{*2}}\,(\mathbf{J}_1\times\mathbf{B}_1) + \frac{1}{ne}\Big[(\nabla\cdot\mathbf{J}_1)\mathbf{J}_1 + (\mathbf{J}_1\cdot\nabla)\mathbf{J}_1\Big]. \tag{2.33}$$

Using Eqs. (2.32) and (2.33), the total induced current density inside a plasmonic resonant meta-atom can be written as the sum of a linear and a nonlinear contribution. The linear current is

$$\mathbf{J}_{\mathrm{lin}}(\mathbf{r},\omega) = \frac{i\,\varepsilon_0\,\omega_p^2}{\omega + i\gamma}\,\mathbf{E}_1'(\mathbf{r},\omega), \tag{2.34}$$

and the second-order current density that drives the SH response is [136]

$$\begin{aligned}
\mathbf{J}_{\mathrm{NL}}(\mathbf{r},2\omega) = {}& \frac{\varepsilon_0\,\omega_p^2}{ne\,(2\omega^2 + i\omega\gamma)}\,\mathbf{E}_1'(\mathbf{r},\omega)\,\left[\nabla\cdot\mathbf{J}_{\mathrm{lin}}(\mathbf{r},\omega)\right]\\
&+ \frac{i\,\varepsilon_0\,\omega_p^2}{ne\,(2\omega + i\gamma)}\,\left[\mathbf{J}_{\mathrm{lin}}(\mathbf{r},\omega)\times\mathbf{B}_1'(\mathbf{r},\omega)\right]\\
&- \frac{i\,m^*\,\varepsilon_0\,\omega_p^2}{n^2e^3\,(2\omega + i\gamma)}\,\Big\{(\nabla\cdot\mathbf{J}_{\mathrm{lin}})\,\mathbf{J}_{\mathrm{lin}} + \left[\mathbf{J}_{\mathrm{lin}}\cdot\nabla\right]\mathbf{J}_{\mathrm{lin}}\Big\}(\mathbf{r},\omega).
\end{aligned} \tag{2.35}$$

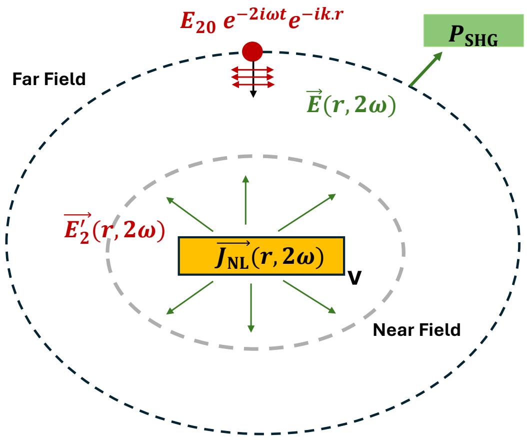

FIGURE 2.8: Lorentz–reciprocity theory application for SHG from a resonant plasmonic meta-atom.

To predict the radiated SH field, we recall Lorentz reciprocity as the following form of [119, 135]

$$\int_V \mathbf{J}_{\mathrm{NL}} \cdot \mathbf{E}_2' \, dV \;=\; \int_V \mathbf{J}_{2\omega} \cdot \mathbf{E}_2 \, dV. \tag{2.36}$$

Here, the nonlinear current $\mathbf{J}_{\mathrm{NL}}$ within the meta-atom volume acts as a source for the far-field $\mathbf{E}_2$ at 2ω. A virtual current $\mathbf{J}_{2\omega}$ placed in the far field and oscillating at 2ω illuminates the structure from detection direction and produces a local field $\mathbf{E}_2'$ inside the meta-atom [137]. Since local source is defined in the far field, its radiation can be approximated by a plane wave. For a current dipole of length Δl polarized along $\hat{\mathbf{j}}$ with complex amplitude J_0, the incident field at 2ω becomes [119]

$$\mathbf{E}_{20}(\mathbf{r}, 2\omega) = \frac{-\,i(2\omega)\,\mu\,\Delta l\, J_0}{4\pi r}\, e^{-ik_2 r - i(2\omega)t}\, \hat{\mathbf{j}}, \tag{2.37}$$

where, $k_2 = \frac{2\omega}{c}\, n(2\omega)$ is the wavevector in backward direction. Accordingly, the SH field emitted by the meta-atom into far-field along the polarization axis of $\hat{\mathbf{j}}$ can be defined as

$$\mathbf{E}_2 \cdot \hat{\mathbf{j}} = \frac{\omega^3\, \mu\, e^{i(2\omega)t}}{4\pi r} \int_V \mathbf{J}_{\mathrm{NL}} \cdot \frac{\mathbf{E'}_2}{|E_{20}|}\, dV, \tag{2.38}$$

where r is the distance between meta-atom at the center of coordinates and local dipole source at the far-field.

Figure 2.8 shows the Lorentz–reciprocity schematic for SHG from a plasmonic meta-atom. Under optical pumping, a nonlinear current density $\mathbf{J}_{\mathrm{NL}}(\mathbf{r}, 2\omega)$ is induced within the meta-atom volume V and radiates a SH

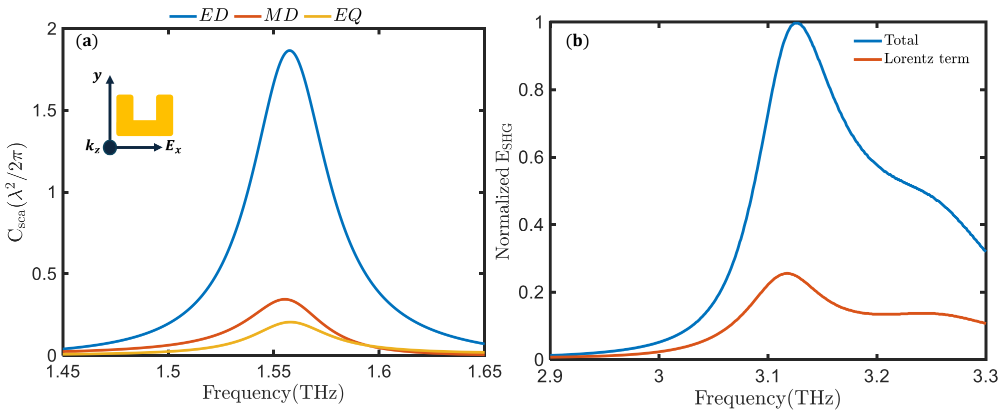

FIGURE 2.9: (a) Multipolar decomposition of the SCS of the U-shaped InSb plasmonic meta-molecule, showing dominant ED and weaker MD, and EQ resonances. (b) Normalized SH E-field obtained via the NLST. The Lorentz term enhances SHG near 3.25 THz due to contribution of the magnetic resonance modes.

field $\mathbf{E}(\mathbf{r}, 2\omega)$ into the far field, as a forward problem . In the reciprocal part, a plane wave of amplitude E_{20} illuminates the structure from detector side and generates a local reception field, $\mathbf{E}_2'(\mathbf{r}, 2\omega)$ inside the meta-atom. The SH power P_{SHG} is proportional to the squared magnitude of the overlap integral between the induced NL current and generated local field at the SH frequency, $P_{\mathrm{SHG}} \propto \left|\int_V \mathbf{J}_{\mathrm{NL}} \cdot \mathbf{E}_2'/|E_{20}|\, dV\right|^2$.

Figure 2.9 presents a numerical study of SHG enhancement in an asymmetric U-shaped InSb plasmonic meta-molecule operating in the THz regime [138]. The intentional asymmetry enables even-order responses, while the LSPRs provide strong near-field confinement employed to amplify the nonlinear sources. The SH response is obtained using a nonlinear scattering theory (NLST) that combines the hydrodynamic model with Lorentz reciprocity. In Fig. 2.9(a), the SCS is decomposed into multipolar contributions using Eq. (2.18) for an x-polarized plane wave propagating along $+\hat{\mathbf{z}}$. A dominant ED resonance originates from the LSPRs of horizontal arm. Constructive coupling of the LSPRs between two vertical arms drives a circular surface current that excites MD and EQ resonances. Strong spectral overlap of these resonant modes enhances the Lorentz term in the nonlinear current, as shown in Eq. (2.35). Figure 2.9(b) shows the SH E-field amplitude obtained from the NLST overlap integral given in Eq. (2.38). The main SH peak near 3.1 THz follows the local field enhancement due to LSPRs, while a weaker resonance around 3.25 THz shows the Lorentz term contribution which becomes prominent when electric and magnetic resonances are excited simultaneously [135].

A transition from single meta-atom to the collective behavior of metasurfaces is crucial, as practical devices rely on arrayed surfaces to enhance SH efficiently. In these structures, each meta-atom acts as a localized NL current source, and their mutual coupling defines the overall emission of the metasurface. The collective NL source within each unit cell is evaluated from Eq. (2.35) at the pump frequency ω, and the emitted harmonic fields are then obtained using the reciprocity method. Accordingly, by considering the unit-cell area S and free space impedance $\eta = \sqrt{\mu/\varepsilon}$, the SH E-field emitted or radiated by the metasurface in free space, in the forward direction, is given by [139]

$$\mathbf{E}_{\mathrm{FW}}(\mathbf{r}, 2\omega)\cdot\hat{\mathbf{j}} = \frac{\eta}{2S}\int_V \mathbf{J}_{\mathrm{NL}}(\mathbf{r}, 2\omega)\cdot\frac{\mathbf{E}^{2\omega}(\mathbf{r})}{|E_{20}|}\, dV\,. \tag{2.39}$$

The corresponding forward SH intensity is defined as [118]

$$I_{\mathrm{SH}}^{\mathrm{FW}} = \frac{1}{2\eta}\left|\mathbf{E}_{\mathrm{FW}}(\mathbf{r}, 2\omega)\right|^2. \tag{2.40}$$

Equations (2.39)–(2.40) extend the NLST framework to metasurfaces with well-defined nonlinear current sources inside resonant meta-atoms. The collective far-field response of a metasurface then arises from the mutual near-field interactions within the unit cell, which determine the forward emission.

2.8 Conclusion

In this chapter, we focused on the fundamental physics of metamaterials and metasurfaces by studying both individual resonant meta-atoms and their collective optical behavior. Using the semi numerical induced current method, we investigate the contributions of multipole moments to the far-field radiation of arbitrarily shaped resonant meta-atoms over a broad spectral range. This microscopic approach enables accurate modeling of single resonators and can be extended to practical large area metasurfaces. The collective optical response is governed by near-field interactions between neighboring meta-atoms, which provides a powerful route to engineer metasurfaces with tailored functionalities.

Plasmonic and ENZ metasurfaces exploit free electron dynamics to achieve giant local field enhancement or abrupt phase accumulation, while high-index dielectric resonators utilize electric and magnetic Mie resonances with low intrinsic loss to realize strong light confinement. These distinct mechanisms make metasurfaces compact and versatile platforms for advanced optical sensing, imaging, and beam steering applications.

Engineered metasurfaces also offer unique opportunities to enhance nonlinear optical processes such as SHG, high harmonic generation, and wavelength conversion. By exploiting strong local field confinement, symmetry breaking, and high-Q resonances, nonlinear responses can be dramatically amplified. Symmetry broken plasmonic meta-atoms, for instance, enable efficient SHG for real-time, high-resolution microscopy, while high-index metasurfaces support cavity-like modes that enhance nonlinear wave mixing. To study these effects, the NLST is employed as a rigorous framework for analyzing the nonlinear response.

Chapter 3

InSb-Based THz Plasmonic Metasurface

3.1 Contribution Statement

Building on the well-established expertise of our group in III–V semiconductor devices and metasurfaces, I proposed the idea of exploring THz metasurfaces based on III–V semiconductors, and further developed this concept through regular meetings with Prof. Dolgaleva. I performed the numerical modelling for this work using 3D-FDTD simulations. In addition, to evaluate the response of the proposed metasurface in a finite-array configuration that is more representative of practical fabrication, I used the MATLAB-based lattice-sum approach (LSA) developed in our group by Dr. Reshef and Dr. Huttunen. The first draft of the manuscript was written by me together with A. Amini and L. Shirafkan Dizaj.

Professor Dolgaleva supervised the project and led the development of the manuscript. All co-authors contributed to the revision process and approved the final version.

Conference publications related to this project are listed below:

- Aghili, Sina, *et al.* "Plasmonic Response of InSb Grating for Sensing Applications in the Terahertz Regime."*Advanced Photonic Congress (APC)*. Optica Publishing Group, 2020.
- Aghili, Sina, *et al.* "InSb-based THz Plasmonic Array with High Resonances." *Frontiers in Optics*. Optica Publishing Group, 2020.
- Aghili, Sina, *et al.* "THz ultra-narrow resonance metasurface based on InSb metamolecules." *2021 Photonics North (PN)*. IEEE, 2021.

3.2 Article

The results of this project were published in *Optics Communications* [48], and this chapter is based on the following article.

Optics Communications 508 (2022) 127805

Contents lists available at ScienceDirect

Optics Communications

journal homepage: www.elsevier.com/locate/optcom

THz plasmonic metasurface based on a periodic array of InSb metamolecules with narrow resonances

Sina Aghili [a], Aydin Amini [b], Leyla Shirafkan Dizaj [c], Ksenia Dolgaleva [a,d,*]

[a] School of Electrical Engineering and Computer Science, University of Ottawa, Ottawa, Ontario K1N 6N5, Canada
[b] Department of Engineering Physics, McMaster University, Hamilton, Ontario L8S 4L7, Canada
[c] Department of Energy Engineering and Physics, Amirkabir University of Technology, Tehran 158754413, Iran
[d] Department of Physics, University of Ottawa, Ottawa, Ontario K1N 6N5, Canada

A R T I C L E I N F O

Keywords:
THz plasmonic metasurface
Surface lattice resonance (SLR)
Localized surface plasmon resonances (LSPRs)
Lattice sum approach (LSA)

A B S T R A C T

We propose an indium antimonide (InSb) THz plasmonic metasurface featuring a surface lattice resonance (SLR) with the quality factor of Q ~ 375 and theoretically investigate the plasmonic response of the ensemble of InSb metamolecules. The localized surface plasmon resonances (LSPRs) of individual metamolecules couple together through Rayleigh Anomaly (RA) diffraction, leading to the appearance of the SLR at 0.75 THz , suitable for biophotonic applications. The major advantage of the proposed metasurface over metal-based ones in the THz regime is the tunability of SLR frequency by changing the carrier concentration. Apart from SLR, it is possible to achieve additional resonances by tuning the superstrate thickness exploiting Fabry–Perot (FP)-like cavity effects. Achieving a narrow-linewidth SLR and the resultant remarkable local-field enhancement in the InSb-based metasurface opens the door to a wide range of applications. Conducive to optical manipulation and sensing, the capability of the proposed metasurface is examined in plasmonic tweezing and medium-perturbation sensing fields.

1. Introduction

Plasmonic materials, artificial metal–dielectric structures, have attracted much attention due to their ability to confine light down to a sub-wavelength scale beyond the diffraction limit [1]. This property relies on the existence of surface plasmon polaritons (SPPs), coupled collective oscillations of free electrons with light, appearing at the metal–dielectric interface [2]. Extended plasmonic structures support SPPs that transport optical power as longitudinal bounded surface waves [3,4]. Sub-wavelength plasmonic structures, comprised of metal particles (metamolecules) residing on a dielectric substrate, exhibit localized surface plasmon resonances (LSPRs) that allow one to enhance the electromagnetic field near the metamolecules [5]. In the latter case, one can tune LSPR by adjusting the nanostructures' shape, size, and material selection [6]. Near-field enhancement, flexible tuning, and no demand for phase matching [7] are the unique features that have attracted much interest toward LSPs. Plasmonic devices based on LSP modes have a very wide range of applications including filtering [8], sensing [9], modulation [10], imaging [11], tweezing [12], photovoltaic devices [13], and spectroscopy [14].

Intrinsic absorption losses of metals and radiative and non-radiative losses [15] of conventional plasmonic materials result in broadband LSPRs and overshadow the efficiency of plasmonic devices for some specific applications. As a solution, an alternative kind of resonances, surface lattice resonances (SLRs), characteristic of an arrangement of metal nanoparticles into a regular array, were recently considered [15–17]. When metamolecules juxtapose in a periodic array, individual LSP modes couple together through Rayleigh Anomaly (RA) diffraction [18]. The far-field coupling suppresses the radiative losses, and constructive interference of scattered waves reinforces the LSPRs to achieve an extraordinary in-plane lattice resonance that compensates for the non-radiative losses [19]. Ultra-narrow SLRs with high-Q factors ($Q = f_{\mathrm{res}}/\Delta f$, where f_{res} is the LSPR frequency and Δf is the resonance bandwidth) are more versatile compared to the localized ones.

SLRs have been studied in Meta surfaces with different shapes and arrangements, consisting of metal [20], metal–insulator–metal (MIM) [21], and all-dielectric metamolecules [22] in the visible and near-IR spectral ranges. They have been considered for various applications, such as nanolasers [23], ultrasensitive tools [24], and modulators [25]. Moreover, the advent of SLR was a milestone in the evolution of nonlinear plasmonics [26]; plasmonic metasurfaces with ultra-narrow lattice resonances can help one enhance nonlinear optical interactions [27,28].

The SLR of plasmonic arrays is often modeled using the coupled-dipole method [29] or lattice sum approach (LSA) [30,31], which is a simplified version of the discrete dipole approximation (DDA) [32].

* Corresponding author at: School of Electrical Engineering and Computer Science, University of Ottawa, Ottawa, Ontario K1N 6N5, Canada.
E-mail address: ksenia.dolgaleva@uottawa.ca (K. Dolgaleva).

https://doi.org/10.1016/j.optcom.2021.127805
Received 22 September 2021; Received in revised form 5 December 2021; Accepted 12 December 2021
Available online 20 December 2021

Using plasmonic devices is not limited to a specific frequency region, and their applications can be extended to ultraviolet and mid-infrared spectral ranges. Unique spectral properties of THz waves with broad bandwidth allow them to penetrate certain materials and excite rotational molecular resonances. These properties enable a wide range of applications such as high-speed wireless communications [33], sensing [34], imaging [35], and nonlinear THz photonics [36,37]. The low power of THz sources and limitations of existing THz detection techniques impede the observation of nonlinear optical effects at the THz frequency range and represent the main challenges associated with traditional THz-based devices [38]. THz plasmonic devices can allow one to confine THz waves down to a small volume creating a high-intensity region, thereby solving the insufficient power problem of THz sources for inducing efficient nonlinear optical interactions [39].

To date, spoof surface plasmon structures [40] and metamaterials [41,42] have been conventional methods of engineering THz plasmonic devices to enhance light–matter interactions at the sub-wavelength scale. Despite the high potential of metamaterials in developing a new generation of compact THz devices, metallic blocks as commonly used elements in these structures introduce huge absorption losses. These losses need to be compensated by creating more complex structural configurations [43]. With its superb plasmonic and optoelectronic properties and active tuning mechanisms, Graphene has also been considered for THz plasmonic metamaterials [44]. However, graphene-based metamaterials require complicated fabrication processes [45]. One can use semiconductors as active plasmonic materials to realize THz plasmonic devices as an alternative to the above approaches. The capability of semiconductors to mimic the plasmonic behavior of metals in the visible spectral range enables simple plasmonic devices operation in the THz regime [46].

THz metamaterials are relatively well-studied, but only a few reports are available in the SLR-based metasurfaces area for THz frequency operation. Metasurfaces represent a subgroup of metamaterials where nearly flat metamolecules are arranged in a 2D array [47]. Metasurfaces are promising miniaturized structures which can be employed to achieve unique characteristics of SLRs at THz frequencies to enable devices with ultra-narrow resonances, simple configurations, and conventional fabrication processes [48].

The first report in this field belongs to Rivas et al. (2003); they presented a narrow plasmonic resonance in a periodic array of holes consisting of highly doped silicon metamolecules [49]. In 2011, B. Ng et al. used a metallic metasurface to realize SLR to improve the sensitivity of a THz liquid sensor [50]. In 2015, Schaafsma et al. used silicon and gallium arsenide (GaAs) metasurfaces to examine an SLR for THz wave modulation [51]. Later, in 2017, Wang et al. proposed an ultra-narrow THz perfect light absorber based on GaAs metamolecules for sensing applications [52].

In addition to GaAs, InSb is another III–V semiconductor capable of realizing plasmonic metasurfaces in the THz regime [53]. This material has all the prerequisite characteristics for realizing THz plasmonic metasurfaces, including a small bandgap, high free-carrier concentration, high electron mobility, and low effective electron mass. These characteristics play an essential role in choosing suitable semiconductors for THz plasmonic devices and enable InSb to surpass other semiconducting candidates such as GaAs and InAs [46]. Furthermore, the optical/electrical properties of InSb can be tuned passively by impurity doping or actively by thermal, electrical, or optical excitations. Although the semiconductors cannot compete with metals in the plasmonic efficiency, tunability of semiconductors and ease of fabrication are their advantages over metals.

In this work, we propose an InSb-based metasurface for achieving a high-Q SLR at low THz frequency range. To design our THz metasurface, we perform three-dimensional finite difference time domain (3D-FDTD) simulations [54] and use LSA to validate our results. The proposed structure exhibits narrow resonances and features high electric field confinement, suitable for tweezing and sensing applications. Owing to the narrow line shape of SLR, the light–matter interaction is expected to be efficient, which makes the proposed device suitable for tracking medium perturbations. Additionally, extensive in-plane light confinement to the array due to far-field coupling among metamolecules forms a hot region resulting in a highly attractive gradient force that can manipulate the suspended microparticles close to the metasurface. The ability to demonstrate hot spots and manipulate a suspended microparticle make the metasurfaces suitable for the application of optical tweezers.

The manuscript is organized as follows: Section 2 describes the methods, the proposed metasurface structure, and characteristics. Section 3 introduces the performance of the proposed metasurface. Section 4 describes optical sensing and tweezing applications of the proposed structure, and Section 5 is devoted to the conclusions.

2. Methodology and proposed structure

InSb, a promising active plasmonic material, exhibits high carrier concentration, high electron mobility ($\mu = 41000\ \mathrm{cm^2/V\ s}$), and small bandgap energy ($\mathrm{E_g} = 0.17$ eV). One can use the modified Drude model to express the conductive properties of InSb at THz frequencies [55]. The complex dielectric permittivity of InSb in the absence of a magnetic field can be expressed as

$$\varepsilon = \begin{pmatrix} \varepsilon_{xx} & 0 & 0 \\ 0 & \varepsilon_{yy} & 0 \\ 0 & 0 & \varepsilon_{zz} \end{pmatrix}, \tag{1}$$

where

$$\varepsilon_{ii} = \varepsilon_\infty - \frac{\omega_p^2}{\omega^2 + i\gamma_p\omega}, \tag{2}$$

($i = x.y.z$), and ε_∞ is the high-frequency permittivity, ω_p is the plasma frequency, and γ is the damping constant that plays an important role in determining the linewidth of the plasmonic resonance and the absorption losses of the plasmonic material. The plasma frequency of InSb [see Eq. (3)] can be tuned by varying the free-carrier concentration N either thermally [56] or by electrical excitation [57]:

$$\omega_p = \sqrt{\frac{Ne^2}{\varepsilon_0 m^*}}, \tag{3}$$

where e is the charge of electron and m^* is the effective mass of InSb.

According to Eq. (3), higher plasma frequencies can be achieved by increasing N due to a dynamic response to the imposed charge separation, in which the restoration force is proportional to the concentration of the displaced charges. To evaluate the effect of free-carrier concentration, we considered an individual rectangular InSb metamolecule with the planar dimensions of $L_x = 60$ μm.$L_y = 30$ μm and the thickness of $L_z = 200$ nm inside a homogeneous medium ($n = 1.8$) under normal plane wave illumination. Fig. 1(a) demonstrates the blueshift and broadening in FWHM of LSPR with increased free-carrier concentration. InSb is intrinsically an n-type semiconductor, and the injection to the conduction band can be performed by doping tellurium (Te) [58]. The mobility of electrons exceeds the holes [59], and the small bandgap ensures sufficient free-electron concentration in the conduction band. For lower carrier concentration, due to the lack of enough free electrons in the conduction band, the light screening is weak, and the metamolecule behaves as a dielectric that scatters only a small fraction of the incident light. With increasing N, the resonance frequency is blueshifted and the resultant higher amplitudes of scattering cross-section represent the plasmonic behavior of InSb in the moderate doping range. When N increases further, InSb behaves like a metal with higher non-radiative damping, leading to a broad-band resonance with a lower resonance peak.

Besides the active tuning of plasmonic resonances in InSb through adjusting the free-carrier concentration, LSPRs can also be passively manipulated by varying the size of the metamolecule [see Fig. 1(b)].

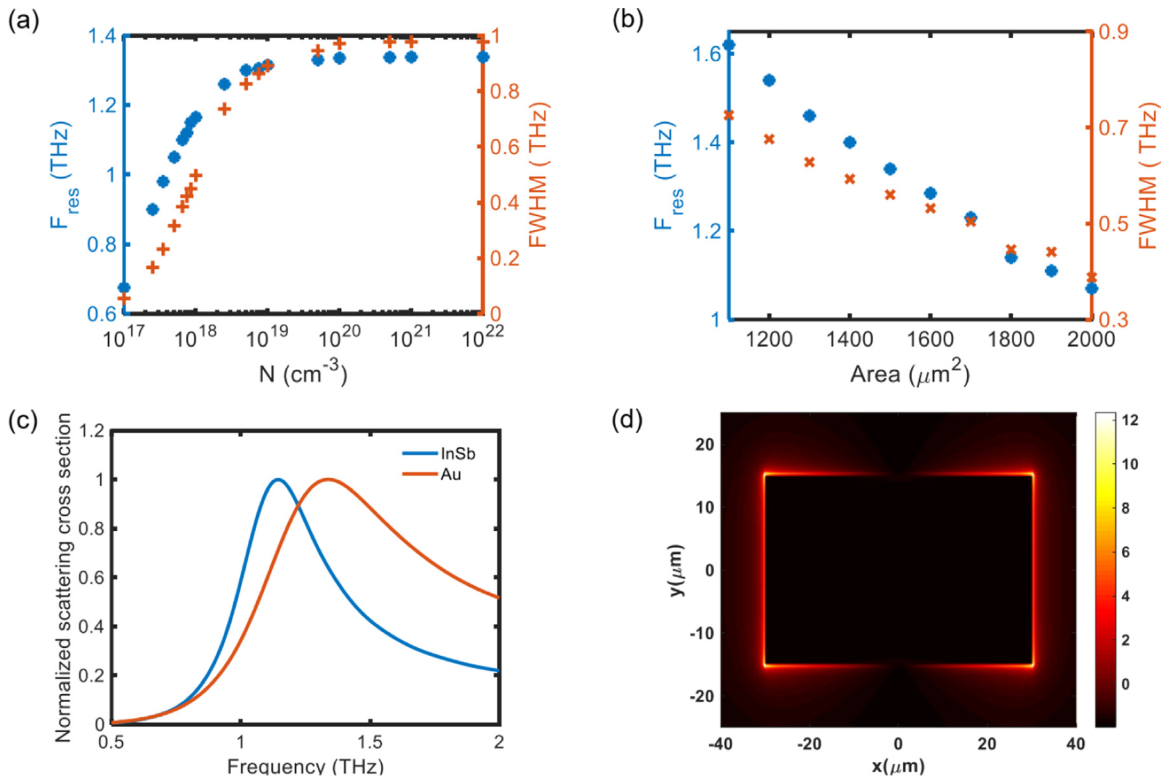

Fig. 1. LSP resonance frequency and full-width at half-maximum (FWHM) as a function of (a) carrier concentration (N) with $L_x = 60$ μm.$L_y = 30$ μm.$L_z = 200$ nm. (b) Metamolecule area at the fixed $N \approx 8.5 \times 10^{17}$ cm^{-3}, FWHM and resonance frequency are obtained from the scattering cross-section of an individual InSb metamolecule. (c) Scattering cross-section of Au particle ($N \approx 5.9 \times 10^{22}$ cm^{-3}) is compared to that of InSb particle ($N \approx 8.5 \times 10^{17}$ cm^{-3}) in THz regime. (d) 2D electric field snapshot of the individual InSb metamolecule at LSPR frequency ($f = 1.1$ THz) with $N \approx 8.5 \times 10^{17}$ cm^{-3} is obtained from FDTD simulations.

An increase in the metamolecule's area results in an expansion of the interaction cross-section that augments the amplitude of the scattering cross-section and reduces the FWHM [60]. The larger the particles, the lower the resonance frequency because of the decrease in the restoring force between an electron and a positive ion as the distance between them increases.

Akin to the conventional plasmonic materials, InSb shows considerable negative values of the real part of its permittivity at the THz frequencies. The imaginary part is related to the material's ohmic losses, much smaller than those of metals at the THz frequencies [60]. The scattering cross-section of a single InSb metamolecule is compared to that of an Au particle of the same geometry [see. Fig. 1(c)]. For a single InSb metamolecule, increasing the free-carrier concentration results in higher ohmic losses [see Fig. 1(a)] since the electronic states in the conduction band become occupied and free carriers cannot find any unoccupied states to move through the crystal under the influence of the incident light. In Fig. 1(c), the higher carrier concentration of Au particles ($N \approx 5.9 \times 10^{22}$ cm^{-3}) results in a broader resonance lineshape, making InSb a better choice for plasmonic applications in the THz regime. Similar to noble metals, InSb can also confine and enhance the electric field in its near-field region. As shown in Fig. 1(d), an x-polarized plane wave at the resonance frequency can excite LSPR that oscillates in the incident wave direction in which the electric field intensity is confined to the surface.

2.1. Design of the metasurface

To achieve high-Q-factor narrow plasmonic resonances, we ought to mitigate radiative and non-radiative losses associated with LSPR. In a periodic array of metamolecules, near-field [61] or far-field hybridization [62] of resonant plasmonic eigenstates can occur. When the distance between the particles is very small compared to the wavelength, near-field resonances of LSPs hybridize together. Such hybrid resonance states appear to be shifted without any significant alteration in their linewidth [5].

Table 1
Geometrical parameters of the proposed InSb metasurface, schematically depicted in Fig. 2.

Parameters	Value
P_x	200 [μm]
P_y	220 [μm]
L_x	60 [μm]
L_y	30 [μm]
L_z	200 [nm]

If the designed metasurface has the lattice constant on the order of the incident wavelength, far-field waves scatter by metamolecules couple together through RA diffraction, and an in-plane SLR can emerge at the RA frequency [63], given by

$$f_{\mathrm{RA}} = \frac{mc}{nP(1 \pm \sin\theta)}, \quad m = 1, 2, 3, \ldots \tag{4}$$

where m is the order of diffraction, P is the lattice constant (see Table 1) of the periodic array in the direction orthogonal to the polarization of light (y-direction in this work, see Fig. 2), c is the speed of light, n is the refractive index of the surrounding homogeneous medium, and θ is the angle of incidence light. Eq. (4) reveals that the RA frequency depends on the refractive index of the surrounding medium and the periodicity of the structure.

To achieve an in-plane SLR at the THz frequencies, which is applicable for biophotonic devices, we propose a simple InSb-based metasurface, which is schematically depicted in Fig. 2. The lattice constants and the medium refractive index should be defined in a way to realize a lattice resonance at low frequencies (0.2 to 1 THz), since the THz wave penetration depth in biological samples is significant in this regime [64]. Metamolecules are embedded in a Polyethylene naphthalate (PEN) layer with a refractive index of ∼1.8 that can serve as

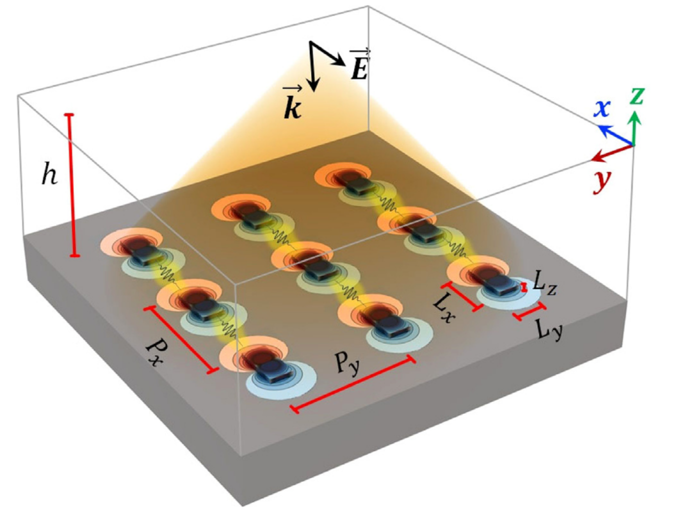

Fig. 2. Schematic of the proposed InSb metasurface and the geometrical parameters of the unit cell are provided in Table 1. The periodic array is embedded inside a homogeneous environment, with the substrate and superstrate having the same refractive indices (n = 1.8). A plane wave launches on the metasurface from the bottom of the substrate with the wavevector (k) and the polarization (E) along z and x directions, respectively. The confined light in each particle in the x-direction represents the LSPRs, and the constructive diffraction of light by each particle is represented by short wave packets which cause an in-plane surface wave called SLR.

the homogeneous background medium [50]. Although the presence of a homogeneous medium helps to form high-Q resonance, a slight increase in the refractive index of substrate or superstrate would not appear as a significant decrease in the Q-factor. Only SLR frequency experiences pronounced redshift [65], making the device suitable for sensing applications. The lattice constants of the proposed metasurface are P_x = 200 μm and P_y = 220 μm. Due to the RA condition, diffraction is only constructive in (1 0 0) direction, leading to a formation of an in-plane SLR at the frequency of 0.75 THz.

Besides the refractive index and the lattice constant, the amplitude and linewidth of SLR rely on spectral characteristics of individual LSPRs. The size of metamolecule should be such that it is possible to realize a strong LSPR with narrow bandwidth. According to Fig. 1b, the bandwidth of LSPR is inversely proportional to the metamolecule's area. In the case of metasurface, as LSPRs approach the Rayleigh anomaly (RA) frequency, SLR starts to emerge and get enhanced, and the linewidth becomes narrower [51]. Metamolecules with smaller areas excite the LSPR at the frequencies higher than f_{RA} = 0.75 THz, and due to the lack of spectral overlap between the LSPR and RA frequencies, the Q-factor drops significantly. On the other hand, metamolecules with larger areas guarantee a larger spectral overlap between LSPR and RA frequencies. However, larger-size metamolecules will not necessarily result in a higher-Q SLR due to the reduction of the gap distance between metamolecules. Our numerical analysis has demonstrated that, for designing an efficient metasurface in terms of Q-factor and size to operate at the THz frequencies less than 1 THz, an InSb metamolecule with L_x = 60 μm and L_y = 30 μm is an optimum choice as a building block of the proposed structure. The superstrate thickness (100 μm < h < 30 mm) is responsible for the number of additional resonances via LSPR splitting [66]. It should be noted that, compared to the noble metals, InSb shows higher plasmonic efficiency only in an array with simple-shaped particles (rectangle in this case). For complex metallic structures, the Q-factor in the THz regime can reach values on the order of 10^4 at the expense of increasing fabrication complexity and lack of tunability [67].

2.2. Methods

We used 3D-FDTD simulations to model an infinite InSb metasurface. An InSb metamolecule is considered a unit cell in a 2D square lattice. Due to the periodicity of the metasurface along with the x and y directions, periodic boundary conditions are applied in these directions. A perfectly matched layer (PML) boundary condition limits the simulation box in the out-of-plane direction so that the outward scattered light from the metamolecules is absorbed by the PML layers. A plane-wave source launches on the metasurface from the substrate side. The rigorous mesh sizes are set to be $\Delta x = \Delta y = 1$ μm and $\Delta z = 4$ nm.

It is impractical to consider an infinite array in the design process. Therefore, it is crucial to determine finite dimensions of the array with a fixed number of metamolecules. In 2019, Reshef et al. utilized LSA to analyze a finite array of Au metamolecules, the best semi-analytical tool to evaluate lattice resonances of finite metasurfaces. Moreover, it is well suited for comparing the numerical results with experimental data [66]. The plasmonic response of a finite metasurface using LSA can be obtained by considering the local field acting on a single metamolecule. This field is comprised of an incident wave and scattered waves from other metamolecules [16]. The ability to take the effect of the finite upper cladding thickness into account gives LSA an advantage over other approaches [30]. Using the LSA approach, the transmission spectrum of a finite metasurface can be written as

$$T(\omega) = 1 - \frac{4\pi k}{P_x P_y} \operatorname{Im}\left[\alpha^*\right], \tag{5}$$

where α^* is the effective polarizability representing the optical response of the metasurface, defined as

$$\alpha^*(\omega) = \frac{\alpha(\omega)}{1 - \alpha(\omega) S(\omega)}. \tag{6}$$

In modified long-wavelength approximation, the polarizability of a single particle encompasses the dynamic depolarization $\left(2ik^3\alpha^{\text{static}}/3\right)$ and radiative damping $\left(2k^2\alpha^{\text{static}}/3d\right)$ as

$$\alpha(\omega) = \frac{\alpha^{\text{static}}}{1 - \frac{2}{3}ik^3\alpha^{\text{static}} - \frac{2k^2}{d}\alpha^{\text{static}}}, \tag{7}$$

with the effective particle length (d) and wavevector (k) of light around the particle. Eqs. (6) and (7) show that the effective polarizability depends strongly on the plasmonic response of an individual metamolecule given by its static polarizability

$$\alpha^{\text{static}}(\omega) = \frac{A_0}{\omega - \omega_0 + i\gamma}, \tag{8}$$

where A_0 is a constant parameter that can be determined numerically or experimentally by fitting, $\omega_0 = 2\pi f_{\text{LSP}}$ and γ is the linewidth related to the lifetime of LSPR representing the quality factor of a single metamolecule. Another essential parameter in Eq. (6) for effective polarizability is the lattice sum $S(\omega)$. Lattice sum helps to consider the effects of in-plane hybridization of LSPRs through RA diffraction (S_{in}), and out-of-plane hybridization between the cavity modes, and LSPRs (S_{out}) through superstrate reflections in the calculations. S(ω) is determined by the expression

$$S(\omega) = S_{\text{in}} + S_{\text{out}} = \sum_{j=1}^{L} \frac{e^{i\vec{k}.\vec{r}_j}}{r_j}\left[k^2\left(1+\sin\theta_j\right) + \frac{\left(1 - ikr_j\right)\left(3\cos^2\theta_j - 2\right)}{r_j^2}\right], \tag{9}$$

where r_j is the distance to the jth dipole from the main dipole, θ_j is the angle between r_j and the dipole moment component (p_x in this work), and L is the number of the nearest-neighbor dipoles.

3. Results and discussion

In the proposed metasurface, metamolecules scatter the incident light, while the phase-matched coupling of such scattered fields through RA diffraction mitigates the radiative damping of LSPRs. Furthermore, the constructive interference between the light scattered by a metamolecule and the incident light reinforces the resonance of the neighboring particles and vice versa, which partially compensates for non-radiative losses of LSPs and realizes an extraordinary lattice resonance called SLR. The transmission spectrum of the InSb

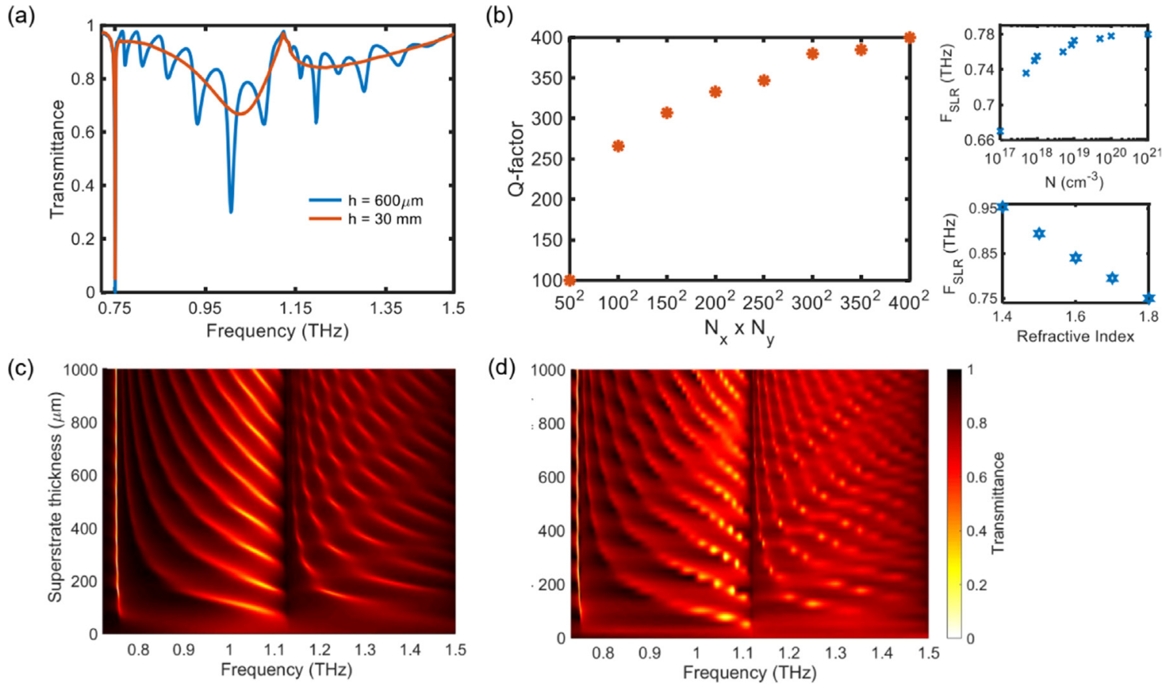

Fig. 3. (a) Effect of the superstrate thickness on the transmission of the InSb metasurface. A finite superstrate thickness (h = 600 μm) results in additional resonances, and a quasi-infinite one (h = 30 mm) suppresses these resonances. (b) Q-factor of SLR versus the number of metamolecules in the array at the fixed SLR frequency (f = 0.75 THz). The top and lower right curves demonstrate the shift in SLR frequency by changing the carrier concentration and refractive index of the surrounding medium, respectively. (c and d) Transmission of the metasurface plotted as a function of the superstrate thickness and frequency is obtained using LSA (c) and 3D-FDTD (d). Besides the SLR with the resonance frequency f = 0.75 THz additional resonances emerge in the proposed metasurface due to the out-of-plane hybridization of LSPR.

metasurface represents an SLR $\left(f_{RA} = 0.75\ \text{THz}\right)$ with Q = 375 [see Fig. 3(a)]. The material above the superstrate is air with a lower refractive index, reflecting the light at the upper interface. On the other hand, the metamolecules, at frequencies other than SLR, play the role of lower partial mirror that scatters light outward, thereby forming a cavity-like medium. Embedding the InSb metasurface in a cavity medium leads to the LSPR splitting due to the out-of-plane hybridization exciting additional narrow resonances that can be tuned by the superstrate thicknesses. When the superstrate thickness is finite, the InSb metasurface supports additional resonances close to the LSPR frequency $\left(f_{=}1.1\ \text{THz}\right)$ but the quasi-infinite one (h > 30 mm) eliminates these narrow resonances, and the broad LSPR remains unchanged [see Fig. 3(a)].

In LSA, the local field at the position of each metamolecule includes the incident field and scattered fields from other metamolecules. Adding extra metamolecule in LSA calculations means that the radiative losses will be further suppressed, and the reinforcement of LSPs would be stronger. As expected, the Q-factor of SLR increases by increasing the number of metamolecules and converges to its maximum for a higher number of metamolecules [see Fig. 3(b)]. However, there is a trade-off between the Q-factor and fabrication limits. As investigated in [68], the area of a metasurface cannot exceed 10^4 metamolecules. Therefore, the array is set to 300 × 300 metamolecules.

The lower right curve in Fig. 3(b) shows the redshift of SLR frequency for increasing values of the refractive index of the homogeneous medium surrounding the metasurface. As shown by the top right curve in Fig. 3(b), the SLR frequency is also sensitive to the carrier concentration of metamolecules which is the advantage of the proposed metasurface over its metal-based counterpart in the THz regime. The LSPR frequency blueshifts, and the resulting SLR frequency forms at higher frequencies by increasing the carrier concentration.

Fig. 3(c) and (d) demonstrate the 2D snapshot of the transmission spectrum of the metasurface for different values of the superstrate thickness versus frequency. There is an agreement between the results obtained from a finite array with 300 × 300 metamolecules in the x-y plane using LSA and an infinite array using 3D-FDTD simulations. Increasing the superstrate thickness leads to more additional resonances with lower amplitudes originating from an out-of-plane hybridization between LSP modes in the x-z plane. In addition, destructive interferences of LSP and FP modes make a gap around f = 1.15 THz which bleaches the plasmonic resonances for all the superstrate thicknesses.

Fig. 4(a) depicts the transmission spectra of the metasurface for a superstrate thickness h = 425 μm obtained by 3D-FDTD simulation. This thickness was chosen to show the SLR and additional resonances in a single frame. The electric field distributions of the corresponding narrow resonances are used to study the nature of the resonances. The SLR originates from the far-field radiative coupling of LSPRs and results in an electric field highly confined in the x-y plane. As a result, cavity modes do not affect the emergence of SLR mode [see Fig. 4(b) and (d)]. In-plane SLR can be distinguished from LSPRs because of its remarkable electric field enhancement factor, confined to the 2D lattice rather than being scattered or limited to the edge of individual metamolecules. On the other hand, Fig. 4(c) determines the origin of the additional resonances arising from the out-of-plane hybridization of LSP and cavity modes associated with the superstrate thickness.

From Fig. 4(d), it is obvious that the incident wave at the SLR frequency is almost confined to the metasurface in the plane of the array. This confinement and the narrow nature of the resonance at SLR frequency open the door for applications that require high resolution and enhanced localized electric field. To corroborate this claim, we consider sensing and tweezing applications for our proposed metasurface.

4. Applications

4.1. THz liquid sensor

The proposed metasurface can monitor any small perturbation in the surrounding medium as a liquid THz sensor. LSPR of a metamolecule is a standing longitudinal wave with near-zero momentum. The average permittivity should be zero to have a longitudinal wave;

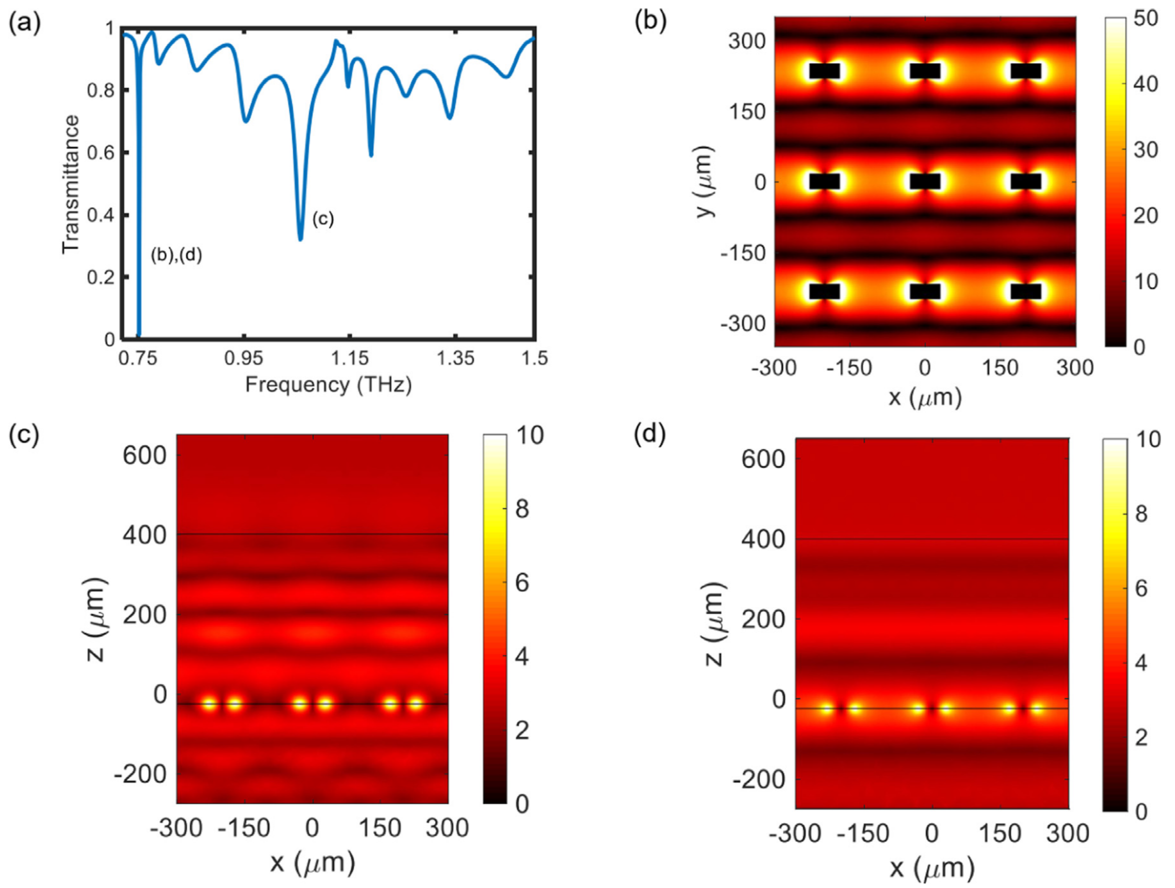

Fig. 4. (a) Transmission profile of the metasurface with the superstrate thickness $h = 425$ μm. (b) Distribution of the electric field intensity at SLR frequency for an array of InSb metamolecules. LSPRs couple together through RA diffraction leading to a remarkable electric field intensity in the *x*-*y* plane. (c) Out-of-plane hybridization between LSPRs and cavity modes results in additional resonances of the metasurface in the *x*-*z* plane. (d) Electric field intensity profile at the SLR frequency shows the hybridization between LSPRs by confining the large fraction of light at the interface between the substrate and superstrate.

this condition is called the Fröhlich condition [69]. Plasmonic particles have negative permittivity, and they cannot satisfy this condition alone. Immersing plasmonic particles inside material with positive permittivity (dielectric) allows one to achieve zero permittivity. The Fröhlich condition only occurs at a specific frequency (Fröhlich frequency) due to the dispersion of the refractive index of the plasmonic particles and that of the surrounding dielectric medium. Consequently, the LSPR depends strongly on the optical properties of its surrounding medium. Since SLR naturally obeys the behavior of LSPR, it follows the Fröhlich resonant condition that any change in optical properties of the metasurface surrounding would change the SLR resonance frequency.

To evaluate the performance of the InSb metasurface as a liquid sensor, we fixed the refractive index of the substrate at 1.46 (Silica). We slightly increased the refractive index of the superstrate ($1.46 < n < 1.48$) to show the sensitivity of the proposed metasurface to a small variation in the refractive index of the environment. This range can be associated with different fluids encompassing the substrated metasurface, similar to the schematic depicted in Fig. 6. Fig. 5(a) shows the redshift in the transmission spectra for the perturbation in the refractive index of the superstrate. This shift can be explained by the RA condition given by Eq. (4), in which the refractive index appears in the denominator of the equation.

The Figure of Merit (FOM), Fig. 5(b), gives an insight into the change in the Q-factor of SLR with an increase of the refractive index of the superstrate. FOM is defined as the sensitivity $\left(S_f = \Delta f_{SLR}/\Delta n\right)$ divided by the bandwidth $\left(FOM = S_f/FWHM\right)$. This explains a decrease in FOM with an increase in the refractive index and FWHM. Higher refractive indices result in a spectral broadening (Lower Q-factor) of SLR. The sensitivity of the proposed structure is 2.67 THz/RIU, and the average value of the FOM is 131.7 RIU^{-1}, demonstrating the maximum FOM compared to the other studies summarized in Table 2.

4.2. THz plasmonic tweezer

The proposed metasurface can confine light to the in-plane array of the metamolecules and form a hot-spot region. In tweezing applications, a suspended particle tends to move toward a region with a higher electric field intensity. Realizing a hot-spot region via the metasurface exerts an attractive gradient force on the object and manipulates it toward the region with high electric field intensity. The suspended particle near the metasurface experiences Lorentz force according to [70]

$$\langle F\rangle = \frac{\alpha'}{2} E_0 \nabla E_0 + \frac{\alpha''}{2} E_0^2 \nabla \phi, \tag{10}$$

where E_0 and ϕ are the amplitude and phase of the incident wave and $\alpha = \alpha' + i\alpha''$ is the suspended particle's polarizability. The first term on the right-hand side of the equation is the gradient force originating from the redistribution of the electric field intensity within the structure. The second term of the equation is the scattering force originating from the incident radiation. In our work, the suspended particle is much smaller than the incident wavelength ($\lambda \approx 330$ μm), so the effects of scattering forces on the particle are negligible, and the gradient forces are dominant [10,12].

The particle's polarizability plays a crucial role in determining whether the induced optical forces are attractive or repulsive. The additional degrees of freedom in tuning the resonance frequency and adjusting the polarizability available in core–shell particles make them more attractive for tweezing applications than their uniform counterparts. We consider an InSb-Silicon core–shell microparticle with a core

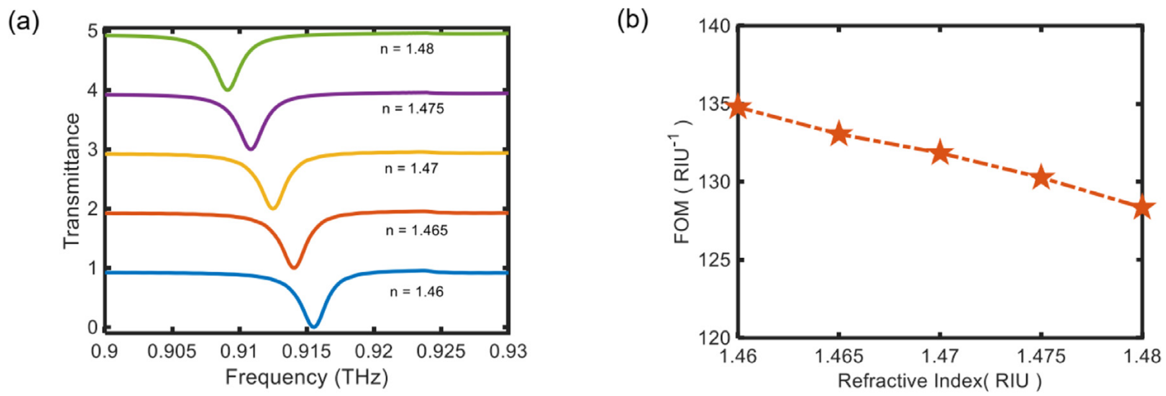

Fig. 5. (a) Transmission spectra of the metasurface as a function of frequency for various superstrate indices. SLR redshifts by increasing the refractive index of the superstrate. (b) FOM versus the refractive index of the superstrate, which represents the sensitivity over the FWHM of the proposed THz liquid sensor.

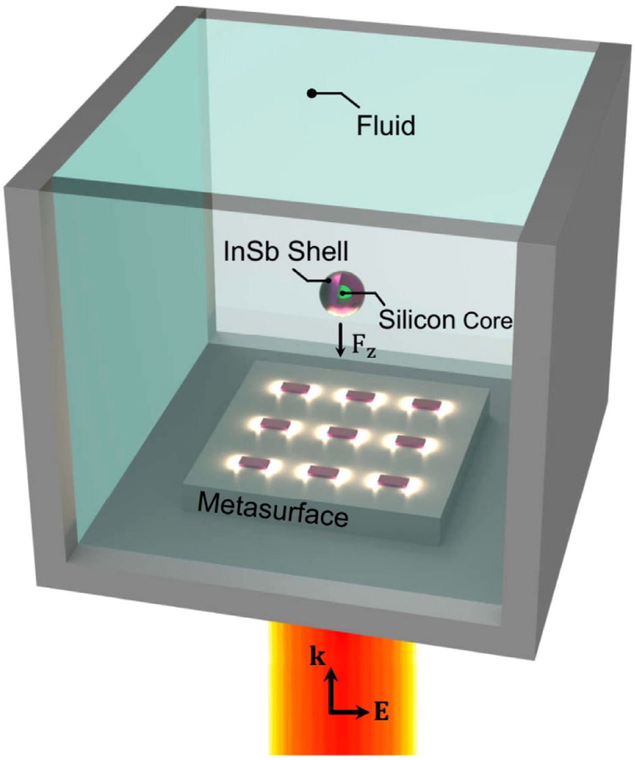

Fig. 6. Schematic view of the proposed metasurface acting as a plasmonic tweezer. The suspended microparticle is made of silicon core with $r = 2$ μm and InSb shell with $r = 3$ μm. The refractive index of the fluid inside the container is $n = 1.46$. An x-polarized plane wave illuminates the structure from below and the z-component of the optical force (F_z) is calculated in the position of the suspended microparticle. The structural parameters for the metasurface are the same as before (see Table 1), and the optical forces are analyzed at the SLR frequency.

radius of 2 μm and a shell radius of 5 μm as the suspended particle. The polarizability of a core–shell particle is described as

$$\alpha = 4\pi r^3 \frac{2\left(\varepsilon_{\text{shell}} - \varepsilon_m\right) + \left(\varepsilon_{\text{core}} + 2\varepsilon_{\text{shell}}\right) + V_{core}\left(\varepsilon_{\text{core}} - \varepsilon_{\text{shell}}\right)\left(1 + 2\varepsilon_{\text{shell}}\right)}{\left(\varepsilon_{\text{shell}} + 2\right)\left(\varepsilon_{\text{core}} + 2\varepsilon_{\text{shell}}\right) + V_{\text{core}}\left(2\varepsilon_{shell} - 2\right)\left(\varepsilon_{\text{core}} - \varepsilon_{\text{shell}}\right)} \tag{11}$$

where ε_m, $\varepsilon_{\text{core}}$, and $\varepsilon_{\text{shell}}$ are the permittivity of the surrounding medium, core, and shell, respectively; r is the radius of the particle, and V_{core} is the volume occupied by the core. Thanks to the plasmonic behavior of InSb, the suspended particle exhibits a high local-field enhancement which strengthens the induced optical forces. Depending on the particle's permittivity, the real part of the polarizability can be positive or negative. For the positive polarizability, the forces acting on the particle are repulsive, while the imposed forces are attractive for the negative one. Consequently, the attractive gradient force can exert an optical pulling force on the particle.

The schematic in Fig. 6 includes a container full of fluid with a refractive index close to the metasurface's substrate ($n = 1.46$). This fluid can act as a superstrate and can provide a homogeneous background medium for InSb metasurface. By launching the plane wave from the substrate side, we induce SLR at $f = 0.916$ THz which forms a hot-spot region at the in-plane array of InSb metamolecules. The real and imaginary parts of the polarizability for the suspended particle are depicted in Fig. 7(a). The real part of the polarizability at the SLR frequency is negative. The attractive gradient force is the consequence of high electric field intensity and negative real part of polarizability at the SLR frequency; the particle experiences a pulling force.

Fig. 7(b) shows the z-component of the optical force with and without the metasurface. In the absence of the metasurface, the scattering force is dominant, and the particle mostly experiences the optical pushing force along $+z$ direction. In the presence of the metasurface, optical pulling force manipulates the particle along $-z$ direction. The strength of the pulling force reaches its maximum value at the SLR frequency.

Fig. 7(c) illustrates the 2D snapshot of the electric field intensity at the SLR frequency. The electric field intensity distribution indicates a hot spot at the position of the metasurface, increasing the tendency of the suspended particle with negative polarizability to move toward this high-intensity region. The formation of the hot-spot region enables the tweezing application for the proposed metasurface.

Besides the material and structural properties of the suspended microparticle and metasurface, the applied optical forces also depend on the particle's distance from the metasurface. This dependency can be understood from the electrostatic force acting between the electric dipoles, wherein the force inversely depends on the distance between the microparticle and metasurface. Fig. 7(d) shows the strength of the optical forces as a function of the distance between the suspended particle and the metasurface. As the particle approaches the hot-spot region, the pulling forces act on the particle increase.

5. Conclusion

In summary, we studied the plasmonic response of a single InSb metamolecule at the THz frequencies, which can be actively adjusted by varying the free-carrier concentration or passively through changing the geometrical parameters of the metamolecule. Intrinsic non-radiative losses of InSb lead to a broadband LSPR (Q < 10). When the InSb metamolecules are placed in an ordered periodic array, the coupling of LSPRs via RA diffraction leads to an extraordinary lattice

Table 2
A comparison between the sensitivity and FOM of different types of metamaterials.

Type	Material	Frequency	Sensitivity	FOM	Reference
Surface plasmon resonance	Black phosphorus	THz	2.52 THz/RIU	N/A	[71]
Plasmon induced transparency	Graphene	THz	4.31 THz/RIU	N/A	[72]
Fano resonance	Au	GHz	105 GHz/RIU	7.51	[73]
Bound state in the continuum	Silicon	THz	2.31 THz/RIU	12.7	[74]
Spoof surface plasmons	Au	THz	197 THz/RIU	19.86	[75]
Toroidal dipole resonance	$LiTaO_3$	GHz	490 GHz/RIU	25.352	[76]
Plasmon induced transparency	Graphene	THz	4.2 THz/RIU	43,31	[77]
Split ring resonators	Au	THz	1.12 THz/RIU	50.69	[78]
Split ring resonators	Au	THz	0.38 THz/RIU	63.83	[79]
SLR	InSb	THz	2.67 THz/RIU	131.7	This work

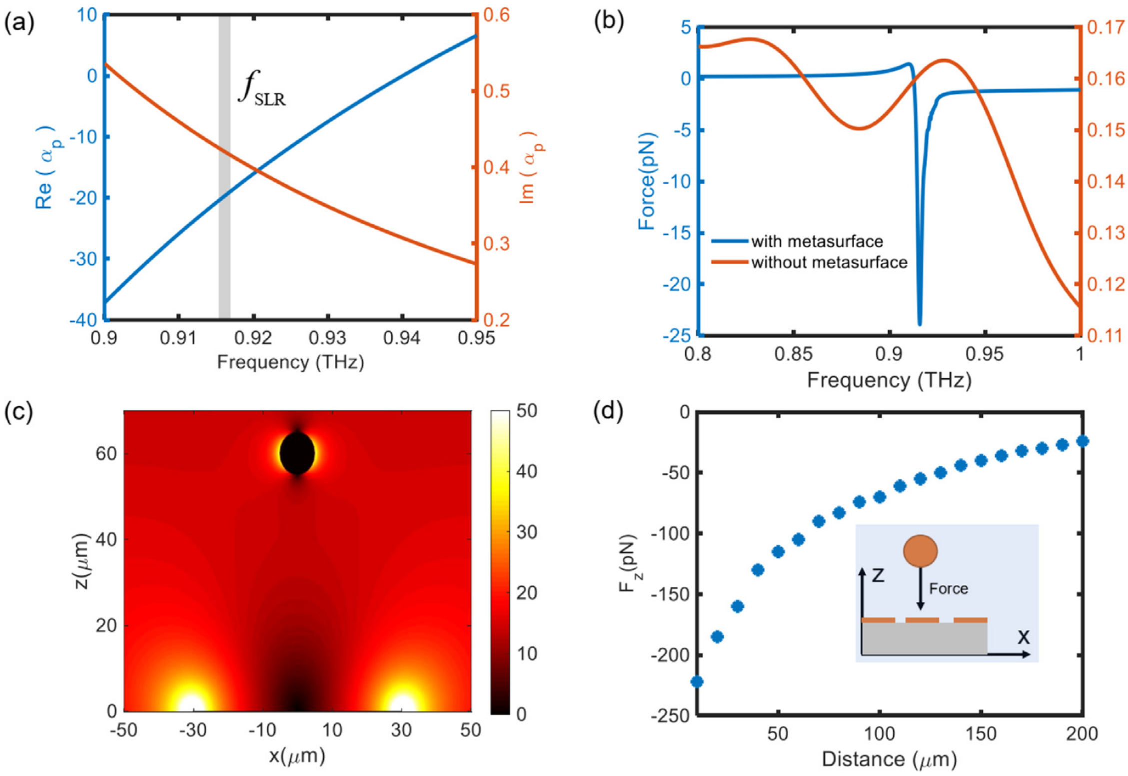

Fig. 7. (a) Real and imaginary parts of the polarizability of a suspended microparticle. The gray ribbon shows the spectral range of the SLR frequency. The real part of the polarizability accounts for the gradient force, while the imaginary part gives rise to the gradient force. (b) Optical pulling forces spectrum in the presence and the absence of the metasurface. (c) Electric field distribution at the SLR frequency in the *x*-*z* plane. (d) Optical forces versus distance of the suspended microparticle from the metasurface. The inset schematically shows the direction of the pulling forces imposed on the particle. In all these calculations, the substrate of the metasurface is silicon with a refractive index of 1.46, and the fluid where the microparticle is suspended is chosen to have the refractive index close to that of silica ensure homogeneity.

resonance at the RA frequency. This resonance depends strongly on the lattice constant and the refractive index of the surrounding homogeneous medium. We used 3D-FDTD simulations and LSA to obtain the plasmonic response of the metasurface. The results represent a narrow resonance at 0.75 THz (Q ≈ 375) arising from the in-plane hybridization of LSPRs. It is also possible to realize a higher Q-factor metasurface at the expense of increasing fabrication complexity. By breaking the symmetry of metamolecules and designing a complex unit cell, metamolecules can support sub-radiant (dark) modes. The constructive interactions between the incident wave and sub-radiant modes of the metamolecules can enable an ultra-high Q SLR. We have also demonstrated that additional narrow resonances can appear throughout the out-of-plane hybridization between LSPRs and FP modes. The number, strength, and resonance frequency of such resonances can be engineered by tuning the thickness of the superstrate. Simple geometry, substantial electric field enhancement factor, and high-Q resonances are the main features of the proposed structure. Practically speaking, this design can be used for harmonic generations, plasmonic tweezing, and sensing applications in the THz regime.

Funding

This research was undertaken thanks in part to funding from Canada Research Chairs program, Natural Sciences and Engineering Research Council's, Canada Discovery funding program [RGPIN-2020-03989], The Ontario Early Researcher Award, Canada, and the Canada First Research Excellence Fund.

Declaration of competing interest

The authors declare that they have no known competing financial interests or personal relationships that could have appeared to influence the work reported in this paper.

Data availability

The data that support the results of this study are available from the corresponding author upon reasonable request.

Acknowledgments

The authors would like to thank Orad Reshef and Mikko J. Huttunenn for discussions.

References

[1] D.K. Gramotnev, S.I. Bozhevolnyi, Plasmonics beyond the diffraction limit, Nat. Photonics. 4 (2010) 83–91.
[2] S.J. Oldenburg, R.D. Averitt, S.L. Westcott, N.J. Halas, Nanoengineering of optical resonances, Chem. Phys. Lett. 288 (1998) 243–247.
[3] S.I. Bozhevolnyi, V.S. Volkov, E. Devaux, J.-Y. Laluet, T.W. Ebbesen, Channel plasmon subwavelength waveguide components including interferometers and ring resonators, Nature 440 (2006) 508–511.
[4] A. Amini, S. Aghili, S. Golmohammadi, P. Gasemi, Design of microelectromechanically tunable metal–insulator–metal plasmonic band-pass/stop filter based on slit waveguides, Opt. Commun. 403 (2017) 226–233, http://dx.doi.org/10.1016/j.optcom.2017.07.042.
[5] A. Amini, S. Golmohammadi, S. Aghili, Plasmonic response of graphene-like metallic-molecular nanocluster for optical applications, Opt. Eng. 57 (2018) 77104.
[6] K.L. Kelly, E. Coronado, L.L. Zhao, G.C. Schatz, The optical properties of metal nanoparticles: the influence of size, shape, and dielectric environment, 2003.
[7] M. Quinten, A. Leitner, J.R. Krenn, F.R. Aussenegg, Electromagnetic energy transport via linear chains of silver nanoparticles, Opt. Lett. 23 (1998) 1331–1333.
[8] S. Yokogawa, S.P. Burgos, H.A. Atwater, Plasmonic color filters for CMOS image sensor applications, Nano Lett. 12 (2012) 4349–4354.
[9] A. Portela, O. Calvo-Lozano, M.-C. Estevez, A.M. Escuela, L.M. Lechuga, Optical nanogap antennas as plasmonic biosensors for the detection of miRNA biomarkers, J. Mater. Chem. B. 8 (2020) 4310–4317.
[10] A.S. Shalin, P. Ginzburg, P.A. Belov, Y.S. Kivshar, A.V. Zayats, Nano-opto-mechanical effects in plasmonic waveguides, Laser Photonics Rev. 8 (2014) 131–136.
[11] M. Nicolas, I. Soumahoro, L. Zhang, G. Guida, W.D. de Marcillac, D. Demaille, C. Schwob, S. Boujday, B. Gallas, Mueller micropolarimeter for color imaging of aluminum metasurfaces, JOSA B. 38 (2021) 1184–1191.
[12] S. Aghili, S. Golmohammadi, A. Amini, Proposing an on/off optical router in telecom wavelength using plasmonic tweezer, Opt. Commun. 427 (2018) 95–100.
[13] C.-L. Huang, G. Kumar, G.D. Sharma, F.-C. Chen, Plasmonic effects of copper nanoparticles in polymer photovoltaic devices for outdoor and indoor applications, Appl. Phys. Lett. 116 (2020) 253302.
[14] D.D. Firsov, O.S. Komkov, V.A. Solov'ev, A.N. Semenov, S.V. Ivanov, Infrared photoreflectance of insb-based two-dimensional nanostructures, JOSA B. 36 (2019) 910–916.
[15] V.G. Kravets, A.V. Kabashin, W.L. Barnes, A.N. Grigorenko, Plasmonic surface lattice resonances: a review of properties and applications, Chem. Rev. 118 (2018) 5912–5951.
[16] M.S. Bin-Alam, O. Reshef, Y. Mamchur, M.Z. Alam, G. Carlow, J. Upham, B.T. Sullivan, J.-M. Ménard, M.J. Huttunen, R.W. Boyd, Ultra-high-q resonances in plasmonic metasurfaces, Nature Commun. 12 (2021) 1–8.
[17] B. Auguié, W.L. Barnes, Collective resonances in gold nanoparticle arrays, Phys. Rev. Lett. 101 (2008) 143902.
[18] A.T.M.A. Rahman, P. Majewski, K. Vasilev, Extraordinary optical transmission: coupling of the wood–Rayleigh anomaly and the Fabry–Perot resonance, Opt. Lett. 37 (2012) 1742–1744.
[19] S.V. Boriskina, T.A. Cooper, L. Zeng, G. Ni, J.K. Tong, Y. Tsurimaki, Y. Huang, L. Meroueh, G. Mahan, G. Chen, Losses in plasmonics: from mitigating energy dissipation to embracing loss-enabled functionalities, Adv. Opt. Photonics. 9 (2017) 775–827, http://dx.doi.org/10.1364/AOP.9.000775.
[20] D. Khlopin, F. Laux, W.P. Wardley, J. Martin, G.A. Wurtz, J. Plain, N. Bonod, A.V. Zayats, W. Dickson, D. Gérard, Lattice modes and plasmonic linewidth engineering in gold and aluminum nanoparticle arrays, JOSA B. 34 (2017) 691–700.
[21] A. Yu, W. Li, Y. Wang, T. Li, Surface lattice resonances based on parallel coupling in metal–insulator–metal stacks, Opt. Express 26 (2018) 20695–20707.
[22] G.W. Castellanos, P. Bai, J. Gómez Rivas, Lattice resonances in dielectric metasurfaces, J. Appl. Phys. 125 (2019) 213105.
[23] A. Yang, T.B. Hoang, M. Dridi, C. Deeb, M.H. Mikkelsen, G.C. Schatz, T.W. Odom, Real-time tunable lasing from plasmonic nanocavity arrays, Nature Commun. 6 (2015) 1–7.
[24] L.Y.M. Tobing, A.M. Soehartono, A.D. Mueller, K.-T. Yong, W. Fan, D.H. Zhang, Hybridized surface lattice modes in intercalated 3-disk plasmonic crystals for high figure-of-merit plasmonic sensing, Nanoscale (2021).
[25] A. Yang, A.J. Hryn, M.R. Bourgeois, W.-K. Lee, J. Hu, G.C. Schatz, T.W. Odom, Programmable and reversible plasmon mode engineering, Proc. Natl. Acad. Sci. 113 (2016) 14201–14206.
[26] M. Kauranen, A.V. Zayats, Nonlinear plasmonics, Nat. Photonics. 6 (2012) 737–748.
[27] M.S. Bin-Alam, J. Baxter, K.M. Awan, A. Kiviniemi, Y. Mamchur, A.C. Lesina, K.L. Tsakmakidis, M.J. Huttunen, L. Ramunno, K. Dolgaleva, Hyperpolarizability of plasmonic meta-atoms in metasurfaces, Nano Lett. (2020).
[28] M.J. Huttunen, P. Rasekh, R.W. Boyd, K. Dolgaleva, Using surface lattice resonances to engineer nonlinear optical processes in metal nanoparticle arrays, Phys. Rev. A. 97 (2018) 53817.
[29] P.C. Chaumet, A. Sentenac, A. Rahmani, Coupled dipole method for scatterers with large permittivity, Phys. Rev. E. 70 (2004) 36606.
[30] M.J. Huttunen, K. Dolgaleva, P. Törmä, R.W. Boyd, Ultra-strong polarization dependence of surface lattice resonances with out-of-plane plasmon oscillations, Opt. Express 24 (2016) 28279–28289.
[31] M.J. Huttunen, O. Reshef, T. Stolt, K. Dolgaleva, R.W. Boyd, M. Kauranen, Efficient nonlinear metasurfaces by using multiresonant high-q plasmonic arrays, JOSA B. 36 (2019) E30–E35.
[32] V.L.Y. Loke, M.P. Mengüç, T.A. Nieminen, Discrete-dipole approximation with surface interaction: Computational toolbox for MATLAB, J. Quant. Spectrosc. Radiat. Transfer 112 (2011) 1711–1725.
[33] I.F. Akyildiz, J.M. Jornet, C. Han, Terahertz band: Next frontier for wireless communications, Phys. Commun. 12 (2014) 16–32.
[34] J.F. Federici, B. Schulkin, F. Huang, D. Gary, R. Barat, F. Oliveira, D. Zimdars, THz imaging and sensing for security applications—explosives, weapons and drugs, Semicond. Sci. Technol. 20 (2005) S266.
[35] Z.D. Taylor, R.S. Singh, D.B. Bennett, P. Tewari, C.P. Kealey, N. Bajwa, M.O. Culjat, A. Stojadinovic, H. Lee, J.-P. Hubschman, THz medical imaging: in vivo hydration sensing, IEEE Trans. Terahertz Sci. Technol. 1 (2011) 201–219.
[36] P. Rasekh, M. Saliminabi, M. Yildirim, R.W. Boyd, J.-M. Ménard, K. Dolgaleva, Propagation of broadband THz pulses: effects of dispersion, diffraction and time-varying nonlinear refraction, Opt. Express 28 (2020) 3237–3248.
[37] P. Rasekh, A. Safari, M. Yildirim, R. Bhardwaj, J.-M. Ménard, K. Dolgaleva, R.W. Boyd, Terahertz nonlinear spectroscopy of water vapor, ACS Photonics. (2021).
[38] M. Tonouchi, Cutting-edge terahertz technology, Nat. Photonics. 1 (2007) 97–105.
[39] A. Rusina, M. Durach, K.A. Nelson, M.I. Stockman, Nanoconcentration of terahertz radiation in plasmonic waveguides, Opt. Express 16 (2008) 18576–18589.
[40] C.R. Williams, S.R. Andrews, S.A. Maier, A.I. Fernández-Domínguez, L. Martín-Moreno, F.J. García-Vidal, Highly confined guiding of terahertz surface plasmon polaritons on structured metal surfaces, Nat. Photonics. 2 (2008) 175–179.
[41] L. Gingras, A. Jaber, A. Maleki, O. Reshef, K. Dolgaleva, R.W. Boyd, J.-M. Ménard, Ultrafast modulation of the spectral filtering properties of a THz metasurface, Opt. Express 28 (2020) 20296–20304.
[42] T.C. Tan, E. Plum, R. Singh, Surface lattice resonances in THz metamaterials, in: Photonics, Multidisciplinary Digital Publishing Institute, 2019, p. 75.
[43] Y. Cheng, H. Zou, J. Yang, X. Mao, R. Gong, Dual and broadband terahertz metamaterial absorber based on a compact resonator structure, Opt. Mater. Express. 8 (2018) 3104–3114.
[44] B. Jafari, H. Soofi, K. Abbasian, Low. voltage, High modulation depth graphene THz modulator employing Fabry–Perot resonance in a metal/dielectric/graphene sandwich structure, Opt. Commun. 472 (2020) 125911.
[45] Y. Li, Z. Feng, L. Huang, K. Essa, E. Bilotti, H. Zhang, T. Peijs, L. Hao, Additive manufacturing high performance graphene-based composites: A review, Compos. Part A Appl. Sci. Manuf. 124 (2019) 105483.
[46] J. Chochol, K. Postava, M. Čada, M. Vanwolleghem, M. Mičica, L. Halagačka, J.-F. Lampin, J. Pištora, Plasmonic behavior of III-v semiconductors in far-infrared and terahertz range, J. Eur. Opt. Soc. Publ. 13 (2017) 1–8.
[47] T.J. Cui, S. Liu, L. Zhang, Information metamaterials and metasurfaces, J. Mater. Chem. C. 5 (2017) 3644–3668.
[48] S. Liu, P. Yue, S. Zhang, M. Wang, H. Dai, Y. Chen, Z. Nie, Y. Cui, J. Han, H. Duan, Metasurfaces composed of plasmonic molecules: Hybridization between parallel and orthogonal surface lattice resonances, Adv. Opt. Mater. 8 (2020) 1901109.
[49] J.G. Rivas, C. Schotsch, P.H. Bolivar, H. Kurz, Enhanced transmission of THz radiation through subwavelength holes, Phys. Rev. B. 68 (2003) 201306.
[50] B. Ng, S.M. Hanham, V. Giannini, Z.C. Chen, M. Tang, Y.F. Liew, N. Klein, M.H. Hong, S.A. Maier, Lattice resonances in antenna arrays for liquid sensing in the terahertz regime, Opt. Express 19 (2011) 14653–14661.
[51] M.C. Schaafsma, THZ resonances in semiconductor structures, 2015.
[52] B.-X. Wang, W.-Q. Huang, L.-L. Wang, Ultra-narrow terahertz perfect light absorber based on surface lattice resonance of a sandwich resonator for sensing applications, RSC Adv. 7 (2017) 42956–42963.
[53] L. Deng, J. Teng, H. Liu, Q.Y. Wu, J. Tang, X. Zhang, S.A. Maier, K.P. Lim, C.Y. Ngo, S.F. Yoon, Direct optical tuning of the terahertz plasmonic response of InSb subwavelength gratings, Adv. Opt. Mater. 1 (2013) 128–132.
[54] D.M. Sullivan, Electromagnetic Simulation using the FDTD Method, John Wiley & Sons, 2013.
[55] G.P. Zouros, G.D. Kolezas, E. Almpanis, K.L. Tsakmakidis, Three-dimensional giant invisibility to superscattering enhancement induced by Zeeman-split modes, ACS Photonics. 8 (2021) 1407–1412.
[56] M. Moridsadat, S. Golmohammadi, H. Baghban, Tunable multiband plasmonic response of indium antimonide touching microrings in the terahertz range, Appl. Opt. 57 (2018) 4368–4375.

[57] J. Chochol, K. Postava, M. Čada, J. Pištora, Experimental demonstration of magnetoplasmon polariton at InSb (InAs)/dielectric interface for terahertz sensor application, Sci. Rep. 7 (2017) 1–8.
[58] J. Chochol, K. Postava, M. Čada, M. Vanwolleghem, L. Halagačka, J.-F. Lampin, J. Pištora, Magneto-optical properties of InSb for terahertz applications, AIP Adv. 6 (2016) 115021.
[59] Y.J. Jung, M.K. Park, S.I. Tae, K.H. Lee, H.J. Lee, Electron transport and energy-band structure of InSb, J. Appl. Phys. 69 (1991) 3109–3114.
[60] V. Giannini, A. Berrier, S.A. Maier, J.A. Sánchez-Gil, J.G. Rivas, Scattering efficiency and near field enhancement of active semiconductor plasmonic antennas at terahertz frequencies, Opt. Express 18 (2010) 2797–2807.
[61] E. Prodan, C. Radloff, N.J. Halas, P. Nordlander, A hybridization model for the plasmon response of complex nanostructures, Science (80-.). 302 (2003) 419–422.
[62] V.A. Markel, Coupled-dipole approach to scattering of light from a one-dimensional periodic dipole structure, J. Modern Opt. 40 (1993) 2281–2291.
[63] R.W. Wood, XLII, On a remarkable case of uneven distribution of light in a diffraction grating spectrum, London, Edinburgh, Dublin Philos, Mag. J. Sci. 4 (1902) 396–402.
[64] O.P. Cherkasova, D.S. Serdyukov, E.F. Nemova, A.S. Ratushnyak, A.S. Kucheryavenko, I.N. Dolganova, G. Xu, M. Skorobogatiy, I.V. Reshetov, P.S. Timashev, Cellular effects of terahertz waves, J. Biomed. Opt. 26 (2021) 90902.
[65] J.-Y. Lee, H.-C. Shih, C.-T. Hong, T.K. Chou, Measurement of refractive index change by surface plasmon resonance and phase quadrature interferometry, Opt. Commun. 276 (2007) 283–287.
[66] O. Reshef, M. Saad-Bin-Alam, M.J. Huttunen, G. Carlow, B.T. Sullivan, J.-M. Ménard, K. Dolgaleva, R.W. Boyd, Multiresonant high-Q plasmonic metasurfaces, Nano Lett. 19 (2019) 6429–6434.
[67] F. Yan, Q. Li, Z. Wang, H. Tian, L. Li, Extremely high Q-factor terahertz metasurface using reconstructive coherent mode resonance, Opt. Express 29 (2021) 7015–7023.
[68] A. Lechner, T. Feller, Q. Song, B. Kopera, L. Heindl, M. Drechsler, S. Rosenfeldt, M. Retsch, Scalable synthesis of smooth PS@ TiO2 core–shell and TiO2 hollow spheres in the (sub) micron size range: understanding synthesis and calcination parameters, Colloid Polym. Sci. (2020).
[69] R.D. Averitt, S.L. Westcott, N.J. Halas, Linear optical properties of gold nanoshells, JOSA B. 16 (1999) 1824–1832.
[70] L. Novotny, B. Hecht, Principles of Nano-Optics, Cambridge University Press, 2012.
[71] X. Lu, X. Zeng, H. Lv, Y. Han, Z. Mou, C. Liu, S. Wang, S. Teng, Polarization controllable plasmonic focusing based on nanometer holes, Nanotechnology 31 (2020) 135201.
[72] S.-X. Xia, X. Zhai, L.-L. Wang, S.-C. Wen, Plasmonically induced transparency in double-layered graphene nanoribbons, Photonics Res. 6 (2018) 692–702.
[73] Q. Xie, G.-X. Dong, B.-X. Wang, W.-Q. Huang, High-q Fano resonance in terahertz frequency based on an asymmetric metamaterial resonator, Nanoscale Res. Lett. 13 (2018) 1–7.
[74] T. Ma, Q. Huang, H. He, Y. Zhao, Xi. Lin, Y. Lu, All-dielectric metamaterial analogue of electromagnetically induced transparency and its sensing application in terahertz range, Opt. Express 27 (2019) 16624–16634.
[75] X. Chen, W. Fan, Ultrasensitive terahertz metamaterial sensor based on spoof surface plasmon, Sci. Rep. 7 (2017) 1–8.
[76] Y. Wang, Z. Han, Y. Du, J. Qin, Ultrasensitive terahertz sensing with high-Q toroidal dipole resonance governed by bound states in the continuum in all-dielectric metasurface, Nanophotonics 10 (2021) 1295–1307.
[77] W. Cui, C. Li, H. Ma, H. Xu, Z. Yi, X. Ren, X. Cao, Z. He, Z. Liu, Excellent sensing based on dual-plasmon induced transparency in graphene metasurface, Phys. E Low-Dimensional Syst. Nanostructures 134 (2021) 114850.
[78] J. Yang, Y.-S. Lin, Design of tunable terahertz metamaterial sensor with single-and dual-resonance characteristic, Nanomaterials 11 (2021) 2212.
[79] J. Zhong, X. Xu, Y.-S. Lin, Tunable terahertz metamaterial with electromagnetically induced transparency characteristic for sensing application, Nanomaterials 11 (2021) 2175.

Chapter 4

Dynamic Control of Spontaneous Emission via III-V Metamaterials

4.1 Contribution Statement

I initially became familiar with the concept of dynamically controlling the photon production rate of an emitter using a resonant optical antenna through discussions with Dr. Alaee. The core concept of this project was jointly developed by Dr. Alaee and me during regular meetings, and it was further refined through continuous guidance and feedback from Prof. Dolgaleva.

The modelling work was carried out by Dr. Alaee and me using a semi-numerical framework implemented in the RF Module of COMSOL. I was responsible for performing the simulations and carrying out the optimization studies. Together with Prof. Dolgaleva and Dr. Alaee, I analyzed the results and refined the proposed designs, and I also benefited from technical discussions with E. Mobini. To further investigate and optimize the coupled system, A. Ahmadnejad and M. R. Mohammadpour contributed by implementing a machine-learning-based optimization, which supported the main physical mechanisms and the key simulated outputs.

I wrote the first draft of the manuscript and prepared the figures, which were substantially improved based on feedback from Prof. Dolgaleva, Prof. Rockstuhl, and Dr. Alaee. The project was led by Dr. Alaee and Prof. Dolgaleva. All co-authors contributed to the revision process and approved the final version.

Conference publications related to this project are listed below:

- Aghili, Sina, *et al.* "InSb-based THz Plasmonic Antenna for Dynamic Control of Radiative Decay Rate of Quantum Emitters." *2023 Photonics North (PN)*. IEEE, 2023.
- Aghili, Sina, *et al.* "High-Q Tunable THz Plasmonic Metasurface based on InSb Particles." *2023 48th International Conference on Infrared, Millimeter, and Terahertz Waves (IRMMW-THz)*. IEEE, 2023.
- Aghili, Sina, *et al.* "THz Emission Engineering Using Resonant III-V Semiconductor Metamaterials." *2025 Photonics North (PN)*. IEEE, 2025.

4.2 Article

The results of this project were published in *Journal of Physics: Photonics* [140], and this chapter is based on the following article.

IOP Publishing *J. Phys. Photonics* **6** (2024) 035011 https://doi.org/10.1088/2515-7647/ad4c34

Journal of Physics: Photonics

CrossMark

OPEN ACCESS

RECEIVED
25 January 2024

REVISED
24 April 2024

ACCEPTED FOR PUBLICATION
15 May 2024

PUBLISHED
28 May 2024

PAPER

Dynamic control of spontaneous emission using magnetized InSb higher-order-mode antennas

Sina Aghili[1], Rasoul Alaee[2,3,*], Amirreza Ahmadnejad[4], Ehsan Mobini[2], Mohammadreza Mohammadpour[2], Carsten Rockstuhl[3,5] and Ksenia Dolgaleva[1,2]

1 School of Electrical Engineering and Computer Science, University of Ottawa, Ottawa, Ontario K1N 6N5, Canada
2 Department of Physics, University of Ottawa, Ottawa, Ontario K1N 6N5, Canada
3 Karlsruhe Institute of Technology, Institute of Theoretical Solid State Physics, D-76131 Karlsruhe, Germany
4 Department of Electrical Engineering, Sharif University of Technology, Tehran 11155-4365, Iran
5 Institute of Nanotechnology, Karlsruhe Institute of Technology, D-76344 Eggenstein-Leopoldshafen, Germany
* Author to whom any correspondence should be addressed.

E-mail: rasoul.alaee@gmail.com

Keywords: active antenna, indium antimonide (InSb), local density of states, multipole moments, radiative decay rate, Zeeman-splitting effect, III-V semiconductors

Supplementary material for this article is available online

Abstract

We exploit InSb's magnetic-induced optical properties to design THz sub-wavelength antennas that actively tune the radiative decay rates of dipole emitters at their proximity. The proposed designs include a spherical InSb antenna and a cylindrical Si-InSb hybrid antenna demonstrating distinct behaviors. The former dramatically enhances both radiative and non-radiative decay rates in the epsilon-near-zero region due to the dominant contribution of the Zeeman-splitting electric octupole mode. The latter realizes significant radiative decay rate enhancement via magnetic octupole mode, mitigating the quenching process and accelerating the photon production rate. A deep-learning-based optimization of emitter positioning further enhances the quantum efficiency of the proposed hybrid system. These novel mechanisms are promising for tunable THz single-photon sources in integrated quantum networks.

1. Introduction

It has been long appreciated that the local density of states (LDOS), as seen by a quantum emitter, can be altered in a structured electromagnetic environment [1, 2]. The spontaneous emission (SE) rate and transition dipole strength, as the functional characteristics of a quantum emitter, greatly rely on LDOS variations [3]. In simple terms, the electric or magnetic dipole transition of quantum emitters, when considered as two-level systems, can couple to photonic resonances. Then, the enhancement of the LDOS, thanks to the structured photonic environment, accelerates the spontaneous transition rates of the quantum emitter. The SE rate enhancement is of great interest to diverse applications, including quantum source emission engineering [4–6], ultra-brighter optoelectronic devices [7–10], enhanced light–matter interaction for fluorescence spectroscopy [11–13], and single-photon sources (SPSs) [14–16].

Optical resonators are high-potential devices that can serve as the structured electromagnetic media for quantum emitters by providing an enhanced LDOS [17, 18]. Radiative coupling channels emerge in a coupled emitter-resonator system, allowing one to improve the SE rate of the quantum emitter. Microcavities [19], photonic crystals, and hyperbolic metamaterials [20–22] have been extensively explored as closed-cavity platforms with the potential to enhance the SE rate of quantum emitters significantly. In recent decades, optical antennas have been the subject of this extensive research. Optical antennas are open resonators composed of sub-wavelength dielectric or metallic elements that transfer the energy of their resonance modes to quantum emitters via radiative and non-radiative channels [23–25]. Enhanced light–matter interaction at the deep sub-wavelength scale is the distinguishing advantage of antennas over cavities. This leads to LDOS enhancement of quantum emitters in the coupled emitter-antenna systems. In this direction, metallic antennas enable one to modify the SE rate of quantum emitters due to the high near-field enhancement attained by localized surface plasmon resonances (LSPRs) [26–30]. Metallic nanorods [31] and ring resonators [32] are highly effective plasmonic sub-wavelength antennas for enhancing the SE rate of quantum emitters through the excitation of LSPRs, including transversal and longitudinal plasmonic modes in nanorods, and concurrent electric and magnetic resonant modes in ring resonators. In general, coupled emitter-plasmonic antenna systems usually introduce dominant non-radiative channels due to high Joule heating losses of metallic building blocks, resulting in low quantum efficiency for the coupled systems.

Alternative designs have been investigated to mitigate dissipation losses of plasmonic antennas. Interestingly, it was shown that plasmonic devices using a dielectric spacer could avoid or limit non-radiative decay channels [33]. This idea has flourished by employing dielectric optical antennas in a wide range of applications such as surface-enhanced Raman spectroscopy [34], surface-enhanced fluorescence [35], directional light emission [36], nonlinear processes [37], and Huygens sources [38]. Furthermore, optically induced electric and magnetic Mie resonances make high-index dielectric antennas capable of efficiently engineering the SE rate of quantum emitters with electric or magnetic transition dipole moment [39–42]. Besides the coexistence of electric and magnetic multipolar resonances at the sub-wavelength scale, unique characteristics such as negligible inherent losses and comparable near-field enhancement with metallic analogs enable high-index dielectric structures to suppress non-radiative channels and robustify radiative channels in the coupled emitter-dielectric antenna systems. Concentric hollow structures [43], Yagi-Uda designs [44], dimers [45], and oligomers [46] have been numerically and experimentally investigated to use the high potential of dielectric sub-wavelength antennas in engineering the SE rate of quantum emitters.

Among the reported cases exploited to control the SE rate of quantum emitters for specific applications, the research has been mostly limited to passive approaches such as design, material, and shape to improve the efficiency of the coupled emitter-photonic systems. Here, we aim to employ active antennas to dynamically control the SE or radiative decay rate of quantum emitters near the proposed antennas. By applying an external static magnetic field, we dynamically tune the scattering response of an optical antenna, leading to the radiative decay rate variations of a quantum emitter. In this respect, we need a material whose optical properties can be modulated upon magnetization [47]. Hence, indium antimonide (InSb), a III-V semiconductor with unique features of nonreciprocity, magnetoplasmonics, and magnetic tunability in the THz region [48–50], has been exploited to achieve an active sub-wavelength antenna. Without a static magnetic field, the scattering response of a spherical InSb antenna is divided into plasmonic, epsilon-near-zero (ENZ), and dielectric regions. By placing an electric dipole (ED) source close to the antenna as the quantum emitter, we observe different types of electromagnetic behaviors in the coupled emitter-antenna system. Non-radiative channels dominate the plasmonic region due to inherent losses of InSb below the plasma frequency, resulting in the quenching process. A transparency window corresponds to the ENZ region; hence, the quantum emitter does not experience the impact of the antenna. The coexistence of electric and magnetic multipolar resonances is observed in the dielectric region, leading to SE rate enhancement associated with dominant radiative channels. In the presence of the static magnetic field, the scattering characteristics of the InSb antenna are dramatically changed. The quenching effect becomes much more intense in the plasmonic region. Therefore, the radiative decay rate is negligible compared to the non-radiative one. The ENZ region completely disappears due to the Zeeman-splitting effect of plasmonic modes, and the quantum emitter experiences considerable radiative decay rate variations compared to the unmagnetized case. Despite dynamic control of the emission characteristics of the ED emitter via the magnetized InSb antenna, dominant non-radiative processes degrade the efficiency of the proposed antenna across the studied spectral range. To solve this limitation, as the next step, a hybrid dielectric antenna composed of Silicon (Si) and InSb layers has been proposed to serve as the high-index dielectric antenna, leading to a high radiative decay rate enhancement for the coupled magnetic dipole (MD) and ED emitter-antenna systems. Dual-band SE rate enhancement, robust magnetic response, and high quantum efficiency are important advantages realized by the magnetized hybrid antenna, opening up a possibility for the emergence of tunable magnetic SPSs.

2. Methodology

The spontaneous decay of a two-level system, the so-called quantum emitter, is a radiating process at a quantum level that can be estimated by Fermi's golden rule [51]. When we consider the interaction of quantum emitters with optical antennas as open resonators and lossy media, the normalized total decay rate ($\Gamma_{\mathrm{tot}}/\Gamma_0$) must be defined by LDOS in the form of [51]

$$\frac{\Gamma_{\mathrm{tot}}}{\Gamma_0} = \frac{\rho_n(\boldsymbol{r}_0,\omega)}{\rho_0(\boldsymbol{r}_0,\omega)} = \frac{\boldsymbol{n}_p^T \, \mathrm{Im}\left[\overleftrightarrow{\boldsymbol{G}}_s(\boldsymbol{r}_0,\boldsymbol{r}_0;\omega) + \overleftrightarrow{\boldsymbol{G}}_0(\boldsymbol{r}_0,\boldsymbol{r}_0;\omega)\right]\boldsymbol{n}_p}{\boldsymbol{n}_p^T \, \mathrm{Im}\left[\overleftrightarrow{\boldsymbol{G}}_0(\boldsymbol{r}_0,\boldsymbol{r}_0;\omega)\right]\boldsymbol{n}_p}, \tag{1}$$

where $\rho_n(\boldsymbol{r}_0,\omega)$ and $\rho_0(\boldsymbol{r}_0,\omega)$ represent the LDOS at the position $\boldsymbol{r}_0$ of the quantum emitter with a transition frequency ω in the presence and absence of the optical sub-wavelength antenna, respectively. The LDOS at the position of the quantum emitter is computed using the imaginary part of the Green function [23], and $\boldsymbol{n}_p$ indicates the polarization's unit vector. Without the antenna, the LDOS only depends on the electromagnetic field generated by the quantum emitter ($\overleftrightarrow{\boldsymbol{G}_0}(\boldsymbol{r}_0,\boldsymbol{r}_0;\omega)$) at its position. Besides the self-generated field, in the presence of the antenna, the LDOS has another contribution from the electromagnetic field scattered by the antenna ($\overleftrightarrow{\boldsymbol{G}_s}(\boldsymbol{r}_0,\boldsymbol{r}_0;\omega)$) at the emitter position, showing the impact of the local field provided by optical sub-wavelength antennas on the total decay rate modification. The contribution of the LDOS to engineering the decay rates of a quantum emitter is a common point of classical and quantum electrodynamics [51]. From a classical point of view, a quantum emitter can be modeled by a point-like dipole as an oscillating current source located near an antenna. Both electrodynamical and classical approaches agree when the intrinsic quantum yield of the point-like quantum source is unity. The total decay rate is defined as the ratio of the total emitted power of a dipole source in the presence of the antenna to its total emitted power in the absence of the antenna in the form of

$$\frac{\Gamma_{\mathrm{tot}}}{\Gamma_0} = \frac{\Gamma_{\mathrm{r}} + \Gamma_{\mathrm{nr}}}{\Gamma_0} = \frac{P_{\mathrm{r}} + P_{\mathrm{nr}}}{P_0}, \tag{2}$$

where the radiative and non-radiative decay rates are denoted by Γ_{r} and Γ_{nr}, respectively. Here, P_{r} and P_{nr} are also the scattered and absorbed powers by the antenna, respectively. The part of the total power incident on the antenna decays into the non-radiative channels due to the inherent losses of the antenna [23, 51]. The remaining fraction of the radiation escapes from the coupled emitter-antenna system to free space as far-field radiation. It is thus necessary to calculate the corresponding powers represented in equation (2) using the Poynting theorem [52]. The total emitted power is obtained by integrating the Poynting vector flux over a surface enclosing the dipole source without the antenna. The far-field radiation of the coupled emitter-antenna system is computed by placing a Poynting vector surface integral around the entire system. The dissipated power is proportional to the power loss density, determined by a volume integral around the antenna.

In this study, we use COMSOL Multiphysics RF module package 6 to numerically compute the coupled emitter-antenna system's power rates corresponding to the dipole source's total decay rate [53, 54]. Owing to the inherent duality in classical electrodynamics, particularly in Maxwell's equations, the far-field radiation patterns of a quantum emitter possessing a transition magnetic dipole (MD) moment are indistinguishable from those with an ED moment. Consequently, the same numerical Poynting theorem applicable to EDs can be employed within COMSOL's RF module to compute the total decay rate of an MD emitter. The distinction lies in the necessity to define a point source with a transition MD moment within the simulation model.

3. Results

3.1. Spherical InSb antenna

The primary purpose of this study is to investigate how a static magnetic field applied to an optical antenna dynamically modifies the radiative decay rate of a dipole emitter in the weak-coupling regime. We first consider a spherical InSb antenna embedded in free space to serve as a sub-wavelength THz antenna. The antenna's radius is set to 30 μm, corresponding to the operation frequency range of 1.2–3 THz, matching the range of InSb's plasma frequency. The antenna's geometry and spectral range are chosen such that the antenna can support multipolar electromagnetic resonance modes. Upon magnetic excitation perpendicular to the incidence plane, the dielectric permittivity of InSb becomes anisotropic. It enables the Zeeman-splitting effects on the electronic energy levels of the material proportional to the cyclotron frequency of $\omega_c = eB/m^*$ depending on the external magnetic field (B), electron charge (e) and effective mass of the n-doped InSb ($m^* = 0.0142\,m_0$). The applied magnetic field strength is $B = 0.2$ T, a threshold

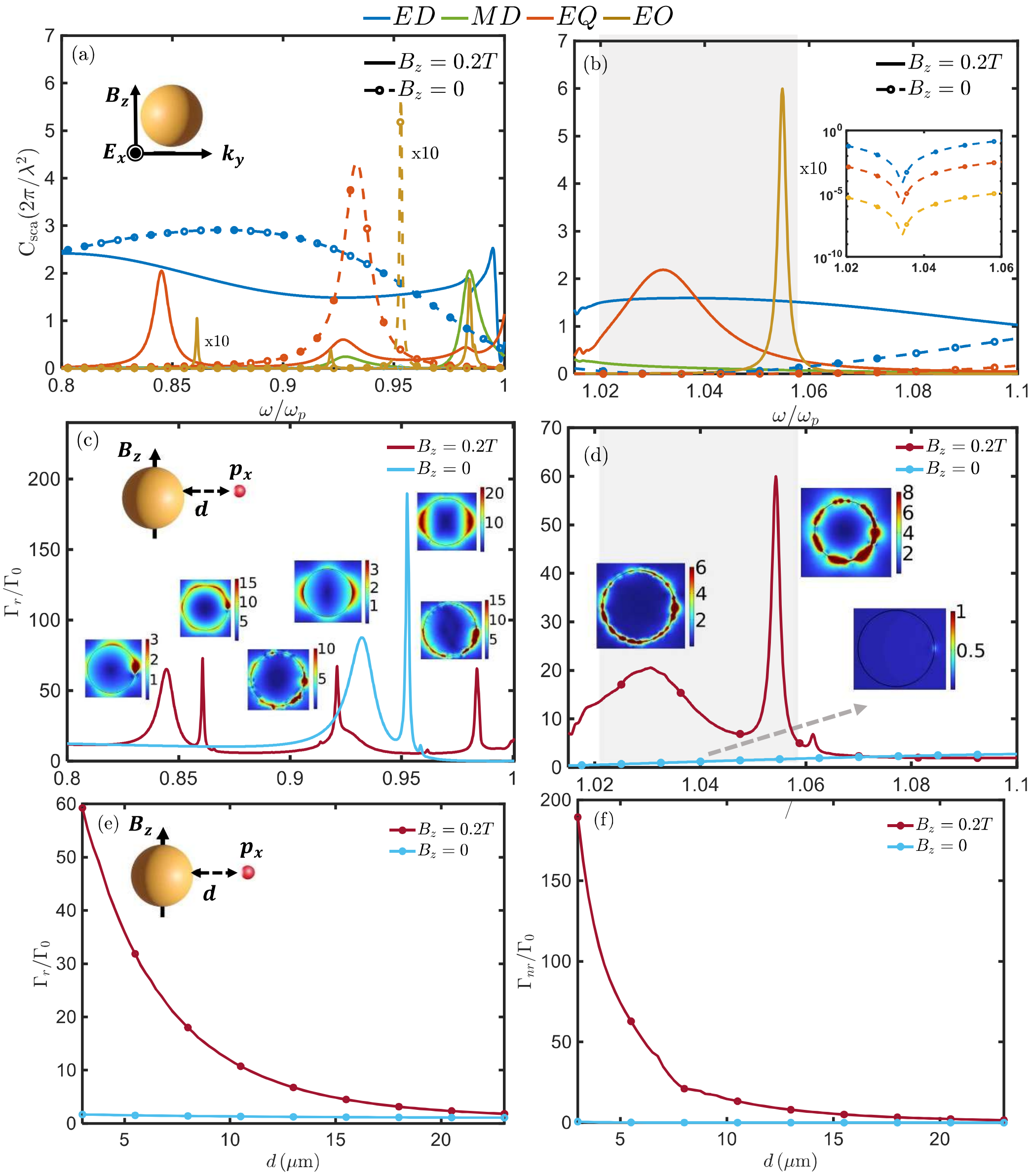

Figure 1. (a) and (b) The comparison of SCS spectra of the spherical InSb antenna in the static magnetic field's presence (solid lines) and absence (dashed lines). The external magnetic field ($B_z = 0.2$ T) is applied along the z-direction to dynamically modify the scattering characteristics of the antenna in the plasmonic (a) and ENZ (b) regions. (c) and (d) The spectral features of the radiative decay rate of the x-oriented ED source, which is placed at a distance of $d = 3\ \mu$m from the antenna. (c) For frequencies lower than ω_p, the coupled system realizes an enhanced multi-band radiative decay rate upon magnetization, while the unmagnetized case demonstrates a larger enhancement factor in a single band. (d) Due to the presence of Zeeman-splitting resonances, the radiative decay rate significantly improves in the ENZ region, highlighted by the gray area. The insets are the normalized electric field distributions around the coupled emitter-antenna system, displaying how the ED source excites electric resonant modes of the antenna through the radiative coupling channels. Variations of the radiative (e) and non-radiative (f) decay rates as a function of coupling distance (d) at the fixed frequency of $\omega/\omega_p = 1.05$.

value ensuring the Zeeman-splitting effect in the InSb semiconductor. Márquez and Sirvent [55]. (See supporting information for more detail.)

To gain insight into the light interaction with InSb semiconductor, we evaluate the scattering characteristics of the proposed antenna using multipolar decomposition [56]. We consider a linearly x-polarized plane wave with the wave vector **k** propagating along the y-direction (the illumination direction). By applying a static magnetic field along the z-direction, we induce anisotropy in the dielectric permittivity of InSb, thereby dynamically modifying the scattered light characteristics (see figure S1).

As shown in figure 1(a), the magnetically induced anisotropy lifts the mode degeneracy, leading to separated plasmonic resonances in the magnetized InSb antenna at frequencies lower than and around ω_p. The Zeeman-splitting effect results in new resonant modes whose spectral positions can be predicted [55].

The splits in atomic energy levels are linearly proportional to the Bohr magneton in the presence of weak magnetic fields. In the presence of the magnetic field $B_z = 0.2$ T, a narrow linewidth electric octupole (EO) resonance at $\omega/\omega_p = 0.951$ splits into multi-band EO resonances, where a peak at $\omega/\omega_p = 1.055$ considerably amplifies the antenna's scattering response. The magnitudes of the EO resonances have been multiplied by ten to emphasize their critical role in the radiated power, as shown in figures 1(a) and (b). A parent electric quadrupole (EQ) mode at $\omega/\omega_p = 0.94$ is split into two distinct EQ resonances at $\omega_{-,\mathrm{EQ}}/\omega_p = 0.84$ and $\omega_{+,\mathrm{EQ}}/\omega_p = 1.035$. Moreover, a broad ED mode is also split into resonances at $\omega_{-,\mathrm{ED}}/\omega_p = 0.8$ and $\omega_{+,\mathrm{ED}}/\omega_p = 0.99$. Contrary to the unmagnetized scenario, when an applied magnetic field couples with localized surface plasmon resonances, it can excite magneto-plasmonic modes. This results in the contribution of MD resonances to the antenna's spectral response, as depicted in figures 1(a) and (b).

The unmagnetized InSb antenna also experiences a plasmonic to ENZ transition response at frequencies slightly higher than ω_p. This electromagnetic behavior provides invisibility, highlighted by a gray box in figure 1(b). The inset depicts the minimum contributions of the multipoles, leading to an almost negligible scattering response, rendering the antenna nearly invisible. In the presence of the magnetic field $B_z = 0.2$ T, the electromagnetic response of the antenna supports a strong splitting of the EQ mode at $\omega/\omega_p = 1.035$ and a high-Q EO mode at $\omega/\omega_p = 1.055$, leading to a transition from invisibility to visibility associated with a 60-fold enhancement of the total scattering cross section (SCS). Besides splitting the EQ and EO modes, broadband ED and MD resonances also contribute to the SCS of the magnetized InSb antenna.

The contribution of the LDOS to the total decay rate of a quantum emitter implies that local electric field enhancement provided by the plasmonic characteristics of the InSb antenna significantly improves the radiative decay rate of an emitter coupled to the antenna. Such a unique feature motivates us to study the dynamic engineering of a dipole emitter's radiative decay rate in microscale proximity to the spherical InSb antenna beyond a quasi-static approximation. In this direction, the InSb antenna is fed by an x-oriented ED source with the coupling distance of $d = 3\ \mu$m. The coupled system balances the divergent effects at this distance, avoiding the reduction of the emitter to a plane wave at larger distances and mitigating the dominant non-radiative Forster rate energy transfer (FRET) at closer ranges [23]. The nature and orientation of the emitter also play important roles in coupled system design, enabling the selective excitation of the resonant modes of the antenna [57].

Figures 1(c) and (d) depict the dependence of the radiative decay rate on frequency for the InSb antenna excited by the x-oriented ED source. Without the magnetic field, as shown in figure 1(c), the radiative decay rate witnesses a significant enhancement in the frequency range from $\omega/\omega_p = 0.9$ to 0.95, corresponding to the spectral interval of the parent EQ and EO resonances. The radiative decay rate experiences approximately 200-fold enhancement due to the EO resonance with a high Q-factor, while a broader EQ resonance leads to a lower enhancement. On the other hand, the magnetized coupled system realizes multi-band radiative decay rate enhancement owing to the contribution of Zeeman-splitting EO, EQ, and ED modes to the radiative coupling channels. The mechanisms of the radiative decay rate enhancement around frequencies of $\omega/\omega_p = 0.85$ and 0.925 are similar to the unmagnetized case. Lower Zeeman-splitting EO and EQ modes resonantly interact with the transition moment of the ED source, realizing up to 50-fold radiative decay rate enhancement at $\omega/\omega_p = 0.85$. As shown in figure 1(c), another enhancement arises from the EO and EQ modes at $\omega/\omega_p = 0.925$, where the latter broadens the spectral response of the radiative decay rate. Another maximum radiative decay rate is also observed at $\omega/\omega_p = 0.98$, resulting from the higher Zeeman-splitting EO resonance.

An interesting behavior of the magnetized InSb antenna is observed in figure 1(d), where the radiative decay rate enhances up to 60 times due to the resonant interaction of the ED source's transition moment with both the broad EQ and higher Zeeman-splitting EO modes. However, without the magnetic field, the InSb antenna is invisible; thus, the radiative decay rate equals one across the spectral range highlighted by the gray area. As mentioned earlier, the antenna can dissipate the emitted energy of the ED source either radiatively or non-radiatively. In the coupled emitter-antenna system, the radiative decay rate channel corresponds to the antenna's scattered electromagnetic field at the emitter position. In contrast, the non-radiative decay rate channel is proportional to the absorption losses of the antenna.

As mentioned earlier, the coupling distance (d) is another crucial parameter modifying the total decay rate. Figures 1(e) and (f) indicates the distance dependence of the radiative and non-radiative decay rates at the fixed frequency of $\omega/\omega_p = 1.05$ associated with the transparent window of the InSb antenna. Under zero magnetization, the radiative decay rate is unity, irrespective of the coupling distance, since the antenna is invisible and the surrounding electromagnetic environment evokes free space for the dipole source. By applying the static magnetic field $B_z = 0.2$ T, Zeeman-splitting modes realize a 60-fold enhancement for the radiative decay rate when the ED source and the antenna are in close proximity. By increasing the coupling distance, the resonant interaction of splitting modes with the ED source's transition moment weakens, and thus the enhancement factor decreases. For longer distances, the enhancement factor is unity as the dipole

IOP Publishing J. Phys. Photonics 6 (2024) 035011 S Aghili et al

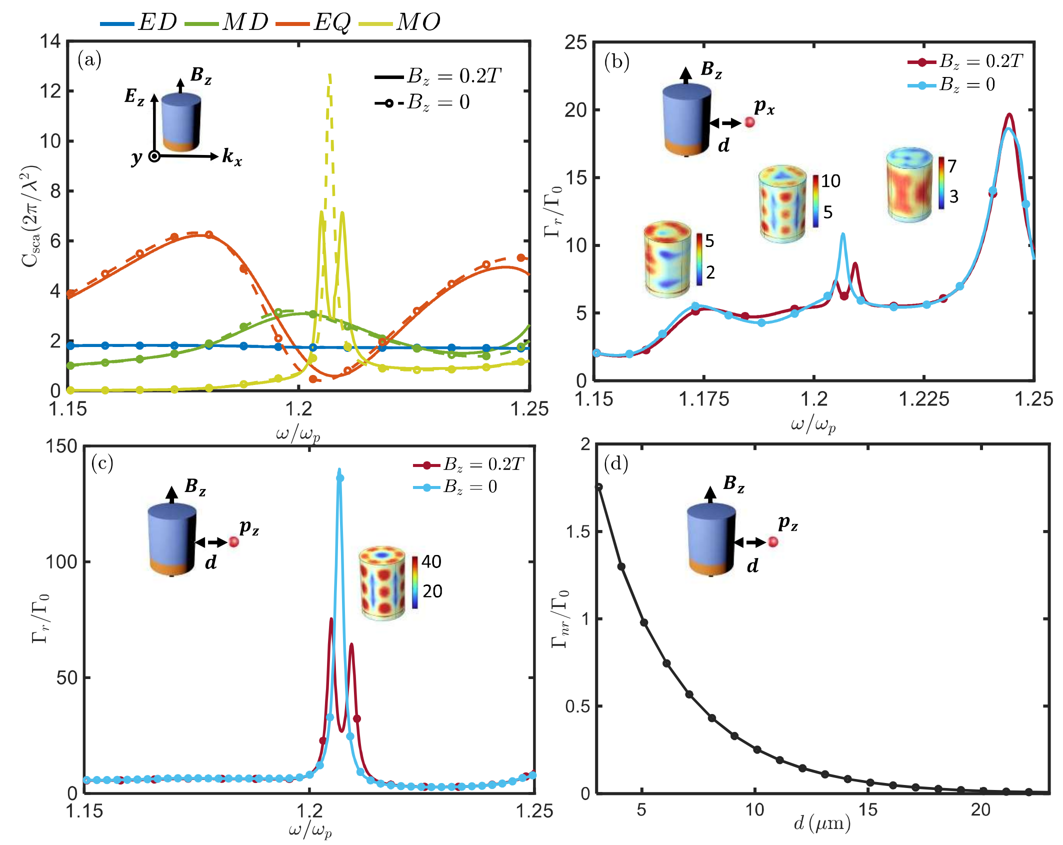

Figure 2. (a) The scattering spectra of the hybrid antenna under plane-wave illumination in the static magnetic field's presence (solid lines) and absence (dashed lines). By applying the static magnetic field ($B_z = 0.2$ T) along the z-direction, multipole moments experience a slight redshift due to the Zeeman effect, while the high-Q parent MO mode splits into two resonant modes in the spectral interval from $\omega/\omega_p = 1.2$ to 1.22. (b) The enhancement of the radiative decay rate for the coupled system is driven by an x-oriented ED emitter as a function of frequency. In this orientation, every multipole moment contributes radiatively to the coupling channels. The insets, showing the normalized electric-field distributions for each resonance peak, highlight the relatively weak coupling between the multipole moments and the ED source. (c) The radiative decay rate of the z-oriented ED source located near the hybrid antenna with the coupling distance of $d = 3$ μm. The spectral response of the radiative decay rate demonstrates a strong dual-band enhancement factor upon magnetization, whereas the maximum radiative decay rate enhancement is recorded under zero magnetic bias. The insets display the normalized electric-field distribution of the MO resonance peak excited by the ED emitter. (d) The non-radiative decay rate of the magnetized system versus coupling distance upon the z-oriented ED emitter excitation at the fixed frequency of $\omega/\omega_p = 1.205$ corresponding to the resonance frequency of the MO mode.

source cannot 'feel' the antenna (see figure 1(e)). As shown in figure 1(f), the unmagnetized coupled emitter-antenna experiences a zero non-radiative decay rate due to the invisibility of the antenna. Under a biased magnetic field of $B_z = 0.2$ T, a strong near-field interaction between the ED source's transition moment and the broad ED mode of the antenna dramatically enhances the non-radiative decay rate for shorter coupling distances due to FRET phenomena. This non-radiative dipole-dipole interaction becomes ineffective for longer coupling distances, so the non-radiative decay rate falls to zero far from the antenna (see figure 1(f)). The magnetized InSb antenna is an active photonic device that allows us to realize dynamic tunable multi-band SE rate enhancement. However, the total emitted power of the ED source is mainly absorbed by the antenna in the near-field region due to significant Joule heating losses of the InSb material, as shown in figure 1(f). Dominant non-radiative channels in the coupled system design give rise to a low quantum efficiency for the antenna, impairing the high free-space radiation rate required for SPSs. We propose an all-dielectric antenna featuring a high quantum efficiency in the following.

3.2. Hybrid Si-InSb antenna

Let us consider a hybrid cylindrical antenna composed of silicon (Si) and InSb layers with the same radii of $r = 35$ μm in the THz regime (depicted in figure 2). The Si layer, as a high-index and low-loss material, comprises the antenna's upper part with a height of $h_1 = 80\ \mu$m to harness the Joule heating losses of the design. The dielectric permittivity of Si is set to $\varepsilon_{Si} = 10.6$ since the material shows a constant permittivity with negligible inherent losses in the studied frequency range. The lower part is made of InSb with a height of $h_2 = 8\ \mu$m to supply the magneto-optical properties required for this active antenna. The design principle resides in two aspects. First, the aspect ratio, $(h_1 + h_2)/r$, of the cylindrical antenna is optimized to support scattering resonances with high Q factors [58]. Second, a given spectral range far from the main absorption band of InSb is chosen such that the material shows moderate positive dielectric permittivity and low losses, as shown in figure S1. When both constituent elements of the antenna exhibit dielectric behaviors, an induced displacement current exceeds the conductive one in the desired frequency range, and thus the all-dielectric antenna can excite robust concurrent electric and magnetic resonances (See figure S3).

In figure 2, we investigate the radiative decay rate variations of an emitter with ED transition near the hybrid antenna with the coupling distance of $d = 3\ \mu$m. We show the SCS of the cylindrical antenna under plane-wave illumination in figure 2(a). In the presence of a magnetic field $B_z = 0.2$ T, a dominant narrow linewidth magnetic octupole (MO) mode is split into distinct resonances due to the Zeeman effect, while the other broadband multipole resonances experience slight blue-shifts. Two MO resonances at frequencies of $\omega_{-,MO}/\omega_p = 1.202$ and $\omega_{+,MO}/\omega_p = 1.206$ result from a parent MO resonance at $\omega/\omega_p = 1.204$. Positioning the x-oriented ED source perpendicular to the hybrid antenna's nearest surface, specifically at the side, enhances the radiative decay rate by a factor of 20 around $\omega/\omega_p = 1.24$, due to the strong contribution from the broad EQ mode to the radiative coupling channels. In this configuration, the high-Q MO mode has only weak coupling with the emitter, resulting in a more modest, 10-fold enhancement of the radiative factor around the resonance frequency of the MO mode (see figure 2(b)).

Under a magnetic bias $B_z = 0.2$ T, the coupled system retains multi-band radiative decay rate enhancement, akin to the unmagnetized case. However, the contribution of the MO splitting modes to the radiative coupling channels undergoes further attenuation due to the Zeeman effect.

Considering the significant impact of the emitter's orientation on decay-rate enhancement, we examine a configuration in which a z-oriented ED emitter is aligned parallel to the incident polarization and situated at the side position relative to the antenna, as illustrated in figure 2(c). Under zero magnetization, the MO mode strongly contributes to the radiative coupling channels, and the radiative decay rate experiences up to a 140-fold enhancement. As shown in figure 2(c), the coupled system can enhance the dual-band radiative decay rate when the magnetized antenna supports the MO splitting resonances. The insets display the normalized electric field distributions of the coupled system, allowing us to perceive the contribution of multipole moments in the coupling channels. In figure figure 2(b), the emitter is oriented perpendicularly to the antenna's surface and the incident electric field, predominantly stimulates the electric multipolar resonances. In contrast, figure 2(c) shows that an emitter parallel to the antenna's surface and the incident electric field tends to couple more effectively with the magnetic multipolar resonances.

Figure 2(d) depicts the non-radiative decay rate of the z-oriented ED source as a function of the coupling distance (d), highlighting that the power absorbed by the antenna at the MO mode's resonance frequency, corresponding to the maximum radiative decay rate, is negligible. This verifies the superior performance of the proposed all-dielectric antenna in minimizing dissipative losses compared to plasmonic coupled systems, demonstrated by the significantly reduced non-radiative decay rate relative to the radiative decay rate in the near-field region. As demonstrated in figure 2, a magnetic hotspot is achieved due to the MO resonance with a high Q factor, promising highly efficient control of the radiative decay rate of an MD emitter.

An x-oriented MD emitter, located perpendicular to the closest surface of the antenna, enables the strong radiative coupling channels with the MO resonant modes in the spectral range from $\omega/\omega_p = 1.2$ to 1.21. In the coupled MD emitter-antenna system, the radiative decay rate demonstrates a 600-fold enhancement due to a narrow-linewidth MO resonance under a zero-bias magnetic field that can be engineered in the presence of the applied magnetic field (See figure 3(a)). Hence, selective emission is another promising advantage of the magnetized hybrid antenna in which spectral bands of the enhanced radiative decay highly depend on the applied magnetic field's strength. Increasing the applied magnetic field makes resonance peaks well-separated across a broader spectral range. The Zeeman-splitting effect is linearly proportional to the cyclotron frequency for magnetic fields $B_z < 0.3$ T, and the split lines are symmetrical to the original resonance peak observed at $B_z = 0$. Based on Bohr magneton approximation, we cannot estimate the spectral position of splitting resonances for larger magnetic field values. New resonance peaks are asymmetrically separated compared to the original resonance. As demonstrated in figure 3(b), higher-frequency splitting

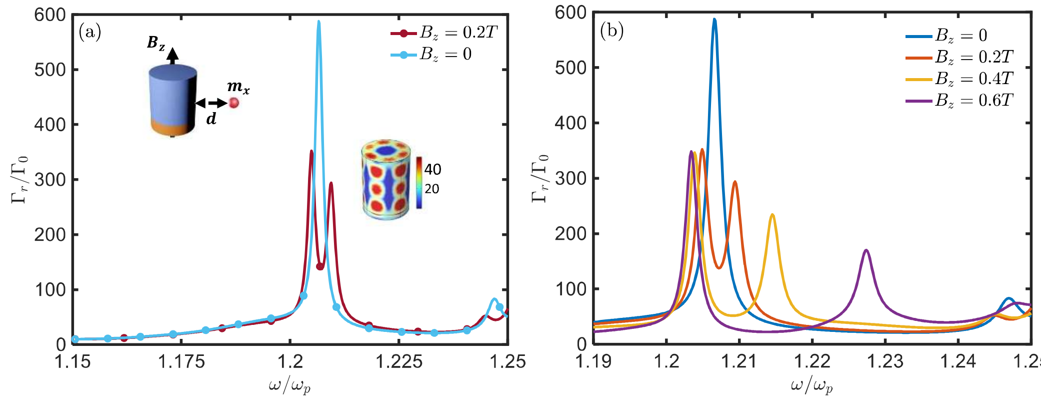

Figure 3. (a) Frequency-dependent radiative decay rate of the x-oriented MD emitter positioned near the hybrid antenna. The high-Q MO resonance generates substantial radiative coupling with the emitter's transition MD moment, leading to a 600-fold enhancement in the photon production rate (b). Dynamically tunable dual-band radiative decay rate enhancement of the x-oriented MD source employing the applied magnetic field increment in the frequency range corresponding to the high-Q MO mode.

resonances experience considerable blue-shifts while lower ones are slightly red-shifted under a biased magnetic field $B_z > 0.3$ T.

3.3. Optimized coupled system design

As highlighted previously, the normalized total decay rate depends on the position, orientation, and type of the dipole source or quantum emitter. Evaluating decay rates based on varied antenna parameters presents complexity and labor intensiveness such that numerical and semi-analytical methods often ignore mutual interactions, leading to suboptimal results. To address this challenge, we employ advanced deep-learning methods recognized for navigating complex and multi-dimensional datasets. We propose a convolutional neural network (CNN) architecture to discern spatial intricacies within the coupled emitter-antenna system. This CNN design adopts several convolutional layers, employing rectified linear unit (ReLU) activation to determine hierarchical data representations. CNN output undergoes flattening and feeds into dense layers for predictive analysis.

As illustrated in figure 4(a), the CNN inputs encompass the spatial coordinates of the quantum emitter, the operational frequency, the value of the applied static magnetic field, and the type of quantum emitter. The initial computational step involves the convolution layer of $C_i = \mathrm{ReLU}(\mathrm{Conv}(X, W_i) + b_i)$, where C_i determines each layer output. Here, X represents the input data, W_i is the weight matrix for the ith filter and b_i is its corresponding bias. The ReLU function introduces non-linearity, allowing the model to adjust its prediction. This operation is repeated for $i = 1$ to N, where N is the total number of filters in the convolution layer.

The output is passed through fully connected layers, and the network undergoes a flattening process, converting the 2D data structure from the convolution layer into a 1D vector. This process of transformation is represented as $\mathrm{FC} = \mathrm{ReLU}(W_{\mathrm{FC}} \times \mathrm{Flatten}(C_N) + b_{\mathrm{FC}})$, where W_{FC} represents the weight matrix and b_{FC} is the bias for the fully connected layers. The network concludes with the output layer, which uses the expression of $\hat{Y} = W_{\mathrm{out}} \times \mathrm{FC} + b_{\mathrm{out}}$, where the output $\hat{Y}$ demonstrates the estimated radiative or non-radiative decay rate.

Utilizing our approach, we can determine both the type and optimal positioning of a quantum emitter near an antenna to optimize radiative decay rates. Figure 4(b) illustrates the radiative decay rate for a dipole source positioned variably around the antenna's external surface. Notably, an x-oriented MD source placed adjacent to the hybrid antenna at $(37\,\mu\mathrm{m}, 0\,\mu\mathrm{m}, 40\,\mu\mathrm{m})$ reaches an enhancement factor of 700 at the frequency range corresponding to the MO mode's resonance frequency under zero magnetization. To verify this prediction, figure 4(c) displays the simulation result of both radiative and non-radiative decay rates for m_x dipole source at its prime location, mirroring CNN's predictive output. The inset presents the far-field radiation pattern of the maximum value corresponding to the dominant MO mode in a non-magnetized state.

IOP Publishing J. Phys. Photonics 6 (2024) 035011 S Aghili et al

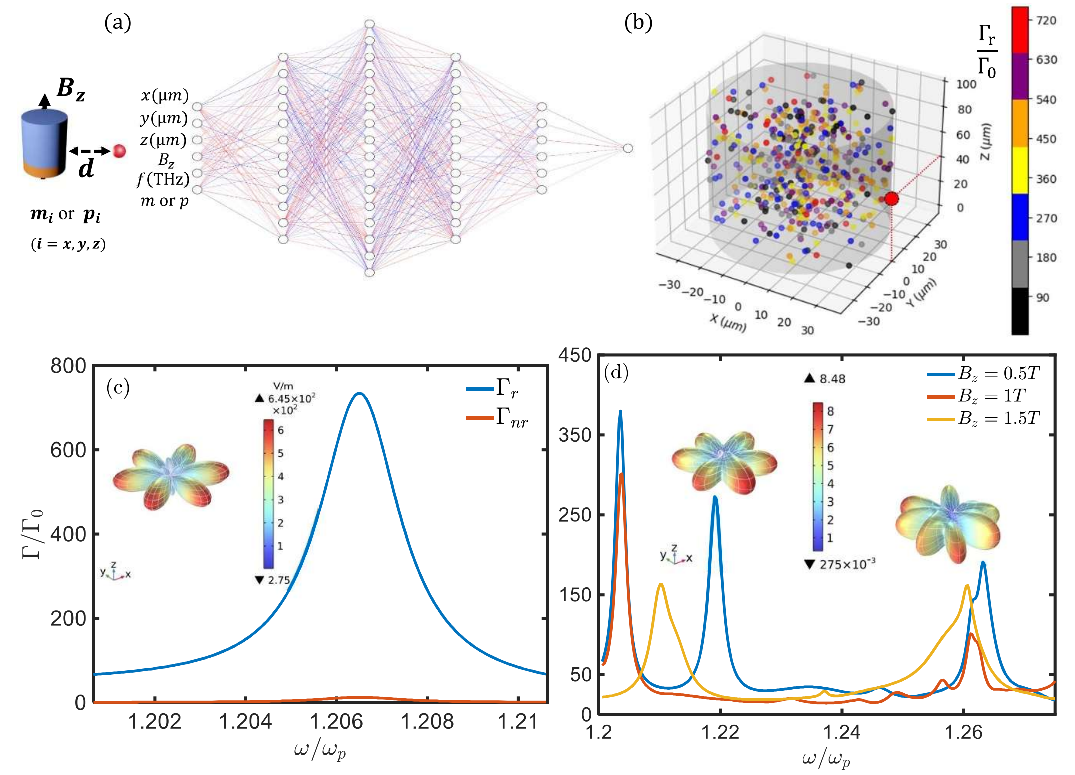

Figure 4. (a) The CNN architecture is tailored to identify the ideal position of a variably oriented dipole source that yields the maximum radiative decay rate near the hybrid antenna. This approach holds the constant coupling distance ($d = 3$ μm). (b) The radiative decay rate of the m_x dipole source at varied positions around the hybrid antenna's outer surface. The CNN prediction indicates a seven-fold enhancement factor when m_x is situated at (37 μm, 0 μm, 40 μm) within the frequency range corresponding to the MO mode in a non-magnetized state (c). The radiative and non-radiative decay rates of the m_x dipole source at its optimal position align with the MO mode's resonant frequency in a non-magnetized environment under numerical simulation. The maximum value of the radiative decay rate validates the CNN prediction. The inset highlights the far-field radiation pattern, emphasizing the dominant radiation efficiency of the MO mode in free space. (d) The radiative decay rate variations for three different values of the applied magnetic field. The Zeeman-splitting effect becomes broader with the increment in the applied magnetic field, while the enhancement factor decreases compared to the absence of the magnetic field. The insets display the spatial variations of the far-field electric-field patterns corresponding to radiative decay rate maxima at the resonant frequencies of $\omega/\omega_p = 1.207 (B_z = 1.5\,\mathrm{T})$ and $\omega/\omega_p = 1.264\ (B_z = 1\,\mathrm{T})$.

4. Conclusions

In this study, we numerically investigated the impact of an active antenna on the total decay rate of an emitter. The active antenna allows one to dynamically manipulate the scattering response by external agents. InSb material, a III-V semiconductor with strong magneto-optical properties in the THz region, has been employed to realize the active antenna that can modify light–matter interaction via an applied static magnetic field. We used the multipole decomposition method to obtain the SCS of the antenna under plane-wave illumination. The scattering response of the antenna allows us to determine which type of emitters efficiently interact with the antenna.

In the first section, we proposed a spherical InSb antenna to modify the radiative decay rate of an ED source upon magnetization. We have shown that the radiative decay rate experiences a multi-band enhancement when the magnetized antenna has plasmonic features. In contrast, the maximum enhancement factor of about 200 times is observed for the unmagnetized case. Moreover, a transition from invisibility to visibility has been shown in the ENZ region such that the transparent antenna turns into a strong scatterer under a biased magnetic field. Thus, the radiative decay rate dramatically increases by up to 60 times. However, the proposed active antenna suffers from high Joule heating losses, impairing its quantum efficiency associated with a low photon production rate.

To mitigate this limitation, we proposed a cylindrical hybrid antenna composed of Si and InSb layers to act as an all-dielectric active antenna. Due to its robust magnetic resonance, we have found that the hybrid antenna is very promising for dynamic control of the radiative decay rate of an MD emitter. Results show that the magnetized hybrid antenna achieves an enhanced tunable dual-band radiative decay rate for the MD source, so each band represents enhancement factors of several hundred. Moreover, we have found that the hybrid antenna harnesses non-radiative processes, leading to high quantum efficiency.

Finally, we employed a modified deep-learning CNN to determine the emitter's position within the coupled system precisely. This position maximizes the radiative decay rate when an x-oriented MD source, located at the coordinates $(37\,\mu\text{m}, 0\,\mu\text{m}, 40\,\mu\text{m})$, couples with the hybrid antenna. Remarkably, this configuration boosts the radiative decay rate up to 720 times under zero magnetization. This finding was further validated through numerical simulations using Comsol, confirming the prediction of our modified deep-learning network. Offering dynamic splitting bandwidth via the proposed coupled system holds significant potential for designing tunable THz SPSs suitable for practical quantum applications.

Data availability statement

All data that support the findings of this study are included within the article (and any supplementary files).

ORCID iDs

Sina Aghili https://orcid.org/0009-0006-9641-4241
Carsten Rockstuhl https://orcid.org/0000-0002-5868-0526

References

[1] Drexhage K H 1970 Influence of a dielectric interface on fluorescence decay time *J. Lumin.* **1** 693–701
[2] Purcell E M, Cutler Torrey H and Pound R V 1946 Resonance absorption by nuclear magnetic moments in a solid *Phys. Rev.* **69** 37
[3] Glauber R J and Lewenstein M 1991 Quantum optics of dielectric media *Phys. Rev.* A **43** 467
[4] Paesani S, Borghi M, Signorini S, Maïnos A, Pavesi L and Laing A 2020 Near-ideal spontaneous photon sources in silicon quantum photonics *Nat. Commun.* **11** 1–6
[5] Choi S, Tran T T, Elbadawi C, Lobo C, Wang X, Juodkazis S, Seniutinas G, Toth M and Aharonovich I 2016 Engineering and localization of quantum emitters in large hexagonal boron nitride layers *ACS Appl. Mater. Interfaces* **8** 29642–8
[6] Wang R, Ikezawa M, Sakuma Y, Takeda H, Ikeda N, Sugimoto Y, Sakoda K, Yamada Y and Masumoto Y 2020 Enhanced spontaneous emission rates for single isoelectronic luminescence centers in photonic crystal cavities *ACS Photonics* **7** 321–6
[7] Arbel D, Berkovitch N, Nevet A, Peer A, Cohen S, Ritter D and Orenstein M 2011 Light emission rate enhancement from inp MQW by plasmon nano-antenna arrays *Opt. Express* **19** 9807–13
[8] Romeira B and Fiore A 2018 Purcell effect in the stimulated and spontaneous emission rates of nanoscale semiconductor lasers *IEEE J. Quantum Electron.* **54** 1–12
[9] Wang F, Jin S, Sun W, Lin J, You B, Li Y, Zhang B, Hayat T, Alsaedi A and Tan Z' 2018 Enhancing the performance of blue quantum dots light-emitting diodes through interface engineering with deoxyribonucleic acid *Adv. Opt. Mater.* **6** 1800578
[10] Peng Y, Li Z, Tongwei W, Wang Y-T, Tong X, Chuan-Feng Li, Wang Z, Wei S-H, Zhang Y and Liu H 2019 Nanowire quantum dot surface engineering for high temperature single photon emission *ACS Nano* **13** 13492–500
[11] Russell K J, Liu T-L, Cui S and Evelyn L H 2012 Large spontaneous emission enhancement in plasmonic nanocavities *Nat. Photon.* **6** 459–62
[12] Tam F, Goodrich G P, Johnson B R and Halas N J 2007 Plasmonic enhancement of molecular fluorescence *Nano Lett.* **7** 496–501
[13] Cambiasso J, Grinblat G, Li Y, Rakovich A, Cortés E and Maier S A 2017 Bridging the gap between dielectric nanophotonics and the visible regime with effectively lossless gallium phosphide antennas *Nano Lett.* **17** 1219–25
[14] Aharonovich I, Englund D and Toth M 2016 Solid-state single-photon emitters *Nat. Photon.* **10** 631–41
[15] Buckley S and Rivoire K J 2012 Engineered quantum dot single-photon sources *Rep. Prog. Phys.* **75** 126503
[16] Alexander Lohrmann A, Johnson B C, McCallum and J C and Castelletto 2017 A review on single photon sources in silicon carbide *Rep. Prog. Phys.* **80** 034502
[17] Purcell E M 1995 Spontaneous emission probabilities at radio frequencies *Confined Electrons and Photons* (Springer) pp 839–839
[18] Haroche S, Raimond J-M and Dowling J P 2014 Exploring the quantum: atoms, cavities and photons *Am. J. Phys.* **82** 86–87
[19] Qian Z, Shan L, Zhang X, Liu Q, Yun M, Gong Q and Ying G 2021 Spontaneous emission in micro-or nanophotonic structures *PhotoniX* **2** 1–35
[20] Inam F A, Ahmed N, Steel M J and Castelletto S 2018 Hyperbolic metamaterial resonator–antenna scheme for large, broadband emission enhancement and single-photon collection *J. Opt. Soc. Am.* B **35** 2153–62
[21] Ahmed N, Akhtar S and Inam F A 2020 Hyperbolic metamaterial-based metal–dielectric resonator-antenna designs for GHZ photon collection rates from wide-range solid-state single-photon sources *J. Opt. Soc. Am.* B **37** 3469–77
[22] Guclu C, Shan Luk T, Wang G T and Capolino F 2014 Radiative emission enhancement using nano-antennas made of hyperbolic metamaterial resonators *Appl. Phys. Lett.* **105** 123101
[23] Bonod N 2020 Controlling spontaneous emission with dielectric optical antennas *Dielectric Metamaterials* (Elsevier) pp 109–44
[24] Agio M 2012 Optical antennas as nanoscale resonators *Nanoscale* **4** 692–706
[25] Taminiau T H, Stefani F D, Segerink F B and Van Hulst N F 2008 Optical antennas direct single-molecule emission *Nat. Photon.* **2** 234–7
[26] Cui L, Zhu Y, Abbasi M, Ahmadivand A, Gerislioglu B, Nordlander P and Natelson D 2020 Electrically driven hot-carrier generation and above-threshold light emission in plasmonic tunnel junctions *Nano Lett.* **20** 6067–75
[27] Anger P, Bharadwaj P and Novotny L 2006 Enhancement and quenching of single-molecule fluorescence *Phys. Rev. Lett.* **96** 113002
[28] Hua Mi, Wang L, Zhang Y, Zhao G and Jiang R 2019 Control of the emission from electric and magnetic dipoles by gold nanocup antennas *Opt. Express* **27** 14221–30
[29] Jiang Q, Roy P, Claude J-Bit and Wenger Jome 2021 Single photon source from a nanoantenna-trapped single quantum dot *Nano Lett.* **21** 7030–6

[30] Aghili S, Golmohammadi S and Amini A 2018 Proposing an on/off optical router in telecom wavelength using plasmonic tweezer *Opt. Commun.* **427** 95–100
[31] Rogobete L, Kaminski F, Agio M and Sandoghdar V 2007 Design of plasmonic nanoantennae for enhancing spontaneous emission *Opt. Lett.* **32** 1623–5
[32] Hein S M and Giessen H 2013 Tailoring magnetic dipole emission with plasmonic split-ring resonators *Phys. Rev. Lett.* **111** 026803
[33] Dhawan A R *et al* 2020 Extreme multiexciton emission from deterministically assembled single-emitter subwavelength plasmonic patch antennas *Light: Sci. Appl.* **9** 1–9
[34] Dmitriev P A, Baranov D G, Milichko V A, Makarov S V, Mukhin I S, Samusev A K, Krasnok A E, Belov P A and Kivshar Y S 2016 Resonant Raman scattering from silicon nanoparticles enhanced by magnetic response *Nanoscale* **8** 9721–6
[35] Iwanaga M 2018 All-dielectric metasurfaces with high-fluorescence-enhancing capability *Appl. Sci.* **8** 1328
[36] Cheng L, Alaee R, Safari A, Karimi M, Zhang L and Boyd R W 2021 Superscattering, superabsorption and nonreciprocity in nonlinear antennas *ACS Photonics* **8** 585–91
[37] Mobini E, Alaee R, Boyd R W and Dolgaleva K 2021 Giant asymmetric second-harmonic generation in bianisotropic metasurfaces based on bound states in the continuum *ACS Photonics* **8** 3234–40
[38] Liu S, Vaskin A, Campione S, Wolf O, Sinclair M B, Reno J, Keeler G A, Staude I and Brener I 2017 Huygens metasurfaces enabled by magnetic dipole resonance tuning in split dielectric nanoresonators *Nano Lett.* **17** 4297–303
[39] Yang Y, Zhu B and Dai H 2020 Strong magnetic field enhancement and magnetic purcell effect in a dielectric disk-ring composite nanocavity *J. Opt. Soc. Am.* B **37** 702–8
[40] Rolly B, Bebey B, Bidault S, Stout B and Bonod N 2012 Promoting magnetic dipolar transition in trivalent lanthanide ions with lossless mie resonances *Phys. Rev.* B **85** 245432
[41] Elli Stamatopoulou P and Tserkezis C 2021 Role of emitter position and orientation on silicon nanoparticle-enhanced fluorescence *OSA Continuum* **4** 918–32
[42] Chew H 1987 Transition rates of atoms near spherical surfaces *J. Chem. Phys.* **87** 1355–60
[43] Aslan E 2021 Engineering of dual-band magnetic dipole decay rate enhancement with concentric hollow nanodisk resonators *Opt. Mater.* **113** 110871
[44] Filonov D S, Krasnok A E, Slobozhanyuk A P, Kapitanova P V, Nenasheva E A, Kivshar Y S and Belov P A 2012 Experimental verification of the concept of all-dielectric nanoantennas *Appl. Phys. Lett.* **100** 201113
[45] Krasnok A, Glybovski S, Petrov M, Makarov S, Savelev R, Belov P, Simovski C and Kivshar Y 2016 Demonstration of the enhanced purcell factor in all-dielectric structures *Appl. Phys. Lett.* **108** 211105
[46] Rocco D, Lamprianidis A, Miroshnichenko A E and De Angelis C 2020 Giant electric and magnetic purcell factor in dielectric oligomers *J. Opt. Soc. Am.* B **37** 2738–44
[47] Zouros G P, Kolezas G D, Almpanis E and Tsakmakidis K L 2021 Three-dimensional giant invisibility to superscattering enhancement induced by zeeman-split modes *ACS Photonics* **8** 1407–12
[48] Chochol J, Postava K, Čada M, Vanwolleghem M, Halagačka L, Lampin J-F and Pištora J 2016 Magneto-optical properties of insb for terahertz applications *AIP Adv.* **6** 115021
[49] Liu W, Chang A Y, Schaller R D and Talapin D V 2012 Colloidal insb nanocrystals *J. Am. Chem. Soc.* **134** 20258–61
[50] Pandya S G and Kordesch M E 2015 Characterization of insb nanoparticles synthesized using inert gas condensation *Nanoscale Res. Lett.* **10** 1–7
[51] Novotny L and Hecht B 2012 *Principles of Nano-Optics* (Cambridge University Press)
[52] Alhalaby H, Zaraket H and Principe M 2021 Enhanced photoluminescence with dielectric nanostructures: a review *Results Opt.* **3** 100073
[53] Comsol Software (available at: www.comsol.com) (Accessed 19 May 2024)
[54] Chen Y, Nielsen T R, Gregersen N, Lodahl P and Mørk J 2010 Finite-element modeling of spontaneous emission of a quantum emitter at nanoscale proximity to plasmonic waveguides *Phys. Rev.* B **81** 125431
[55] Márquez A and Sirvent R E 2020 Terahertz response of plasmonic nanoparticles: plasmonic Zeeman effect *Opt. Express* **28** 39005–16
[56] Alaee R, Rockstuhl C and Corbaton I F 2018 An electromagnetic multipole expansion beyond the long-wavelength approximation *Opt. Commun.* **407** 17–21
[57] Schmidt M K, Esteban R, Sáenz J J, Suárez-Lacalle I, Mackowski S and Aizpurua J 2012 Dielectric antennas-a suitable platform for controlling magnetic dipolar emission *Opt. Express* **20** 13636–50
[58] Rybin M V, Koshelev K L, Sadrieva Z F, Samusev K B, Bogdanov A A, Limonov M F and Kivshar Y S 2017 High-q supercavity modes in subwavelength dielectric resonators *Phys. Rev. Lett.* **119** 243901

Supplemental Material

1 Dielectric Permittivity of InSb

We use the Drude model to express the permittivity tensor of InSb at THz frequencies, denoted by

$$\varepsilon\left(\omega\right)=\left[\begin{array}{ccc}\varepsilon_{xx} & \varepsilon_{xy} & 0\\ \varepsilon_{yx} & \varepsilon_{yy} & 0\\ 0 & 0 & \varepsilon_{zz}\end{array}\right], \tag{1}$$

where the tensor elements of Eq. (1) are defined as

$$\varepsilon_{zz}\left(\omega\right)=\varepsilon_{\infty}-\frac{\omega_p^2}{\omega^2+i\gamma_p\omega}, \tag{2}$$

$$\varepsilon_{xx}\left(\omega\right)=\varepsilon_{yy}\left(\omega\right)=\varepsilon_{\infty}-\frac{\omega_p^2\left(\omega^2+i\gamma_p\omega\right)}{\left(\omega^2+i\gamma_p\omega\right)^2-\omega_c^2\omega^2}, \tag{3}$$

$$\varepsilon_{xy}\left(\omega\right)=-\varepsilon_{yx}\left(\omega\right)=-i\frac{\omega_p^2\omega_c\omega}{\left(\omega^2+i\gamma_p\omega\right)^2-\omega_c^2\omega^2}. \tag{4}$$

We consider the parameters of an n-doped InSb semiconductor [1, 2], where $\varepsilon_{\infty}=15.6$ is the background permittivity, $\omega_p=12.56\times10^{12}$ rad/s is the plasma frequency, $\gamma_p=0.01\omega_p$ as the damping constant represents the Ohmic losses of InSb, and $\omega_c=eB_z/m^*$ is the cyclotron frequency depending on the external magnetic field (B_z), electron charge (e) and effective mass ($m^*=0.0142\,m_0$). The low effective mass of InSb results in a strong anisotropy under a weak external magnetic field [3, 2, 4]. Figure S1 compares the spectral dependency of InSb's complex permittivities in the presence and absence of the applied magnetic field.

Without the magnetic field ($B_z=0$), off-diagonal elements of the InSb permittivity disappear due to the cyclotron frequency dependence. On the other hand, diagonal elements are identical, showing negative real parts at lower frequencies than ω_p, and positive values for the imaginary parts across the whole spectral range (Fig. S1a and c). Under zero magnetization, the optical response of InSb only depends on the real part of $\varepsilon_{zz}(\omega)$ so that its negative values result in a plasmonic behavior [5], and the positive ones turn the material into a relatively high-index dielectric [2]. The positive values of its imaginary part demonstrate the Ohmic losses of InSb, specifically in the plasmonic region. In the presence of the magnetic field ($B_z=0.2$ T), the real parts of the components remain almost unchanged, and only $\varepsilon_{xx}(\omega)$ increases at lower frequencies compared to the previous case (Fig. S1b). On the other hand, the imaginary parts of the magnetized components experience major variations, in which off-diagonal components demonstrate

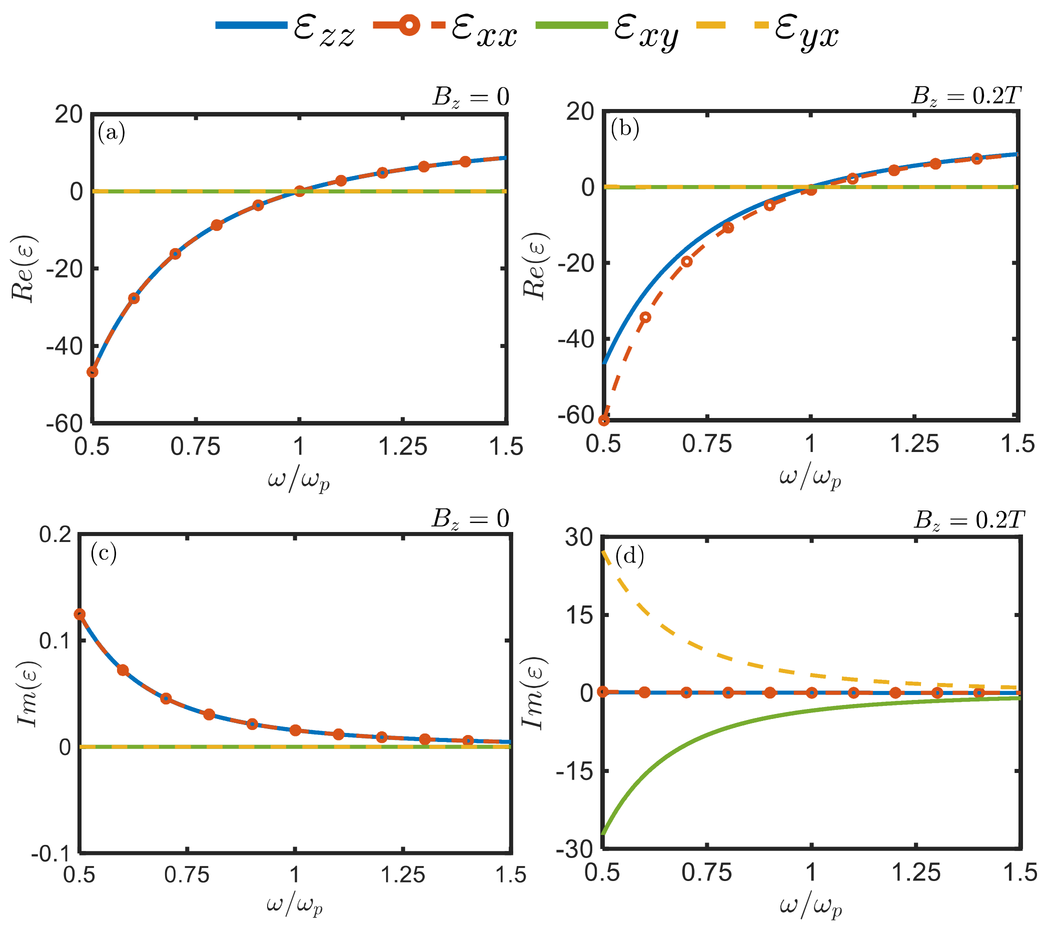

Figure S1: (a, c) Real and imaginary parts of InSb's dielectric permittivity as functions of frequency under zero magnetization ($B_z = 0$). The diagonal elements are identical, while the off-diagonal ones vanish due to cyclotron frequency dependence. (a) The real part of the diagonal elements is negative at frequencies $\omega/\omega_p < 1$, representing the plasmonic region of InSb. For frequencies $\omega/\omega_p > 1$, InSb is a dielectric material due to the positive real part of its permittivity. (c) The positive imaginary part of the diagonal elements is larger in the plasmonic region, denoting the Joule heating losses of InSb as the plasmonic material. (b, d) The real and imaginary parts of InSb's permittivity as functions of frequency upon magnetization ($B_z = 0.2$ T). (b) The real parts of the diagonal elements increas compared to the unmagnetized case, and $\varepsilon_{xx}(\omega)$ dissociates from $\varepsilon_{zz}(\omega)$ at lower frequencies. On the other hand, the off-diagonal elements remain almost unchanged, similar to the previous case. (d) In the presence of the applied magnetic field, the imaginary part of the diagonal elements is negligible, while the off-diagonal ones demonstrate considerable variations. $\varepsilon_{xy}(\omega)$ shows negative values across the studied spectral range so that it improves the plasmonic behavior of InSb at frequencies $\omega/\omega_p < 1$. On the other hand, $\varepsilon_{yx}(\omega)$ is positive throughout the broad spectral range, increasing absorption losses of the material.

the same values with different signs. As shown in Fig. S1(d), $\varepsilon_{xy}(\omega)$ indicates the negative values that can robustify the plasmonic behavior of InSb in agreement with the negative real parts of the diagonal components, whereas $\varepsilon_{yx}(\omega)$ increases the Ohmic losses of the material in the plasmonic region due to its considerable positive values.

2 Scattering Cross Section of the Single Resonant Antenna

We first evaluated the scattering characteristics of the proposed antenna using multipolar decomposition [6]. The incident light can induce an electric conductive or displacement current on the antenna such that the scattered field originates from the induced oscillating current carrying multipole moments mentioned in Eq. (S11). The respective induced current is described as $J(r,\omega) = i\omega\varepsilon_0(\varepsilon(\omega) - 1)E(r,\omega)$, where $\varepsilon(\omega)$ is the dielectric permittivity of the antenna and $E(r,\omega)$ describes the electric field distribution around and inside the antenna that can be numerically calculated by the RF module of COMSOL version 6 software. By having the electric-induced current, we can obtain the proposed antenna's total scattering cross-section (SCS) based on the contribution of multipole moments as follows:

$$p_\alpha = -\frac{1}{i\omega}\left[\int J_\alpha \, dv + \frac{k^2}{10}\int (\mathbf{J}.\mathbf{r})\, r_\alpha - 2r^2 J_\alpha \, dv + \frac{k^4}{280}\int 3r^4 J_\alpha - 2r^2 \left(\mathbf{r}.\mathbf{J}\right) r_\alpha \, dv\right], \tag{5}$$

$$m_\alpha = \frac{1}{2}\left[\int \left(\mathbf{r}\times\mathbf{J}\right)_\alpha \, dv - \frac{k^2}{10}\int r^2 \left(\mathbf{r}\times\mathbf{J}\right)_\alpha \, dv\right], \tag{6}$$

$$\begin{aligned} Q^e_{\alpha\beta} = -\frac{1}{i\omega}\Bigg[&\int (r_\alpha\beta + r_\beta\alpha) - \frac{2}{3}(\mathbf{r}\cdot\mathbf{J})\delta_{\alpha\beta} dV \\ &+ \frac{k^2}{42}\int (4(\mathbf{r}\cdot\mathbf{J}) r_\alpha r_\beta + 2\delta_{\alpha\beta}(\mathbf{J}\cdot\mathbf{r})^2 - 5r^2(r_\alpha\beta + r_\beta\alpha))dV\Bigg], \end{aligned} \tag{7}$$

$$Q^m_{\alpha\beta} = \frac{1}{3}\left[\int r_\alpha \left(\mathbf{r}\times\mathbf{J}\right)_\beta + r_\beta \left(\mathbf{r}\times\mathbf{J}\right)_\alpha \, dv - \frac{k^2}{4}\int r^2 \left(r_\alpha \left(\mathbf{r}\times\mathbf{J}\right)_\beta + r_\beta \left(\mathbf{r}\times\mathbf{J}\right)_\alpha \, dv\right)\right], \tag{8}$$

$$\begin{aligned} O^e_{\alpha\beta\gamma} = -\frac{1}{i\omega}\Big[&\int r_\alpha r_\beta J_\gamma + r_\beta r_\gamma J_\alpha + r_\gamma r_\alpha J_\beta - \frac{1}{5}\delta_{\alpha\beta}\left(r^2 J_\gamma + 2\left(\mathbf{r}.\mathbf{J}\right) r_\gamma\right) \\ &- \frac{1}{5}\delta_{\beta\gamma}\left(r^2 J_\alpha + 2\left(\mathbf{r}.\mathbf{J}\right) r_\alpha\right) - \frac{1}{5}\delta_{\gamma\alpha}\left(r^2 J_\beta + 2\left(\mathbf{r}.\mathbf{J}\right) r_\beta\right) \, dv\Big], \end{aligned} \tag{9}$$

$$\begin{aligned} O^m_{\alpha\beta\gamma} = \frac{1}{24}\Big[&\int \left(r_\alpha r_\beta \left(\mathbf{r}\times\mathbf{J}\right)_\gamma + r_\beta r_\gamma \left(\mathbf{r}\times\mathbf{J}\right)_\alpha + r_\gamma r_\alpha \left(\mathbf{r}\times\mathbf{J}\right)_\beta\right) \\ &- \frac{1}{5}\delta_{\alpha\beta} r^2 \left(\mathbf{r}\times\mathbf{J}\right)_\gamma - \frac{1}{5}\delta_{\beta\gamma} r^2 \left(\mathbf{r}\times\mathbf{J}\right)_\alpha - \frac{1}{5}\delta_{\gamma\alpha} r^2 \left(\mathbf{r}\times\mathbf{J}\right)_\beta \, dv\Big], \end{aligned} \tag{10}$$

and the scattering cross-section from the antenna can be expressed in terms of multipole moments provided by Eqs. (5) to (10) as

$$C_{\mathrm{sca}}^{\mathrm{tot}} = \frac{k^4}{6\pi\varepsilon_0^2\left|E_{\mathrm{inc}}\right|^2}\left|p_\alpha\right|^2 + \frac{k^4}{6\pi c^2\varepsilon_0^2\left|E_{\mathrm{inc}}\right|^2}\left|m_\alpha\right|^2 + \frac{k^6}{160\pi\varepsilon_0^2\left|E_{\mathrm{inc}}\right|^2}\sum_{\alpha\beta}\left|Q_{\alpha\beta}^e\right|^2$$
$$+\frac{k^6}{80\pi c^2\varepsilon_0^2\left|E_{\mathrm{inc}}\right|^2}\sum_{\alpha\beta}\left|Q_{\alpha\beta}^m\right|^2 + \frac{k^8}{1890\pi\varepsilon_0^2\left|E_{\mathrm{inc}}\right|^2}\sum_{\alpha\beta\gamma}\left|O_{\alpha\beta\gamma}^e\right|^2 + \frac{k^8}{1890\pi c^2\varepsilon_0^2\left|E_{\mathrm{inc}}\right|^2}\sum_{\alpha\beta\gamma}\left|O_{\alpha\beta\gamma}^m\right|^2. \tag{11}$$

Here p_α/m_α, $Q_{\alpha\beta}^e/Q_{\alpha\beta}^m$, and $O_{\alpha\beta\gamma}^e/O_{\alpha\beta\gamma}^m$ are electric/magnetic dipole moments, electric/magnetic quadrupole moments, and electric/magnetic octupole moments, respectively, c is the speed of light, E_0 represents the electric field magnitude of the incident light, and $\alpha, \beta, \gamma = x, y, z$.

2.1 Spherical InSb Antenna

We consider a linearly x-polarized plane wave propagating with the wavevector $\mathbf{k}$ along the y illumination direction. By applying a static magnetic field, we dynamically modify the scattered light characteristics of the antenna owing to the anisotropic behavior observed in InSb dielectric permittivity (See Fig. S1).

Fig. S2 shows the SCS of the InSb antenna, allowing us to identify the electromagnetic resonant modes excited in the system. The spectral response of the SCS is divided into three specific regions corresponding to InSb's dielectric permittivity shown in Fig. S1(a). The induced electric conductive current excites a broad ED, a narrow EQ, and an ultra-narrow EO with a very small magnitude corresponding to negative values of InSb's permittivity to realize a plasmonic antenna in the studied frequency range of ${}^{\omega}/_{\omega_p} < 1$. The total SCS of the antenna at frequencies slightly higher than ω_p nearly vanishes to provide a transparent region associated with near-zero values of InSb permittivity. An induced circular displacement current is excited inside the antenna at higher frequencies, so the total SCS also has contributions from magnetic dipole (MD) and magnetic quadrupole (MQ) modes. The concurrent support of multipolar electric and magnetic resonances realizes a dielectric antenna associated with positive real parts of InSb permittivity. The scattering response of the antenna is dramatically enhanced in the transparent region under an applied magnetic field due to the contribution of the splitting EQ and EO resonant modes, as shown in Fig. S2(b).

5

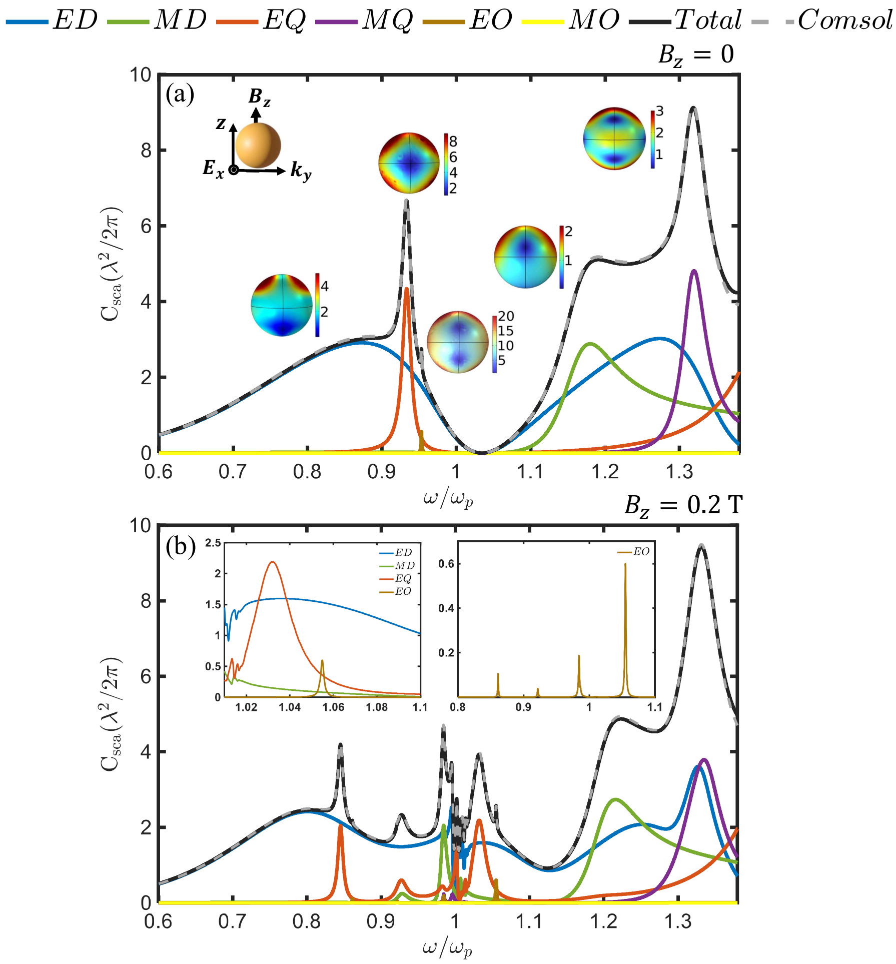

Figure S2: The scattering characteristics of the spherical InSb antenna with the radius $r = 30\ \mu$m under x-polarized plane wave illumination with the wavevector k_y, (a) in the absence and (b) in presence of the applied magnetic field. (a) The total SCS of the antenna indicates five resonance peaks arising from the contribution of the dominant ED, MD, EQ, MQ, and EO modes. The insets demonstrate the antenna's instantaneous normalized electric field distributions corresponding to the total SCS maxima, further clarifying the nature of the electromagnetic resonant modes. (b) The scattering characteristics of the antenna are modified upon magnetization where the Zeeman splitting effect makes the originally invisible structures visibile around $^{\omega}/_{\omega_p} = 1$. The insets specifically focus on the SCS of the magnetized antenna in the ENZ region. Here, the high-Q multiband EO resonant modes significantly influence the antenna's scattering response.

Fig. S2 shows the SCS of the InSb antenna, allowing us to identify the electromagnetic resonant modes excited in the system. The spectral response of the SCS is divided into three specific regions corresponding to InSb's dielectric permittivity shown in Fig. S1(a). The induced electric conductive current excites a broad ED, a narrow EQ, and an ultra-narrow EO with a very small magnitude corresponding to negative values of InSb's permittivity to realize a plasmonic antenna in the studied frequency range of $\omega/\omega_p < 1$. The total SCS of the antenna at frequencies slightly higher than ω_p nearly vanishes to provide a transparent region associated with near-zero values of InSb permittivity. An induced circular displacement current is excited inside the antenna at higher frequencies, so the total SCS also has contributions from magnetic dipole (MD) and magnetic quadrupole (MQ) modes. The concurrent support of multipolar electric and magnetic resonances realizes a dielectric antenna associated with positive real parts of InSb permittivity. The scattering response of the antenna is dramatically enhanced in the transparent region under an applied magnetic field due to the contribution of the splitting EQ and EO resonant modes, as shown in Fig. S2(b).

2.2 Hybrid Antenna

In this section, we scrutinize the scattering response of the hybrid antenna excited by a linearly z-polarized plane wave impinging along the x-axis, as shown in Fig. S3. The antenna is made of a lower InSb layer and an upper Si layer with a radius of 35 μm and a height of 8 μm and 80 μm, respectively. Under zero magnetization, the multipolar decomposition of SCS reveals a resonance with a high Q factor in the spectral interval around $\omega/\omega_p = 1.22$, corresponding to the contributions of the dominant MO mode, which is splitted into two resonant modes with high-Q factors upon weak magnetization. The insets demonstrate the normalized instantaneous electric field distributions of the total SCS maxima, allowing us to elucidate how the incident wave resonantly interacts with the antenna. The anti-parallel electric field's polarizability at the opposite sides of the dielectric cylinder induces a circular displacement current, leading to a narrow-linewidth MO resonance inside the particle.

3 Optimization Method Algorithm

Our methodology employs stochastic gradient descent (SGD) to refine our model's parameters iteratively. SGD fine-tunes the CNN's weights and biases by minimizing the MSE loss. Given the intricate high-dimensional nature of the coupled system features, we use a genetic algorithm to pinpoint the most relevant feature subset. This algorithm evolves a population of feature sets over multiple iterations, leveraging crossover and mutation techniques. The effectiveness of each feature set is assessed through the accuracy of CNN's predictions.

In our validation, we conduct rigorous tests on a contemporary dataset encompassing diverse antenna systems. Our deep learning model outperforms conventional regression

7

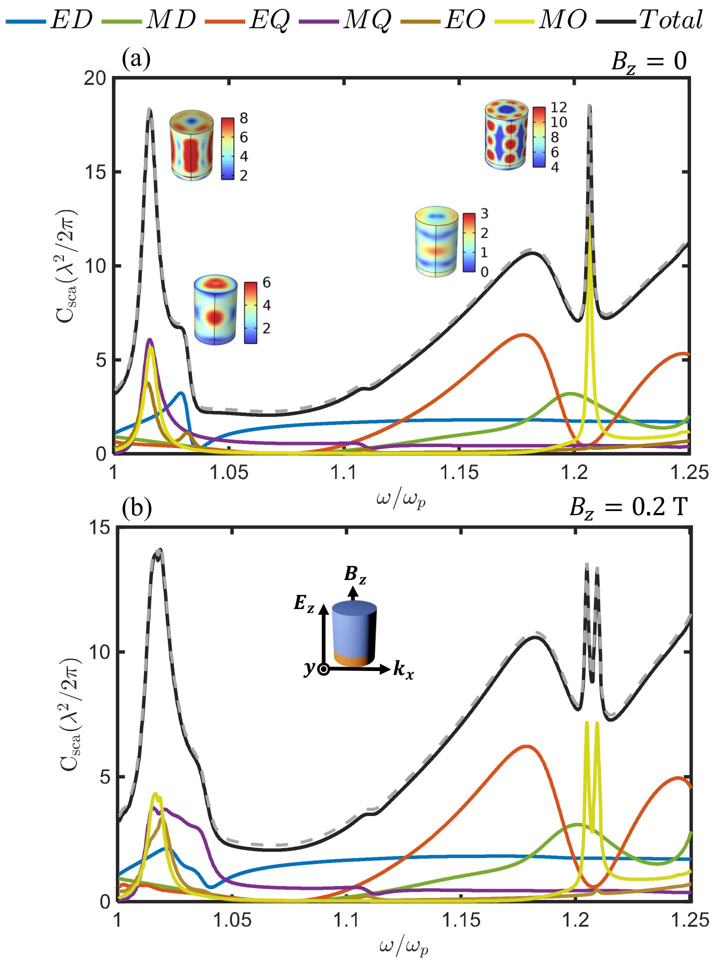

Figure S3: The SCS of the hybrid cylindrical antenna under z-polarized plane wave illumination with the wavevector k_x (a) in the absence and (b) in presence of the applied static magnetic field. The scattering response of the antenna supports all multipole moments across the studied spectral range in which the contribution of the MO mode is significant and experiences the Zeeman splitting effect upon magnetization, leading to the splitted MO resonant modes, as shown in panel (b). The upper part of the antenna is made of a Si layer with the height and radius of 80 and 35 μm, respectively. InSb layer comprises the lower part of the antenna with the height and radius of 8 and 35 μm, respectively. The insets show the instantaneous normalized electric field distributions around the antenna corresponding to the total SCS maxima.

techniques. Furthermore, the genetic algorithm adaptly discerns the paramount features crucial for precise decay rate prediction. Overall, integrating deep learning with genetic algorithm-driven feature selection presents a significant advancement in addressing challenges in coupled emitter-antenna systems (See. Algorithm 1).

4 References

[1] Grigorios P Zouros, Georgios D Kolezas, Evangelos Almpanis, Konstantinos Baskourelos, Tomasz P Stefański, and Kosmas L Tsakmakidis. Magnetic switching of kerker scattering in spherical microresonators. *Nanophotonics*, 9(12):4033–4041, 2020.

[2] Grigorios P Zouros, Georgios D Kolezas, Evangelos Almpanis, and Kosmas L Tsakmakidis. Three-dimensional giant invisibility to superscattering enhancement induced by zeeman-split modes. *ACS Photonics*, 8(5):1407–1412, 2021.

[3] Jan Chochol, Kamil Postava, Michael Čada, Mathias Vanwolleghem, Lukáš Halagačka, Jean-François Lampin, and Jaromír Pištora. Magneto-optical properties of insb for terahertz applications. *AIP Advances*, 6(11):115021, 2016.

[4] A Márquez and R Esquivel-Sirvent. Terahertz response of plasmonic nanoparticles: Plasmonic zeeman effect. *Optics Express*, 28(26):39005–39016, 2020.

[5] Sina Aghili, Aydin Amini, Leyla Shirafkan Dizaj, and Ksenia Dolgaleva. Thz plasmonic metasurface based on a periodic array of insb metamolecules with narrow resonances. *Optics Communications*, 508:127805, 2022.

[6] Aso Rahimzadegan, Theodosios D Karamanos, Rasoul Alaee, Aristeidis G Lamprianidis, Dominik Beutel, Robert W Boyd, and Carsten Rockstuhl. A comprehensive multipolar theory for periodic metasurfaces. *Advanced Optical Materials*, 10(10):2102059, 2022.

Algorithm 1 Enhanced Deep Learning and Genetic Algorithms for radiative decay rate prediction

Data Preprocessing:
Normalize spatial coordinates (x, y, z)
Apply one-hot encoding for frequency and applied magnetic field
Neural Network Initialization:
Set up neural network architecture with random weights and biases
Genetic Algorithm Parameters:
Set population size P, number of generations G, and mutation rate M
Initialize population of feature sets F with P individuals
Deep Learning Training:
Define the number of epochs and learning rate
for each epoch **do**
    Compute predicted radiative decay rate $\hat{Y}$
    Compute MSE loss: $MSE = \frac{1}{n}\sum_{i=1}^{n}(Y_i - \hat{Y}_i)^2$
    Update model parameters via optimizer (e.g., SGD)
end for
Genetic Optimization:
for generation $g = 1$ to G **do**
    Evaluate fitness of each feature set $f \in F$ using the neural network
    Select best-performing individuals for mating pool $MatingPool$
    Populate $NewF$ by applying genetic operations on $MatingPool$
    for each feature set $f \in NewF$ **do**
        if random value $< M$ **then**
            Introduce mutation to f
        end if
    end for
    Update population: $F \leftarrow NewF$
end for
Optimal Features:
Select feature set with topmost fitness value from the final population
Final Prediction:
Predict radiative decay rate using the selected feature set

Chapter 5

SHG Plasmonic Metasurface with Randomly Oriented Meta-Atoms

5.1 Introduction

Optical imaging has become an essential tool for probing the structural and functional properties of complex materials and biological samples. Conventional techniques, such as confocal microscopy and fluorescence imaging, are widely used to detect and monitor intracellular variations [141]. While these approaches are effective for far-field microscopy, they primarily probe spatially averaged responses and remain constrained by diffraction-limited resolution in label-free and real-time imaging applications [142, 143]. These limitations are further pronounced in biological media, where scattering and absorption reduce signal strength and limit imaging speed [144].

Nonlinear optical microscopy offers an alternative imaging paradigm by exploiting frequency conversion processes to generate intrinsic optical contrast that is sensitive to molecular symmetry, orientation, and structural ordering [145]. A broad range of nonlinear techniques, including two-photon excited fluorescence, second-harmonic generation (SHG), third-harmonic generation (THG), coherent anti-Stokes Raman scattering, and stimulated Raman scattering, has emerged as powerful, high spatiotemporal resolution, and non-invasive diagnostic tools [145]. These modalities have enabled significant advances in biomedical imaging [145, 146], ultrafast microscopy [147], and nonlinear spectroscopic analysis [148]. In particular, nonlinear microscopy is well suited for probing real-time subcellular dynamics of polar biomolecular structures, such as microtubules, collagen, α-amino acids, and muscle myosin [149].

Despite these advantages, nonlinear optical responses arising from higher-order light–matter interactions are inherently weak and therefore often require high excitation power, typically provided by pulsed laser sources. In conventional bulk nonlinear platforms, efficient frequency conversion further depends on satisfying phase-matching conditions, which generally require materials and structures with extended interaction lengths and high Q-factors, such as photonic crystal fibers or quasi-phase-matched periodically poled materials [150, 151]. Moreover, the use of high excitation power may induce photodamage or photobleaching in biological samples, limiting the applicability of bulk nonlinear systems for compact, high-resolution, and biologically compatible imaging platforms.

Plasmonics provides an effective strategy for overcoming the fundamental limitations of conventional optical imaging by enabling strong confinement and enhancement of electromagnetic fields at the nanoscale [152]. Through the excitation of localized surface plasmon resonances (LSPRs) in metallic meta-atoms and surface plasmon polaritons (SPPs) at metal–dielectric interfaces, optical energy can be concentrated into deeply sub-wavelength volumes, leading to a substantial increase in local field intensity without increasing the input power [30]. This capability has enabled a wide range of plasmonics-assisted imaging and sensing techniques. Among these, surface-enhanced Raman scattering (SERS) exploits plasmon-induced field enhancement to amplify intrinsically weak vibrational signals, achieving sensitivities far beyond those of conventional Raman spectroscopy [153]. In parallel, plasmonic meta-atoms have been incorporated into near-field imaging approaches, including atomic force microscopy (AFM) [154] and scanning near-field optical microscopy (SNOM) [155], to achieve high spatial resolution through surface-localized probing, thereby overcoming diffraction limitations and weak optical responses [156].

Plasmonics has also emerged as a powerful platform for nonlinear optical processes beyond its linear imaging and sensing applications. In plasmonic meta-atoms, strong electromagnetic field confinement enables efficient nonlinear frequency conversion in a phase-matching-free regime [35], eliminating the need for long interaction lengths that are typically required in bulk nonlinear media. Noble metals, as commonly used plasmonic materials, possess centrosymmetric crystal lattices that suppress even-order nonlinear optical interactions [157]. Consequently, plasmonic meta-atoms are engineered with non-centrosymmetric geometries to support even-order nonlinear processes. Under resonant excitation, LSPRs strongly enhance the local pump field, giving rise to local nonlinear current sources that oscillate at frequencies different from the excitation frequency and act as efficient emitters of nonlinear radiation. Within this framework, plasmonic structures can either enhance nonlinear signals generated in nearby materials or operate as intrinsic ultrafast nonlinear emitters when inversion symmetry is broken at the nanoscale [158].

Plasmonic metasurfaces extend this concept by arranging resonant meta-atoms into planar arrays, enabling collective effects that provide additional degrees of freedom to engineer nonlinear generation and radiation. In particular, periodic metasurfaces can support surface lattice resonances (SLRs), which arise from the constructive coupling of individual LSPRs through in-plane Rayleigh-anomaly diffraction channels [159]. Compared to single resonant meta-atoms, SLRs exhibit higher Q-factors and more spatially distributed electromagnetic field enhancement, which significantly increases the effective light–matter interaction strength and improves nonlinear conversion efficiency near the metasurface plane. Moreover, plasmonic metasurfaces can be engineered such that plasmonic resonances occur at both the pump and output nonlinear frequencies [126]. Resonances at these frequencies simultaneously enhance the generation of nonlinear signals and their emission or radiation into the far-field, enabling compact and high efficiency nonlinear metasurface architectures.

Notably, coherent nonlinear processes such as SHG can be directly enhanced in plasmonic resonant devices [122]. At the nanoscale, SHG in plasmonic systems is described in terms of induced nonlinear current densities. Anharmonic oscillations of conduction electrons under intense optical excitation generate oscillating nonlinear currents at the second-harmonic frequency, which act as coherent radiation sources. The induced nonlinear current in plasmonic meta-atoms depends on the dominant second-order susceptibility tensor elements χ_{ijk}, and can be expressed as [119]

$$\begin{aligned}\mathbf{J}^{\mathrm{NL}} = -i\,2\omega\,\epsilon_0\Big(&\chi_{nnn}E_nE_n\hat{\mathbf{n}} + \chi_{ntt}E_{t_1}E_{t_1}\hat{\mathbf{n}} + \chi_{ntt}E_{t_2}E_{t_2}\hat{\mathbf{n}}\\ &+ \chi_{ttn}E_{t_1}E_n\hat{\mathbf{t}}_1 + \chi_{ttn}E_{t_2}E_n\hat{\mathbf{t}}_2\Big),\end{aligned} \tag{5.1}$$

where the linear local electric field generated by the resonant plasmonic meta-atoms can be written as

$$\mathbf{E}(\omega) = E_n\hat{\mathbf{n}} + E_{t_1}\hat{\mathbf{t}}_1 + E_{t_2}\hat{\mathbf{t}}_2. \tag{5.2}$$

Here, $\hat{\mathbf{n}}$ denotes the surface normal unit vector, while $\hat{\mathbf{t}}_1$ and $\hat{\mathbf{t}}_2$ are orthogonal tangential unit vectors to the meta-atom surface. By assuming a negligible contribution from bulk nonlinearities in plasmonic meta-atoms, the overall SHG response is governed by the strength of excited second harmonic dipole moments generated by the induced nonlinear surface currents.

From a biological imaging perspective, SHG is well suited for real-time probing of polar and anisotropic structures, as many biological assemblies, such as microtubules, possess intrinsic polarity and can be treated as asymmetrical configurations [160]. However, SHG intensity is strongly polarization dependent and varies with the relative orientation between the nonlinear emitter and the incident optical field [161, 162]. While this orientation sensitivity provides rich structural information, it becomes a practical challenge when emitters are not aligned or exhibit dynamically varying orientations. Motivated by this limitation, this chapter focuses on a randomly oriented SHG plasmonic metasurface as an engineered nonlinear platform to identify how meta-atom orientation governs the measured SH response. In this approach, meta-atoms are distributed in different orientations such that, under a different excitation polarization, only specific orientations efficiently couple to the pump field, generate strong plasmon-enhanced nonlinear currents, and contribute substantially to SH emission, while other orientations remain inactive. This random-orientation architecture therefore clarifies which orientation channels dominate the overall emission and how the SH response evolves in structurally disordered systems.

5.2 Design and Modeling

In this section, the SH response of a plasmonic metasurface composed of asymmetrical L-shaped meta-atoms with different orientations is investigated. Figure 5.1 shows the unit cell of the proposed metasurface, where gold L-shaped meta-atoms are placed on a silica substrate. An interparticle spacing of 1 μm is chosen to suppress near-field coupling and avoid hybridization between the plasmonic resonances of neighboring meta-atoms. The lattice constants of the metasurface unit cell in the x–y plane are set to

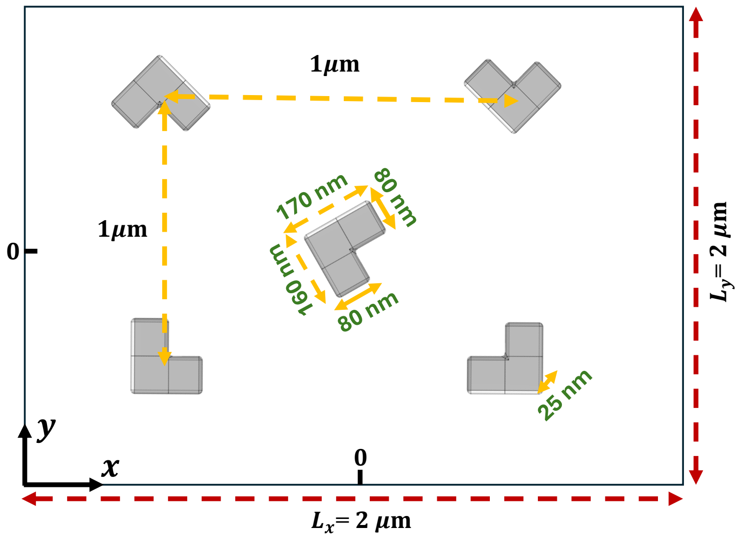

FIGURE 5.1: Unit cell of the plasmonic metasurface composed of asymmetrical L-shaped gold meta-atoms with different orientations on a silica substrate.

$L_x = L_y = 2\ \mu$m. The geometrical parameters of the L-shaped meta-atoms consist of two orthogonal arms with lengths of 180 nm and 170 nm, a width of 80 nm, and a thickness of 25 nm. To eliminate non-physical field singularities associated with sharp corners and to reflect realistic fabrication conditions, the edges of the meta-atoms are rounded with a curvature radius of 10 nm [163]. In addition, a chromium adhesion layer with a thickness of 3 nm, which is essential in the fabrication process [162], is included beneath the gold meta-atoms to accurately estimate the optical response of the plasmonic metasurface.

As the first step, we study the linear optical response of the proposed metasurface using full-wave simulations performed in COMSOL software. The complex permittivity of gold is described by the Drude model with a plasma frequency of $\omega_p = 1.781 \times 10^{14}$ rad/s, free carrier concentration $N = 8.56 \times 10^{22}$ cm^{-3}, damping constant $\gamma = 3.35 \times 10^{13}$ rad/s, and effective mass $m^* = 7.83 \times 10^{-29}$ kg [30, 164]. The metasurface is excited by a normally incident, linearly polarized plane wave propagating along the z-direction.

Figure 5.2 shows the transmission spectra of the metasurface under x- and y-polarized excitations. The metasurface exhibits two pronounced resonances at wavelengths around 800 nm and 1100 nm, which originate from individual ED-LSPR modes of the randomly oriented meta-atoms. The strong polarization dependence of these resonances arises from the L-shaped

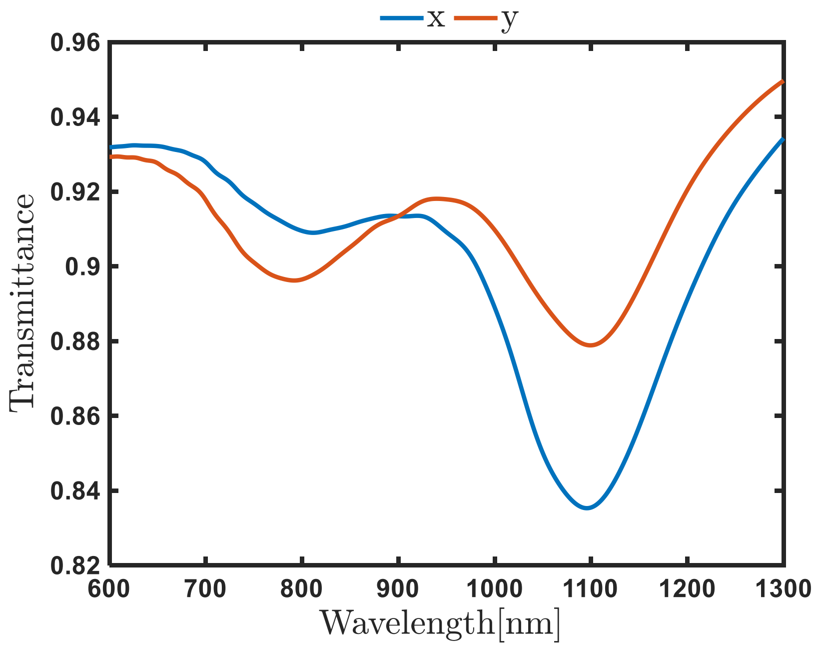

FIGURE 5.2: Transmission spectra of the plasmonic metasurface under x- and y-polarized plane wave excitation propagating along the z-direction, showing polarization-dependent LSPRs around 800 nm and 1100 nm.

geometry of the meta-atoms, which supports distinct current distributions and effective dipole moments along its two orthogonal arms [165, 166]. Under x-polarized excitation, the incident electric field strongly couples to the longer effective current path of the meta-atoms projected along the x-direction, giving rise to a dominant red-shifted resonance around 1100 nm. In contrast, under y-polarized excitation, a higher-energy resonance emerges near 800 nm, which is stronger than that observed for the x-polarized case. This behavior originates from the efficient coupling of the incident electric field to a shorter effective current path supported by the meta-atoms [167].

Following the polarization-dependent transmission spectra shown in Fig. 5.2, the near-field response of the metasurface is analyzed to assess the contribution of the randomly oriented meta-atoms to the observed resonances. Figure 5.3 shows the plasmon-assisted field enhancement within the metasurface unit cell at the resonance wavelengths under x- and y-polarized plane wave excitation.

For x-polarized excitation at the wavelength of 1100 nm, as shown in Fig. 5.3(a), pronounced local field enhancement is observed for the V-shaped meta-atoms, where the incident polarization is oriented across their gap, exciting a bright plasmon mode and generating hotspots at the antenna

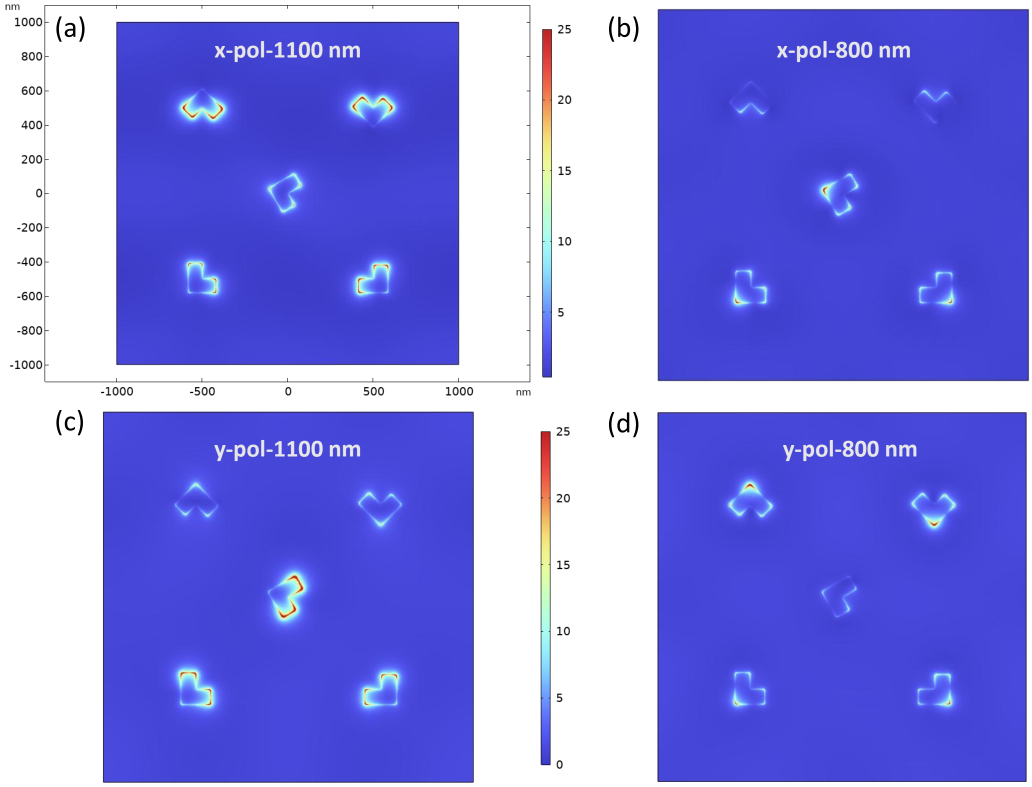

FIGURE 5.3: Local linear E-field enhancement distributions within the metasurface unit cell at resonance wavelengths under (a,b) x-polarized and (c,d) y-polarized plane wave excitation, showing orientation-dependent LSPRs of the meta-atoms.

tips. In addition, the L-shaped meta-atoms positioned at the bottom of the unit cell exhibit remarkable field enhancement which is consistent with the low-energy bent longitudinal current mode reported for asymmetric L-shaped antennas [165], in which charge accumulation at the outer corners leads to strong local field enhancement. Figure 5.3(b) shows the near-field distribution within the metasurface unit cell at the resonance wavelength of 800 nm, where the local field enhancement becomes strongly orientation dependent. In this case, the L-shaped and rotated central meta-atoms exhibit pronounced hotspots that are localized near the junctions of their arms, consistent with the higher-energy mode of L-shaped meta-atoms characterized by out-of-phase longitudinal current oscillations on the two arms [165]. By contrast, the V-shaped elements remain weakly excited at this wavelength under x-polarized illumination.

Under y-polarized excitation, the V-shaped meta-atoms remain nearly inactive at the resonance wavelength of 1100 nm, whereas the L-shaped meta-atoms exhibit strong local field enhancement, as shown in Fig. 5.3(c). This behavior follows the polarization selectivity of the low-energy bent longitudinal mode supported by L-shaped meta-atoms, such that only those orientations whose effective dipole has a large projection along the y-direction are efficiently driven. In particular, the rotated central meta-atom couples most strongly under y-polarization and therefore produces the dominant local field enhancement observed in the unit cell. Finally, at the wavelength of 800 nm under y-polarized excitation, as shown in Fig. 5.3(d), the local field enhancement is associated with the higher-energy mode of the L-shaped meta-atoms in which the two arms oscillate out of phase, leading to enhanced fields concentrated near the junctions of their arms. In this case, only orientations providing sufficient modal overlap with the incident y-polarized field exhibit strong hotspots, whereas the central meta-atom remains weakly excited due to inefficient coupling under this excitation condition.

The local field enhancement of the individual meta-atoms provides direct insight into which orientations dominate the linear optical response, and hence control the SHG behavior of the metasurface. In ultrathin media such as plasmonic metasurfaces, which operate in a phase-matching-free regime, SHG is evaluated as a nonlinear scattering process. In this framework, the SH emission is governed by the strength and spatial distribution of local induced nonlinear current sources that oscillate within the metasurface plane and radiate into free space over a broad range of angles.

As the next step of this study, the nonlinear SH response of the metasurface is obtained using a two-step modeling process. In the first step, the linear electromagnetic response of the metasurface at the pump light frequencies is calculated using the RF module of COMSOL software. The resulting local linear electromagnetic fields are then substituted into Eq. (2.35) to compute the induced nonlinear current components defined within the hydrodynamic model. These nonlinear currents are defined within the volume of the meta-atoms in the unit cell and act as localized nonlinear sources distributed across the metasurface plane, oscillating at the SH frequency of the incident pump light. In the second step, a frequency-domain scattering problem is solved using the same COMSOL software's module, where the induced nonlinear currents serve as the only excitation sources at the SH frequency, while the background electromagnetic field is set to zero. The resulting SH radiation emitted by these current sources is collected in the forward direction using a planar monitor positioned 200 nm above the metasurface. The forward SH response is quantified by collecting the Poynting vector flux at the SH

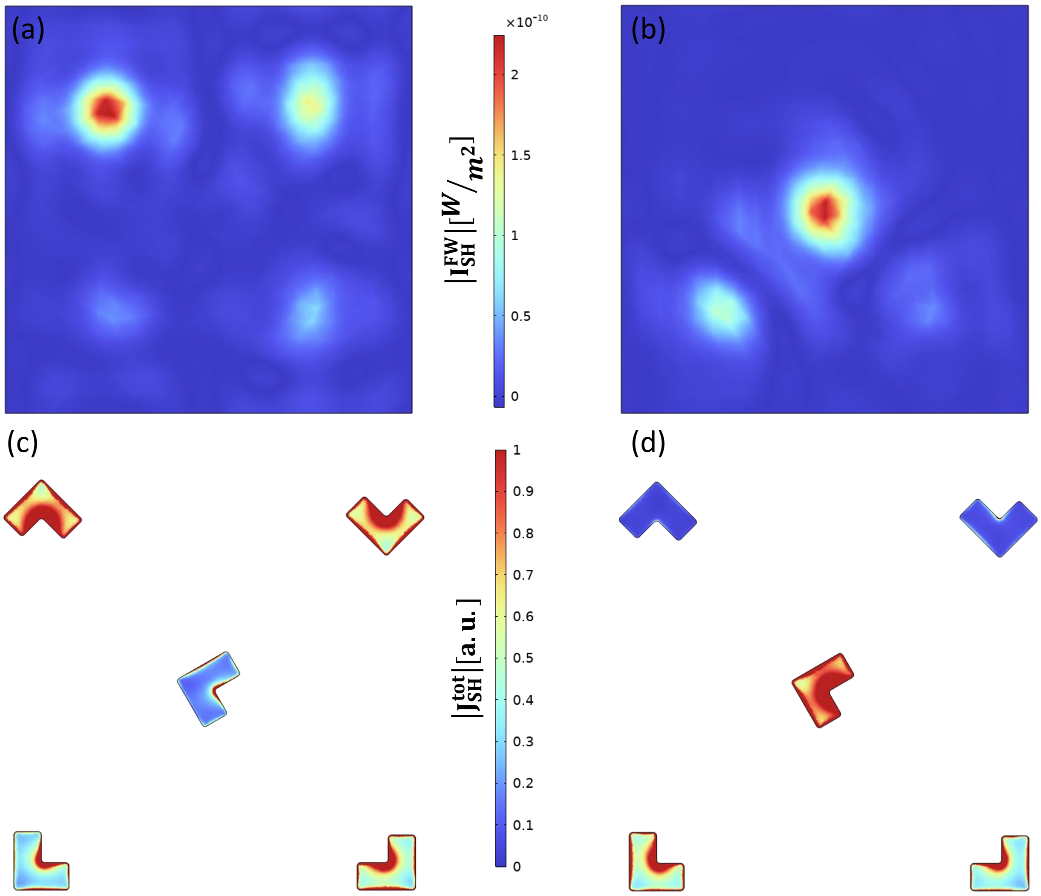

FIGURE 5.4: Near-field distributions of the forward SH response of the plasmonic metasurface. (a,b) Forward SH intensity profiles under x- and y-polarized pump excitation at 1100 nm. (c,d) Corresponding total induced nonlinear SH current distributions within the meta-atoms, highlighting orientation-selective SH emission channels.

frequency, which provides direct access to the near-field distribution of the radiated SH intensity.

Figure 5.4 presents both the forward SH near-field intensity and the corresponding spatial distribution of the total induced SH current inside the meta-atoms. For x-polarized pump light at the LSPR wavelength of 1100 nm, Fig. 5.4(a) shows that the strongest forward SH intensity originates mainly from the V-shaped meta-atoms located at the top of the unit cell. This behavior is consistent with Fig. 5.4(c), where $|\mathbf{J}_{\mathrm{SH}}^{\mathrm{tot}}|$ is significantly larger on the same V-shaped meta-atoms due to the strong local electric-field enhancement supported by these orientations. The L-shaped meta-atoms at the bottom of the unit cell also induce noticeable $|\mathbf{J}_{\mathrm{SH}}^{\mathrm{tot}}|$ in Fig. 5.4(c). However, their contribution to the near-field SH intensity profile in Fig. 5.4(a) is much weaker than that of the V-shaped meta-atoms.

Under y-polarized pump light at the same LSPR wavelength of 1100 nm, the dominant SH emission channel changes. Figure 5.4(b) exhibits a pronounced SH hotspot localized around the rotated V-shaped meta-atom at the center of the unit cell. This observation is supported by Fig. 5.4(d), where the strongest $|\mathbf{J}_{\mathrm{SH}}^{\mathrm{tot}}|$ is localized on the same meta-atom, while the V-shaped meta-atoms remain inactive and the L-shaped meta-atoms at the bottom of the unit cell emit only weak SH signals. At the LSPR wavelength of 1100 nm for both x- and y-polarized excitation, the remaining orientations contribute weakly to the SH response because their effective current distributions are not efficiently driven by the incident field. These orientations can emit stronger SH radiation at the LSPR wavelength of 800 nm. However, based on additional evaluations not reported here, their emission strength is approximately two orders of magnitude lower than the SH intensity observed in Fig. 5.4(a) and Fig. 5.4(b).

5.3 Experimental Results

Following the numerical evaluation of the proposed metasurface, this section focuses on its experimental linear characterization to assess its transmission spectral response. The sample was fabricated by Dr. Lais Fuji dos Santos using electron-beam lithography. The structure consists of gold meta-atoms with a thickness of 25 nm deposited on a 0.5 mm-thick glass substrate, and a 3 nm chromium adhesion layer was used to enhance adhesion of the gold to the substrate.

Figure 5.5(a) shows a schematic of the optical setup used to measure the transmission spectra of the metasurface. The diverging light from a broadband supercontinuum laser source is first collimated using lens L1 with a focal length of $f = 35$ mm, and then aligned along the main optical axis using two mirrors, M1 and M2. A polarizer is placed after the mirrors to control the polarization state of the beam incident on the sample. Two apertures, A1 and A2, are positioned along the optical path to ensure that the beam center passes through the sample along a straight trajectory. The beam is then focused onto the sample by lens L2 with a focal length of $f = 50$ mm. The forward-scattered light from the sample is collected using a microscope objective with a focal length of $f = 17$ mm. At the final stage of the setup, the collected light is collimated by lens L3 with a focal length of $f = 70$ mm and coupled into a multi-mode fiber with a core diameter of 400 μm using a fiber coupler. The output light is analyzed by an optical spectrum analyzer to record the transmission spectrum of the metasurface.

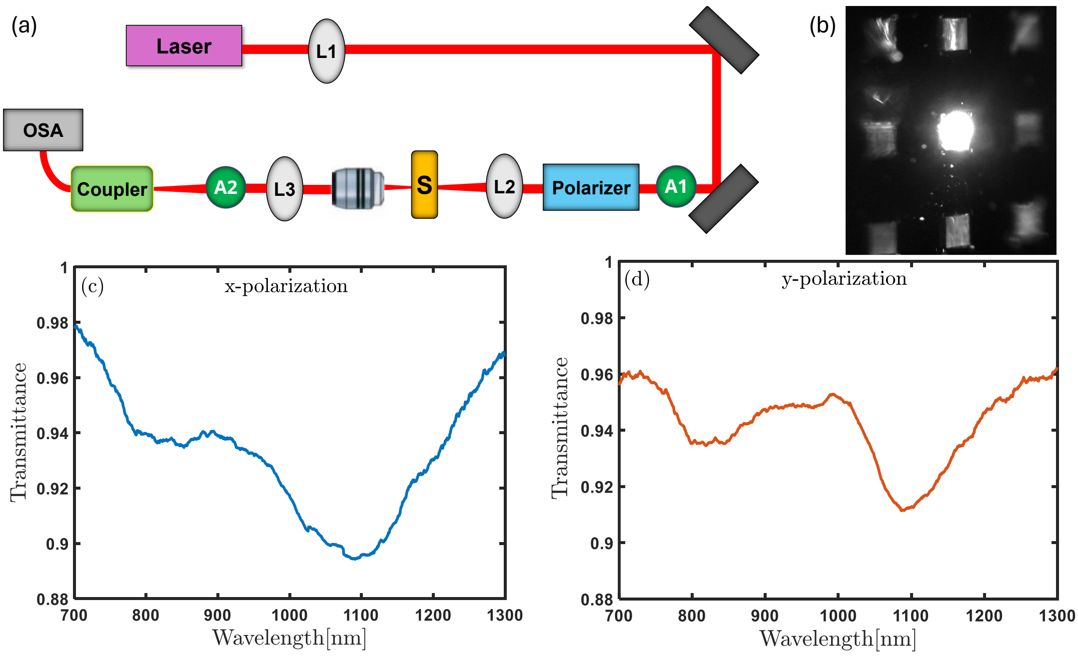

FIGURE 5.5: (a) Experimental setup used to measure the metasurface transmission spectrum. (b) Image of the beam incident on a single metasurface within the fabricated sample. (c,d) Measured transmission spectra of the metasurface under x- and y-polarized beams, respectively.

Figure 5.5(b) presents an image of the fabricated sample captured by a microscopy camera, showing an array of nine metasurfaces, each with an area of $480 \times 480\ \mu\text{m}^2$. Each metasurface is composed of unit cells identical to that illustrated in Fig. 5.1. The meta-atoms within each unit cell are randomly oriented, with sufficient inter-particle spacing to suppress near-field coupling between individual plasmonic resonances. As shown in Fig. 5.5(b), the laser beam is focused to cover the entire area of the metasurface, ensuring a high signal-to-noise ratio for accurate transmission measurements. Figures 5.5(c) and 5.5(d) present the experimentally measured transmission spectra of the metasurface under x- and y-polarized excitation, respectively. The results show extrema near 800 nm and 1100 nm, corresponding to the LSPRs of the meta-atoms, in good agreement with the simulated results shown in Fig. 5.2.

To image the SH response from randomly oriented meta-atoms, we fabricated an additional metasurface, as shown in Fig. 5.6. The basic repeating block comprises five meta-atom variants (two L-shaped and three V-shaped orientations), with each variant repeated five times, resulting in a total of 25 meta-atoms per block. This 25-element block is replicated 19 times along the horizontal direction. Along the vertical direction, each meta-atom is repeated 480 times, yielding an area of $480 \times 480\ \mu m^2$. Figure 5.6(a) shows the metasurface layout that the narrow red stripes contain the L-shaped meta-atoms in two orientations, and the wider blue stripes contain the V-shaped meta-atoms in three orientations. Figure 5.6(b) provides a magnified view of the layout, where the L-shaped and V-shaped meta-atoms are highlighted in red and blue, respectively. With a lattice constant of $1\ \mu m$ in both the x and y directions, near-field coupling between adjacent meta-atoms is negligible. Consequently, the metasurface fabricated for SHG imaging supports only individual LSPRs, and its linear optical response is identical to that of the metasurface based on the unit cell shown in Fig. 5.1.

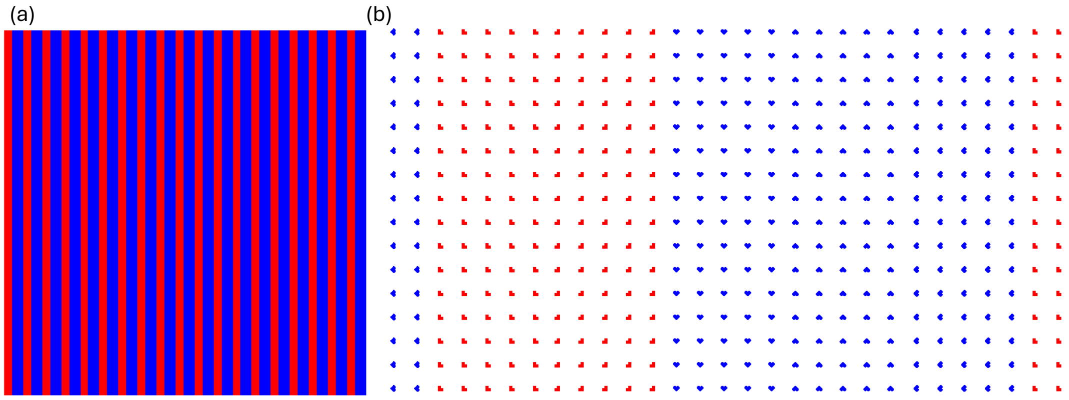

FIGURE 5.6: (a) Layout design of the metasurface used for SHG imaging. The narrow red stripes contain L-shaped meta-atoms in two orientations, and the wide blue stripes contain V-shaped meta-atoms in three orientations. (b) Magnified view showing the arrangement and shape diversity of the meta-atoms, with L-shaped and V-shaped antennae highlighted in red and blue, respectively. The layout design was prepared by Dr. Lais Fuji dos Santos.

To obtain SH images from the sample, we used a home-built SHG microscope in Prof. François Légaré's laboratory. The sample was excited with an ytterbium (Yb) fiber laser delivering 125 fs pulses at a central wavelength of 1030 nm and a repetition rate of 25 MHz. The average excitation power was in the range 30–50 mW.

Before performing SHG imaging, we evaluate the spatial distribution of the forward-emitted SH signal by numerically modeling a finite metasurface that reproduces the formation of fabricated layout, as shown in Fig. 5.7(a). The forward SH response is calculated using the approach described in Section 2.7.1. A planar monitor located above the metasurface is used to map the near-field distribution of the forward SH intensity.

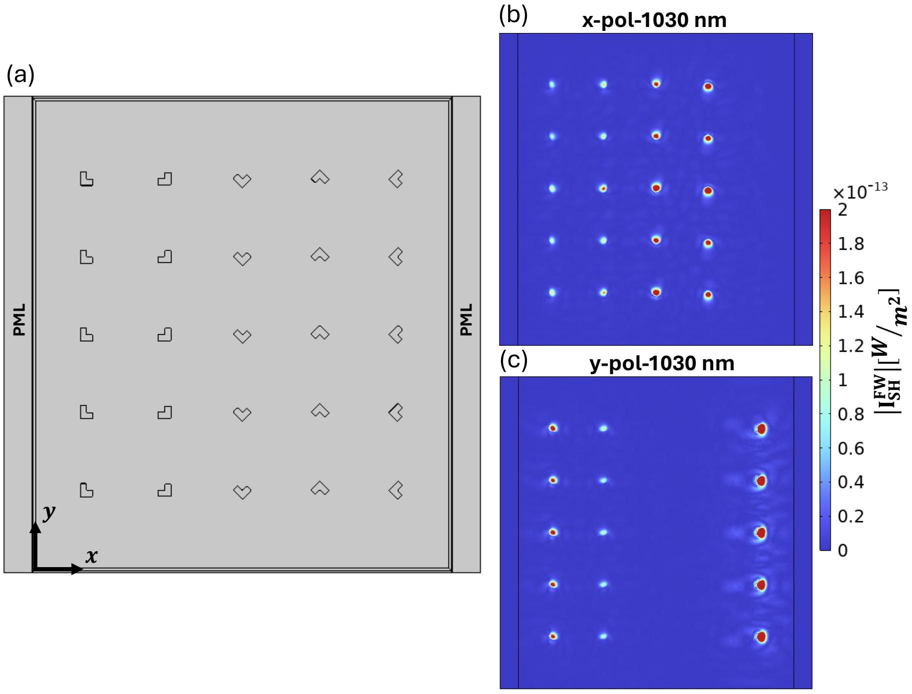

FIGURE 5.7: (a) Finite metasurface geometry used in the simulation. Spatial distribution of the forward SH intensity I_{SH}^{FW} evaluated on the plane monitor 200 nm above the metasurface under (b) x-polarized and (c) y-polarized excitation at the pump wavelength of 1030 nm.

Figure 5.7(b) shows the simulated forward SH intensity under an x-polarized plane wave excitation at 1030 nm, as the wavelength of pump light, matching the laser source wavelength used in the microscope. The V-shaped meta-atoms dominate the SH response, whereas the L-shaped meta-atoms produce a weaker yet detectable signal. By contrast, the column containing the rotated V-shaped meta-atoms completely disappears under this polarization. Under a y-polarized excitation at the pump wavelength 1030 nm, the rotated V-shaped column becomes the strongest component, and the L-shaped meta-atoms also contribute to the overall SH intensity profile, while the two columns of V-shaped meta-atoms become inactive, as shown in Fig. 5.7(c). These results are consistent with the orientation-selective SH emission channels identified in the unit-cell simulations in Fig. 5.4(a) and Fig. 5.4(b).

Figure 5.8 presents the recorded SHG images of the metasurface under x- and y-polarized excitation at 1030 nm as the wavelength of pump light. Owing to the finite spatial resolution of the SHG microscope, the images do not resolve the contributions of individual meta-atom orientations within each stripe. By comparing the image recorded under x-polarized excitation, shown in

Fig. 5.8(a), with the simulated results in Fig. 5.7(b) and the metasurface layout in Fig. 5.6, we infer that the wider stripes containing V-shaped meta-atoms appear brighter, whereas the narrow stripes containing L-shaped meta-atoms exhibit no observable response. We expected a more uniform brightness over the full vertical extent of each wide stripe, but the image exhibits noticeable nonuniformity.

Under y-polarized excitation, the narrow stripes are brighter than the wide stripes, as shown in Fig. 5.8(b). This enhanced response is not solely from the L-shaped meta-atoms. As shown in Fig. 5.6(b), the proximity of the rotated V-shaped meta-atom columns to the narrow stripes results in a strong SH signal under y-polarization. The rotated V-shaped meta-atom columns are the dominant component in SHG, as demonstrated in Fig. 5.7(c).

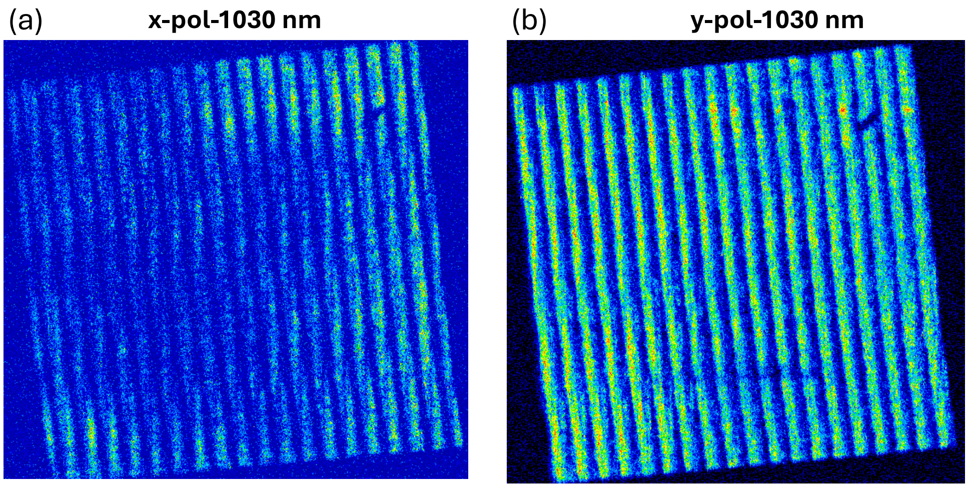

FIGURE 5.8: SHG images of the fabricated metasurface recorded under (a) x-polarized and (b) y-polarized excitation at the pump wavelength of 1030 nm. Under x-polarized excitation, the wider stripes containing the V-shaped meta-atoms appear brighter. However, the brightness is nonuniform along the vertical direction, in contrast to the uniform response observed in the simulations. Under y-polarized excitation, the narrow stripes containing the L-shaped meta-atoms are brighter than the wider stripes. This strong SHG signal under y-polarization probably arises from the column of rotated V-shaped meta-atoms positioned adjacent to the narrow stripes, as shown in Fig. 5.6.

At this stage of the project, we aimed to image the distribution of SH intensity from each meta-atom orientation. While the SHG images confirm that the metasurface generates a detectable SH signal, the orientation of meta-atoms remain unresolved.

5.4 Conclusion

In this chapter, we designed and investigated a plasmonic metasurface composed of randomly oriented meta-atoms to study SHG. Linear simulations and transmission measurements confirmed resonant behaviour near 800 nm and 1100 nm, arising from the ED-LSPRs of the constituent meta-atoms. Using nonlinear simulations, we predicted the spatial distribution of the forward SH intensity and showed that different meta-atom orientations govern the SH response of the metasurface depending on the polarization of the pump light.

To experimentally image the SH response, we fabricated a metasurface layout in which different orientations of L-shaped and V-shaped meta-atoms are repeated vertically and arranged into a stripe pattern that enables classification of the response. The narrow stripes contain L-shaped meta-atoms with two orientations, whereas the wide stripes contain V-shaped meta-atoms with three orientations. SHG microscopy at the pump wavelength of 1030 nm confirmed that the metasurface generates a measurable SH signal and exhibits polarization-dependent contrast at the stripe level. However, the limited spatial resolution of the microscope and the observed nonuniformity of the stripe brightness along the vertical direction prevent direct identification of the contribution from each individual orientation.

Chapter 6

Plasmonic Metasurfaces for SHG Microscopy Applications

6.1 Contribution Statement

This study grew out of a main collaborative project between the research groups of Prof. Dolgaleva and Prof. Ramunno on SHG plasmonic metasurfaces with randomly oriented meta-atoms, as discussed in the previous chapter. During the regular meetings of this collaboration, I conceived and pursued the idea of improving the efficiency of a plasmonic SHG metasurface specifically for near-field microscopy applications. The idea was then developed through regular discussions with Prof. Dolgaleva and technical input from A. Thulaseedharan and Dr. Lais Fujii dos Santos, which helped refine the proposed structure and keep it compatible with future fabrication.

My main contributions to this chapter included (i) proposing the SHG enhancement mechanism based on a hybrid resonance, and defining the design direction, (ii) performing the numerical simulations and optimization using nonlinear scattering theory (NLST) implemented in COMSOL, and (iii) preparing and interpreting the main results. The theoretical framework and interpretation were further refined based on comments from Prof. Ramunno, and M. R. Mohammadpour and I examined the outcomes through a comprehensive and relevant literature review to benchmark the proposed mechanism.

I wrote the first draft of the manuscript and prepared the figures, and the draft was substantially improved through feedback from Prof. Dolgaleva and Prof. Ramunno. All aspects of the project were supervised by Prof. Dolgaleva, and all co-authors approved the final manuscript.

The conference publications related to this project is listed below:

- Aghili, Sina, and Ksenia Dolgaleva. "Second Harmonic Enhancement with a U-shaped InSb Plasmonic Antenna in the THz Regime."*Advanced Photonic Congress (APC)*. Optica Publishing Group, 2024.

6.2 Article

The results of this project were published in *Journal of the Optical Society of America B* [218], and this chapter is based on the following article.

1024 Vol. 43, No. 5 / May 2026 / Journal of the Optical Society of America B Research Article

Journal of the Optical Society of America B

OPTICAL PHYSICS

Bi-layered stack plasmonic metasurface for high-resolution near-field second-harmonic generation microscopy applications

Sina Aghili,[1] Mohammadreza Mohammadpour,[2] Athulya Thulaseedharan,[2] Lais Fujii dos Santos,[1] Lora Ramunno,[2] and Ksenia Dolgaleva[1,2]

[1]School of Electrical and Computer Engineering, University of Ottawa, 25 Templeton St., Ottawa, Ontario K1N 6N5, Canada
[2]Department of Physics, University of Ottawa, 25 Templeton St., Ottawa, Ontario K1N 6N5, Canada

Received 5 December 2025; revised 23 March 2026; accepted 31 March 2026; posted 31 March 2026; published 22 April 2026

This work presents a comparative numerical study of three plasmonic metasurface designs for near-field second-harmonic generation (SHG) microscopy applications requiring enhanced forward (FW) second-harmonic (SH) emission and high near-field resolution. We compare a localized surface plasmon resonance (LSPR)-based metasurface, a surface-lattice resonance (SLR)-based metasurface, and a bi-layered stack metasurface. All designs employ V-shaped gold nanoantennae as the nonlinear building blocks, providing high local-field enhancement at the pump wavelength and driving SH emission in the UV–visible range. The LSPR-based metasurface provides acceptable near-field resolution but limited FW emission. On the other hand, the SLR-based design, thanks to higher Q-factor enhancement through collective resonances, boosts the SH emission, while the near-field resolution is inhibited due to the required thick cladding of the SLR-based metasurface design. The proposed bi-layered metasurface integrates a passive, centrosymmetric nanobar array supporting an SLR beneath the nonlinear V-antenna layer, separated by a spacer optimized for vertical interaction. This design results in a 200× increase in FW SH emission intensity and enhanced near-field resolution compared to the LSPR case. The results demonstrate that the stack plasmonic metasurface enables simultaneous optimization of SHG efficiency and resolution, promising for plasmonic-assisted near-field SHG microscopy applications.

https://doi.org/10.1364/JOSAB.586760

1. INTRODUCTION

Second-harmonic generation (SHG) is a coherent second-order nonlinear optical process characterized by an ultrafast emission, governed by a material's second-order susceptibility, which is intrinsically sensitive to structural polarity [1]. The SHG process nearly vanishes in centrosymmetric media but is remarkably enhanced in non-centrosymmetric environments, providing physical insight into the concentration of polar structures [2].

Notably, many biomolecules possess twisted or chiral geometries that induce localized polarity when optically excited in the visible to near-infrared range, resulting in weak but detectable second-harmonic (SH) emission in the ultraviolet–visible spectrum [3,4]. The interplay of structural asymmetry, nanosecond-scale fluctuations in spatial concentration, and polarity-induced emission characteristics in these twisted biomolecules [5,6] enables the SHG process serving as an instantaneous, highly sensitive, and label-free contrast mechanism for bioimaging and real-time SH microscopy. This allows the direct probing of intrinsic second-order polarizability in complex biomolecular systems, specifically those associated with early-stage neurodegenerative disorders [7]. However, conventional SHG microscopy based on bulk nonlinear crystals faces significant limitations. The weak intrinsic nonlinearity of biological samples, diffraction-limited spatial resolution, and strict dependence on phase accumulation over a long interaction length constrain the near-field SHG resolution. These factors obscure the nanoscale features of biomolecules and subcellular dynamics [8].

Plasmonic metasurfaces offer a powerful alternative by concentrating optical fields at deeply subwavelength scales [9,10], well beyond the diffraction limit, thereby overcoming the limitations of phase matching and interaction length that constrain the efficiency of conventional bulk nonlinear platforms [11,12]. This intense electromagnetic field localization can amplify both the pump and the SH emission response at polarity-sensitive interfaces, enabling SHG at sub-femtosecond timescales [13]. Moreover, because many biological tissues and micro-organisms exhibit nonlinear activities in the UV–visible spectral window, SHG metasurfaces composed of asymmetric metallic nanoparticles, specifically noble metals like gold, are highly desirable for bio-compatible SHG platforms [14–16].

Research Article Vol. 43, No. 5 / May 2026 / *Journal of the Optical Society of America B* 1025

Various designs have been explored to enhance forward (FW) emission and near-field resolution of SHG in plasmonic gold metasurfaces in the UV–visible spectral window. One of the most widely used approaches relies on localized surface plasmon resonances (LSPRs) excited in asymmetric metallic subwavelength antennae, such as L-shaped, T-shaped, U-shaped, or G-shaped antennae, which can amplify the SH response [17–20]. Despite the ability of LSPR-based metasurfaces to improve near-field enhancement, these designs inherently suffer from low quality (Q) factors due to intrinsic Ohmic and radiative losses. This limitation reduces the energy accumulation of light–matter interaction and weakens the SH emission intensity in free space.

In parallel with plasmonic platforms, all-dielectric metasurfaces based on high-index, low-loss resonant nanoantennae have emerged as an alternative approach to enhancing nonlinear frequency conversion. In these structures, resonances are induced by displacement currents, giving rise to Mie resonances and high-Q states such as bound states in the continuum (BICs), which enable strong electromagnetic energy build-up inside the dielectric antenna volume and enhance harmonic generation through the intrinsic material nonlinearity [21,22]. In addition, high-index, low-loss dielectric nanoantennae can support multiple electric and magnetic multipolar modes, providing additional degrees of freedom for engineering nonlinear enhancement mechanisms in metaphotonics [23]. Furthermore, all-dielectric metasurfaces that support BIC resonances can achieve ultra-high Q and exhibit Fano-like resonances, thereby further strengthening light–matter interactions for efficient nonlinear conversion [24,25]. However, at deep sub-wavelength scales, the local-field enhancement achievable with dielectric antennae is considerably lower than that of plasmonic nanoantennae. In dielectric nanoantennae, the local-field enhancement requires sufficient optical size and field retardation to sustain oscillating currents. When the thickness of the dielectric antenna becomes too small, the local-field enhancement is significantly reduced [26,27], resulting in a weaker nonlinear response than that of the corresponding plasmonic nanoantenna.

Plasmonic metasurfaces supporting surface lattice resonances (SLRs) have been introduced to achieve high Q-factor and boost SH nonlinear response [28–31]. SLR arises from the coupling of individual LSPRs with in-plane Rayleigh anomaly diffraction, resulting in a collective resonance that exhibits a narrow spectral linewidth and enables strong electric-field enhancement across the metasurface plane, perpendicular to the emission direction. Although SLR-based metasurfaces strengthen nonlinear interactions via high-Q collective resonances, their excitation typically requires thick, index-matched dielectric claddings to maintain the resonance Q-factor. This environment confines most of the generated SH wavevector components within or along the metasurface plane, suppressing their coupling into free-space emission channels. Consequently, the SHG signal remains largely trapped, resulting in moderate FW SH emission and, more critically, blurring of near-field resolution, which deteriorates spatial polarity variations essential for microscopy applications [15].

Beyond LSPRs and SLRs, several additional strategies have been explored to enhance FW emission and near-field resolution of SHG in plasmonic metasurfaces. One promising approach involves doubly resonant metasurfaces, which are geometrically engineered to support simultaneous resonances at both the fundamental and SH wavelengths, thus significantly boosting SHG efficiency [32–34]. In many such configurations, auxiliary symmetric elements are placed adjacent to the nonlinear antennae to amplify the induced nonlinear local current sources. However, while this approach amplifies the overall SHG signal, it can reduce sensitivity to local variations of the main object, a critical limitation for near-field SHG microscopy, where resolving subwavelength spatial features is essential. Despite their distinct physical mechanisms and resonance strategies, most SHG plasmonic metasurface designs remain constrained in the context of near-field SHG microscopy, where both high spatial resolution and detectable FW SHG emission are necessary.

These limitations have recently shifted attention from planar metasurfaces toward vertically stacked metasurfaces, which offer remarkable design flexibility and enhanced performance for engineering linear and nonlinear optical processes such as tailoring optical dispersion, controlling diffraction, and exceptional transmission and reflection [35–37]. A notable work in this direction involves multi-layered L-shaped plasmonic metasurfaces vertically stacked along the propagation axis, which demonstrated enhanced second-harmonic emission in the backward direction [38]. While backward SHG efficiency was demonstrated, the near-field resolution, particularly at the top emitting layer, remains uncharacterized, leaving its efficiency for near-field SHG resolution unresolved.

Motivated by these challenges, we propose a new stack design based on gold plasmonic metasurfaces, specifically designed to achieve enhanced FW emission and near-field resolution for SHG in the UV–visible range. In contrast to previous multilayered designs, our structure integrates a nonlinear upper metasurface composed of asymmetric V-shaped antennae supporting LSPRs, and a linear lower metasurface made of centrosymmetric rectangular nanoantennae engineered to support a high-Q SLR within the pump wavelength range. In this configuration, the lower metasurface acts as a passive resonator, generating a spectrally narrow and spatially coherent mode that strongly enhances the electromagnetic field within and around the upper nonlinear metasurface. Due to their centrosymmetric geometry, the rectangular antennae do not contribute directly to SHG, enabling the enhanced pumped light to be transferred to the upper layer without an inter-quasi-phase-matching bottleneck. The upper V-shaped antennae are engineered to support LSPRs over the predefined pump wavelength range. Vertical coupling to the high-Q SLR metasurface gives rise to a spectrally narrow, Fano-like resonance, leading to intense localized excitation in the V-antennae. Triggered by the SLR-enhanced pump field incident from below, the antennae generate FW SH emission and improve near-field resolution, which is critical for SHG microscopy.

In this study, we perform a numerical analysis of three distinct plasmonic metasurface structures to evaluate the efficiency of the proposed stack design for SHG in microscopy applications. For comparison, we consider conventional single-layer metasurfaces, one supporting LSPRs and the other supporting SLRs, both composed of identical V-shaped gold nanoantennae. All platforms are evaluated under identical excitation conditions, geometrical parameters, and background refractive indices to ensure consistent verification. The lattice constants of the metasurfaces are selected to maintain a fixed pump wavelength range across all configurations. For the LSPR-based metasurface, the lattice constants are chosen to prevent near-field plasmonic hybridization between the V-shaped nanoantennae, ensuring that the targeted pump wavelength range is primarily determined by their intrinsic LSPR resonance. For the remaining metasurface designs, the lattice constants are then engineered to spectrally align their plasmonic responses with the same target pump wavelength range. The results demonstrate that the stack design simultaneously enhances near-field resolution and SH emission into free space. This performance makes the stack plasmonic metasurface a promising solution for high-resolution near-field SHG microscopy in the UV–visible spectral range.

2. METHODOLOGY

The SHG process arises from the anharmonic motion of accelerated electrons driven by a strong optical pump. In this regime, the electron response within the material becomes nonlinear, inducing local current sources that oscillate at twice the frequency of the incident field. This nonlinear induced current acts as a source term in the inhomogeneous wave equation, determining both the amplitude and spatial characteristics of the emitted SH signal. In bulk nonlinear materials, SHG efficiency relies on satisfying the phase-matching condition. However, in ultra-thin media such as plasmonic metasurfaces, operating in a phase-matching-free regime, SHG emission is a nonlinear scattering phenomenon governed by the strength of local induced nonlinear current sources that oscillate at the metasurface plane and emit incoherently in all directions and a broad range of angles [39–41].

In this work, we investigate SHG in a plasmonic metasurface composed of resonant gold nanoantennae. When illuminated by the pump field, each nanoantenna supports LSPRs that concentrate electromagnetic energy into a subwavelength region, which induces nonlinear oscillating currents inside the nanoantenna. The hydrodynamic model is applied to find local nonlinear sources [42,43]. In this case, the induced nonlinear volume current within the plasmonic nanoantenna is defined as [44,45]

$$\begin{aligned}\mathbf{J}(\mathbf{r},2\omega) &= \frac{\varepsilon_0\omega_p^2}{Ne(2\omega^2+i\omega\gamma)}\mathbf{E}_{\mathrm{loc}}(\mathbf{r},\omega)(\nabla\cdot\mathbf{J}_{\mathrm{Lin}}(\mathbf{r},\omega))\\ &+\frac{i\varepsilon_0\omega_p^2}{Ne(2\omega+i\gamma)}\mathbf{J}_{\mathrm{Lin}}(\mathbf{r},\omega)\times\mathbf{B}_{\mathrm{loc}}(\mathbf{r},\omega)\\ &-\frac{im^*\omega_p^2\varepsilon_0}{N^2e^3(2\omega+i\gamma)}\left[(\nabla\cdot\mathbf{J}_{\mathrm{Lin}}(\mathbf{r},\omega))\mathbf{J}_{\mathrm{Lin}}(\mathbf{r},\omega)\right.\\ &\left.+(\mathbf{J}_{\mathrm{Lin}}(\mathbf{r},\omega)\cdot\nabla)\mathbf{J}_{\mathrm{Lin}}(\mathbf{r},\omega)\right],\end{aligned} \tag{1}$$

where N, m^*, e, and γ are the density, effective mass, charge, and damping factor of free carriers, respectively. The electric field and magnetic flux density components inside the resonant nanoantenna in the unit cell are described by $\mathbf{E}_{\mathrm{loc}}(\mathbf{r},\omega)$ and $\mathbf{B}_{\mathrm{loc}}(\mathbf{r},\omega)$, respectively, and the linear induced current within the plasmonic nanoantenna is expressed by

$$\mathbf{J}_{\mathrm{Lin}}(\mathbf{r},\omega)=\frac{i}{\omega+i\gamma}\frac{Ne^2}{m^*}\mathbf{E}_{\mathrm{loc}}(\mathbf{r},\omega). \tag{2}$$

The first term of Eq. (1) indicates the non-uniform spatial distribution of carriers, influencing nonlinear processes. The second term arises from the Lorentz force acting on free carriers, specifically strong for objects supporting circularly induced currents, such as highly asymmetric nanoantennae. The last term describes the nonlocal contributions to the nonlinear current, where spatial variations in the free carrier density and velocity lead to a nonlinear response. By utilizing the induced nonlinear current source $\mathbf{J}(\mathbf{r},2\omega)$ within the nanoantenna volume, we apply the Lorentz reciprocity theorem in the following form [46]:

$$\int_V \mathbf{J}(\mathbf{r},2\omega)\cdot\mathbf{E}^{2\omega}(\mathbf{r})\mathrm{d}V=\int_S \mathbf{E}(\mathbf{r},2\omega)\cdot\mathbf{J}^{2\omega}(\mathbf{r})\mathrm{d}S, \tag{3}$$

which links the microscopic nonlinear current $\mathbf{J}(\mathbf{r},2\omega)$ distributed inside the nanoantenna to the emitted SH field $\mathbf{E}(\mathbf{r},2\omega)$ at a virtual monitor surface S placed above the metasurface in free space. For the LSPR-based and bi-layered stack metasurfaces, the monitor plane S is placed 200 nm above the metasurface plane in free space, and for the SLR-based metasurface, it is positioned at the cladding–free-space interface. According to the theory, a virtual surface current $\mathbf{J}^{2\omega}$ is used to excite the unit cell from the monitor in the backward direction, resulting in a potential SH electric field $\mathbf{E}^{2\omega}(\mathbf{r})$ at the nanoantenna surface in the unit cell. Assuming the virtual surface current corresponds to a normally incident plane-wave excitation with amplitude $\mathbf{E}^{2\omega}_{\mathrm{inc}}$, the surface current density can be expressed as $\mathbf{J}^{2\omega}=2\mathbf{E}^{2\omega}_{\mathrm{inc}}/\eta$, where η is the free space impedance [47]. Substituting this into Eq. (3) gives the expression for the emitted SH electric field:

$$\mathbf{E}(\mathbf{r},2\omega)=\frac{\eta}{2S}\int_V\frac{\mathbf{J}(\mathbf{r},2\omega)\cdot\mathbf{E}^{2\omega}(\mathbf{r})}{E^{2\omega}_{\mathrm{inc}}}\mathrm{d}V, \tag{4}$$

where S is the monitor area, equal to the unit cell area of the metasurfaces, and the FW SH intensity is expressed by $\mathrm{I}^{\mathrm{FW}}_{\mathrm{SH}}=\frac{1}{2\eta}|\mathbf{E}(\mathbf{r},2\omega)|^2$ [48].

To model the nonlinear optical response of the plasmonic metasurfaces, we employ the COMSOL Multiphysics software [49], using the Wave Optics module, to find the linear and nonlinear electromagnetic response of the plasmonic system. The gold material parameters [50] used in the model [see Eqs. (1) and (2)], are $\omega_p=1.781\times10^{14}$ rad/s, $N=8.56\times10^{22}$ cm^{-3}, $\gamma=3.35\times10^{13}$ rad/s, and $m^*=7.83\times10^{-29}$ kg. The nonlinear simulation includes a two-step method [51,52]. First, a full-wave frequency-domain simulation is performed to determine the local electromagnetic fields and nonlinear current densities based on the hydrodynamic model, as defined in Eq. (1) at the pump frequency. In the second step, the SH scattered electromagnetic fields are modeled using Lorentz reciprocity. The NL signal emits in all directions, and the SH intensity is obtained by integrating the upward Poynting flux collected by the monitor planes S placed in the free space above the metasurface. In addition to the SH intensity,

Research Article Vol. 43, No. 5 / May 2026 / Journal of the Optical Society of America B 1027

the spatial profile of the nonlinear induced current of $\mathbf{J}(\mathbf{r}, 2\omega)$ is extracted. This two-step modeling process provides a prediction of the SH emission strength of the nonlinear metasurface under plane wave excitation.

3. DESIGN AND RESULTS

In this work, among various asymmetrical nanoantenna geometries, the V-shaped design is chosen as the building block of the proposed SHG plasmonic metasurfaces due to its ability to support spectrally and spatially overlapping LSPRs under both x- and y-polarized excitations [34,53]. The similar V-shaped nanoantennae, with identical geometrical and optical parameters, are employed in the proposed metasurfaces. A linearly polarized plane wave at normal incidence is also used as the excitation source across all simulations to ensure consistent comparisons. The antenna arms are designed with the lengths $l_1 = 125$ nm and $l_2 = 115$ nm, an opening angle of 75°, width $w = 60$ nm, and thickness $h = 30$ nm. Due to the geometry-dependent nature of LSPRs, the dimensions are carefully chosen to support a resonant linear optical response in the near-infrared (NIR) regime while enabling second-harmonic generation in the visible–UV range.

To evaluate the resonant behavior of the nanoantenna, before the metasurface designs, we find the scattering cross-section (SCS) of the single V-shaped antenna in free space under both x- and y-polarized plane wave excitations at normal incidence along the z direction. The SCS is spectrally decomposed based on multipole expansion into electric dipole (ED), magnetic dipole (MD), and electric quadrupole (EQ) modes using the method developed in our previous work [54]. Figure 1 presents the spectral contributions of resonant multipoles to the SCS under both x- and y-polarized excitations. The SCS spectra exhibit a dominant ED resonance centered at approximately 750 nm, with a stronger response under the x-polarized source, as shown in Fig. 1(a), compared to the y-polarized case shown in Fig. 1(b). The near-field profiles at the resonance peaks are also presented for comparison of the spatial characteristics of the resonances. These confirm that the ED-LSPRs are excited around 750 nm under both polarizations, showing strong spatial and spectral overlaps.

As the first platform, we design an LSPR-based SHG metasurface, where the SH emission originates solely from the local-field enhancement provided by the LSPRs of the nanoantennae. In this design, V-shaped gold nanoantennae are arranged periodically on a silica substrate with a refractive index of $n = 1.45$, while the cladding is free space, as shown in Fig. 2(a). The metasurface unit cell has the lattice constants of $a_x = 600$ nm and $a_y = 800$ nm, ensuring the LSPRs remain localized within individual antennae without collective interactions. Under x-polarized plane wave excitation with a propagation direction along the z direction, the transmittance spectrum exhibits a broad ED-LSPR near 1050 nm, characteristic of a low Q-factor, presented in Fig. 2(b). A redshift relative to the free-space resonance of the single nanoantenna, as shown in Fig. 1(a), is observed due to the presence of the substrate. The inset in Fig. 2(b) shows the spatial profile of the electric field at the resonance, revealing strong localization around the antenna tips and within the nano gap. Figure 2(c) displays the wavelength-dependent FW SH intensity I_{SH}^{FW}, collected by the plane monitor S. A prominent peak appears around 525 nm due to the local-field enhancement from LSPRs at the pump wavelength, and the inset of Fig. 2(c) shows the spatial profile of the SH emission intensity. This intensity of the LSPR-based metasurface serves as a reference for evaluating and comparing both the emission strength and its spatial profile in the subsequent metasurface designs.

As the second platform, we design an SLR-based metasurface that features a higher-Q plasmonic resonance, in contrast to the LSPR-based design, which suffers from a broadband resonance with a Q-factor of nearly 3. The higher Q-factor of the second metasurface originates from the constructive far-field coupling of individual LSPRs through in-plane Rayleigh anomaly diffraction, resulting in a collective resonance. The SLR wavelength for the $(i, 0)$ diffraction order is given by [55]

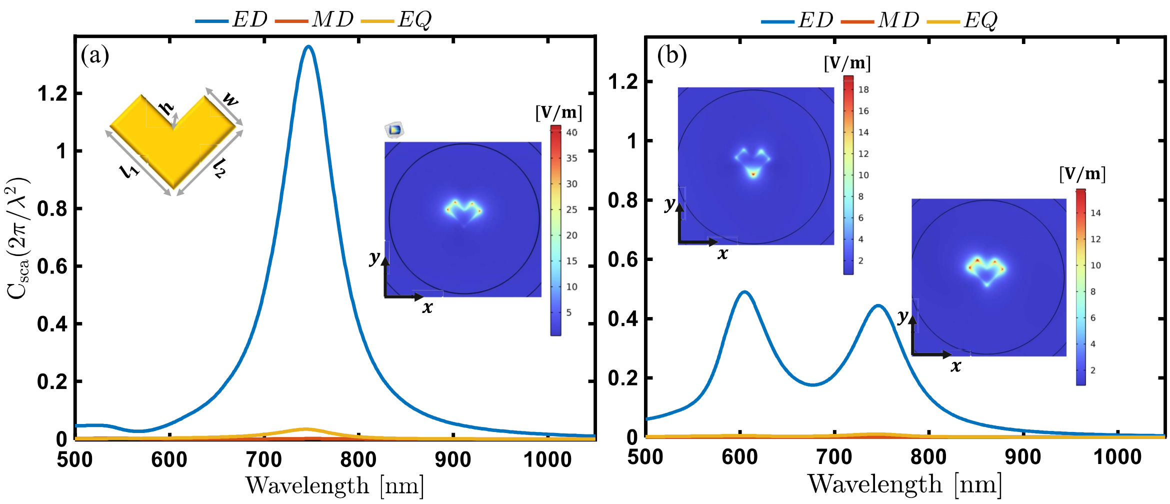

Fig. 1. Linear SCS and near-field profiles of the single V-shaped nanoantenna under (a) x- and (b) y-polarized incident plane wave with a wavevector along the z direction. Dominant ED- and weak EQ-LSPRs appear near 750 nm in both cases, with effective spatial matching. The nanoantenna also supports another strong ED-LSPR at 600 nm under y-polarized excitation, which achieves a hotspot at the bottom of the arms.

1028 Vol. 43, No. 5 / May 2026 / *Journal of the Optical Society of America B* **Research Article**

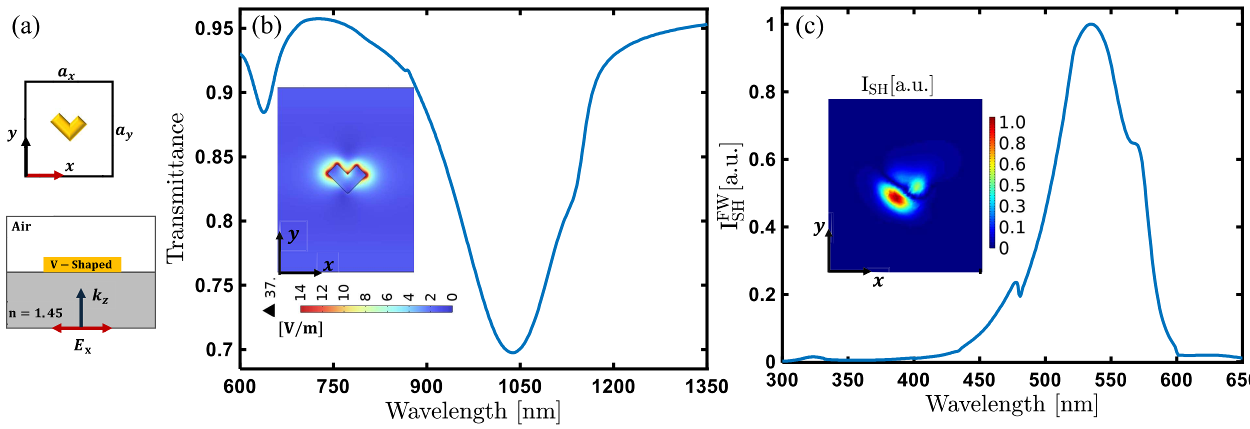

Fig. 2. (a) Unit cell and geometry of the LSPR-based metasurface design composed of asymmetrical V-shaped nanoantennae. (b) Transmittance spectral response shows LSPRs at the pump wavelength of 1050 nm. The inset illustrates the significant local-field enhancement resulting from the resonance. (c) The FW SH emission intensity of the metasurface with the SH response at 525 nm, and the inset presents the spatial profile of the SH intensity.

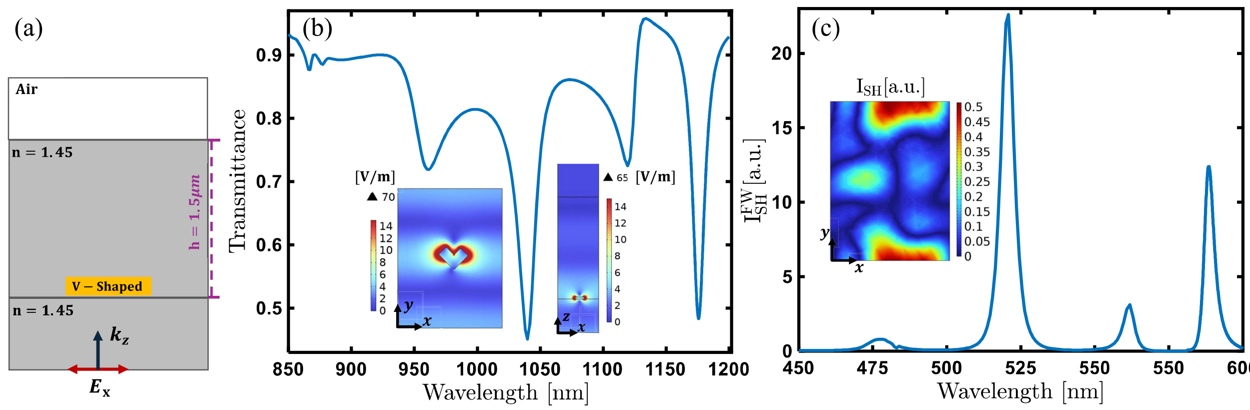

Fig. 3. (a) Schematic of the metasurface composed of V-shaped nanoantennae embedded in a uniform-index environment with a thick silica cladding of $h = 1.5$ μm. (b) Linear transmittance spectrum showing the lattice resonance with Q = 90 at the pump wavelength of 1050 nm, with insets showing the electric-field profiles in the $x - y$ and $x - z$ planes. These reveal strong light confinement and standing-wave behavior near the metasurface. (c) Forward SH intensity spectrum demonstrates enhanced emission near 525 nm due to the SLR, a 20-fold intensity increase compared to the LSPR-based design. The inset shows reduced spatial resolution due to emission distortion caused by the thick cladding.

$$\lambda_{\mathrm{SLR}}^{(i,0)} = a_y \left(\frac{n}{|i|} - \frac{\sin(\theta)}{i} \right), \tag{5}$$

where $i = 1$ corresponds to a lattice resonance along the x direction, n is the refractive index of the surrounding medium, and θ is the angle of incidence, which is set to zero in this study. The metasurface unit cell has lattice constants $a_x = 600$ nm and $a_y = 800$ nm. The cladding thickness is set to $h = 1.5$ μm to support multiple lattice resonances [56,57], which enables achieving a high-Q plasmonic resonance within the targeted pump wavelength range. Figure 3(a) shows the SLR-based metasurface, where the V-shaped nanoantennae are embedded in a uniform refractive index environment with $n = 1.45$. The metasurface is illuminated by the normally incident x-polarized plane wave from the substrate along the z direction, and the FW SH response is collected at the interface of the cladding thickness and free space.

As shown in Fig. 3(b), the transmittance spectrum demonstrates multiple resonances due to Fabry–Perot-like behavior arising from the thick cladding. Among them, we focus on a lattice resonance with a Q-factor of 90, centered near 1050 nm, which can act as the pump wavelength range. The insets in Fig. 3(b) show the local electric-field distributions in the $x - y$ and $x - z$ planes, highlighting the lattice field confinement near the metasurface plane. This standing-wave-like field distribution significantly enhances light–matter interaction time, thereby enhancing the SHG process. The corresponding FW SH intensity spectrum is presented in Fig. 3(c). Due to the multi-resonant nature of the structure, the response exhibits multiple peaks, with a dominant signal emerging near 525 nm. Remarkably, the FW SH intensity is enhanced 20 times compared to the LSPR-based metasurface. However, the spatial profile of the emission intensity deforms at low resolution, making it difficult to resolve the nanoantenna's orientation. This is caused by the thick cladding layer that distorts the spatial pattern by confining the SH emission within the cladding and suppressing out-coupling into free space [38,58].

Research Article Vol. 43, No. 5 / May 2026 / Journal of the Optical Society of America B 1029

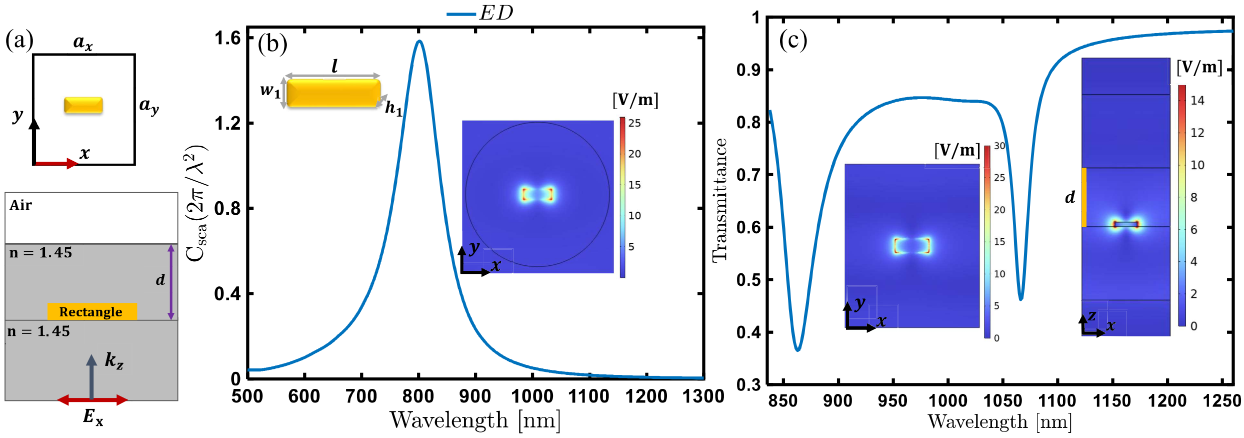

Fig. 4. (a) Schematic of the linear metasurface composed of the periodic array of gold nanobars embedded in the uniform refractive index background of $n = 1.45$, the lattice constants of $a_x = 600$ nm and $a_y = 731$ nm, and the cladding thickness of $d = 400$ nm. (b) Scattering spectrum of the single bar nanoantenna showing a broad ED-LSPR centered around 800 nm. (c) Transmittance spectrum of the metasurface, exhibiting an SLR with Q = 100 at the pump wavelength range around 1060 nm. Insets display electric-field distributions in the $x - y$ and $x - z$ cross-sectional planes, highlighting strong field confinement in the spacer region above the metasurface.

As the final platform, we design a bi-layered plasmonic metasurface composed of two functionally distinct layers. The bottom layer consists of a centrosymmetric array of gold nanobars engineered to support a high-Q SLR at the pump wavelength. This passive metasurface acts as a linear field amplifier, generating a collective resonance that significantly enhances the local electromagnetic field within the spacer region without contributing to the nonlinear response. Before designing the full stack, we first engineer the lower linear metasurface to ensure maximum amplification of the pump light interacting with the upper nonlinear layer. For this purpose, bar nanoantennae with dimensions $l = 150$ nm, $w_1 = 60$ nm, and $h_1 = 30$ nm are selected as the building blocks. Figure 4(b) illustrates the SCS of a single bar nanoantenna, which supports a broad ED-LSPR centered at 800 nm under the x-polarized plane wave excitation with the wavevector along the z direction. The configuration of the bar nanoantennae in a periodic array is shown in Fig. 4(a), where the metasurface is sandwiched between the substrate and a spacer layer of thickness d. This spacer layer serves as the cladding for the lower metasurface and, simultaneously, as the substrate for the upper layer in the full stack design. The lattice constants are set to $a_x = 600$ nm and $a_y = 731$ nm, and the nanobar array is embedded in a uniform refractive index environment with $n = 1.45$ to excite an SLR within the targeted pump wavelength range under the defined plane wave excitation. For the single-layer bar metasurface, the spacer thickness is set to $d = 400$ nm to illustrate the electric-field profile of the SLR mode, which is uniformly distributed around the bar metasurface plane. As shown in Fig. 4(c), the transmittance spectrum exhibits an SLR with a Q-factor of 100, centered around the resonance wavelength of 1060 nm. The insets of Fig. 4(c) show the electric-field profiles in the $x - y$ and $x - z$ cross-sectional planes, confirming strong field confinement near the metasurface plane within the spacer layer. The $x - z$ field profile highlights the vertical extent of the SLR-enhanced electric field supported by the bar metasurface, which plays a key role in defining the effective interaction zone [59] for the bi-layered stack design.

The upper layer consists of a nonlinear metasurface composed of V-shaped gold nanoantennae, positioned above the linear metasurface and separated by a spacer layer of thickness d, as shown in Fig. 5(a). Similar to the previous metasurfaces, the stack metasurface is excited by an x-polarized plane wave propagating along the z direction. The lattice constants are $a_x = 600$ nm and $a_y = 731$ nm, identical to those used for the bar metasurface. In this configuration, the upper metasurface supports a broadband LSPR within the pump wavelength range and spectrally close to the SLR supported by the lower metasurface, as shown in Fig. 4(c). Consequently, the spacer thickness d plays a critical role in governing both the SLR response of the lower layer (in the presence of the upper layer) and the strength of the vertical coupling between the two metasurfaces.

Figure 5(b) presents the transmission spectra of the stack metasurface for various spacer thicknesses. For $d = 100$ nm, the spacer is too thin to sustain a well-defined SLR in the lower metasurface, and the response is dominated by the broadband LSPR of the V-shaped metasurface, centered near 1050 nm. As the spacer thickness increases, the lower metasurface supports an SLR that can couple efficiently to the upper nonlinear metasurface. For $d = 200$, 300, and 350 nm, this interaction produces a split spectral response comprising a narrow, Fano-like resonance near 1090 nm together with a broader feature spanning approximately 1000–1050 nm. The narrow resonance mode reaches a Q-factor of 73 at $d = 200$ nm, indicating strong LSPR–SLR vertical interaction. As d increases to 350 nm, the narrow resonance weakens, slightly redshifts, and the separation between the split resonances decreases. For $d = 400$ nm, the splitting largely disappears, and the spectrum blueshifts toward the parent SLR mode of the lower metasurface near 1060 nm. This behavior confirms that, at larger thicknesses of the spacer layer, the coupling between the two layers diminishes, and hence the enhanced SLR field remains confined near the lower metasurface plane and does not efficiently excite the nonlinear

1030 Vol. 43, No. 5 / May 2026 / Journal of the Optical Society of America B Research Article

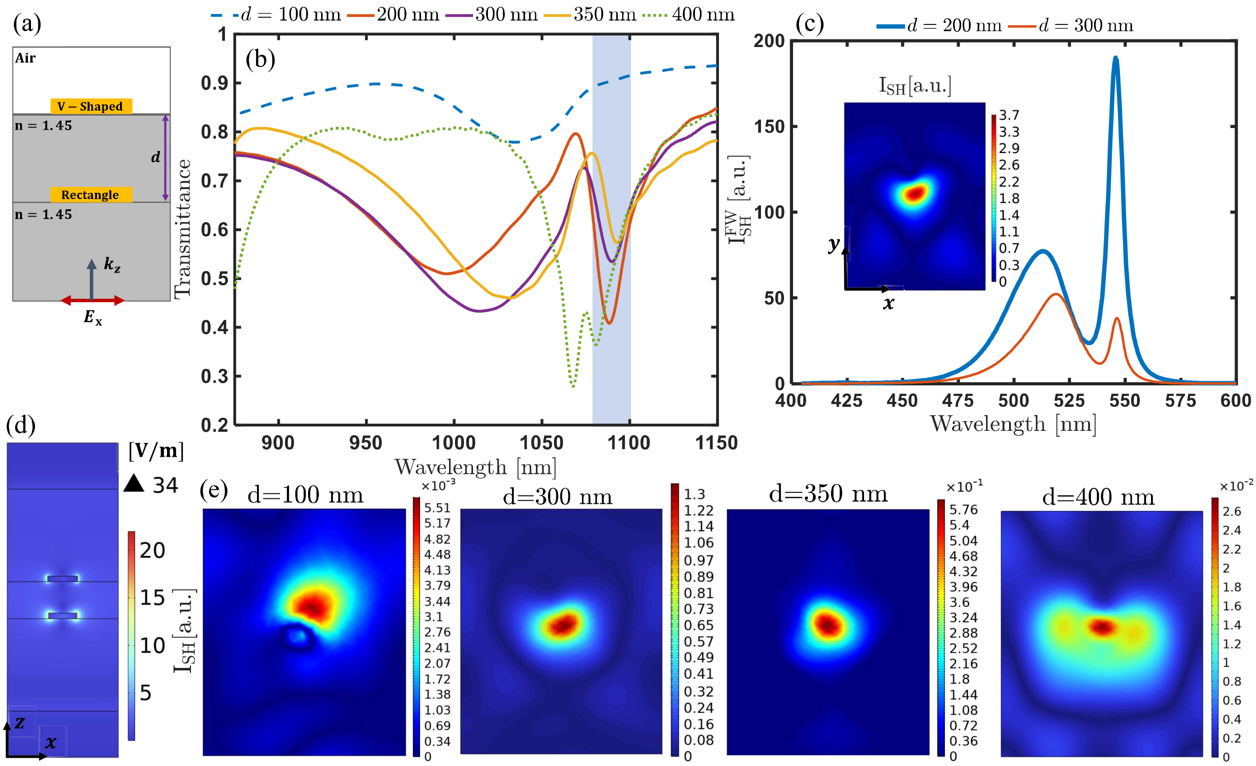

Fig. 5. (a) Bi-layered plasmonic metasurface consisting of a bottom linear metasurface and an upper nonlinear metasurface, separated by a spacer layer of thickness d and excited by a plane-wave source incident from the substrate. (b) Transmittance spectra of the stacked metasurface for different spacer thicknesses, showing narrow resonances around 1090 nm with a dominant response for $d = 200$ nm. (c) FW SH intensity of the bi-layered metasurface for two spacer thicknesses, demonstrating an approximately 200× enhancement factor in SH response compared to the LSPR-based metasurface. The inset shows the near-field SH intensity within the metasurface unit cell for $d = 200$ nm. (d) Electric-field profile in the $x - z$ plane at the resonance wavelength of 1090 nm for $d = 200$ nm. (e) Spatial profiles of the near-field SH intensity within the metasurface unit cell for different spacer thicknesses.

upper metasurface. To evaluate the maximum enhancement of the FW SH response, we focus on spacer thicknesses of $d = 200$ and 300 nm, which both exhibit a narrow resonance centered around 1090 nm, enabling a direct comparison under nearly identical spectral conditions, as highlighted in Fig. 5(b).

Figure 5(c) shows the FW SH emission for $d = 200$ nm and $d = 300$ nm. At $d = 200$ nm, the SHG response reaches an enhancement of approximately 200× compared to the LSPR-based metasurface, with a strong SH peak near 545 nm, corresponding to the narrow resonance near 1090 nm. When the spacer thickness increases to $d = 300$ nm, the SHG intensity decreases significantly, consistent with weaker vertical coupling and reduced local-field enhancement in the nonlinear metasurface. This reduction arises because the SLR electric field becomes increasingly confined near the lower metasurface plane as the cladding or spacer thickness increases, limiting the field overlap with the upper nonlinear layer. The inset of Fig. 5(c) shows the SH near-field intensity profile for $d = 200$ nm, confirming improved spatial resolution of the V-shaped nanoantenna compared to the LSPR-based metasurface. Figure 5(d) presents the $x - z$ plane electric-field distribution at the resonance wavelength of 1090 nm for $d = 200$ nm, showing that the SLR field confined in the lower layer couples upward to excite the LSPR of the V-shaped nanoantennae.

Finally, Fig. 5(e) compares the near-field SH intensity profiles at 545 nm for different spacer thicknesses. For $d = 300$ nm, the spatial pattern of the V-shaped nanoantenna remains resolvable with sufficient contrast, whereas at $d = 350$ nm, the pattern is still distinguishable but with reduced resolution. In contrast, for $d = 100$ nm and $d = 400$ nm, both the SH intensity and spatial resolution deteriorate markedly, consistent with the resonance shifting away from 1090 nm as observed in the transmittance spectra. Overall, these results demonstrate that efficient vertical LSPR–SLR coupling yields a spectrally narrow, Fano-like resonance near the pump wavelength (1090 nm) for spacer thicknesses in the range of 200–350 nm. While this narrow spectral response persists across this range, it weakens as d increases, leading to a significantly reduced FW SH response from the upper nonlinear metasurface. Consequently, the optimal SHG enhancement and near-field resolution are achieved at $d = 200$ nm.

The emitted SH signal of the stack metasurface originates from the local current sources distributed across the nanoantenna induced by the enhanced pump field, as defined in Eq. (1). Figure 6 presents the spatial profiles of the current components over the V-shaped nanoantenna placed within the stack unit cell. The results show that J_y^{SH} is the dominant component, while J_z^{SH} contributes moderately and J_x^{SH} remains minimal.

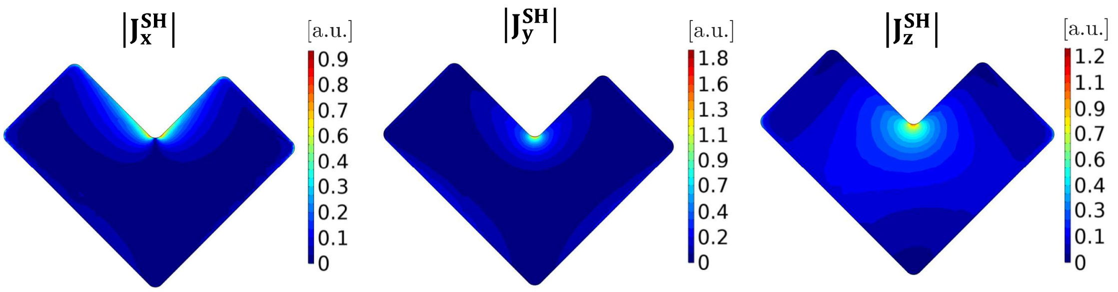

Fig. 6. Distribution profiles of SH current components of J_x^{SH}, J_y^{SH}, and J_z^{SH} induced on the V-shaped antenna located in the stack metasurface's unit cell.

Table 1. Comparison of SHG Enhancement Factors Reported for Different Platforms[a]

Ref.	Structure	Mechanism	Emission Direction	Enhancement
[60]	WSe_2 on gold trenches	Surface plasmon wave	BW	7000
[61]	WS_2 on silicon metasurface	Quasi-BIC	Not stated	1140
[31]	Plasmonic metasurface	SLR	Not stated	450
Our work	Plasmonic metasurface	LSPR + SLR	FW	200
[62]	Split-ring resonator	SLR	Not stated	30
[63]	Plasmonic metasurface	LSPR	FW	10

[a]FW and BW denote forward and backward emission, respectively.

4. CONCLUSION

The efficiency and spatial resolution of SHG emission in plasmonic metasurfaces are strongly determined by how resonant near-field confinement and emission outcoupling are engineered. To address this, we investigated three platforms, an LSPR-based metasurface, an SLR-based metasurface, and a bi-layered stack metasurface under identical material properties, background refractive indices, and excitation conditions to ensure a consistent comparison. The in-plane lattice constants are selected for each platform to place its dominant plasmonic resonance within the same pump wavelength range. In particular, for the bi-layered stack metasurface, the lattice constants are intentionally engineered to realize a high-Q SLR around the pump wavelength and to maintain spectral alignment with the LSPR of the nonlinear metasurface, required for the efficient vertical LSPR-SLR coupling. The LSPR-based metasurface achieved strong local-field enhancement but limited FW emission, while the SLR-based platform achieved higher-Q resonances at the cost of reduced near-field resolution due to dielectric embedding. In contrast, the stack plasmonic metasurface utilized the advantages of both, where a passive SLR-supporting nanobar layer amplified the pump field and an upper nonlinear V-shaped antenna layer converted this energy into FW SH emission. Optimized vertical coupling through the spacer enabled efficient FW outcoupling and strong near-field resolution. This bi-layered design achieved a 200× raise in FW SH intensity and enhanced near-field resolution compared to the LSPR case while avoiding the emission blurring characteristic of the SLR configuration.

Table 1 summarizes the SHG enhancement factors reported for representative platforms. Hybrid structures based on two-dimensional (2D) materials, such as tungsten diselenide (WSe_2), can provide very large SHG enhancement. However, in [60], the enhanced SH signal was collected in the backward direction, which may be less attractive for bio-compatible SHG microscopy applications. The hybrid platform consisting of a 2D material integrated with a dielectric metasurface supporting a high-Q quasi-BIC resonance, as reported in [61], also exhibits a very high enhancement factor and has been proposed as a promising platform for SHG microscopy applications. In contrast, the SLR-based SH enhancement reported for a plasmonic metasurface in [31] was demonstrated in an SHG spectroscopy configuration. In our work, the proposed bi-layered metasurface already provides a strong FW SH response and is designed within a framework that supports systematic scalability of the enhancement factor. Specifically, the upper metasurface can be redesigned as a supercell containing multiple V-shaped nanoantennae while preserving the lattice constants required for the SLR of the lower layer. This would introduce near-field hybridization among the upper-layer antennae, which are driven by the strong and spatially extended pump field generated by the SLR supported in the lower metasurface, and could therefore lead to an even larger FW SH enhancement.

The analysis of the induced nonlinear current components further revealed that J_y dominates over J_x and J_z. Overall, the bi-layered stack plasmonic metasurface demonstrates an efficient method to overcome the trade-offs of planar metasurface designs, realizing both enhanced FW emission and near-field resolution. These results highlight the strong potential of the proposed platform for near-field SHG microscopy, enabling the local probing of the SH response of biomolecules within the hotspot region generated by the plasmonic nanoantenna in the upper metasurface.

Funding. NSERC CREATE TrUST program; NSERC Discovery Grant; Ontario Early Researchers Award; Canada Research Chairs).

Acknowledgment. K. Dolgaleva acknowledges project funding through the NSERC CREATE TrUST program, NSERC Discovery Grant, the Ontario Early Researchers Award, and Canada Research Chairs.

Disclosures. The authors declare no conflicts of interest.

Data availability. Data underlying the results presented in this paper are not publicly available at this time but may be obtained from the authors upon reasonable request.

Supplemental document. See Supplement 1 for supporting content.

REFERENCES

1. M. Kauranen and A. V. Zayats, "Nonlinear plasmonics," Nat. Photonics **6**, 737–748 (2012).
2. M. J. Huttunen, R. Czaplicki, and M. Kauranen, "Nonlinear plasmonic metasurfaces," J. Nonlinear Opt. Phys. Mater. **28**, 19500012 (2019).
3. S. Zhang, L. Liu, S. Ren, *et al.*, "Recent advances in nonlinear optics for bio-imaging applications," Opto-Electron. Adv. **3**, 200003 (2020).
4. P. Pantazis, J. Maloney, D. Wu, *et al.*, "Second harmonic generating (shg) nanoprobes for in vivo imaging," Proc. Natl. Acad. Sci. **107**, 14535–14540 (2010).
5. D. A. Dombeck, K. A. Kasischke, H. D. Vishwasrao, *et al.*, "Uniform polarity microtubule assemblies imaged in native brain tissue by second-harmonic generation microscopy," Proc. Natl. Acad. Sci. **100**, 7081–7086 (2003).
6. G. Deka, C.-K. Sun, K. Fujita, *et al.*, "Nonlinear plasmonic imaging techniques and their biological applications," Nanophotonics **6**, 31–49 (2017).
7. P. W. Baas, J. S. Deitch, M. M. Black, *et al.*, "Polarity orientation of microtubules in hippocampal neurons: uniformity in the axon and nonuniformity in the dendrite," Proc. Natl. Acad. Sci. **85**, 8335–8339 (1988).
8. A. Aghigh, S Bancelin, M. Rivard, *et al.*, "Second harmonic generation microscopy: a powerful tool for bio-imaging," Biophys. Rev. **15**, 43–70 (2023).
9. S. Aghili, S. Golmohammadi, and A. Amini, "Proposing an on/off optical router in telecom wavelength using plasmonic tweezer," Opt. Commun. **427**, 95–100 (2018).
10. A. Amini, S. Golmohammadi, and S. Aghili, "Plasmonic response of graphene-like metallic-molecular nanocluster for optical applications," Opt. Eng. **57**, 077104 (2018).
11. J. Butet, P.-F. Brevet, and O. J. F. Martin, "Optical second harmonic generation in plasmonic nanostructures: from fundamental principles to advanced applications," ACS Nano **9**, 10545–10562 (2015).
12. R. Kolkowski, T. K. Hakala, A. Shevchenko, *et al.*, "Nonlinear nonlocal metasurfaces," Appl. Phys. Lett. **122**, 160502 (2023).
13. C. Schlickriede, N. Waterman, B. Reineke, *et al.*, "Imaging through nonlinear metalens using second harmonic generation," Adv. Mater. **30**, 1703843 (2018).
14. M. B. Alexandre Bouhelier, A. Hartschuh, and L. Novotny, "Near-field second-harmonic generation induced by local field enhancement," Phys. Rev. Lett. **90**, 013903 (2003).
15. B. Shen, L. Liu, Y. Li, *et al.*, "Nonlinear spectral-imaging study of second-and third-harmonic enhancements by surface-lattice resonances," Adv. Opt. Mater. **8**, 1901981 (2020).
16. Y. Chu, M. G. Banaee, and K. B. Crozier, "Double-resonance plasmon substrates for surface-enhanced raman scattering with enhancement at excitation and stokes frequencies," ACS Nano **4**, 2804–2810 (2010).
17. S. Linden, F. B. P. Niesler, J. Förstner, *et al.*, "Collective effects in second-harmonic generation from split-ring-resonator arrays," Phys. Rev. Lett. **109**, 015502 (2012).
18. B. K. Canfield, H. Husu, J. Laukkanen, *et al.*, "Local field asymmetry drives second-harmonic generation in noncentrosymmetric nanodimers," Nano Lett. **7**, 1251–1255 (2007).
19. R. Czaplicki, A. Kiviniemi, M. J. Huttunen, *et al.*, "Less is more: enhancement of second-harmonic generation from metasurfaces by reduced nanoparticle density," Nano Lett. **18**, 7709–7714 (2018).
20. M. S. Bin-Alam, J. Baxter, K. M. Awan, *et al.*, "Hyperpolarizability of plasmonic meta-atoms in metasurfaces," Nano Lett. **21**, 51–59 (2020).
21. Y. Gao, Y. Fan, Y. Wang, *et al.*, "Nonlinear holographic all-dielectric metasurfaces," Nano Lett. **18**, 8054–8061 (2018).
22. M. R. Shcherbakov, D. N. Neshev, B. Hopkins, *et al.*, "Enhanced third-harmonic generation in silicon nanoparticles driven by magnetic response," Nano Lett. **14**, 6488–6492 (2014).
23. Y. Kivshar, "All-dielectric meta-optics and non-linear nanophotonics," Natl. Sci. Rev. **5**, 144–158 (2018).
24. W. Tang, Q. Zhao, Z. Wang, *et al.*, "Realizing high-efficiency third harmonic generation via accidental bound states in the continuum," Opt. Lett. **49**, 1169–1172 (2024).
25. K. Koshelev, G. Favraud, A. Bogdanov, *et al.*, "Nonradiating photonics with resonant dielectric nanostructures," Nanophotonics **8**, 725–745 (2019).
26. M. Caldarola, P. Albella, E. Cortés, *et al.*, "Non-plasmonic nanoantennas for surface enhanced spectroscopies with ultra-low heat conversion," Nat. Commun. **6**(1), 7915 (2015).
27. J. Van de Groep and A. Polman, "Designing dielectric resonators on substrates: combining magnetic and electric resonances," Opt. Express **21**, 26285–26302 (2013).
28. M. J. Huttunen, P. Rasekh, R. W. Boyd, *et al.*, "Using surface lattice resonances to engineer nonlinear optical processes in metal nanoparticle arrays," Phys. Rev. A **97**, 053817 (2018).
29. M. J. Huttunen, O. Reshef, T. Stolt, *et al.*, "Efficient nonlinear metasurfaces by using multiresonant high-q plasmonic arrays," J. Opt. Soc. Am. B **36**, E30–E35 (2019).
30. M. S. Bin-Alam, O. Reshef, R. N. Ahmad, *et al.*, "Cross-polarized surface lattice resonances in a rectangular lattice plasmonic metasurface," Opt. Lett. **47**, 2105–2108 (2022).
31. D. C. Hooper, C. Kuppe, D. Wang, *et al.*, "Second harmonic spectroscopy of surface lattice resonances," Nano Lett. **19**, 165–172 (2018).
32. K. Thyagarajan, S. Rivier, A. Lovera, *et al.*, "Enhanced second-harmonic generation from double resonant plasmonic antennae," Opt. Express **20**, 12860–12865 (2012).
33. K.-Y. Yang, J. Butet, C. Yan, *et al.*, "Enhancement mechanisms of the second harmonic generation from double resonant aluminum nanostructures," Acs Photonics **4**, 1522–1530 (2017).
34. R. Czaplicki, H. Husu, R. Siikanen, *et al.*, "Enhancement of second-harmonic generation from metal nanoparticles by passive elements," Phys. Rev. Lett. **110**, 093902 (2013).
35. J. Sperrhake, M. Decker, M. Falkner, *et al.*, "Analyzing the polarization response of a chiral metasurface stack by semi-analytic modeling," Opt. Express **27**, 1236–1248 (2019).
36. J. Sperrhake, M. Falkner, M. Steinert, *et al.*, "Experimental validation of the fundamental mode approximation for stacked metasurfaces and its application to the treatment of arbitrary period ratios," APL Photonics **6**, 096109 (2021).
37. C. Menzel, C. Helgert, E.-B. K. Carsten Rockstuhl, *et al.*, "Asymmetric transmission of linearly polarized light at optical metamaterials," Phys. Rev. Lett. **104**, 253902 (2010).
38. T. Stolt, J. Kim, S. Héron, *et al.*, "Backward phase-matched second-harmonic generation from stacked metasurfaces," Phys. Rev. Lett. **126**, 033901 (2021).
39. K. Achouri, Y. Vahabzadeh, and C. Caloz, "Mathematical synthesis and analysis of nonlinear metasurfaces," arXiv (2017).
40. S. A. Jalil, K. M. Awan, J. Baxter, *et al.*, "Spectroscopic signatures of plasmonic near-fields on high-harmonic emission," Laser Photonics Rev. **17**, 2300448 (2023).
41. J. Baxter, A. C. Lesina, and L. Ramunno, "Hyperpolarizability of plasmonic nanostructures: a method to quantify," in *Light-Matter Interactions Towards the Nanoscale* (2022), p. 243.
42. C. Ciracì, E. Poutrina, M. Scalora, *et al.*, "Origin of second-harmonic generation enhancement in optical split-ring resonators," Phys. Rev. B—Condens. Matter Mater. Phys. **85**, 201403 (2012).
43. E. Rahimi and R. Gordon, "Nonlinear plasmonic metasurfaces," Adv. Opt. Mater. **6**, 1800274 (2018).
44. J. S. Gomez-Diaz, M. Tymchenko, J. Lee, *et al.*, "Nonlinear processes in multi-quantum-well plasmonic metasurfaces: electromagnetic response, saturation effects, limits, and potentials," Phys. Rev. B **92**, 125429 (2015).
45. T. Zahedi, Z. H. Firouzeh, and A. Z. Nezhad, "Design and modeling of third-harmonic plasmonic metasurfaces coupled to multi-quantum well structures," J. Opt. Soc. Am. B **36**, 2429–2437 (2019).
46. J. Lee, "Nonlinear and wavelength-tunable plasmonic metasurfaces and devices," PhD thesis (2014).

Research Article **Vol. 43, No. 5 / May 2026 / *Journal of the Optical Society of America B*** **1033**

47. C. A. Balanis, *Balanis' Advanced Engineering Electromagnetics* (John Wiley & Sons, 2024).
48. R. W. Boyd, A. L. Gaeta, and E. Giese, "Nonlinear optics," in *Springer Handbook of Atomic, Molecular, and Optical Physics* (Springer, 2008), pp. 1097–1110.
49. COMSOL, "COMSOL Multiphysics v6.2," (2024) https://www.comsol.com.
50. D. Krause, C. W. Teplin, and C. T. Rogers, "Optical surface second harmonic measurements of isotropic thin-film metals: gold, silver, copper, aluminum, and tantalum," J. Appl. Phys. **96**, 3626–3634 (2004).
51. K. O'Brien, H. Suchowski, J. Rho, *et al.*, "Predicting nonlinear properties of metamaterials from the linear response," Nat. Mater. **14**, 379–383 (2015).
52. E. Mobini, R. Alaee, R. W. Boyd, *et al.*, "Giant asymmetric second-harmonic generation in bianisotropic metasurfaces based on bound states in the continuum," ACS Photonics **8**, 3234–3240 (2021).
53. A. Verneuil, A. Di Francescantonio, A. Zilli, *et al.*, "Far-field mapping and efficient beaming of second harmonic by a plasmonic metagrating," Nanophotonics **13**, 3609–3614 (2024).
54. S. Aghili, R. Alaee, A. Ahmadnejad, *et al.*, "Dynamic control of spontaneous emission using magnetized InSb higher-order-mode antennas," J. Phys. Photonics **6**, 035011 (2024).
55. A. Movsesyan, L. V. Besteiro, X.-T. Kong, *et al.*, "Engineering strongly chiral plasmonic lattices with achiral unit cells for sensing and photodetection," Adv. Opt. Mater. **10**, 2101943 (2022).
56. S. Aghili, A. Amini, L. S. Dizaj, *et al.*, "THz plasmonic metasurface based on a periodic array of InSb metamolecules with narrow resonances," Opt. Commun. **508**, 127805 (2022).
57. M. S. Bin-Alam, O. Reshef, M. Z. A. Yaryna Mamchur, *et al.*, "Ultra-high-Q resonances in plasmonic metasurfaces," Nat. Commun. **12**, 974 (2021).
58. K. Koshelev, Y. Tang, K. Li, *et al.*, "Nonlinear metasurfaces governed by bound states in the continuum," Acs Photonics **6**, 1639–1644 (2019).
59. Y. Zeng, H. Qian, M. J. Rozin, *et al.*, "Enhanced second harmonic generation in double-resonance colloidal metasurfaces," Adv. Funct. Mater. **28**, 1803019 (2018).
60. Z. Wang, Z. Dong, H. Zhu, *et al.*, "Selectively plasmon-enhanced second-harmonic generation from monolayer tungsten diselenide on flexible substrates," ACS Nano **12**, 1859–1867 (2018).
61. N. Bernhardt, K. Koshelev, S. J. U. White, *et al.*, "Quasi-bic resonant enhancement of second-harmonic generation in ws_2 monolayers," Nano Lett. **20**, 5309–5314 (2020).
62. L. Michaeli, S. Keren-Zur, O. Avayu, *et al.*, "Nonlinear surface lattice resonance in plasmonic nanoparticle arrays," Phys. Rev. Lett. **118**, 243904 (2017).
63. R. Czaplicki, A. Kiviniemi, J. Laukkanen, *et al.*, "Surface lattice resonances in second-harmonic generation from metasurfaces," Opt. Lett. **41**, 2684–2687 (2016).

Chapter 7

Higher-Order Waveguide Bragg Gratings for DFB Lasers

7.1 Introduction

In previous chapters, we studied how resonant meta-atoms shape light–matter interaction for linear and nonlinear functions at deeply sub-wavelength scales. In contrast, this chapter focuses on waveguides as engineered multilayer structures that confine and transport optical power with manageable loss and dispersion. Fig. 7.1 presents a symmetric slab waveguide with refractive indices $n_1 > n_2$, where n_1 is the core index and n_2 is the cladding index. An optical wave propagating in the core region with higher index can be described by [210]

$$\mathbf{E}(\mathbf{r}, t) = \hat{\mathbf{s}}\, E_0(x, y)\, A(z, t)\, \mathrm{e}^{j\,(\beta_0 z - \omega_0 t)}\,, \tag{7.1}$$

where $\hat{\mathbf{s}}$ denotes the unit vector along the polarization direction governed by the electric field distribution $E_0(x, y)$ in the transverse plane, and $A(z, t)$ is the envelope function of the longitudinal field with propagation constant β_0 along the z-direction. The factor $e^{\mathrm{j}(\beta_0 z - \omega_0 t)}$ represents a plane wave traveling with phase velocity ω_0/β_0 [79]. The time-invariant transverse E-field $E_0(x, y)$ satisfies the scalar wave equation

$$\left(\frac{\partial^2}{\partial x^2} + \frac{\partial^2}{\partial y^2}\right) E_0(x, y) + k_0^2 n^2(x, y, \omega_0)\, E_0(x, y) = \beta_0^2\, E_0(x, y)\,, \tag{7.2}$$

corresponding to a propagation constant defined as $\beta_0 = k_0 n_{\mathrm{eff}}$, where the effective index n_{eff} satisfies $n_2 < n_{\mathrm{eff}} < n_1$. This wave equation admits multiple solutions (E_0, β_0), comprising guided and leaky modes. For

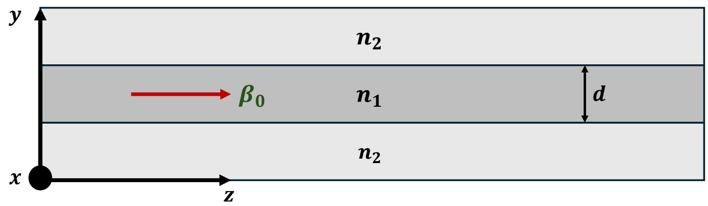

FIGURE 7.1: Schematic of the symmetric slab waveguide structure with core refractive index n_1 and cladding refractive indices n_2. The optical field propagates along the z-axis with a propagation constant β_0.

guidance to occur, the following quantities must be positive [211]

$$k_0^2 n_1^2 - \beta_0^2 \; > \; 0, \qquad \beta_0^2 - k_0^2 n_2^2 \; > \; 0, \tag{7.3}$$

ensuring standing wave oscillation in the core region and evanescent decay in the cladding. By defining the core thickness of d, as

$$0 \; < \; d \; < \; \frac{\lambda}{2}\left(n_1^2 - n_2^2\right)^{-1/2}, \tag{7.4}$$

the waveguide supports only one eigenfunction, known as the transverse electric (TE) fundamental mode, with a dominant E-field component along the x-direction [211].

By placing reflective mirrors at both ends of the core layer as the guided region, the slab waveguide acts as a Fabry–Perot (FP) cavity that provides optical feedback for semiconductor laser sources. In this configuration, the optical field resonates between the two facet mirrors along the z-direction and the cavity resonant frequency is described by

$$f_m = \frac{mc}{2\, n_{\text{eff}}\, L}, \tag{7.5}$$

where m is an integer representing the longitudinal mode number and L is the cavity length. As m increases, the FP cavity supports multiple longitudinal modes, with a frequency spacing of $\delta f = c/(2n_{\text{eff}}L)$. Since the facet mirrors lack wavelength selectivity, these resonant modes at different frequencies can oscillate simultaneously and emit through the output facet with lower reflectivity. Due to the overlap of these modes with the inherently broad stimulated emission spectrum of the semiconductor gain medium, the FP cavity exhibits multi-mode behavior, resulting in a wide spectral output characteristic of FP-based semiconductor lasers.

7.2 Waveguide Bragg Gratings

The growing demand for bandwidth-hungry applications and high-speed data access has shifted attention toward semiconductor lasers with narrow spectral emission in the telecommunication wavelength windows. Dispersion in optical fibers causes temporal broadening of optical signals during long-haul transmission. Consequently, coherent optical communication systems require laser sources that operate in continuous-wave (CW) mode. This condition is achieved by maintaining single-mode oscillation in both the transverse and longitudinal directions.

The principle of population inversion of free carriers in excited states, which provides stimulated optical gain, is common to all semiconductor laser diodes. The distinction between different types of semiconductor lasers arises from the cavity design, as the cavity defines optical feedback mechanism, governs modal selectivity, and controls spectral purity. Distributed-feedback (DFB) lasers employ wavelength-selective cavities that enable narrow band emission and precise control of the lasing spectrum. These properties make DFB lasers superior to FP lasers, which rely on facet mirrors for optical feedback and typically support multiple longitudinal modes.

In DFB structures, the cavity is formed by a waveguide Bragg grating (WBG), as shown in Fig. 7.2. A periodic corrugation is embedded into the slab waveguide along the propagation direction. This configuration ensures that only wavelength components close to the Bragg resonance condition can build up inside the cavity. The WBG thus acts as a narrow band-pass filter, suppressing undesired wavelength components far from the Bragg wavelength. In this case, the lasing wavelength is determined by the Bragg condition [211], as

$$\lambda = \frac{2\Lambda n_{\text{eff}}}{M}, \tag{7.6}$$

where Λ is the grating period, and M denotes the grating order. This relation also describes the Bragg resonance wavelength($\lambda \approx \lambda_B$), which is directly proportional to the grating period and inversely proportional to the grating order.

First-order WBGs are the standard choice for most DFB laser designs because they provide strong optical feedback for the fundamental mode with minimal radiation loss [77]. In the first-order WBG, the optical field propagates along the longitudinal direction and diffracts directly backward along $-z$,

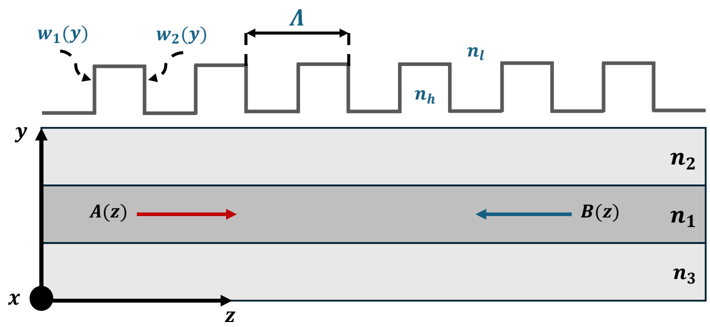

FIGURE 7.2: Schematic of a WBG showing forward and backward guided waves $A(z)$ and $B(z)$ within the guide region or cavity. The grating period Λ and edge functions $w_1(y)$ and $w_2(y)$ define the refractive index modulation between n_h and n_l.

establishing the feedback necessary for amplification. However, implementing a first-order grating at telecom wavelength range is challenging, as the short grating period requires high-resolution patterning, making the fabrication process complex [212]. In contrast, higher-order gratings ease these fabrication constraints due to their larger period [70]. Higher-order WBGs can support diffraction order modes in addition to the fundamental TE mode propagating within the guided region of the slab waveguide [76]. The partial modes radiate with wavenumbers

$$\beta_m = \beta_0 + \frac{2m\pi}{\Lambda}, \tag{7.7}$$

where m is the diffraction order, and $\beta_0 = \frac{M\pi}{\Lambda}$ is the wavenumber of fundamental mode for a WBG with order $M > 1$. At the Bragg resonance wavelength, these partial modes can interact constructively or destructively with the fundamental mode [213]. Thus, the electromagnetic analysis of a higher-order WBG must be described as wave propagation in a periodic structure. In this framework, the transverse E-field component of the fundamental mode is represented as an infinite sum of standing waves along the z-direction in Floquet–Bloch theorem form [214], as

$$E_x(x,y,z) = \sum_m E_x^{(m)}(x,y,z)e^{j\beta_m z}, \tag{7.8}$$

that satisfies the scalar wave equation defined as

$$\nabla^2 E_x(x,y,z) + k_0^2 n^2(x,y,z) E_x(x,y,z) = 0. \tag{7.9}$$

The grating layer, acting as a weak perturbation source in the waveguide, periodically modulates the refractive index along the propagation direction. The three-dimensional refractive-index profile of the grating region can be described by

$$n^2(x,y,z) = n_0^2(x,y,z) + \sum_{q\neq 0} A_q(x,y) e^{\frac{j2\pi qz}{\Lambda}}, \tag{7.10}$$

where the harmonic Fourier components $A_q(x,y)$ define the periodic refractive-index variations determined by the corrugation shape. For an arbitrarily shaped grating profile, A_q is governed by

$$A_q(x,y) = \frac{(n_l^2 - n_h^2)}{j2\pi q}\left[e^{\left(-j\frac{2\pi q w_2(y)}{\Lambda}\right)} - e^{\left(-j\frac{2\pi q w_1(y)}{\Lambda}\right)}\right], \tag{7.11}$$

where, as shown in Fig. 7.2, the functions $w_1(y)$ and $w_2(y)$ represent the leading and trailing edges of the grating profile, respectively, and n_h and n_l are the refractive indices of the intact (higher-index) and etched (lower-index) regions, respectively. The averaged refractive index of the grating region over single period is obtained by substituting $q = 0$ into Eq. (7.11), denoted as $n_0^2(x,y,z)$, and is given by

$$n_0^2(x,y,z) = n_h^2\left[w_2(y) - w_1(y)\right] + \frac{n_l^2}{\Lambda}\left[\Lambda + w_1(y) - w_2(y)\right], \tag{7.12}$$

which represents the uniform refractive index profile of the grating region in the transverse plane of the WBG. Accordingly, by substituting Eq. (7.8) and Eq. (7.10) into Eq. (7.9), the wave equation can be expressed as

$$\begin{aligned}\nabla^2 E_x^{(m)}(r) + k_0^2\left[n_0^2(r) - \beta_m^2\right] E_x^{(m)}(r) = \\ -2j\beta_m \frac{\partial E_x^{(m)}(r)}{\partial z} - k_0^2 \sum_{q\neq 0} A_q(x,y) E_x^{(m-q)}(r),\end{aligned} \tag{7.13}$$

where $r = (x,y,z)$ denotes the spatial coordinates. Higher-order WBG supports two guided modes corresponding to the forward ($m = 0$) and backward ($m = -M$) propagating waves. Using the Floquet–Bloch theorem, as shown in Eq. (7.8), these guided waves are defined as

$$\begin{aligned}E_x^{(0)}(r) &= A(z)\, E_0(x,y)\, e^{j\beta_0 z}, \\ E_x^{(-M)}(r) &= B(z)\, E_0(x,y)\, e^{j\beta_{-M} z},\end{aligned} \tag{7.14}$$

where $A(z)$ and $B(z)$ are the complex envelopes describing the forward (FW) and backward (BW) longitudinal modes propagating contra-directionally in the guided region of the WBG, respectively.

By substituting $m = 0$ and $m = -M$ into Eq. (7.7), the wavenumbers of guided waves are defined as $\beta_0 = -\beta_{-M} = \frac{M\pi}{\Lambda}$. Accordingly, the general form of the optical field traveling inside the higher-order WBG cavity is given by

$$\mathbf{E}(\mathbf{r}) = \hat{\mathbf{x}} \left\{ E_0(x,y) \left[A(z)e^{j\beta_0 z} + B(z)e^{-j\beta_0 z} \right] + \sum_{m\neq 0,-M} E^{(m)}(r)e^{j\beta_m z} \right\}, \quad (7.15)$$

where the impact of radiative waves on the longitudinal modes is negligible due to their adiabatic variation along both the FW and BW propagation directions. By assuming the slowly varying envelope approximation and considering $m = 0$ in Eq. (7.13), the FW wave equation becomes

$$\begin{aligned} A(z)\left[\nabla_\perp^2 E_0(x,y) + E_0(x,y)\left(k_0^2 n_0^2(r) - \beta_0^2\right)\right] &= -2j\beta_0 \frac{\partial A(z)}{\partial z} \\ -k_0^2 A_M(x,y)B(z)E_0(x,y) - k_0^2 &\sum_{q\neq 0,M} A_q(x,y)E^{(-q)}(r), \end{aligned} \quad (7.16)$$

and the BW wave equation is obtained by setting $m = -M$, as follows

$$\begin{aligned} B(z)\left[\nabla_\perp^2 E_0(x,y) + E_0(x,y)\left(k_0^2 n_0^2(r) - \beta_0^2\right)\right] &= +2j\beta_0 \frac{\partial B(z)}{\partial z} \\ -k_0^2 A_{-M}(x,y)A(z)E_0(x,y) - k_0^2 &\sum_{q\neq 0,-M} A_q(x,y)E^{(-M-q)}(r). \end{aligned} \quad (7.17)$$

The left hand-side of these wave equations can be separated into transverse and longitudinal parts. The transverse component, representing the spatial diffraction $\nabla_\perp^2 E_0(x,y)$, is replaced by

$$\nabla_\perp^2 E_0(x,y) = \left(\beta^2 - k_0^2 n_0^2(x,y)\right)E_0(x,y), \quad (7.18)$$

In Eq. (7.16) and (7.17), as the unperturbed part of the WBG has a fixed fundamental mode profile in the transverse (cross-sectional) plane without variation along the z-direction and its propagation constant is given by $\beta = k_0 n_{\text{eff}}$. The refractive index term in the longitudinal part must be redefined in Eq. (7.16) and (7.17) along the z-direction as [79]

$$n_0^2(r) \approx n_0^2(x,y) + 2n_0(x,y)\Delta n(z) - j\frac{2}{k_0}n_0(x,y)\left(G(z) - \alpha(r)\right), \quad (7.19)$$

where $G(z)$ and $\Delta n(z)$ are the induced gain and associated refractive index change, respectively, introduced by an externally applied electrical bias in active WBGs, while these terms are zero for passive WBGs. The term $\alpha(r)$ accounts for optical losses in the guided region, arising from free-carrier absorption and scattering due to intraband processes [79]. By substituting Eq. (7.18) and (7.19) into Eq. (7.16), the FW wave equation is defined as

$$\begin{aligned}
\frac{dA(z)}{dz}E_0(x,y) + A(z)E_0(x,y)\Bigg[& -j\frac{(\beta^2-\beta_0^2)}{2\beta_0} \\
& -j\frac{k_0^2 n_0(x,y)\Delta n(z)}{\beta_0} - \frac{k_0 n_0(x,y)}{\beta_0}\left(G(z)-\alpha(r)\right)\Bigg] \\
& = j\frac{k_0^2 A_M(x,y)B(z)E_0(x,y)}{2\beta_0} + j\frac{k_0^2}{2\beta_0}\sum_{q\neq 0,M} A_q(x,y)E_x^{(-q)}(r), \quad (7.20)
\end{aligned}$$

where the detuning parameter, describing the deviation between operating and Bragg wavelengths, is described by

$$\delta = \frac{\beta^2-\beta_0^2}{2\beta_0} \approx \beta - \beta_0\,. \quad (7.21)$$

The FW wave equation can be described in terms of optical power by multiplying Eq. (7.20) with $E_0(x,y)$ and then integrating over the entire cross-sectional plane of the WBG, as

$$\begin{aligned}
\frac{dA(z)}{dz}\int_{\mathrm{CS}} E_0^2(x,y)\,dxdy + A(z)\Bigg[& -j\delta\int_{\mathrm{CS}} E_0^2(x,y)\,dxdy \\
& -j\frac{k_0^2\Delta n(z)}{\beta_0}\int_{\mathrm{core}} n_0(x,y)E_0^2(x,y)\,dxdy \\
-\frac{k_0}{\beta_0}\left(G(z)\int_{\mathrm{core}} n_0(x,y)E_0^2(x,y)\,dxdy - \int_{\mathrm{core}} n_0(x,y)E_0^2(x,y)\alpha(r)\,dxdy\right)\Bigg] & \\
= +jB(z)\frac{k_0^2}{2\beta_0}\int_{\mathrm{Gr}} E_0^2(x,y)A_M(x,y)\,dxdy & \\
+j\frac{k_0^2}{2\beta_0}\sum_{q\neq 0,M}\int_{\mathrm{Gr}} E_0(x,y)A_q(x,y)E_x^{(-q)}(r)dxdy\,, & \quad (7.22)
\end{aligned}$$

where the integration of terms containing the optoelectronic parameters is limited to the guided region, and the integration of terms including the Fourier harmonic coefficients is restricted to the grating region. By assuming the following terms as [79]

$$\frac{\int_{\text{core}} n_0(x,y)E_0^2(x,y)\,dxdy}{\int_{\text{CS}} E_0^2(x,y)\,dxdy} \approx \Gamma n_{\text{eff}}\,, \tag{7.23}$$

where the optical confinement factor Γ is

$$\frac{\int_{\text{core}} E_0^2(x,y)\,dxdy}{\int_{\text{CS}} E_0^2(x,y)\,dxdy} \approx \Gamma\,, \tag{7.24}$$

and the uniform absorption loss within the guided region as

$$\frac{\int_{\text{core}} n_0(x,y)E_0^2(x,y)\alpha(r)\,dxdy}{\int_{\text{CS}} E_0^2(x,y)\,dxdy} \approx n_{\text{eff}}\,\alpha(z)\,, \tag{7.25}$$

the FW wave equation simplifies to

$$\begin{aligned} &\frac{dA(z)}{dz} - jA(z)(\delta + k_0\Gamma\Delta n(z)) + A(z)(-\Gamma G(z) + \alpha(z)) \\ &\quad = j\,\frac{k_0^2}{2\beta_0 \int_{\text{CS}} E_0^2(x,y)\,dxdy}\Bigg(B(z)\int_{\text{Gr}} E_0^2(x,y)\,A_M(x,y)\,dxdy \\ &\qquad + \sum_{q\neq 0,M}\int_{\text{Gr}} E_0(x,y)\,A_q(x,y)\,E_x^{(-q)}(r)\,dxdy\Bigg)\,. \end{aligned} \tag{7.26}$$

Neglecting the impact of radiative waves along the z-direction due to their adiabatic variation, the last term of Eq. (7.26) becomes

$$\sum_{q\neq 0,M} E_x^{(-q)}(r) = \sum_{q\neq 0,M}\left[A(z)E_0^{(-q)}(x,y) + B(z)E_{-M}^{(-q)}(x,y)\right], \tag{7.27}$$

where $E_0^{(-q)}(x,y)$ and $E_{-M}^{(-q)}(x,y)$ denote the generated partial modes in the FW and BW directions, respectively. Finally, the modified version of the FW wave equation can be written as

$$\frac{dA(z)}{dz} + A(z)\left(-j\delta - jk_0\Gamma\Delta n(z) - j\kappa_{11} - \Gamma G(z) + \alpha(z)\right) = jB(z)\left(\kappa_M + \kappa_{12}\right)\,, \tag{7.28}$$

where the coupling terms are defined as follows

$$\kappa_M = \frac{k_0^2}{2\beta_0 \int_{\text{CS}} E_0^2(x,y)\,dxdy}\int_{\text{Gr}} E_0^2(x,y)A_M(x,y)\,dxdy, \tag{7.29}$$

$$\kappa_{11} = \frac{k_0^2}{2\beta_0 \int_{\text{CS}} E_0^2(x,y)\,dxdy} \sum_{q\neq 0,M} \int_{\text{Gr}} E_0(x,y) A_q(x,y) E_0^{(-q)}(x,y)\,dxdy\,, \tag{7.30}$$

$$\kappa_{12} = \frac{k_0^2}{2\beta_0 \int_{\text{CS}} E_0^2(x,y)\,dxdy} \sum_{q\neq 0,M} \int_{\text{Gr}} E_0(x,y) A_q(x,y) E_{-M}^{(-q)}(x,y)\,dxdy\,. \tag{7.31}$$

Similarly, the BW wave equation is also described by

$$-\frac{\mathrm{d}B(z)}{\mathrm{d}z} + B(z)(-j\delta - jk_0\Gamma\Delta n(z) - j\kappa_{22} - \Gamma G(z) + \alpha(z)) = jA(z)(\kappa_{-M} + \kappa_{21}) \tag{7.32}$$

where the coupling terms are

$$\kappa_{-M} = \frac{k_0^2}{2\beta_0 \int_{\text{CS}} E_0^2(x,y)\,dxdy} \int_{\text{Gr}} E_0^2(x,y) A_{-M}(x,y)\,dxdy\,, \tag{7.33}$$

$$\kappa_{22} = \frac{k_0^2}{2\beta_0 \int_{\text{CS}} E_0^2(x,y)\,dxdy} \sum_{q\neq 0,-M} \int_{\text{Gr}} E_0(x,y) A_q(x,y) E_{-M}^{(-M-q)}(x,y)\,dxdy\,, \tag{7.34}$$

$$\kappa_{21} = \frac{k_0^2}{2\beta_0 \int_{\text{CS}} E_0^2(x,y)\,dxdy} \sum_{q\neq 0,-M} \int_{\text{Gr}} E_0(x,y) A_q(x,y) E_0^{(-M-q)}(x,y)\,dxdy\,. \tag{7.35}$$

Here, κ_{11} and κ_{22} represent the self-coupling terms, which are identical for all grating shapes [76]. The direct coupling terms, $\kappa_{\pm M}$, and the indirect coupling terms, κ_{12} and κ_{21}, describe the energy exchange between the contra-directional FW and BW propagating waves, with the latter mediated by the radiative waves.

By assuming $\Delta n(z) \approx \Delta n$, $G(z) \approx G$, and $\alpha(z) \approx \bar{\alpha}$ as the uniform parameters inside the guided region under the steady-state condition, the dispersion relation of the higher-order WBG becomes [76, 79]

$$\gamma = \pm\sqrt{[(\Gamma G - \bar{\alpha}) + j(\delta + \Gamma k_0 \Delta n + \kappa_{11})]^2 + [(\kappa_M + \kappa_{12})(\kappa_{-M} + \kappa_{21})]}\,, \tag{7.36}$$

where the effective coupling coefficient in this relation is defined as

$$\kappa_{\text{eff}} = \sqrt{(\kappa_M + \kappa_{12})(\kappa_{-M} + \kappa_{21})}\,, \tag{7.37}$$

which plays an important role in determining the eigenfunction of γ. The paired eigenvalue of an active higher-order WBG is described by

$$\Gamma G + j\delta = \sqrt{\gamma^2 - \kappa_{\text{eff}}^2} - j(\kappa_{11} + \Gamma k_0 \Delta n) + \bar{\alpha}\,, \tag{7.38}$$

where G is the maximum amplification factor that the optical field experiences while propagating within the guided region, and δ is the minimum deviation from the predetermined Bragg wavelength. The transmission and reflection coefficients for passive higher-order WBGs, without external biasing parameters ($G = 0$ and $\Delta n = 0$) and in the absence of facet mirrors at both ends of the guided region, are determined by the contra-directional longitudinal modes of $A(z)$ and $B(z)$ as [76, 215]

$$T = \left| A\left(\frac{L}{2}\right)\right|^2 = \left|\frac{j\gamma(\kappa_{-M} + \kappa_{21})}{j(\kappa_{-M} + \kappa_{21})[\gamma\cosh(\gamma L) - (\alpha + j\delta + j\kappa_{11})\sinh(\gamma L)]}\right|^2, \tag{7.39}$$

$$R = \left| B\left(-\frac{L}{2}\right)\right|^2 = \left|\frac{j(\kappa_{-M} + \kappa_{21})\sinh(\gamma L)}{\gamma\cosh(\gamma L) - (\alpha + j\delta + j\kappa_{11})\sinh(\gamma L)}\right|^2, \tag{7.40}$$

where the length of the guided region is defined as $-\frac{L}{2} \leq z \leq \frac{L}{2}$, and the optical feedback mechanism arises solely from the coupling strength introduced by the grating layer.

As shown in Eq. (7.14), the FW ($m = 0$) and BW ($m = -M$) propagating waves are included in Eq. (7.13) to describe the coupled wave equations, while the fundamental mode of the higher-order WBG is found by Eq. (7.18). To obtain the partial modes that are important for determining the effective coupling coefficients and the corresponding paired eigenvalues, the wave equation is defined as

$$\begin{aligned} &\nabla_\perp^2 E_x^{(m)}(r) + \left(k_0^2 n_0^2(x,y) - \beta_m^2\right) E_x^{(m)}(r) = \\ &-k_0^2\left[A_m(x,y)E_x^{(0)}(r) + A_{m+M}(x,y)E_x^{(-M)}(r)\right], \end{aligned} \tag{7.41}$$

by assuming $\frac{\partial^2}{\partial z^2} \approx 0$, $\frac{\partial}{\partial z} \approx 0$, and $n_0^2(r) \approx n_0^2(x,y)$ due to the negligible impact of uniform gain on partial modes. Using Eq. (7.14) in the source term of Eq. (7.41), the FW wave equation becomes

$$\nabla_\perp^2 E_0^{(m)}(x,y) + \left(k_0^2 n_0^2(x,y) - \beta_m^2\right) E_0^{(m)}(x,y) = -k_0^2 A_m(x,y) E_0(x,y), \tag{7.42}$$

and the BW case is described by

$$\nabla_\perp^2 E_{-M}^{(m)}(x,y) + \left(k_0^2 n_0^2(x,y) - \beta_m^2\right) E_{-M}^{(m)}(x,y) = -k_0^2 A_{m+M}(x,y) E_0(x,y), \tag{7.43}$$

allowing one to find all partial modes in both directions.

Figure 7.3 presents the results of a 1D WBG with a Bragg wavelength of 850 nm [76, 216]. A third-order blazed grating with a thickness of $t_g = 0.2\ \mu$m is defined above the core region, which has a refractive index of $n_{\text{core}} = 3.6$ and a thickness of $t_{\text{core}} = 0.8\ \mu$m. The substrate and cladding layers, with refractive indices of $n = 3.4$, provide optical confinement for the guided mode. Figure 7.3(a) presents the schematic structure in the x–z plane, modeled in COMSOL software [89], where perfectly matched layers (PML) are applied to absorb scattered light in the transverse direction. Figure 7.3(b) shows the refractive index profile of the WBG along x-axis, where the red-highlighted region represents the average index of the grating layer and the blue part shows the refractive index of the core region. According to Eq. (7.10), the average refractive index of the grating region in the transverse direction is described as

$$n_0^2(x) = n_{\text{core}}^2 + \left(n_{\text{clad}}^2 - n_{\text{core}}^2\right)\left(\frac{W_2(x) - W_1(x)}{\Lambda}\right), \tag{7.44}$$

where

$$W_1(x) = \frac{\Delta x}{t_g}, \qquad W_2(x) = \frac{(\Delta - \Lambda)x}{t_g} + \Lambda, \tag{7.45}$$

are the leading and trailing edges of the blazed grating profile, respectively [76]. In this work, the grating period and duty cycle are set to $\Lambda = 356$ nm and $\Delta = 0.25\Lambda$, respectively. The harmonic Fourier coefficient of the grating region is expressed as

$$A_q(x) = \frac{n_{\text{core}}^2 - n_{\text{clad}}^2}{j2\pi q}\left(e^{-j\frac{2\pi q W_2(x)}{\Lambda}} - e^{-j\frac{2\pi q W_1(x)}{\Lambda}}\right). \tag{7.46}$$

The fundamental mode of the WBG is numerically obtained using Eq. (7.18). Figure 7.3(b) presents the E-field profile of the fundamental mode confined within the core region and evanescently leaking to other layers. By including the third-order grating, it is thus necessary to account for the impact of partial modes, as they can interact with the fundamental mode and modify the coupling coefficients, which serve as key parameters of the WBGs. For a third-order grating ($M = 3$), partial modes with diffraction orders in

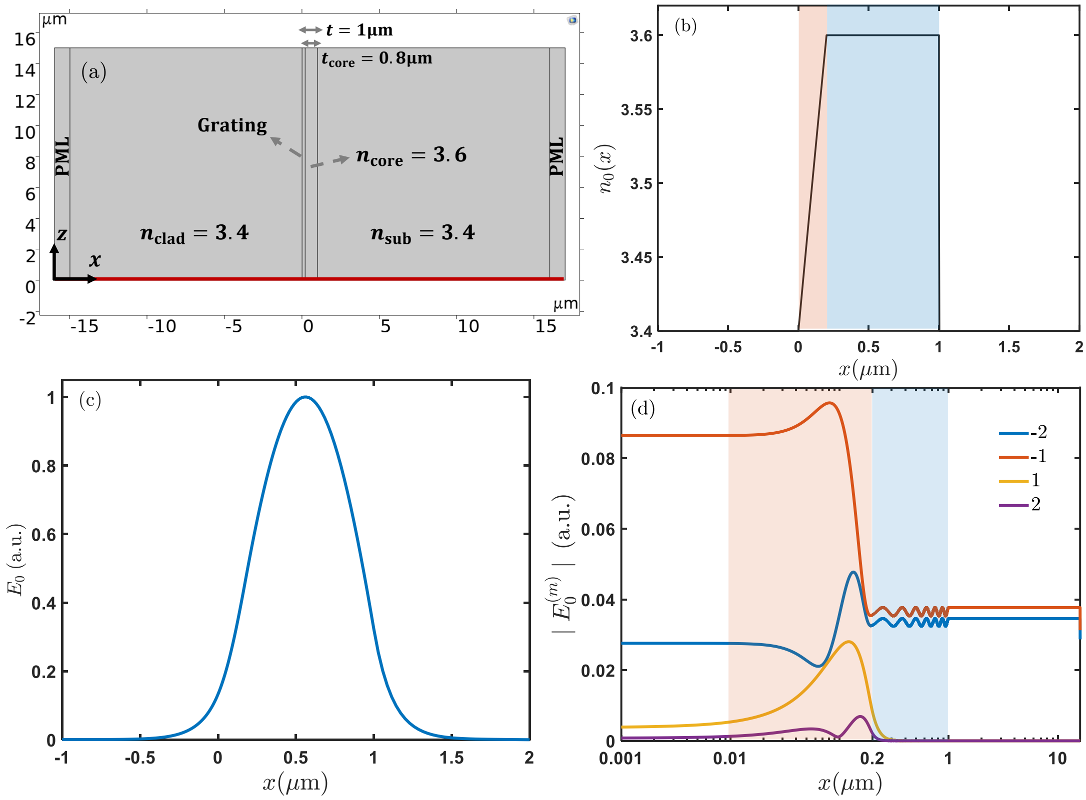

FIGURE 7.3: (a) Schematic cross-sectional view of the third-order blazed WBG structure. (b) Refractive index profile $n_0(x)$ across the transverse direction, where the blue region represents the core region and the red region indicates the grating layer. (c) Fundamental transverse electric field profile $E_0(x)$ confined within the guided region. (d) Transverse profile of the partial modes $|E_0^{(m)}|$ for diffraction orders $m = \pm 1, \pm 2$.

TABLE 7.1: Coupling terms of the third-order blazed WBG.

$\kappa_{11} = \kappa_{22}$ [1/cm]	κ_{12}	κ_{21}	κ_M
$-2.51 + j2.62$	$-1.387 + j2.35$	$-2.53 - j0.03$	$-5.07 - j19.45$

the range of $-3 < m < 3$ are the dominant electric field components interfering with the E-field of fundamental mode. Figure 7.3(d) illustrates the dominant partial modes in the FW case, numerically obtained by solving Eq. (7.42) using COMSOL software. It is evident that these modes are confined within the grating region and exhibit radiative decay away from the grating boundaries. By determining both the fundamental and partial modes, the coupling coefficients can be calculated using Eqs. (7.28) to (7.35) for the fixed duty cycle of $\Delta = 0.25\Lambda$ (Table 7.1).

The coupled wave equations described in Eqs. (7.28) and (7.32) can be used to analyze the output characteristics of higher-order DFB laser sources under threshold conditions in steady-state. In this case, the electrical biasing current provides optical gain inside the guided region of the DFB laser that the threshold gain value $G = g_{\text{th}}$ is estimated by

$$\Gamma g_{\text{th}} = \bar{\alpha} + \alpha_{\text{sca}} + \alpha_{\text{mirror}} + \alpha_0, \tag{7.47}$$

where $\bar{\alpha}$ is the modal loss, $\alpha_{\text{sca}} = 2\text{Im}(\kappa_{11})$ represents the scattering loss of the optical field escaping from the guided region or cavity, α_0 is the free-carrier absorption loss, and $\alpha_{\text{mirror}} = \frac{1}{L}\ln\left(\frac{1}{r_1 r_2}\right)$ is the mirror loss determined by the reflectivities of facet mirrors (r_1, r_2). To analyze DFB lasers at the threshold condition, the coupled wave equations must be solved numerically to obtain the longitudinal modes $A(z)$ and $B(z)$, governed by the eigenvalue pair (g_{th}, δ), where the mirror loss is self-consistently incorporated into these coupled equations as boundary conditions at the facets [211, 217].

7.3 Conclusion

Optical coherent sources require CW operation, achieved through single mode oscillation with narrow bandwidth response. WBGs as the core of DFBLs enable these features using wavelength-selective gratings. Conventional DFBLs often employ first-order gratings for their strong coupling and low loss. However, fabrication challenges and mode degeneracy in first-order DFB lasers impose constraints on the efficiency of their output characteristics.

Higher-order WBGs overcome these limitations by allowing a simpler fabrication process due to their larger grating periods and by introducing complex coupling coefficients. The real part of the effective coupling coefficient represents the strength of the grating, while its phase indicates the longitudinal mode discrimination capability.

This chapter focused on the theory of higher-order WBGs based on the coupled wave equation under steady-state conditions. By considering the influence of radiative waves governed by arbitrary grating shapes, the coupling coefficients were obtained, which play an important role in determining the strength of optical feedback mechanisms in DFBLs. The same analytical approach can also be applied to components where light escapes vertically from the guiding region, such as couplers, interconnectors, and coherent array structures.

The modeling framework presented in this chapter also served as the theoretical basis for the published work *"Finite-difference coupled-mode analysis of waveguide gratings and their optimization for single-mode DFB lasers"* [216]. In addition, the modified coupled wave equation and the effective coupling coefficient formulation described here, including the role of radiative waves in higher-order gratings, were implemented in COMSOL software to validate and confirm the accuracy of the finite-difference model developed by Shayan Saeidi in that paper.

Chapter 8

Short-Cavity Single-Mode On-Chip DFBL Source for Monolithic PICs in the Telecom Range

8.1 Contribution Statement

This project aimed to optimize the performance of an on-chip distributed feedback (DFB) laser designed by INTENGENT, Inc. to operate as an optical emitter in photonic integrated circuits (PICs). This project originated from a collaboration between Prof. Dolgaleva's research group and INTENGENT, Inc., and was initially pursued by Tuhin Paul and Dr. Rosenstein, and after I began my PhD studies, I joined the project through the Mitacs Accelerate internship program. My main contributions were: (i) developing a multi-physics simulation framework in COMSOL to reproduce and optimize the performance of a third-order trapezoidal surface-etched-grating DFB laser, and extending the solver so it can be applied to industry-based DFB designs including laterally coupled or surface-etched higher-order gratings with arbitrary profiles; and (ii) characterizing the available DFB laser chips on the proprietary taper-assisted vertical integration (TAVI) platform provided by INTENGENT company. The modeling workflow and solver implementation were further refined by me through regular meetings with Prof. Dolgaleva, Dr. Tolstikhin, and Dr. Rosenstein.

For the experimental characterization, Dr. Espinosa and I built the initial setup for LIV and PIV measurements to extract the output characteristics of the fabricated samples provided by the company and to establish benchmarks for validating the modeling approach. Ozan Oner later upgraded the setup by improving the output edge-coupling efficiency and by stabilizing the sample temperature, which is critical for reliable optoelectronic characterization. Dr. Flizikowski and Lisa Fischer developed the automated measurement tools. M. R. Mohammadpour and Kushal Jayarathna contributed additional measurements on more samples to further confirm the accuracy of the results.

I carried out the threshold-oriented modelling algorithm, generated the figures for the manuscript, and wrote the initial draft of the paper, except for the experimental sections prepared based on the measurements led by Ozan Oner. The manuscript was further refined through multiple rounds of edits by Prof. Dolgaleva. The project was supervised by Prof. Dolgaleva, and all co-authors approved the final manuscript.

8.2 Article

The results of this project were published in *Journal of Physics D: Applied Physics* [218], and this chapter is based on the following article.

IOP Publishing J. Phys. D: Appl. Phys. 59 (2026) 245101 https://doi.org/10.1088/1361-6463/ae7733

Journal of Physics D: Applied Physics

OPEN ACCESS

RECEIVED
16 December 2025

REVISED
22 May 2026

ACCEPTED FOR PUBLICATION
3 June 2026

PUBLISHED
16 June 2026

PAPER

Short-cavity single-mode on-chip DFBL source for monolithic PICs in the telecom range

Sina Aghili[1], Ozan W Oner[2], Tuhin Paul[1], Mohammadreza Mohammadpour[2], Kushal Jayarathna[1], Lisa Fischer[3], Boris Rosenstein[1], Daniel H G Espinosa[1], Gabriel A S Flizikowski[1] and Ksenia Dolgaleva[1,2,*]

[1] School of Electrical and Computer Engineering, University of Ottawa, 25 Templeton St., Ottawa, Ontario K1N 6N5, Canada
[2] Department of Physics, University of Ottawa, 25 Templeton St., Ottawa, Ontario K1N 6N5, Canada
[3] Department of Physics, Friedrich-Alexander Universität Erlangen-Nürnberg, Staudtstr. 7, 91058 Erlangen, Germany
[*] Author to whom any correspondence should be addressed.

E-mail: ksenia.dolgaleva@uottawa.ca

Keywords: semiconductor lasers, integrated photonics, III–V semiconductors, distributed-feedback lasers

Abstract

We present a numerical study of a third-order surface-etched-grating distributed-feedback laser (DFBL) with narrow band operation around 1275 nm. The device is treated as a representative on-chip source implemented on a proprietary taper-assisted vertical integration (TAVI) platform. A threshold-oriented semi-numerical framework is developed in COMSOL software to analyze cavity dynamics at lasing onset, using steady-state coupled-wave equations that account for the role of radiative waves in the energy exchange between forward and backward propagating waves. Using a numerical shooting method, the model extracts the paired eigenvalues corresponding to threshold gain and detuning. The modeling results demonstrate stable single-mode operation at a cavity length of $L = 200\ \mu$m, enabled by a strong complex coupling coefficient $\kappa_{\text{eff}} = 9.5 + j31.7$ cm^{-1}, whose coupling phase lifts the stop band and suppresses longitudinal mode degeneracy in the output spectral response. The model predicts minimum detuning with lasing near 1274 nm. Experimental characterization of available DFBL chips fabricated on the proprietary TAVI platform shows lasing at 1272.4 nm, in good agreement with simulations. These results support the validity of the proposed framework for capturing the key spectral behavior of higher-order grating DFBLs and highlight its potential for the design and optimization of compact single-mode sources in integrated photonic platforms under limited access to the parameters of the fabricated devices and the associated optoelectronic characteristics.

1. Introduction

The increasing demand for bandwidth-intensive applications and high-speed access has highlighted the importance of coherent optical communication systems [1]. Next-generation coherent optical networks rely on photonic integrated circuits (PICs), which integrate multiple photonic components with well-defined functionalities on a single substrate, significantly reducing the size and complexity of optical infrastructures [2–5].

A critical parameter in PIC design is the performance of on-chip active components, particularly laser sources. Key design requirements for these sources include narrow spectral emission within the telecommunication windows, a high side-mode suppression ratio (SMSR), and low sensitivity to temperature variations and fabrication imperfections. Distributed-feedback lasers (DFBLs), based on a wavelength-selective cavity, can provide single-mode emission with a narrow linewidth, which is critical for minimizing signal distortion over long fiber links and enabling dense wavelength-division multiplexing systems [6, 7].

DFBL cavities rely on multi-beam interference in a periodically perturbed waveguide, where the effective index and/or the modal gain are modulated along the propagation direction. This periodic perturbation provides wavelength selectivity and enhanced optical feedback through engineered grating features [8, 9].

DFBL operation is commonly analyzed using coupled-wave theory, in which the lasing condition is formulated as an eigenvalue problem that yields the threshold gain and the detuning from the Bragg condition. In this formulation, the coupling coefficient is a central design parameter because it strongly influences both the threshold point and the lasing frequency [10]. The coupling coefficient is set by the grating order and pitch, the grating shape and duty cycle, and the overlap between the guided mode and the grating region [11].

The nature of the coupling mechanism depends on the grating etch position relative to the gain region. Buried gratings placed within, or close to, the active region can yield a complex coupling response because the periodic perturbation can include both effective-index modulation and gain modulation [6]. When the grating is defined away from the active region, the feedback is typically dominated by index coupling realized through an effective-index perturbation of the guided mode. In this case, the grating order plays a key role in determining the available diffraction channels and the resulting coupling behavior [8, 10].

First-order gratings can provide strong coupling between contra-directional guided waves while typically exhibiting relatively low radiation loss into diffraction channels, which supports low-threshold operation and short cavity lengths [12, 13]. For first-order gratings positioned sufficiently far from the gain region, the feedback is predominantly index-coupled, and the coupling coefficient is purely real, which can lead to degenerate longitudinal modes with identical net threshold gain corresponding with dual-mode operation [8, 10]. Stable single-mode operation is commonly enforced by lifting this degeneracy, for example, by introducing a phase-shift section along the grating length [14] or by using asymmetric facet coatings [15]. More generally, a complex coupling coefficient with a sufficiently large imaginary part or coupling phase provides another route to break the degeneracy and achieve a single longitudinal mode for lasing [6, 10].

Higher-order gratings open additional diffraction channels that support radiative waves. These radiative waves can interact with the guided waves, providing indirect coupling paths between the forward (FW) and backward (BW) guided waves while also introducing distributed scattering loss [16–18]. As a result, the effective coupling becomes complex, and its magnitude and phase govern the longitudinal mode selectivity and the threshold eigenvalues [8]. Accurate threshold prediction for higher-order DFBLs, therefore, requires capturing not only the fundamental guided mode but also the dominant radiative (partial) modes supported by the grating geometry, since these modes contribute to the coupling and loss terms appearing in the coupled-wave equations. At lasing onset, the optoelectronic parameters can be treated as time independent within a steady-state threshold analysis [8].

Laterally coupled gratings (LCGs) and vertically coupled surface etched gratings (SEGs) are common implementations of higher order gratings positioned away from the active region and compatible with regrowth-free fabrication flows [20–22]. In LCGs, gratings are etched on the sidewalls of ridge waveguides, and the coupling strength is mainly governed by the overlap of the lateral evanescent part of the guided mode with the sidewall grating region [23]. In vertically coupled SEGs, trenches are etched from the top surface of ridge waveguides or upper emitter layers, yielding a vertical refractive index perturbation with potentially high index contrast between etched and unetched regions [24–26]. By vertically confining the modal field distribution, SEGs can increase the overlap between the guided mode and the grating region and therefore support higher coupling coefficients [27–29]. At the same time, scattering and radiation losses must be managed through the grating design [30]. By tailoring the radiative wave content of SEGs through the grating geometry [30, 31], the magnitude and phase of the resulting complex coupling coefficient can be engineered to improve the DFBL threshold response and enable robust single-mode operation at shorter cavity lengths.

In this paper, we present a numerical study of an on-chip DFBL incorporating a third-order SEG vertically coupled to a mesa structure, based on a representative architecture consistent with the taper-assisted vertical integration (TAVI) framework [32] and compatible with regrowth-free processes. Due to proprietary constraints associated with the commercial platform, the exact epitaxial compositions and fabrication details are not disclosed. Instead, the analysis is carried out using an equivalent refractive-index representation that captures the passive optical behavior of the device. A threshold-oriented modeling framework, implemented in COMSOL software [33], is employed to identify conditions for stable single-mode operation at the shortest feasible cavity length. This work focuses on steady-state operation at lasing onset, where the optoelectronic parameters are assumed uniform and time independent along the cavity. Within this framework, the grating geometry is linked to the threshold eigenvalues

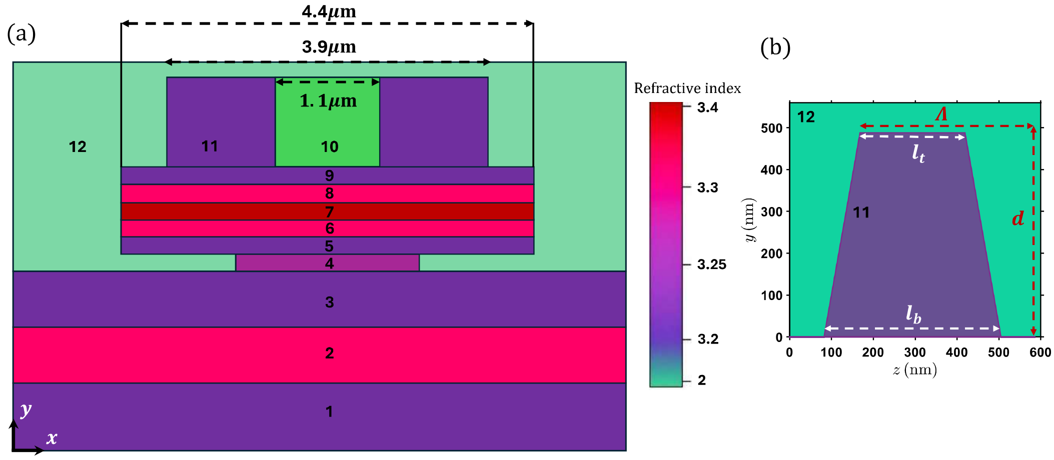

Figure 1. (a) Cross-sectional view of the DFBL in the x–y plane, with light propagation along the z-direction. The numbered layers correspond to table 1 and form three main parts: the substrate (layer 1), the passive router waveguide (layer 2), and the mesa structure extending from the top surface of the lower emitter to the upper emitter (layers 3–11). The third-order trapezoidal SEG (layer 10) is defined at the center of the mesa by etching into the upper emitter. The color bar maps the layer colors to their corresponding refractive indices. (b) One period of the third-order trapezoidal grating profile shown in the y–z plane along the propagation direction (z). The grating has a fixed duty cycle of $\gamma = 0.72$, with geometrical parameters $\Lambda = 586.65$: nm, $d = 488$: nm, $l_\mathrm{b} = 422.6$: nm, and $l_\mathrm{t} = 250.5$: nm, and is filled by the cladding layer (layer 12).

through both direct and radiative-wave-mediated coupling terms and the associated radiative-loss contributions, enabling estimation of the threshold response and the resulting spectral behavior. The lasing wavelength near 1275 nm is set by the available DFBL chips used to validate the simulated results and was not independently selected in this work. The proposed modeling framework is general and can be applied to devices operating at other telecom wavelengths by adjusting the grating parameters and the effective indices accordingly. Experimental characterization of representative DFBL chips fabricated with different cavity lengths on the same TAVI platform is used as a benchmark for validating the model. The comparison between simulations and experiment supports the validity of the proposed framework.

2. Structure and methodology

Figure 1(a) shows the representative vertically integrated DFBL architecture studied here, consistent with the designs reported in [28, 29]. It can be conceptually divided into three parts: (i) a substrate layer (layer 1), (ii) a passive router waveguide (layer 2), and (iii) a mesa structure. The router (layer 2) serves as the passive waveguide that directs the laser output toward other on-chip components. The mesa region comprises the lower and upper emitter layers (layers 3 and 11), referred to here as emitter layers to distinguish them from conventional cladding layers, which serve as functional waveguiding and injection layers in the vertically integrated architecture, with the SEG (layer 10) defined in the upper emitter. The undercut layer (layer 4) and the capping layer (layer 5) form the bottom part of the mesa structure. The waveguiding part of the mesa is formed by the separate-confinement heterostructure (SCH)–multi quantum well (MQW)–SCH stack (layers 6–8). The SEG region and the upper SCH layer are separated by a spacer layer (layer 9). The entire structure is encapsulated in the cladding layer (layer 12), which also fills the etched grating region. In such regrowth-free vertically integrated platforms, the router layer serves as a passive routing plane, and optical transfer between functional regions is achieved through evanescent field coupling defined by the refractive index profile.

Figure 1(b) shows a single period of a trapezoidal grating with order $M = 3$ in the y–z plane, which is made of an upper emitter material (Layer 11), and the etched region is filled with a cladding material (Layer 12).

Figure 1(a) shows the numbered layers, whose refractive indices and geometrical parameters are listed in table 1 and serve as the effective optical parameters used in the modeling. Due to proprietary constraints associated with the commercial device platform, the exact material compositions and doping profiles are not disclosed.

Continuous-wave (CW) operation is a crucial requirement for this on-chip DFBL as a telecom laser source, resulting in a constant and stable output power. In this regime, the system reaches equilibrium,

Table 1. Bottom-to-top layers' specifications of the DFBL.

Layer	Refractive index	Thickness (μm)	Width (μm)
1– Substrate	3.2141	30	6.4
2– Router	3.2842	0.44	6.4
3– Lower emitter	$3.2136 + j2.03 \times 10^{-4}$	0.48	6.4
4– Hole aperture	$3.234 + j1.34 \times 10^{-4}$	0.05	1.8
5– Capping	$3.214 + j1.35 \times 10^{-4}$	0.05	4.4
6– Lower SCH	$3.308 + j3.05 \times 10^{-5}$	0.10	4.4
7– MQW	3.4586	0.123	4.4
8– Upper SCH	$3.28 + j1.1 \times 10^{-5}$	0.20	4.4
9– Spacer	$3.21 + j1.04 \times 10^{-4}$	0.024	3.9
10– SEG	n_{cs}	0.488	1.1
11– Upper emitter	$3.21 + j1.04 \times 10^{-4}$	0.488	3.9
12– Encapsulation	2.04	—	—

with the gain provided by the cavity balancing the total losses. This balance ensures that the photon and carrier densities inside the cavity stabilize, leading to a time-invariant optical field [19]. To determine the lasing onset of the studied DFBL, as shown in figure 1(a), we investigate the interaction between FW and BW waves propagating within the WBG cavity along the z-direction. Under steady-state conditions, the threshold-oriented coupled wave equations can be described by

$$\frac{\mathrm{d}A(z)}{\mathrm{d}z} + A(z)\left[\alpha_{\mathrm{tot}} - (\Gamma+\beta)\,g_{\mathrm{th}}\right] = j\left[\delta_{\mathrm{th}} + k_0\Gamma\Delta n + \Re\{\kappa_{11}\}\right]A(z) + j\left[\kappa_M + \kappa_{12}\right]B(z),$$
$$-\frac{\mathrm{d}B(z)}{\mathrm{d}z} + B(z)\left[\alpha_{\mathrm{tot}} - (\Gamma+\beta)\,g_{\mathrm{th}}\right] = j\left[\delta_{\mathrm{th}} + k_0\Gamma\Delta n + \Re\{\kappa_{22}\}\right]B(z) + j\left[\kappa_{-M} + \kappa_{21}\right]A(z). \quad (1)$$

Here, $A(z)$ and $B(z)$ represent the longitudinal mode components of the FW and BW propagating waves, respectively, with g_{th} denoting the required threshold gain to start lasing. Γ is the confinement factor of the guided mode inside the core or active region of the DFBL. The detuning term δ_{th} represents the deviation between the operating and Bragg wavelengths. The refractive index difference (Δn) is seen by propagating waves within the cavity in the presence and absence of electrical biasing, introducing a phase-shift term to the respective propagating waves. β is the inhomogeneous spontaneous emission factor. The mutual coupling coefficients, κ_{-M} and κ_M, govern energy exchange between the FW and BW waves. The self-coupling terms, κ_{11} and κ_{22}, introduce phase shifts to the respective propagating waves. For all grating geometries, the self-coupling coefficients are equal ($\kappa_{11} = \kappa_{22}$) [8]. Other mutual coupling terms, represented by κ_{12} and κ_{21}, describe interactions between the propagating waves via radiative waves, which can either enhance or diminish the primary mutual coupling coefficients. Another key term, α_{tot}, accounts for total losses that decrease the cavity gain and is defined as $\alpha_{\mathrm{tot}} = 2\Im\{\kappa_{11}\} + \alpha_0$, where $\Im\{\kappa_{11}\}$ is the scattering losses of radiative waves escaping from the cavity and α_0 is the free-carrier absorption losses due to intraband transitions within the active region [34]. The eigenvalue pair $(g_{\mathrm{th}}, \delta_{\mathrm{th}})$ determines the threshold gain required within the cavity to start lasing at a wavelength selected by δ_{th}.

To solve the coupled-wave equations in equation (1) and obtain the optimized threshold lasing response, we first determine the cross-sectional refractive-index profile ($n_{\mathrm{cs}}(x,y)$) of the third-order trapezoidal grating shown in figure 1(b). The transverse refractive index of the grating region in the x–y plane is defined by

$$n_{\mathrm{cs}}(x,y) = \sqrt{n^2_{(\mathrm{L11})}\left[\gamma - \frac{(l_{\mathrm{b}} - l_{\mathrm{t}})}{\Lambda d}\,y\right] + n^2_{(\mathrm{L12})}\left[(1-\gamma) + \frac{(l_{\mathrm{b}} - l_{\mathrm{t}})}{\Lambda d}\,y\right]}, \quad (2)$$

where l_{b} and l_{t} are the larger and smaller arms of the trapezoid, and d is the height of the grating profile. The grating profile is defined by a duty cycle parameter, $\gamma = l_{\mathrm{b}}/\Lambda$, with the grating period Λ that optimizes the feedback efficiency by varying the grating shape from triangular to more rectangular.

The refractive indices of the unetched and etched regions are described by $n_{(\mathrm{L11})}$ and $n_{(\mathrm{L12})}$, respectively. By defining the harmonic Fourier components for the third-order trapezoidal grating along the cavity plane ($y - z$), the refractive index of the grating region is defined as

$$n_{\mathrm{gr}}(x,y,z) = n_{\mathrm{cs}}(x,y) + A_q(x,y)\,\mathrm{e}^{\mathrm{j}(2\pi q/\Lambda)z}, \quad (3)$$

where

$$A_q(x,y) = \frac{\left(n^2_{(\mathrm{L12})} - n^2_{(\mathrm{L11})}\right)}{\pi q} \sin\left(\frac{2\pi q}{\Lambda}\left(\frac{l_\mathrm{b} - l_\mathrm{t}}{2d} y + \frac{\Lambda - l_\mathrm{t}}{2}\right)\right). \tag{4}$$

Here, q is the Fourier coefficient to show higher-order index perturbations along the cavity. In higher-order WBGs, the wavenumbers of FW and BW propagating waves are $\beta_0 = M\pi/\Lambda$ and $\beta_{-M} = -M\pi/\Lambda$, respectively. Besides FW and BW waves, higher-order WBGs can support radiative waves with wavenumbers $\beta_\mathrm{r} = \frac{(M-2m)\pi}{\Lambda}$, with m as the diffraction order, that can be engineered to tune feedback strength and the accumulated coupling phase [19]. These radiative waves can establish a quasi-phase matching condition between the FW and BW propagating waves, and hence provide indirect coupling channels between these contra-directional guided waves. For a third-order grating, diffraction orders of $-3 < m < 3$ are responsible for the dominant radiative waves.

Coupling coefficients are the most important parameters in the coupled-wave equation of equation (1), as they govern how the interacting waves exchange optical energy along the cavity and are determined by

$$\kappa_{\pm M} = \frac{k_0}{2PN_\mathrm{eff}} \iint_\mathrm{Gr} A_{\pm M}(x,y)\, E_0^2(x,y)\, \mathrm{d}x\mathrm{d}y, \tag{5a}$$

$$\kappa_{11} = \frac{k_0}{2PN_\mathrm{eff}} \sum_{q\neq 0,M} \iint_\mathrm{Gr} E_0^{(-q)}(x,y)\, A_q(x,y)\, E_0(x,y)\, \mathrm{d}x\mathrm{d}y, \tag{5b}$$

$$\kappa_{22} = \frac{k_0}{2PN_\mathrm{eff}} \sum_{q\neq 0,-M} \iint_\mathrm{Gr} E_{-M}^{(-M-q)}(x,y)\, A_q(x,y)\, E_0(x,y)\, \mathrm{d}x\mathrm{d}y, \tag{5c}$$

$$\kappa_{12} = \frac{k_0}{2PN_\mathrm{eff}} \sum_{q\neq 0,M} \iint_\mathrm{Gr} E_{-M}^{(-q)}(x,y)\, A_q(x,y)\, E_0(x,y)\, \mathrm{d}x\mathrm{d}y, \tag{5d}$$

$$\kappa_{21} = \frac{k_0}{2PN_\mathrm{eff}} \sum_{q\neq 0,-M} \iint_\mathrm{Gr} E_0^{(-M-q)}(x,y)\, A_q(x,y)\, E_0(x,y)\, \mathrm{d}x\mathrm{d}y. \tag{5e}$$

In the equations of coupling coefficients, $k_0 = 2\pi/\lambda_\mathrm{B}$ is the free-space wavenumber at the Bragg wavelength $\lambda_\mathrm{B} = 1275\,\mathrm{nm}$. The parameter $P = \iint_\mathrm{CS} E_0^2(x,y)\,\mathrm{d}x\mathrm{d}y$ is the optical power in the cross-sectional plane of the whole structure. N_eff is the effective index of the fundamental TE mode, whose electric field component is denoted by $E_0(x,y)$ and is identical for both FW and BW propagating waves. The electric field components of the partial modes in the FW and BW directions are $E_0^{(i)}(x,y)$ and $E_{-M}^{(i)}(x,y)$, respectively, where $i = -q$ or $i = -M - q$ ($i \neq 0, -M$) represents the order of the partial modes. As defined in equations. (5a)–(5e), the coupling coefficients are inherently linked to the grating's geometrical parameters through the term $A_q(x,y)$. By taking the impact of radiative waves into account, we define the effective coupling coefficient as

$$\kappa_\mathrm{eff} = \sqrt{(\kappa_M + \kappa_{12})(\kappa_{-M} + \kappa_{21})}, \tag{6}$$

where $|\kappa_\mathrm{eff}|$ and $\angle\kappa_\mathrm{eff}$ represent the coupling strength and phase, respectively, which determine the optical energy exchange between the FW and BW propagating waves along the structured cavity of the WBG.

The electric field component of the fundamental TE mode is calculated by numerically solving the homogeneous wave equation

$$\frac{\partial^2 E_0(x,y)}{\partial x^2} + \frac{\partial^2 E_0(x,y)}{\partial y^2} + \left(k_0^2 n^2(x,y) - \beta^2\right) E_0(x,y) = 0, \tag{7}$$

where $n(x,y)$ is the transverse refractive index of each layer, and $\beta = 2\pi N_\mathrm{eff}/\lambda_\mathrm{B}$ is the propagation constant of the fundamental mode. The fundamental mode must be partially confined within the core region of the DFBL to facilitate the interaction of its evanescent part with the grating region, and is hence referred to as a quasi-TE mode.

The partial modes radiate perpendicular to the transverse plane of the WBG and are coupled back into the cavity through the grating region, thereby modifying the coupling coefficients, as shown in equations (5*b*)–(6) [11, 31]. These modes are described by a spatial Fourier expansion based on Floquet–Bloch theory [35] and are formulated using the inhomogeneous Helmholtz equations

$$\nabla_\perp^2 E_0^{(m)}(x,y) + \left(k_0^2 n_0^2(x,y) - \beta_m^2\right) E_0^{(m)}(x,y) = -k_0^2 A_m(x,y)\, E_0(x,y)\,, \tag{8a}$$

$$\nabla_\perp^2 E_{-M}^{(m)}(x,y) + \left(k_0^2 n_0^2(x,y) - \beta_m^2\right) E_{-M}^{(m)}(x,y) = -k_0^2 A_{m+M}(x,y)\, E_0(x,y)\,, \tag{8b}$$

where the propagation constants of partial modes are defined by $\beta_m = \beta_0 + 2m\pi/\Lambda$. Equations (8*a*) and (8*b*) determine the generated partial modes in the FW and BW directions, respectively.

In this study, we focus on passive modeling of the DFBL using the refractive indices and geometrical parameters listed in table 1 to determine the optimal eigenvalue pair from equation (1). In the first step, we use the RF Module of COMSOL Multiphysics [33] to numerically solve the homogeneous wave equation (see equation (7)) in the cross-sectional plane and obtain the electric field distribution of the fundamental quasi-TE (guided) mode, $E_0(x,y)$, together with its effective index N_{eff}. In this step, we perform a mode analysis study using a computational domain that is sufficiently large and rigorously meshed, while perfectly matched layers (PMLs) are applied on all outer boundaries to terminate the simulation region. In the second step, using N_{eff} and $E_0(x,y)$ obtained in step one, we employ the general form of the Helmholtz partial differential equation in the Mathematics Module of COMSOL to compute the partial modes in both the FW and BW directions by semi-numerically solving equations (8*a*) and (8*b*), following the finite-element-based simulation method described in our previous work [31]. With the effective index, the guided mode, and the partial modes in hand, we then evaluate the coupling coefficients and the scattering loss of radiative waves required in the coupled-wave equations of equation (1). Finally, by numerically solving equation (1) using the shooting method [6, 11], we find the optimal eigenvalue pair $(g_{\mathrm{th}}, \delta_{\mathrm{th}})$ corresponding to single-mode operation at the shortest feasible cavity length.

3. Results

Figure 2 presents the transverse electric field distribution of the guided mode at the Bragg wavelength $\lambda_{\mathrm{B}} = 1275$ nm for the fixed duty cycle $\gamma = 0.72$. As shown in figure 2(a), the guided mode is partially confined within the MQW region. The SCH layers in the waveguiding section provide the vertical confinement, while the lateral confinement is realized near the bottom of the mesa. In particular, because the SEG does not provide ridge-type lateral guiding by itself, the guided mode is laterally defined at the mesa base through the thin undercut layer and the capping layer above it. The upward evanescent tail of the guided mode penetrates toward the grating region and overlaps with the SEG, enabling vertical evanescent-field coupling to the grating. The spacer layer between the upper SCH and the SEG is set to 24 nm to optimize the modal overlap with the grating region while maintaining mode confinement in the MQW region. The cladding thickness above the grating region is set to 30 nm to provide the refractive index contrast required to reduce scattering loss. The lower evanescent tail of the guided mode extends into the passive router waveguide, enabling optical transfer through vertical evanescent coupling. This coupling is governed by the refractive index contrast in the lower mesa and surrounding layers, and does not rely on a discrete taper section in the present structure. By increasing the duty cycle, the grating shape evolves from triangular to more rectangular while the grating period decreases, as shown in figure 2(c), resulting in the effective index enhancement observed in figure 2(b).

As the next step in the transverse analysis, we calculate the electric field distributions of the partial modes. All allowed partial modes coupled back to the fundamental mode, through the grating layer, can contribute to the cavity interactions and modify the coupling coefficients, which in turn determine the threshold response and the required cavity length of the DFBL. Figure 3 presents the dominant partial modes in the FW direction, corresponding to $E_0^{(-1)}$ and $E_0^{(-2)}$ obtained from equation (8*a*) for the duty cycles $\gamma = 0.39$ and $\gamma = 0.72$. These partial modes disperse across the transverse plane and are absorbed by the surrounding PMLs in the simulation domain. At smaller duty cycles, the grating profile features sharp teeth, forming a high index contrast along the propagation direction. As a result, partial modes escape the cavity and scatter perpendicular to the propagation direction, as shown in figure 3(a). In contrast, at larger duty cycles, the grating profile becomes trapezoidal, leading to a smoother index variation

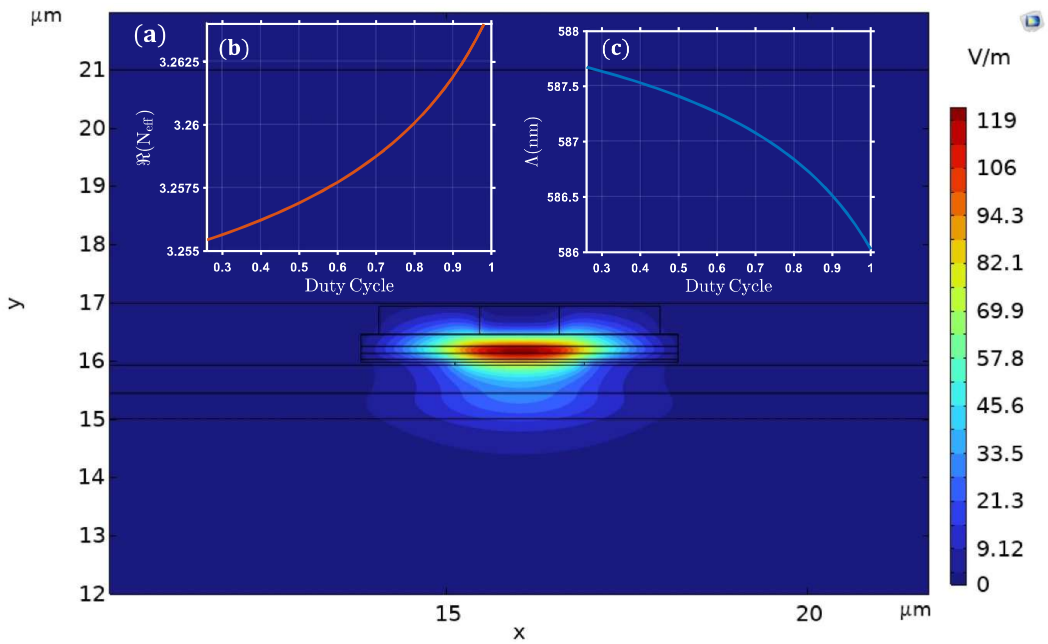

Figure 2. (a) Electric field distribution of the guided mode at the fixed duty cycle of $\gamma = 0.72$. (b) Effective index variation as a function of duty cycle, and (c) the grating period changes as a function of duty cycle.

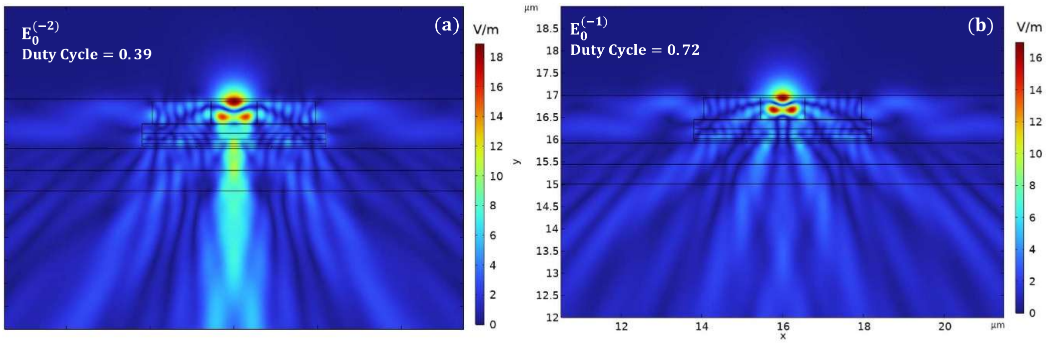

Figure 3. Electric field distributions of the dominant partial modes in the FW direction. (a) $E_0^{(-2)}$ at $\gamma = 0.39$, showing scattering across the transverse plane. (b) $E_0^{(-1)}$ at $\gamma = 0.72$, mainly confined within the grating region.

along the cavity. Consequently, partial modes become more confined within the grating region, as illustrated in figure 3(b).

After determining all interacting modes, we next calculate the direct coupling coefficients (see equation (5*a*)) and the modified coupling coefficients (see equation (6)), which play key roles in extracting the threshold eigenvalue pair from equation (1).

Figure 4 illustrates the magnitude and phase of the effective and direct coupling coefficients as functions of the duty cycle. The effective coupling coefficient is complex due to radiative-wave-mediated interactions, where the coupling magnitude shows the feedback strength and the coupling phase is essential for mode discrimination. The grating induces a periodic effective-index modulation along the cavity through its Fourier harmonic components $A_q(x,y)$. For the third-order case ($M = \pm 3$), this periodicity results in three peaks (i.e., $|M|$ peaks associated with the grating order) in the coupling magnitude at duty cycles around $\gamma = 0.3, 0.6, 0.95$ for both the direct and effective coefficients. As shown in figure 4(a), increasing the duty cycle enhances the transverse refractive index of the grating region, allowing the guided mode to penetrate deeper into it and thereby enhancing the coupling. Conversely, at smaller duty cycles, only a small fraction of the guided mode overlaps with the SEG, leading to weaker coupling. As the duty cycle approaches zero, the index perturbation vanishes and the mutual energy exchange between the propagating waves approaches zero.

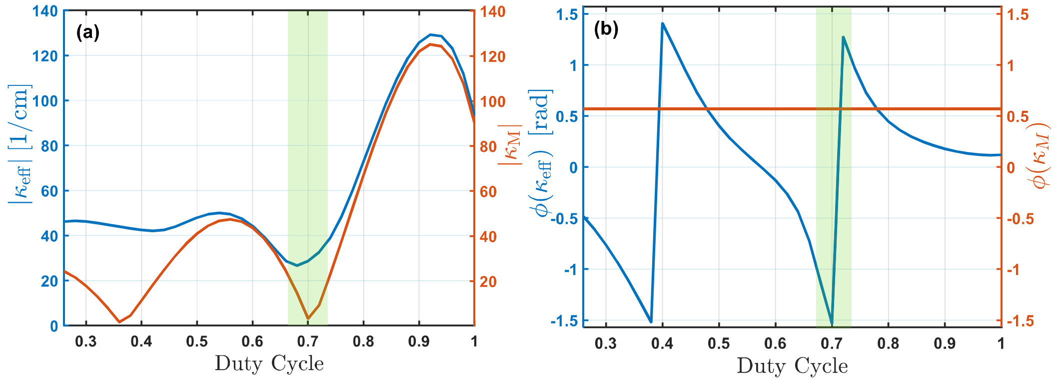

Figure 4. (a) Direct and effective coupling strengths as functions of the duty cycle, exhibiting three peaks at approximately $\gamma =$ 0.3, 0.6, and 0.95, resulting from the periodic modulation of the effective index experienced by the FW and BW propagating waves. (b) Direct and effective coupling phases as functions of the duty cycle. While the direct coupling phase remains constant, the effective coupling phase exhibits two extrema (maxima) at $\gamma = 0.39$ and 0.72. The highlighted region indicates the optimal duty cycle range, with $\gamma = 0.72$ selected for the fabrication process.

The coupling phase exhibits a more complex behavior. As shown in figure 4(b), the direct coupling phase, which neglects radiative interactions, remains monotonic. In contrast, the effective coupling phase undergoes two extrema (i.e., $|M|-1$ extrema) at duty cycles around $\gamma = 0.39, 0.72$ due to quasi-phase matching mediated by radiative waves. By introducing additional optical path differences in the cavity and inducing phase retardation between the FW and BW propagating waves, the contribution of radiative waves enables selective amplification of a resonant wavelength within the cavity and suppresses mode degeneracy.

To ensure stable CW operation of such DFB lasers, the duty cycle must be chosen to provide sufficient coupling strength and a strong coupling phase. As evident from figure 4, duty cycles near 0.39 and 0.72 produce pronounced peaks in the coupling phase response. In the subsequent steps, a duty cycle of approximately $\gamma = 0.72$ is adopted, as it offers a broader fabrication tolerance. At $\gamma = 0.39$, the smaller arm of the trapezoidal grating profile is around $l_t = 56$ nm, which is challenging to fabricate and increases the risk of index-contrast degradation. In contrast, at $\gamma = 0.72$ the smaller arm is $l_t = 250$ nm, which is more compatible with practical fabrication.

The electro-optical parameters of the MQW layer (active region) defined in equation (1) are assumed to be $\Delta n = 3\times10^{-3}$ and $\alpha_0 = 5$ cm^{-1} under threshold conditions. These values are adopted based on representative parameters reported for similar device architectures, as the exact layer compositions and doping profiles of the experimental platform are subject to proprietary constraints and are therefore not disclosed. The spontaneous emission factor is set to the standard value $\beta = 10^{-4}$ for the MQW region [36]. The optical confinement factor is calculated as $\Gamma = \frac{\iint_{\rm MQW} E_0^2(x,y)\,{\rm d}x\,{\rm d}y}{P}$. In practice, the threshold current of the device is influenced not only by the required threshold gain but also by radiative losses associated with the third-order grating and by the reduced injection efficiency characteristic of the regrowth-free N-up architecture.

The coupled wave equations can be solved numerically with the shooting method. The cavity length is discretized along z using fourth-order Runge–Kutta integration, and a Newton–Raphson step iteratively updates the eigenvalue until the boundary conditions at the rear ($z = -L/2$) and front ($z = +L/2$) facets are satisfied [6, 9]. These conditions are written as $A(-L/2) = r_1 B(-L/2)$ and $B(+L/2) = r_2 A(+L/2)$, with an arbitrary initial guess for $B(-L/2)$. By assuming zero reflectivity at both facets ($r_1 = r_2 = 0$), the boundary condition at the output facet directly gives $B(+L/2) = 0$, since no BW wave is generated. The FW-propagating field is then normalized by setting $A(-L/2) = 1$, which does not affect the physical solution, as the transmission coefficient is determined from relative field amplitudes. Under these conditions, the analytical solution for the transmission coefficient of the open cavity is obtained [8, 37].

Figure 5(a) shows the operational eigenvalue pair with minimum threshold gain $g_{\rm th}$ and least deviation of $\delta_{\rm th}$ from the Bragg wavelength of $\delta L = 0$ at each cavity length. After finding L and $(g,\delta)_{\rm th}$, we find the transmission coefficient from the output facet, which demonstrates how the optimized pair

IOP Publishing J. Phys. D: Appl. Phys. 59 (2026) 245101 S Aghili et al

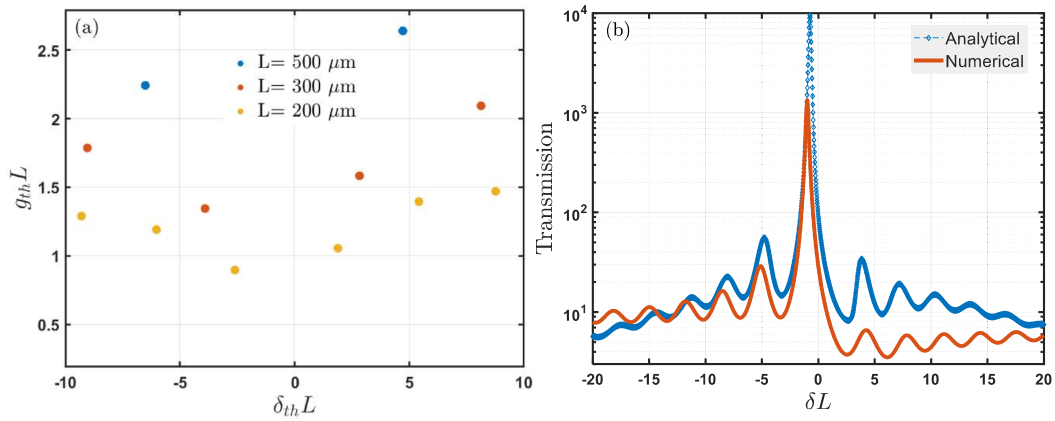

Figure 5. (a) The pair eigenvalues at different cavity lengths. The pair ($g_{\text{th}}L = 0.896$, $\delta_{\text{th}}L = -2.603$) corresponds to the optimal eigenvalue that reaches the lasing condition first. (b) The transmission coefficient as a function of the normalized detuning range, for analytical and numerical calculations. As expected, the analytical result presents the unbounded amplification of the signal at the output facet, while the numerical simulation accurately predicts a dominant single resonance with an amplification factor of 10^3, lasing at the predetermined operating wavelength, adjacent to the Bragg wavelength, represented by $\delta L = 0$. A slight asymmetry in the spectral background around the resonance is observed, which is consistent with the presence of complex coupling in higher-order grating structures.

eigenvalue of ($gL = 0.896$, $\delta L = -2.603$) at $L = 200\,\mu$m determine the lasing onset and suppress the parity symmetric mode which deteriorates the single-mode operation, as shown in figure 5(b). The selection of cavity length of $L = 200\,\mu$m causes closed eigenvalues with moderate net threshold gains, as expected, and slightly increases the gain chance of the oscillating side modes observed in figure 5(b).

Because the design functions as an on-chip source, it is necessary to ensure that the generated optical signal is directed toward the passive router located between the substrate and the lower emitter layers. To investigate optical propagation and its vertical transfer into the passive router, we use the Wave Optics module of the COMSOL software to compute the electric field in a longitudinal y–z cut through the center of the mesa. The guided mode at the MQW region is launched as the input port, and output ports are defined at the waveguiding ends to monitor propagation along the cavity. For this propagation study, we assume a cavity length of $L = 100$ μm, a substrate thickness of 30 μm, a free-space virtual cladding thickness of 8 μm, and PMLs on the outer boundaries, including along the y direction (epitaxial growth). The third-order trapezoidal grating is approximated by equivalent homogeneous layers [6,18,31] at the duty cycle of $\gamma = 0.72$. The resulting longitudinal field distribution is not intended to represent the standing-wave pattern inside a lasing DFB cavity. Instead, it is a wave optics propagation study used to visualize how the guided mode launched in the mesa region couples evanescently into the passive router in the longitudinal y–z plane.

Figure 6 shows that the guided field remains predominantly confined along the propagation direction while a weaker field component transfers into the passive router through vertical evanescent coupling. The layer indices shown in figure 6(b) follow the same numbering as table 1. The pronounced scattering observed near the beginning of the structure originates mainly from radiative and leaky field components excited at the input due to local index discontinuities and the resulting mode mismatch between the launched guided mode and the layered structure. As highlighted in figure 6(b), this radiative contribution is strongest over short propagation distances near the input and then rapidly decays, since these components are not guided and therefore leak into the surrounding regions. These radiative waves spread into the substrate region and are absorbed by the PML boundaries.

Figure 6(c) further confirms that the electric field and optical power remain mainly confined in the waveguiding region at the output, with the strongest field localized around the waveguiding stack (particularly the MQW region), and only vertical tails extending toward the passive router. The observed variation of the field amplitude coupled into the router along z is therefore expected in this passive propagation study. In the router, the coupled field can exhibit constructive and destructive interference along z due to the continuing energy exchange between the guided mode and the router mode, while the envelope is also influenced by passive attenuation included through the complex refractive indices of layers and by radiative waves absorbed by the PML. This redistribution of optical energy between the

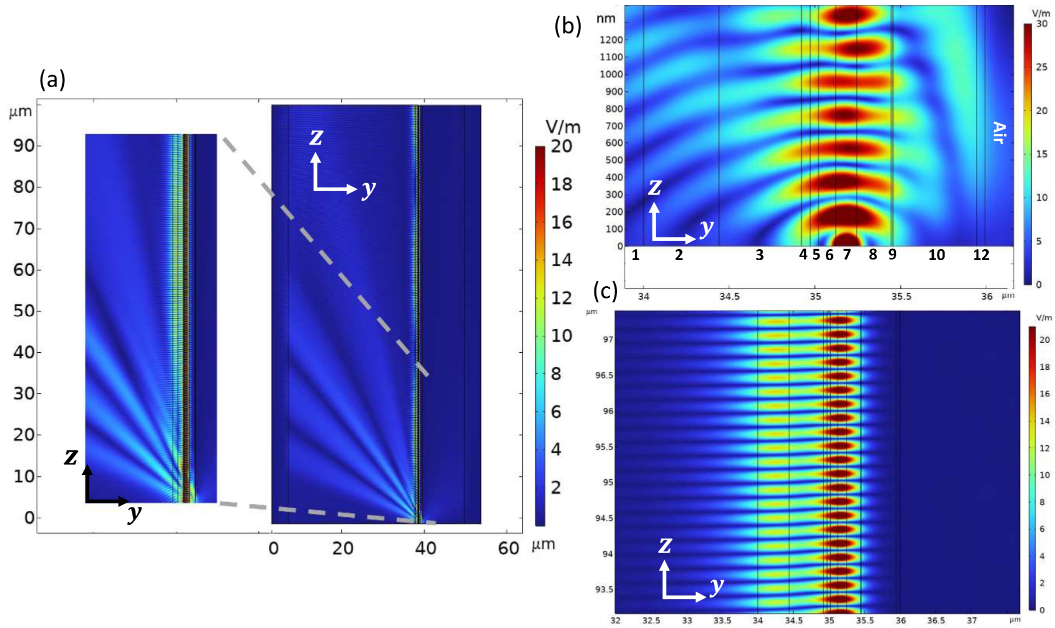

Figure 6. Electric field profile along the DFBL cavity obtained from a wave optics propagation study under guided mode excitation. (a) Longitudinal y–z cut through the mesa center, showing that the field remains confined in the waveguiding region while evanescently coupling into the passive router. The dashed markers indicate a zoomed region between $z = 0$ and 40 μm, showing the vertical coupling of the electric field into the passive router located on the substrate. (b) Enlarged view near the input, highlighting radiative wave components excited at the input that decay rapidly along z. (c) Enlarged view near the output, showing that the field remains mainly concentrated around the waveguiding stack (MQW region) with a weaker evanescent tail extending toward the router. The layer indices shown in (b) follow table 1.

mesa region and the router leads to an apparent variation of the local electric field magnitude along the propagation direction within the passive waveguiding router.

4. Experiment

To validate the DFBL modeling, optical power-current–voltage (PIV) and spectral response measurements are performed at a fixed temperature on available DFBL chips fabricated on a proprietary TAVI platform. The devices were designed and fabricated by commercial partners, and detailed epitaxial compositions and fabrication parameters are not disclosed.

A source meter unit is used to inject current by probing the DFBL signal and ground pads with areas of $230 \times 100\,\mu\text{m}^2$. The DFBL chip is mounted on a 6-axis micro-positioning stage that allows precise control over the alignment in both position and angle. A lensed fiber with a spot diameter of 5 μm is positioned in front of the laser facet using an independent 6-axis stage to collect light via edge-coupling (see figures 7(d) and (e)).

Figure 7(c) shows the average output optical power as a function of the bias current, collected by a lensed fiber placed adjacent to the DFBL output facet after vertical transfer into the passive router. Unlike buried-grating DFB lasers that often exhibit an abrupt threshold knee, the measured P–I characteristic of the regrowth-free N-up DFBL studied here can show a smoother threshold transition [38]. In particular, the third-order grating introduces distributed scattering losses, and the mesa design's principle can reduce injection efficiency; together, these effects broaden the transition from amplified spontaneous emission (ASE) to stimulated emission. We estimate the threshold current as $I_{\text{th}} \approx 25$ mA, as indicated in figure 7(c). The collected output power increases approximately linearly over the range of 100–150 mA and then deviates from linearity and begins to saturate at higher bias. The maximum collected output power is 43.5 mW at $I_{\text{bias}} = 200$ mA and $V = 4.985$ V, corresponding to an electrical dissipation of 997 mW, which is consistent with self-heating-induced saturation at high bias. The wall-plug efficiency (WPE) is defined as the ratio of optical output power to electrical power [39]. Accordingly, the highest measured WPE is 6.38% at $I_{\text{bias}} = 132.66$ mA, where the device consumes 503.2 mW of electrical power.

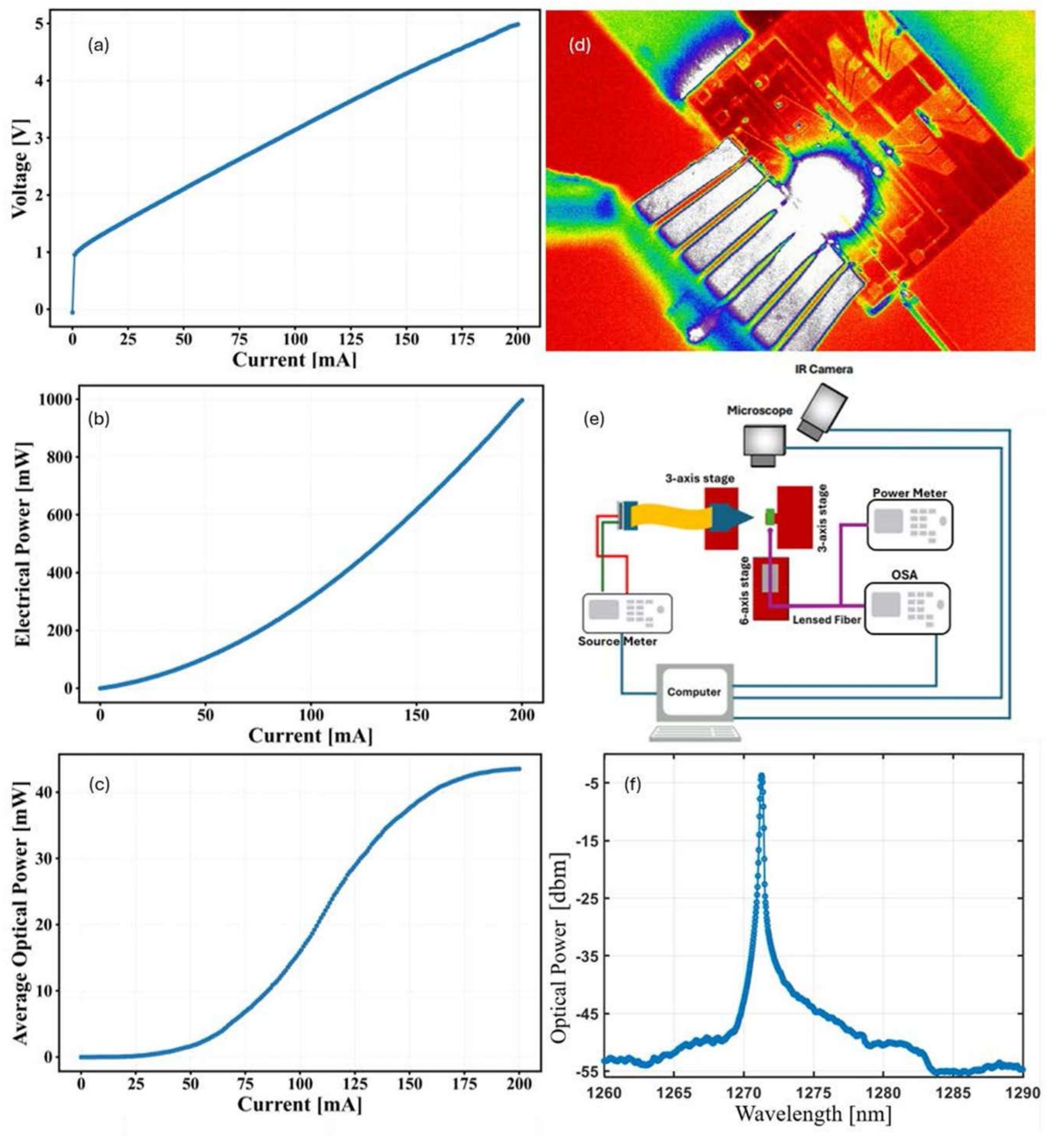

Figure 7. Experimental PIV measurements of the DFBL demonstrating the (a) voltage, (b) electrical power and (c) average optical output power as a function of bias current. (d) Microscope image of DFBL during a PIV experiment. Edge-coupling of the lensed fiber to the chip can be seen in the bottom right corner of the image. (e) Experimental schematic for extracting the PIV characteristics and spectral response of the DFBL. (f) Spectral power as a function of operating wavelength in the O-band, showing a dominant lasing mode at 1272.4 nm with SMSR of 40 dB.

Figure 7(f) presents the output spectrum under a fixed bias current of 75 mA, showing a dominant lasing peak at $\lambda = 1272.4$ nm with SMSR = 40 dB. Since this spectrum is measured well above threshold, including an ASE contribution that distorts the single-mode lasing around $\lambda = 1272.4$ nm. This broad tail can be attributed to the red-shift of the ASE peak spectrum toward the Bragg wavelength, reshaping the output spectral response, which may appear as an asymmetric, one-sided spectral tail [40, 41]. In our measurement, residual reflections in the edge-coupled lensed-fiber setup can also contribute to this asymmetry by perturbing the boundary condition at the output facet.

To assess the predictive capability of the modeling framework, we now compare the key spectral and operational characteristics obtained from the numerical analysis with those measured experimentally. The model predicts stable single-mode operation near the Bragg wavelength, with an optimized cavity length of $L = 200\,\mu$m and lasing expected around $\lambda \approx 1274$ nm, governed by the extracted eigenvalue pair and the complex coupling coefficient. Although the experimentally characterized devices differ in geometry from the optimized configuration and are described using an abstracted refractive-index

Table 2. Comparison of DFBL designs with output characteristics in the telecom band.

References	Platform	Grating type	λ (nm)	δ (nm)	I_{th} (mA)	L (μm)	κ (cm^{-1})	SMSR (dB)	Regrowth-free
This work	InP	3rd–surface etched v	1275	1	25	200	$9.5+j31.7$	40	Y
[42]	SOI+InP	1st–buried	1310	2.1	20	350	156	45	N
[43]	Si+GaAs	1st–laterally etched	1300	1	20	1500	45	50	N
[44]	InP	1st–buried	1320	3	10	250	120	50	N
[45]	GaAs	1st–laterally etched	1300	12	80	1500	20	50	Y
[23]	InP	3rd–laterally etched	1310	4	100	750	$2.32+j12$	45	Y

model, the comparison provides insight into how well the framework captures the dominant physical mechanisms governing DFBL behavior.

The modeling results reveal an optimized configuration at the shortest feasible cavity length of $L = 200$ μm. The corresponding complex coupling coefficient, $\kappa_{eff} = 9.5 + j31.7$ cm^{-1}, exhibits a strong coupling phase that lifts the stop-band and removes longitudinal mode degeneracy, resulting in a single-mode spectral response. The simulated spectral response predicts an operating wavelength of $\lambda = 1274$ nm, obtained from $\lambda = 2\pi N_{eff}/(M\pi/\Lambda - \delta_{th})$ with $N_{eff} = 3.2585$ and $\Lambda = 586.65$ nm.

The experimental measurements of the available DFBL chips, which have a cavity length different from that of the optimized modeled device, demonstrated single-mode lasing at $\lambda = 1272.4$ nm with an SMSR of 40 dB, a threshold current of 25 mA, a maximum optical output power of 43.5 mW at a bias current of 200 mA, and a WPE of 6.38 % at a bias current of 132.66 mA. The close correspondence between the experimental and simulated spectral responses validates the reliability of the modeling approach for optimizing stable single-mode operation of higher-order grating DFBL sources.

5. Conclusion

This work presents a modeling framework for analyzing and optimizing higher-order SEG DFBLs in vertically integrated photonic platforms. By extending the steady-state coupled-wave formalism to include both direct and radiative-wave-mediated coupling mechanisms, the approach captures the role of the complex coupling coefficient in determining threshold conditions and mode selection.

The analysis highlights the importance of the coupling phase in lifting mode degeneracy and enabling stable single-mode operation, particularly in short-cavity regimes. The developed semi-numerical workflow provides a practical and computationally efficient tool for identifying optimal design conditions, including cavity length and grating parameters, without requiring full knowledge of the underlying material stack. The agreement between the modeled behavior and experimental observations supports the validity of the approach for describing the spectral characteristics of DFBL devices implemented on regrowth-free vertically integrated platforms.

Table 2 provides a comparative summary of recent high-performance DFBL designs. Compared to previously reported devices, the present work demonstrates competitive single-mode performance with a relatively short cavity length (200 μm) and strong side-mode suppression, enabled by the engineered complex coupling coefficient associated with the higher-order grating. While some reported designs achieve lower threshold currents or higher coupling strengths, they often rely on regrowth processes or longer cavity lengths. In contrast, the present approach highlights the potential of regrowth-free, higher-order grating configurations to achieve compact and spectrally stable on-chip sources.

Overall, this work demonstrates that higher-order SEGs, when properly engineered, offer a viable path toward compact, single-mode on-chip laser sources. The presented modeling framework can support the design and optimization of such devices for integrated photonic systems in the telecom range, where fabrication constraints and limited access to detailed process information often necessitate abstraction at the device level.

Acknowledgements

The authors acknowledge Dr. Valery Tolstikhin (INTENGENT Inc.) for his contributions to the early stages of this project, including providing the device concept, physical model, and DFBL samples used in this study, as well as for initial technical discussions. The authors further acknowledge the TAVI

Consortium of Global Communications Semiconductors (GCS), Intengent, and VLC Photonics for supplying the DFBL devices. The devices, designed by Intengent and VLC Photonics, were fabricated at GCS based on the proprietary regrowth-free taper-assisted vertical integration (TAVI) platform. The devices, designed by Intengent and VLC Photonics, were fabricated at GCS based on the proprietary regrowth-free taper-assisted vertical integration (TAVI) platform. S A and K D acknowledge the support of Mitacs Accelerate program. L F and K D acknowledge uOttawa–Erlangen Max Planck Centre for Extreme and Quantum Photonics summer student exchange program. We acknowledge the support of the Natural Sciences and Engineering Research Council of Canada (NSERC) Discovery funding program. This research was supported in part by the Canada First Research Excellence Fund on Transformative Quantum Technologies.

Data availability statement

All data that support the findings of this study are included within the article (and any supplementary files).

Author contributions

Sina Aghili 0009-0006-9641-4241
Formal analysis (lead), Investigation (lead), Methodology (equal), Validation (lead), Visualization (equal), Writing – original draft (lead), Writing – review & editing (equal)

Ozan W Oner
Data curation (equal), Formal analysis (supporting), Investigation (supporting), Methodology (equal), Validation (supporting), Visualization (equal), Writing – original draft (supporting), Writing – review & editing (equal)

Tuhin Paul
Data curation (supporting), Formal analysis (supporting), Investigation (supporting), Writing – review & editing (supporting)

Mohammadreza Mohammadpour
Data curation (supporting), Formal analysis (supporting), Investigation (supporting), Validation (supporting), Visualization (supporting), Writing – original draft (supporting), Writing – review & editing (supporting)

Kushal Jayarathna 0009-0006-6791-8301
Data curation (supporting), Formal analysis (supporting), Investigation (supporting), Writing – original draft (supporting)

Lisa Fischer 0009-0007-9759-4405
Data curation (supporting), Formal analysis (supporting), Investigation (supporting)

Boris Rosenstein
Data curation (supporting), Formal analysis (supporting), Investigation (supporting), Methodology (supporting), Supervision (supporting)

Daniel H G Espinosa 0000-0003-0156-6623
Data curation (supporting), Formal analysis (supporting), Investigation (supporting), Methodology (equal), Supervision (equal), Validation (supporting), Writing – review & editing (equal)

Gabriel A S Flizikowski
Data curation (supporting), Formal analysis (supporting), Investigation (supporting), Methodology (supporting), Supervision (supporting)

Ksenia Dolgaleva 0000-0003-3643-679X
Data curation (supporting), Formal analysis (equal), Funding acquisition (lead), Investigation (equal), Methodology (equal), Project administration (lead), Resources (lead), Software (lead), Supervision (lead), Validation (equal), Visualization (supporting), Writing – original draft (supporting), Writing – review & editing (equal)

IOP Publishing J. Phys. D: Appl. Phys. 59 (2026) 245101 S Aghili et al

Appendix. Experimental setup and measurement details

This appendix provides additional details on the experimental setup, measurement procedures, and data acquisition methods used to characterize the DFBL devices. These details are included to support the reproducibility and interpretation of the experimental results presented in the main text.

The samples were mounted on a custom I3000 three-axis stage (Luminos Industries). The stage was designed to facilitate a standard thermo-electric cooler (TEC) positioned directly beneath the aluminum mount holding the sample. The excess heat of the system was removed by connecting the opposite temperature pole of the TEC to a heat exchanger. Nylon screws was used to ensure thermal isolation between both sides of the TEC, preventing parasitic heat conduction. A negative temperature coefficient (NTC) thermistor was bonded within a few millimeters of the chip using thermally conductive adhesive.

To ensure thermal stability during measurements, a closed-loop PID control system, comprising the TEC and the NTC thermistor as feedback components, was employed to maintain a constant temperature of 20°C. It should be noted that temperature fluctuations of approximately 1 °C result in a spectral shift of about 300 pm.

All dies were visually inspected using an optical microscope upon receipt from the foundry. Two wafers from separate fabrication runs were processed. Dies were categorized into three groups based on visual inspection: (i) no visible defects, (ii) minor defects, and (iii) unsuitable for testing. Only defect-free dies were used for optical and electrical characterization.

The P–I–V data shown in figure 8(a)–(c) represent the average of 50 independent sweeps performed on a single cavity. Each sweep used a current step of 1 mA over a range of 0–200 mA. The output power data presented in figure 8(d) were obtained via edge coupling using a lensed fiber and measured with a Yokogawa AQ6370C optical spectrum analyzer (OSA). The spectral range was 1260–1290 nm, recorded in 30 pm increments, with two optical power readings averaged at each wavelength point. The coupling efficiency was optimized through active alignment by iteratively adjusting each axis of the fiber position to maximize the detected output power.

All experiments were automated using `Python` scripts interfacing with a Keithley 2450 source meter, a Newport 2936R power meter, and the Yokogawa AQ6370C OSA. Python drivers for each piece of equipment were created, and experimental methods were then implemented for the PIV and spectral response characterization. The developed codes are available upon request from the corresponding author.

References

[1] Smit M, Williams K and Tol J V D 2019 Past, present and future of InP-based photonic integration *APL Photonics* **4** 050901
[2] Burghart D, Zhang K, Oberhausen W, Köninger A, Boehm G and Belkin M A 2025 Multi-color photonic integrated circuits based on homogeneous integration of quantum cascade lasers *Nat. Commun.* **16** 3563
[3] Niu S, Song Y, Zhang L, Chen Y, Liang L, Wang Y, Qin Li, Jia P, Qiu C and Lei Y *et al* 2022 Research progress of monolithic integrated DFB laser arrays for optical communication *Crystals* **12** 1006
[4] Kuntze S, Tolstikhin V, Fang W, Logvin Y, Watson C, Pimenov K, Moore R, Moore A, Wang H and Oogarah T 2010 Transmitter and receiver solutions for regrowth-free multi-guide vertical integration in InP *Integrated Photonics Research, Silicon and Nanophotonics* (Optica Publishing Group) p ITuC 5
[5] Rostami A, Nejad H B A, Qartavol R M and Saghai H R 2010 Tb/s optical logic gates based on quantum-dot semiconductor optical amplifiers *IEEE J. Quantum Electron.* **46** 354–60
[6] Ghafouri-Shiraz H 2003 *Distributed Feedback Laser Diodes and Optical Tunable Filters* (Wiley)
[7] Akiba S 2018 Distributed feedback laser *Encyclopedic Handbook of Integrated Optics* (CRC Press) pp 42–52
[8] Streifer W, Scifres D R and Burnham R D 1977 Coupled wave analysis of DFB and DBR lasers *IEEE J. Quantum Electron.* **13** 134–41
[9] Streifer W, Burnham R D and Scifres D R 1975 Effect of external reflectors on longitudinal modes of distributed feedback lasers *IEEE J. Quantum Electron.* **11** 154–61
[10] Kogelnik H and Shank C V 1972 Coupled-wave theory of distributed feedback lasers *J. Appl. Phys.* **43** 2327–35
[11] Millett R R, Hinzer K, Hall T J and Schriemer H 2008 Simulation analysis of higher order laterally-coupled distributed feedback lasers *IEEE J. Quantum Electron.* **44** 1145–51
[12] Roelkens G, *et al* 2022 Micro-transfer printing for heterogeneous Si photonic integrated circuits *IEEE J. Sel. Top. Quantum Electron.* **29** 1–14
[13] Augustin L M, Santos R, Haan E D, Kleijn S, Thijs P J A, Latkowski S, Zhao D, Yao W, Bolk J and Ambrosius H *et al* 2017 InP-based generic foundry platform for photonic integrated circuits *IEEE J. Sel. Top. Quantum Electron.* **24** 1–10
[14] Agrawal G P and Bobeck A H 1988 Modeling of distributed feedback semiconductor lasers with axially-varying parameters *IEEE J. Quantum Electron.* **24** 2407–14
[15] Wang L, Gen Lv, Fan Y, Tang K, Sun Z, Gong Y, Chen X, Chiu Y-J, Xiao R and Zhou Y 2024 Highly-reflective facet-coated multi-wavelength DFB laser array with exact wavelength spacings *Opt. Express* **32** 1843–50
[16] Saeidi S, Cheben P, Schmid J H and Berini P 2023 Dirac gratings *Opt. Express* **31** 31200–11
[17] Armaghani S and Rostami A 2024 Superimposed Bragg gratings and entangled biphoton dispersion management *Optics Continuum* **3** 354–67

[18] Kinoshita J 2002 Analysis of radiation mode effects on oscillating properties of DFB lasers *IEEE J. Quantum Electron.* **35** 1569–83
[19] Xun Li 2009 *Optoelectronic Devices: Design, Modeling and Simulation* (Cambridge University Press)
[20] Ding Z, Zhu A, Yang C, Zhan K, Chen Y, Ying Y and Siyuan Y 2025 Single-mode InAs/GaAs quantum-dot DFB laser with oxidized aperture confined surface grating *Appl. Phys. Lett.* **126** 142107.
[21] Zhang N, Qiu B, Zou Y, Fan J, Yue Y, Song Y, Ren Z, Qingmin Li and Xiaohui M 2024 Design and fabrication of 1064-nm high power laterally-coupled dfb semiconductor lasers *I Photonics Technology Letters* (IEEE)
[22] Fricke J, Decker J, Maaßdorf A, Wenzel H, Erbert G, Knigge A and Crump P 2017 DFB lasers with apodized surface gratings for wavelength stabilization and high efficiency *Semicond. Sci. Technol.* **32** 075012
[23] Millett R, Dridi K, Benhsaien A, Schriemer H, Hinzer K and Hall T 2011 Fabrication-tolerant 1310 nm laterally coupled distributed feedback lasers with high side mode suppression ratios *Photonics Nanostructures-Fundam. Appl.* **9** 111–8
[24] Jia S, Liu Z, *et al* 2025 High-efficiency gain-coupled distributed feedback semiconductor laser achieved using a metal surface grating *Opt. Express* **33** 33248–57
[25] Janjua B, Meng Lon I, Yan Z, Charles P, Chen E and Helmy A S 2021 Distributed feedback lasers using surface gratings in Bragg waveguides *Opt. Lett.* **46** 3689–92
[26] Tian K, Zou Y, Shi L, Zhang H, Yingtian X, Fan J, Tang H and Xiaohui M 2022 Simulation analysis of high-order high-duty-cycle surface gratings *Appl. Opt.* **61** 8147–54
[27] Ristic S, Pimenov K, Tolstikhin V, Watson C D and Logvin Y 2013 25 gbps re-growth-free externally modulated laser for multi-guide vertical integration in InP *Integrated Photonics Research, Silicon and Nanophotonics* (Optica Publishing Group) p IW5A–6
[28] Watson C, Tolstikhin V, Pimenov K, Fang W and Logvin Y 2011 On-chip emitter for regrowth-free multi-guide vertical integration in InP *IEEE Photonic Society 24th Annual Meeting* (IEEE) pp 336–7
[29] Watson C, Pimenov K, Tolstikhin V, Fang W, and Logvin Y. Vertically-coupled surface-etched grating DFB laser.
[30] Saeidi S, Fang W, Watson C, Logvin Y and Berini P 2021 Strong and short Bragg waveguide gratings with trapezoidal-shaped grooves *J. Lightwave Technol.* **39** 4395–401
[31] Saeidi S, Aghili S, Paul T, Rosenstein B, Tolstikhin V, Berini P and Dolgaleva K 2025 Finite-difference coupled-mode analysis of waveguide gratings and their optimization for single-mode dfb lasers *J. Opt. Soc. Am. B* **42** 438–45
[32] Tolstikhin V, Saeidi S and Dolgaleva K 2018 Design optimization and tolerance analysis of a spot-size converter for the taper-assisted vertical integration platform in InP *Appl. Opt.* **57** 3586–91
[33] *COMSOL Multiphysics®* v6.2, 2024 (available at: www.comsol.com)
[34] Bulashevich K A, Mymrin V F, Karpov S Y, Demidov D M and Ter-Martirosyan A L 2007 Effect of free-carrier absorption on performance of 808 nm AlGaAs-based high-power laser diodes *Semicond. Sci. Technol.* **22** 502
[35] Yariv A and Gover A 1975 Equivalence of the coupled-mode and Floquet-Bloch formalisms in periodic optical waveguides *Appl. Phys. Lett.* **26** 537
[36] Saeidi S and Berini P 2023 Tunable hybrid plasmonic semiconductor laser based on loss perturbation *IEEE J. Quantum Electron.* **59** 1–8
[37] Paul T 2022 Photonic integration with III-V semiconductor technologies *PhD Thesis* Université d'Ottawa/University of Ottawa
[38] Liau Z L, Flanders D C, and Walpole J N 1988 Process for making a mesa GaInAsP/InP distributed feedback laser
[39] Gokhale M R, Emanuel M A and Benjamin Li 2023 Record high efficiency high-power uncooled 1.31 μm CW-DFB lasers *2023 Optical Fiber Communications Conf. and Exhibition (OFC)* (IEEE) pp 1–3
[40] Grillot F'eric 2010 Advanced semiconductor laser *CNRS Foton* **20** 350
[41] Makino T and Glinski J 1988 Transfer matrix analysis of the amplified spontaneous emission of DFB semiconductor laser amplifiers *IEEE J. Quantum Electron.* **24** 1507–18
[42] Stankovic S, Jones R, Sysak M N, Heck J M, Roelkens G and Van Thourhout D 2012 Hybrid iii–v/si distributed-feedback laser based on adhesive bonding *IEEE Photonics Technol. Lett.* **24** 2155–8
[43] Wan Y,*et al* 2020 1.3 μm quantum dot-distributed feedback lasers directly grown on (001) si *Laser Photonics Rev.* **14** 2000037
[44] Liu G, Zhao G, Zhang G, Liu Y, Qiaoyin L and Guo W 2020 Experimental demonstration of directly modulated DFB lasers with negative chirp over wide temperature operation *J. Lightwave Technol.* **38** 3663–9
[45] Yang Z,*et al* 2022 High-performance distributed feedback quantum dot lasers with laterally coupled dielectric gratings *Photon. Res.* **10** 1271–9

Chapter 9

Conclusion

In this thesis, we investigated two important categories of optical components that are extensively employed in modern photonics. Accordingly, the first part of this dissertation was devoted to sub-wavelength structured components, so-called metamaterials and metasurfaces, where engineered resonant optical antennas or meta-atoms were used to tailor linear and nonlinear light–matter interactions for sensing, filtering, enhanced scattering, spontaneous emission control, and second harmonic generation (SHG). The second part focused on waveguide Bragg gratings (WBGs), with an emphasis on higher-order gratings as practical feedback mechanisms for distributed feedback (DFB) laser sources and regrowth-free photonic integration platforms.

To establish the principal physical mechanisms and modeling approaches for metasurfaces, Chapter 2 was devoted to the theoretical and numerical frameworks required to study both linear and nonlinear metamaterials and metasurfaces. In this chapter, a semi-numerical induced linear current density method was introduced as a practical tool for evaluating multipole contributions and far-field radiation from arbitrarily shaped optical antennas over a broad spectral range. This approach enabled systematic engineering of the scattering response of individual resonant meta-atoms and clarified how their resonant characteristics can be translated into metasurface designs for targeted applications. In addition, Chapter 2 established a conceptual bridge between linear and nonlinear metasurface modeling by introducing nonlinear scattering theory (NLST) as an accurate framework for analyzing SHG in plasmonic structures. Within this framework, induced nonlinear currents inside resonant meta-atoms act as distributed local sources responsible for generating the second harmonic (SH) response.

In Chapter 3, we numerically explored an InSb-based THz plasmonic metasurface that exhibited a narrow linewidth resonance with a high Q-factor. The main outcome of this chapter was to demonstrate that moving beyond a single sub-wavelength resonator toward a carefully engineered periodic meta-molecule array enables the emergence of a surface lattice resonance (SLR). This resonance arises from constructive far-field coupling of localized resonances mediated by an in-plane Rayleigh anomaly diffraction channel. This work further demonstrated that the spectral response of the metasurface can be actively tuned by modifying the free carrier concentration in InSb, and it highlighted the potential of such narrow resonances for applications including plasmonic tweezing and medium perturbation sensing.

As one of the promising applications of resonant optical antennas is the enhancement and control of the radiative decay rate of quantum emitters in coupled systems, Chapter 4 was devoted to the active control of spontaneous emission in the THz regime using magneto-optically tunable III–V based resonant antennas. This chapter developed the concept that the radiative decay channels of a THz emitter can be dynamically engineered using an InSb-based antenna, whose scattering response, including the contribution of multipole moments, can be tuned under weak magnetization. In addition, Chapter 4 proposed a hybrid Si–InSb active antenna concept to achieve strong radiative enhancement for magnetic dipole emitters. A modified deep-learning approach was also employed to optimize the emitter position and maximize the emission enhancement factor in the coupled emitter–antenna system.

In the subsequent two chapters, we focused on plasmonic SHG metasurfaces developed for near-field microscopy and label-free imaging applications. In Chapter 5, we investigated a plasmonic metasurface composed of asymmetrical L-shaped gold meta-atoms arranged in varied orientations, enabling the study of SH response in a structurally disordered system. The underlying motivation for this design was to imitate the evolution of polar biological assemblies, such as microtubules, which can exhibit intrinsic SH responses under intense optical excitation while potentially presenting structural disorder and dynamic reorientation *in vivo*. These characteristics are particularly relevant to the early diagnosis of neurodegenerative disorders. To model such systems, we engineered a nonlinear metasurface in which an intense pump light selectively activated only specific meta-atom orientations, such that the ensemble effectively behaved as a set of orientation-dependent channels for SH radiation. In this design, meta-atoms aligned with the incident polarization were efficiently excited by the pump light and generated strong plasmon-enhanced nonlinear currents, while other orientations remained largely inactive. This approach clarified how dominant emission channels can emerge within a disordered ensemble and provided a practical platform for studying SHG as a function of meta-atom orientation and pump polarization. In addition to numerical modeling, we experimentally characterized the linear optical response of the fabricated metasurface under different polarization states and obtained results in good agreement with the simulations. Finally, SHG microscopy measurements at a pump wavelength of 1030 nm confirmed that the fabricated metasurface produces a measurable SH signal with polarization-dependent contrast. However, the limited spatial resolution and the observed nonuniformity prevent direct identification of the contribution from each individual orientation.

As a complementary study to the previous chapter, Chapter 6 numerically investigated how a plasmonic SHG metasurface can simultaneously achieve improved near-field resolution and enhanced forward emission by comparing different plasmon-assisted SHG enhancement platforms. In this study, we compared an LSPR-based metasurface, an SLR-based periodic metasurface, and a hybrid configuration that benefits from the resonant coupling of localized and lattice responses. To this end, we proposed a bi-layer stacked metasurface consisting of a passive centrosymmetric array that support an SLR to provide field enhancement at the pump frequency, while an upper nonlinear metasurface layer, composed of asymmetrical meta-atoms, induces the local SH current components that govern the radiation process. The main outcome of this chapter was to demonstrate that this stacked architecture can concurrently improve near-field resolution and enhance the forward-collected SH signal, offering a practical platform for SHG microscopy and nanoscale bioimaging, where both signal strength and spatial resolution are critical.

The second part of this thesis focused on engineering WBGs as wavelength-selective feedback mechanisms for DFB laser sources. Chapter 7 established a theoretical framework for light propagation in grating waveguides by developing a coupled wave modeling approach for higher-order WBGs with arbitrary grating profiles. This framework incorporates the contributions of radiative waves in higher-order WBGs and clarified how a complex coupling coefficient can be exploited to control the feedback phase, lift longitudinal mode degeneracy, and engineer a robust single-mode spectral response in realistic DFB cavities.

Chapter 8 was devoted to optimizing the performance of a third-order surface-etched grating DFB laser operating in the telecom band. In this chapter, a threshold-oriented modeling framework was employed to identify the conditions required for stable single-mode operation at the shortest feasible cavity length. In the second part of the study, experimental characterization of available DFB laser chips fabricated on the proprietary taper assisted vertical integration (TAVI) platform was performed to benchmark and validate the modeling approach. The good agreement between simulations and experimental results confirmed the accuracy of the developed modeling process and demonstrated its effectiveness for optimizing DFB laser sources relying on higher-order and arbitrarily shaped grating profiles in regrowth-free integration platforms.

9.1 Future Works

As a prospective research direction, the spontaneous emission control concept developed in Chapter 4 can be extended from a coupled emitter–antenna configuration to a light-emitting metasurface, where a periodic resonant array modifies the electromagnetic environment of quantum emitters and reshapes both radiative and non-radiative decay channels. By exploiting extraordinary collective resonances, such as surface lattice resonances (SLRs), these metasurfaces can provide spectrally narrow and highly directional emission which is promising for single photon sources (SPSs) and dipole emitters, where high brightness and collection efficiency are essential.

Following our investigation of plasmonic SHG metasurfaces, as demonstrated in Chapter 5 and Chapter 6, this concept can be extended toward a hybrid nonlinear metasurface by integrating plasmonic resonators with ultrathin III–V semiconductor heterostructures whose nonlinear susceptibility is governed by intersubband transitions. Since the intersubband nonlinearity is primarily driven by the electric field component normal to the growth direction of the semiconductor layers, the plasmonic resonances can be engineered to enhance this out-of-plane near-field within the heterostructure region. As a result, this hybrid platform can combine the strong local field enhancement of plasmonic metasurfaces with the intrinsically large nonlinear response of semiconductor heterostructures, thereby enabling a significantly stronger nonlinear output compared to bare plasmonic metasurfaces.

A further promising direction emerging from this thesis is the development of nonlinear THz metamaterials that exploit the magneto-optical response of III–V semiconductors, particularly InSb, which remains unexplored in nonlinear THz metasurface platforms. In InSb-based resonant structures, nonlinear interactions can be intensified through Lorentz-force contributions together with higher-order multipole moments, leading to SH responses that can exceed those obtained using conventional plasmon-assisted enhancement mechanisms alone. Extending this concept to InSb THz metasurfaces operating in the magnetoplasmonic regime can enable a dynamically reconfigurable nonlinear platform, where even weak static magnetic fields can shift or split nonlinear resonances and provide active control over the spectral characteristics of the generated nonlinear emission.

For modeling and optimizing the performance of DFB laser sources with higher-order gratings, we used a threshold-oriented semi-numerical framework to study the cavity behavior at lasing onset by solving the steady-state coupled waveequations. In this modeling approach, the induced gain and the refractive index change were assumed to be longitudinally uniform along the cavity. This assumption enabled us to assess threshold lasing conditions under an equilibrium approximation and, therefore, neglect the time evolution of carrier and photon densities by adopting a steady-state condition. For future work related to Chapter 7 and Chapter 8, to evaluate the dynamic response of a higher-order grating DFB laser, the modified coupled wavee quations should be solved in the time domain, where longitudinal variations of carrier density, photon distribution, bias-induced refractive index change, and thermal diffusion play crucial roles in the transient behavior. This modeling framework allows us to investigate spatial non-uniformities in the carrier and photon distributions, namely longitudinal spatial hole burning, which can increase the probability of side-mode lasing and deteriorate the stability of single-mode operation under practical conditions.

References

[1] Patrice Genevet et al. "Recent advances in planar optics: from plasmonic to dielectric metasurfaces". In: *Optica* 4.1 (2017), pp. 139–152.

[2] Richard Soref. "The past, present, and future of silicon photonics". In: *IEEE Journal of selected topics in quantum electronics* 12.6 (2007), pp. 1678–1687.

[3] Joseph W Goodman and Mary E Cox. *Introduction to Fourier optics*. 1969.

[4] Evgeni Popov. "Introduction to diffraction gratings: summary of applications". In: *Gratings: theory and numeric applications* (2012), pp. 1–1.

[5] JM Lerner et al. "Diffraction Gratings Ruled And HolographicÃ¢ â ,¬ â€? A Review". In: *Periodic Structures, Gratings, Moire Patterns, and Diffraction Phenomena I*. Vol. 240. SPIE. 1981, pp. 82–89.

[6] Takeshi Namioka. "17. Diffraction gratings". In: *Experimental Methods in the Physical Sciences*. Vol. 31. Elsevier, 1998, pp. 347–377.

[7] Erwin G Loewen. "Diffraction gratings, ruled and holographic". In: *Applied optics and optical engineering* 9 (2012), pp. 33–71.

[8] Michael P Chrisp. *Convex diffraction grating imaging spectrometer*. Tech. rep. 1999.

[9] Nicolas Bonod and Jérôme Neauport. "Diffraction gratings: from principles to applications in high-intensity lasers". In: *Advances in Optics and Photonics* 8.1 (2016), pp. 156–199.

[10] Hou-Tong Chen, Antoinette J Taylor, and Nanfang Yu. "A review of metasurfaces: physics and applications". In: *Reports on progress in physics* 79.7 (2016), p. 076401.

[11] Muhammad A Butt, Nikolay L Kazanskiy, and Svetlana N Khonina. "Advances in waveguide Bragg grating structures, platforms, and applications: an up-to-date appraisal". In: *Biosensors* 12.7 (2022), p. 497.

[12] Jacob Scheuer. "Metasurfaces-based holography and beam shaping: engineering the phase profile of light". In: *Nanophotonics* 6.1 (2017), pp. 137–152.

[13] Guoxing Zheng et al. "Metasurface holograms reaching 80% efficiency". In: *Nature nanotechnology* 10.4 (2015), pp. 308–312.

[14] Nanfang Yu and Federico Capasso. "Flat optics with designer metasurfaces". In: *Nature materials* 13.2 (2014), pp. 139–150.

[15] Masaki Funabashi et al. "Recent advances in DFB lasers for ultradense WDM applications". In: *IEEE Journal of selected topics in quantum electronics* 10.2 (2004), pp. 312–320.

[16] Hamed Saghaei, Payam Elyasi, and Bhavin J Shastri. "Sinusoidal and rectangular Bragg grating filters: Design, fabrication, and comparative analysis". In: *Journal of Applied Physics* 132.6 (2022).

[17] Mostafa Khalil et al. "Electrically reconfigurable waveguide Bragg grating filters". In: *Optics Express* 30.22 (2022), pp. 39643–39651.

[18] Jaekyung Kim et al. "Tunable metasurfaces towards versatile metalenses and metaholograms: a review". In: *Advanced Photonics* 4.2 (2022), pp. 024001–024001.

[19] Pierre Berini. "Optical beam steering using tunable metasurfaces". In: *Acs Photonics* 9.7 (2022), pp. 2204–2218.

[20] Siqi Li et al. "Metasurface polarization optics: phase manipulation for arbitrary polarization conversion condition". In: *Physical Review Letters* 134.2 (2025), p. 023803.

[21] Sébastien Héron and Patrice Genevet. "1 Metasurfaces, Then and Now". In: *Nonlinear Meta-Optics*. CRC Press, 2020, pp. 1–40.

[22] Jun Guan et al. "Light–matter interactions in hybrid material metasurfaces". In: *Chemical Reviews* 122.19 (2022), pp. 15177–15203.

[23] M Saad Bin-Alam et al. "Ultra-high-Q resonances in plasmonic metasurfaces". In: *Nature communications* 12.1 (2021), p. 974.

[24] Dmitry Khlopin et al. "Lattice modes and plasmonic linewidth engineering in gold and aluminum nanoparticle arrays". In: *Journal of the Optical Society of America B* 34.3 (2017), pp. 691–700.

[25] Artur Movsesyan et al. "Engineering strongly chiral plasmonic lattices with achiral unit cells for sensing and photodetection". In: *Advanced Optical Materials* 10.14 (2022), p. 2101943.

[26] Liye Li et al. "Reflection-type surface lattice resonances in all-metal metasurfaces for refractive index sensing". In: *Photonics Research* 11.12 (2023), pp. 2210–2221.

[27] Lei Xiong et al. "Extremely narrow and actively tunable Mie surface lattice resonances in GeSbTe metasurfaces: Study". In: *Nanomaterials* 12.4 (2022), p. 701.

[28] Lior Michaeli et al. "Nonlinear surface lattice resonance in plasmonic nanoparticle arrays". In: *Physical review letters* 118.24 (2017), p. 243904.

[29] Frédéric Laux, Nicolas Bonod, and Davy Gérard. "Single emitter fluorescence enhancement with surface lattice resonances". In: *The Journal of Physical Chemistry C* 121.24 (2017), pp. 13280–13289.

[30] Stefan A Maier et al. *Plasmonics: fundamentals and applications*. Vol. 1. Springer, 2007.

[31] Ghulam Abbas Khan, Yonghua Lu, and Pei Wang. "Plasmon-enhanced refractive index sensing of biomolecules based on metal–dielectric–metal metasurface in the infrared regime". In: *ACS omega* 9.1 (2023), pp. 1416–1423.

[32] Katherine A Willets and Richard P Van Duyne. "Localized surface plasmon resonance spectroscopy and sensing". In: *Annu. Rev. Phys. Chem.* 58.1 (2007), pp. 267–297.

[33] Valentina Di Meo et al. "Metasurface based on cross-shaped plasmonic nanoantennas as chemical sensor for surface-enhanced infrared absorption spectroscopy". In: *Sensors and Actuators B: Chemical* 286 (2019), pp. 600–607.

[34] Gleb M Akselrod et al. "Probing the mechanisms of large Purcell enhancement in plasmonic nanoantennas". In: *Nature Photonics* 8.11 (2014), pp. 835–840.

[35] Martti Kauranen and Anatoly V Zayats. "Nonlinear plasmonics". In: *Nature photonics* 6.11 (2012), pp. 737–748.

[36] Alexei A Maradudin, J Roy Sambles, and William L Barnes. *Modern plasmonics*. Vol. 4. Elsevier, 2014.

[37] Kirill Koshelev and Yuri Kivshar. "Dielectric resonant metaphotonics". In: *Acs Photonics* 8.1 (2020), pp. 102–112.

[38] Su Xu et al. "Experimental observation of toroidal dipole modes in all-dielectric metasurfaces". In: *Advanced Optical Materials* 7.4 (2019), p. 1801166.

[39] Guanqiao Zhang et al. "Toroidal dipole resonances in all-dielectric oligomer metasurfaces". In: *Advanced Theory and Simulations* 2.10 (2019), p. 1900123.

[40] Seyedeh Mahsa Kamali et al. "A review of dielectric optical metasurfaces for wavefront control". In: *Nanophotonics* 7.6 (2018), pp. 1041–1068.

[41] Nicolas Bonod. "Controlling spontaneous emission with dielectric optical antennas". In: *Dielectric Metamaterials*. Elsevier, 2020, pp. 109–144.

[42] Masayoshi Tonouchi. "Cutting-edge terahertz technology". In: *Nature photonics* 1.2 (2007), pp. 97–105.

[43] John F Federici et al. "THz imaging and sensing for security applications—explosives, weapons and drugs". In: *Semiconductor science and technology* 20.7 (2005), S266.

[44] Anastasia Rusina et al. "Nanoconcentration of terahertz radiation in plasmonic waveguides". In: *Optics express* 16.23 (2008), pp. 18576–18589.

[45] Xueqian Zhang et al. "Terahertz surface plasmonic waves: a review". In: *Advanced Photonics* 2.1 (2020), pp. 014001–014001.

[46] Jan Chochol et al. "Plasmonic behavior of III-V semiconductors in far-infrared and terahertz range". In: *Journal of the European Optical Society-Rapid Publications* 13.1 (2017), p. 13.

[47] Liyuan Deng et al. "Direct optical tuning of the terahertz plasmonic response of InSb subwavelength gratings". In: *Advanced Optical Materials* 1.2 (2013), pp. 128–132.

[48] Sina Aghili et al. "THz plasmonic metasurface based on a periodic array of InSb metamolecules with narrow resonances". In: *Optics Communications* 508 (2022), p. 127805.

[49] Lingbo Xia et al. "Terahertz surface magnetoplasmons modulation with magnetized InSb hole array sheet". In: *Optics Communications* 446 (2019), pp. 84–87.

[50] Jan Chochol et al. "Magneto-optical properties of InSb for terahertz applications". In: *AIP Advances* 6.11 (2016), p. 115021.

[51] Fei Fan et al. "Terahertz polarization converter and one-way transmission based on double-layer magneto-plasmonics of magnetized InSb". In: *Optics express* 24.23 (2016), pp. 26431–26443.

[52] A Márquez and R Esquivel-Sirvent. "Terahertz response of plasmonic nanoparticles: Plasmonic Zeeman Effect". In: *Optics Express* 28.26 (2020), pp. 39005–39016.

[53] Grigorios P Zouros et al. "Three-dimensional giant invisibility to superscattering enhancement induced by Zeeman-split modes". In: *ACS Photonics* 8.5 (2021), pp. 1407–1412.

[54] Sina Aghili et al. "Dynamic Control of Spontaneous Emission Using Magnetized InSb Higher-Order-Mode Antennas". In: *arXiv preprint arXiv:2311.07083* (2023).

[55] Hongchi Lei. "GaAs-based distributed feedback lasers based on GaAs-InGaP regrowth technology". PhD thesis. University of Sheffield, 2017.

[56] Xiaolin Li et al. "Characterization of photonic temperature sensors by comparative human body measurements using waveguide Bragg grating and microring resonator-based sensors". In: *IEEE Sensors Journal* (2025).

[57] Nicola Andriolli, Francesca Bontempi, and Giampiero Contestabile. "InP monolithically integrated transmitters based on high speed directly modulated DFB lasers". In: *IEEE Journal of Selected Topics in Quantum Electronics* 26.5 (2020), pp. 1–6.

[58] Ronald R Millett. "Modeling fabrication, and measurement of laterally-coupled distributed feedback lasers". PhD thesis. University of Ottawa (Canada), 2009.

[59] Marshall I Nathan et al. "Stimulated emission of radiation from GaAs p-n junctions". In: *Applied Physics Letters* 1.3 (1962), pp. 62–64.

[60] Zhores Alferov. "Double heterostructure lasers: early days and future perspectives". In: *IEEE Journal of Selected Topics in Quantum Electronics* 6.6 (2000), pp. 832–840.

[61] Ilya S Tarasov et al. "High power CW (16 W) and pulse (145 W) laser diodes based on quantum well heterostructures". In: *Spectrochimica Acta Part A: Molecular and Biomolecular Spectroscopy* 66.4-5 (2007), pp. 819–823.

[62] Larry A Coldren, Scott W Corzine, and Milan L Mashanovitch. *Diode lasers and photonic integrated circuits*. John Wiley & Sons, 2012.

[63] Yoshinori Nomura et al. "Mode locking in Fabry-Perot semiconductor lasers". In: *Physical Review A* 65.4 (2002), p. 043807.

[64] Shyh Wang. "Principles of distributed feedback and distributed Bragg-reflector lasers". In: *IEEE Journal of Quantum Electronics* 10.4 (1974), pp. 413–427.

[65] Kirill Pimenov et al. "Analysis of high-order surface etched gratings for longitudinal mode selection in DFB lasers". In: *Numerical Simulation of Optoelectronic Devices*. IEEE. 2010, pp. 49–50.

[66] Q Gaimard et al. "Distributed feedback GaSb based laser diodes with buried grating". In: *Applied Physics Letters* 104.16 (2014).

[67] Shinichi Sakamoto et al. "Strongly index-coupled membrane BH-DFB lasers with surface corrugation grating". In: *IEEE Journal of Selected Topics in Quantum Electronics* 13.5 (2007), pp. 1135–1141.

[68] AS Gozdz et al. “Fast direct e-beam lithographic fabrication of first-order gratings for 1.3 μm DFB lasers”. In: *Electronics Letters* 24.2 (1988), pp. 123–125.

[69] Pengfei Zhang et al. “850 nm GaAs/AlGaAs DFB lasers with shallow surface gratings and oxide aperture”. In: *Optics express* 27.22 (2019), pp. 31225–31234.

[70] R Millett et al. “Fabrication-tolerant 1310 nm laterally coupled distributed feedback lasers with high side mode suppression ratios”. In: *Photonics and Nanostructures-Fundamentals and Applications* 9.2 (2011), pp. 111–118.

[71] M Kamp et al. “Lateral coupling–a material independent way to complex coupled DFB lasers”. In: *Optical Materials* 17.1-2 (2001), pp. 19–25.

[72] ML Osowski et al. “A strained-layer InGaAs-GaAs asymmetric cladding gain-coupled DFB laser with titanium surface gratings by metalorganic chemical vapor deposition”. In: *IEEE Photonics Technology Letters* 9.4 (2002), pp. 422–424.

[73] Jorge A Holguín-Lerma, Tien Khee Ng, and Boon S Ooi. “Narrow-line InGaN/GaN green laser diode with high-order distributed-feedback surface grating”. In: *Applied Physics Express* 12.4 (2019), p. 042007.

[74] VI Tolstikhin et al. “One-step growth optical transceiver PIC in InP”. In: *2009 35th European Conference on Optical Communication*. IEEE. 2009, pp. 1–2.

[75] Shen Niu et al. “Research progress of monolithic integrated DFB laser arrays for optical communication”. In: *Crystals* 12.7 (2022), p. 1006.

[76] William Streifer, D Scifres, and Robert Burnham. “coupled waveanalysis of DFB and DBR lasers”. In: *IEEE Journal of Quantum Electronics* 13.4 (2003), pp. 134–141.

[77] Herwig Kogelnik and Charles V Shank. “Coupled-wave theory of distributed feedback lasers”. In: *Journal of applied physics* 43.5 (1972), pp. 2327–2335.

[78] William Streifer, D Scifres, and Robert Burnham. “Coupled wave analysis of DFB and DBR lasers”. In: *IEEE Journal of Quantum Electronics* 13.4 (1977), pp. 134–141.

[79] Xun Li. *Optoelectronic devices: design, modeling, and simulation*. Cambridge University Press, 2009.

[80] Lukas Novotny and Bert Hecht. *Principles of nano-optics*. Cambridge university press, 2012.

[81] Hilmi Volkan Demir and Sergey V Gaponenko. *Applied nanophotonics*. Cambridge University Press, 2018.

[82] Nina Meinzer, William L Barnes, and Ian R Hooper. "Plasmonic meta-atoms and metasurfaces". In: *Nature photonics* 8.12 (2014), pp. 889–898.

[83] M. N. Polyanskiy. "Refractiveindex.info database of optical constants". In: *Scientific Data* 11 (2024). Accessed via `https://refractiveindex.info/`, p. 94. DOI: `10.1038/s41597-023-02898-2`.

[84] M Zahirul Alam et al. "Large optical nonlinearity of nanoantennas coupled to an epsilon-near-zero material". In: *Nature Photonics* 12.2 (2018), pp. 79–83.

[85] M Zahirul Alam, Israel De Leon, and Robert W Boyd. "Large optical nonlinearity of indium tin oxide in its epsilon-near-zero region". In: *Science* 352.6287 (2016), pp. 795–797.

[86] Mikhail V Rybin et al. "High-Q supercavity modes in subwavelength dielectric resonators". In: *Physical review letters* 119.24 (2017), p. 243901.

[87] Sheng Liu et al. "Huygens' metasurfaces enabled by magnetic dipole resonance tuning in split dielectric nanoresonators". In: *Nano letters* 17.7 (2017), pp. 4297–4303.

[88] John David Jackson. *Classical electrodynamics*. John Wiley & Sons, 2021.

[89] COMSOL AB. *COMSOL Multiphysics® (Version 6.2)*. Computer software. Available at: `https://www.comsol.com`. Stockholm, Sweden, 2023.

[90] Andrey B Evlyukhin and Boris N Chichkov. "Multipole decompositions for directional light scattering". In: *Physical Review B* 100.12 (2019), p. 125415.

[91] Rasoul Alaee, Carsten Rockstuhl, and Ivan Fernandez-Corbaton. "Exact multipolar decompositions with applications in nanophotonics". In: *Advanced Optical Materials* 7.1 (2019), p. 1800783.

[92] Egor A Gurvitz et al. "The high-order toroidal moments and anapole states in all-dielectric photonics". In: *Laser & Photonics Reviews* 13.5 (2019), p. 1800266.

[93] Jungho Mun et al. "Describing meta-atoms using the exact higher-order polarizability tensors". In: *ACS Photonics* 7.5 (2020), pp. 1153–1162.

[94] V Savinov, VA Fedotov, and Nikolay I Zheludev. "Toroidal dipolar excitation and macroscopic electromagnetic properties of metamaterials". In: *Physical Review B* 89.20 (2014), p. 205112.

[95] Martin Moskovits. “Surface-enhanced spectroscopy”. In: *Reviews of modern physics* 57.3 (1985), p. 783.

[96] I Rodriguez et al. “Silicon nanoparticles as Raman scattering enhancers”. In: *Nanoscale* 6.11 (2014), pp. 5666–5670.

[97] Mario Agio. “Optical antennas as nanoscale resonators”. In: *Nanoscale* 4.3 (2012), pp. 692–706.

[98] Zhiyuan Qian et al. “Spontaneous emission in micro-or nanophotonic structures”. In: *PhotoniX* 2.1 (2021), p. 21.

[99] A Femius Koenderink. “Single-photon nanoantennas”. In: *ACS photonics* 4.4 (2017), pp. 710–722.

[100] Edward M Purcell, Henry Cutler Torrey, and Robert V Pound. “Resonance absorption by nuclear magnetic moments in a solid”. In: *Physical review* 69.1-2 (1946), p. 37.

[101] Matthew Pelton. “Modified spontaneous emission in nanophotonic structures”. In: *Nature Photonics* 9.7 (2015), pp. 427–435.

[102] Ruoxi Wang et al. “Enhanced spontaneous emission rates for single isoelectronic luminescence centers in photonic crystal cavities”. In: *ACS Photonics* 7.2 (2020), pp. 321–326.

[103] Igor Aharonovich, Dirk Englund, and Milos Toth. “Solid-state single-photon emitters”. In: *Nature photonics* 10.10 (2016), pp. 631–641.

[104] Wenshan Cai and Vladimir Shalaev. “Optical Metamaterials”. In: (2010).

[105] Willie J Padilla, Dimitri N Basov, and David R Smith. “Negative refractive index metamaterials”. In: *Materials today* 9.7-8 (2006), pp. 28–35.

[106] Wei Ting Chen, Alexander Y Zhu, and Federico Capasso. “Flat optics with dispersion-engineered metasurfaces”. In: *Nature Reviews Materials* 5.8 (2020), pp. 604–620.

[107] Jian Wang and Jing Du. “Plasmonic and dielectric metasurfaces: design, fabrication and applications”. In: *Applied Sciences* 6.9 (2016), p. 239.

[108] Aso Rahimzadegan et al. “A comprehensive multipolar theory for periodic metasurfaces”. In: *Advanced Optical Materials* 10.10 (2022), p. 2102059.

[109] Pavel D Terekhov et al. “Multipole analysis of dielectric metasurfaces composed of nonspherical nanoparticles and lattice invisibility effect”. In: *Physical Review B* 99.4 (2019), p. 045424.

[110] Karim Achouri and Christophe Caloz. *Electromagnetic metasurfaces: Theory and applications*. John Wiley & Sons, 2021.

[111] Anton D Utyushev, Vadim I Zakomirnyi, and Ilia L Rasskazov. "Collective lattice resonances: Plasmonics and beyond". In: *Reviews in Physics* 6 (2021), p. 100051.

[112] Bharath Bangalore Rajeeva, Linhan Lin, and Yuebing Zheng. "Design and applications of lattice plasmon resonances". In: *Nano Research* 11.9 (2018), pp. 4423–4440.

[113] Sergey Kruk and Yuri Kivshar. "Functional meta-optics and nanophotonics governed by Mie resonances". In: *Acs Photonics* 4.11 (2017), pp. 2638–2649.

[114] Jorge Olmos-Trigo et al. "Kerker conditions upon lossless, absorption, and optical gain regimes". In: *Physical Review Letters* 125.7 (2020), p. 073205.

[115] Andrey E Miroshnichenko et al. "Nonradiating anapole modes in dielectric nanoparticles". In: *Nature communications* 6.1 (2015), p. 8069.

[116] Kseniia V Baryshnikova et al. "Optical anapoles: concepts and applications". In: *Advanced Optical Materials* 7.14 (2019), p. 1801350.

[117] Andreas Tittl et al. "Imaging-based molecular barcoding with pixelated dielectric metasurfaces". In: *Science* 360.6393 (2018), pp. 1105–1109.

[118] Robert W Boyd, Alexander L Gaeta, and Enno Giese. "Nonlinear optics". In: *Springer Handbook of Atomic, Molecular, and Optical Physics*. Springer, 2008, pp. 1097–1110.

[119] Kevin O'Brien et al. "Predicting nonlinear properties of metamaterials from the linear response". In: *Nature materials* 14.4 (2015), pp. 379–383.

[120] Heykel Aouani et al. "Third-harmonic-upconversion enhancement from a single semiconductor nanoparticle coupled to a plasmonic antenna". In: *Nature nanotechnology* 9.4 (2014), pp. 290–294.

[121] Antonino Calá Lesina, Pierre Calá Berini, and Lora Calá Ramunno. "Modelling of nanophotonic non-linear metasurfaces". In: IET.

[122] Christian Schlickriede et al. "Imaging through nonlinear metalens using second harmonic generation". In: *Advanced Materials* 30.8 (2018), p. 1703843.

[123] Feifan Wang et al. "Nanoscale on-chip all-optical logic parity checker in integrated plasmonic circuits in optical communication range". In: *Scientific reports* 6.1 (2016), p. 24433.

[124] Radoslaw Kolkowski et al. "Nonlinear nonlocal metasurfaces". In: *Applied Physics Letters* 122.16 (2023).

[125] Polina Vabishchevich and Yuri Kivshar. "Nonlinear photonics with metasurfaces". In: *Photonics Research* 11.2 (2023), B50–B64.

[126] Michele Celebrano et al. "Mode matching in multiresonant plasmonic nanoantennas for enhanced second harmonic generation". In: *Nature nanotechnology* 10.5 (2015), pp. 412–417.

[127] Robert Czaplicki et al. "Less is more: enhancement of second-harmonic generation from metasurfaces by reduced nanoparticle density". In: *Nano letters* 18.12 (2018), pp. 7709–7714.

[128] Ehsan Mobini et al. "Giant asymmetric second-harmonic generation in bianisotropic metasurfaces based on bound states in the continuum". In: *Acs Photonics* 8.11 (2021), pp. 3234–3240.

[129] Mohammad Karimi et al. "Time-varying gradient metasurface with applications in all-optical beam steering". In: *Nanophotonics* 12.9 (2023), pp. 1733–1740.

[130] Yiyu Zhou et al. "Broadband frequency translation through time refraction in an epsilon-near-zero material". In: *Nature communications* 11.1 (2020), p. 2180.

[131] Thomas Pertsch and Yuri Kivshar. "Nonlinear optics with resonant metasurfaces". In: *MRS bulletin* 45.3 (2020), pp. 210–220.

[132] Robert C Miller and William A Nordland. "Absolute signs of second-harmonic generation coefficients of piezoelectric crystals". In: *Physical Review B* 2.12 (1970), p. 4896.

[133] Cristian Ciracı, John B Pendry, and David R Smith. "Hydrodynamic model for plasmonics: a macroscopic approach to a microscopic problem". In: *ChemPhysChem* 14.6 (2013), pp. 1109–1116.

[134] Michael Scalora et al. "Second-and third-harmonic generation in metal-based structures". In: *Physical Review A—Atomic, Molecular, and Optical Physics* 82.4 (2010), p. 043828.

[135] Esmaeil Rahimi et al. "Lorentz nanoplasmonics for nonlinear generation". In: *Nano Letters* 18.12 (2018), pp. 8030–8034.

[136] Esmaeil Rahimi and Reuven Gordon. "Nonlinear plasmonic metasurfaces". In: *Advanced Optical Materials* 6.18 (2018), p. 1800274.

[137] J Butet et al. "New numerical methods for the design of efficient nonlinear plasmonic sources of light and nanosensors". In: *Plasmonics: Design, Materials, Fabrication, Characterization, and Applications XIV*. Vol. 9921. SPIE. 2016, pp. 40–45.

[138] Sina Aghili and Ksenia Dolgaleva. "Second Harmonic Enhancement with a U-shaped InSb Plasmonic Antenna in the THz Regime". In: *Nonlinear Photonics*. Optica Publishing Group. 2024, NpTh3C–6.

[139] Taher Zahedi, Zaker Hossein Firouzeh, and Abolghasem Zeidaabadi Nezhad. "Design and modeling of third-harmonic plasmonic metasurfaces coupled to multi-quantum well structures". In: *Journal of the Optical Society of America B* 36.9 (2019), pp. 2429–2437.

[140] Sina Aghili et al. "Dynamic control of spontaneous emission using magnetized InSb higher-order-mode antennas". In: *Journal of Physics: Photonics* 6.3 (2024), p. 035011.

[141] Konstantin Sokolov et al. "Optical systems for in vivo molecular imaging of cancer". In: *Technology in cancer research & treatment* 2.6 (2003), pp. 491–504.

[142] Stefan W Hell. "Far-field optical nanoscopy". In: *science* 316.5828 (2007), pp. 1153–1158.

[143] Masahito Yamanaka et al. "SAX microscopy with fluorescent nanodiamond probes for high-resolution fluorescence imaging". In: *Biomedical optics express* 2.7 (2011), pp. 1946–1954.

[144] Yunze Yang et al. "Label-free tracking of single organelle transportation in cells with nanometer precision using a plasmonic imaging technique". In: *Small* 11.24 (2015), pp. 2878–2884.

[145] Silu Zhang et al. "Recent advances in nonlinear optics for bio-imaging applications". In: *Opto-Electronic Advances* 3.10 (2020), pp. 200003–1.

[146] Francisco J Ávila. "A Review of non-linear optical imaging techniques for cancer detection". In: *Optics* 5.4 (2024), pp. 416–433.

[147] Wei Min et al. "Coherent nonlinear optical imaging: beyond fluorescence microscopy". In: *Annual review of physical chemistry* 62.1 (2011), pp. 507–530.

[148] Ji-Xin Cheng and X Sunney Xie. "Vibrational spectroscopic imaging of living systems: An emerging platform for biology and medicine". In: *Science* 350.6264 (2015), aaa8870.

[149] Fritjof Helmchen and Winfried Denk. "Deep tissue two-photon microscopy". In: *Nature methods* 2.12 (2005), pp. 932–940.

[150] David N Nikogosyan. *Nonlinear optical crystals: a complete survey*. Springer, 2005.

[151] Jorge Bravo-Abad et al. "Enhanced nonlinear optics in photonic-crystal microcavities". In: *Optics express* 15.24 (2007), pp. 16161–16176.

[152] Bo Liedberg, Claes Nylander, and Ingemar Lunström. “Surface plasmon resonance for gas detection and biosensing”. In: *Sensors and actuators* 4 (1983), pp. 299–304.

[153] Shuming Nie and Steven R Emory. “Probing single molecules and single nanoparticles by surface-enhanced Raman scattering”. In: *science* 275.5303 (1997), pp. 1102–1106.

[154] Mark S Anderson. “Locally enhanced Raman spectroscopy with an atomic force microscope”. In: *Applied Physics Letters* 76.21 (2000), pp. 3130–3132.

[155] Nina Mauser and Achim Hartschuh. “Tip-enhanced near-field optical microscopy”. In: *Chemical Society Reviews* 43.4 (2014), pp. 1248–1262.

[156] Anna Bezryadina et al. “High spatiotemporal resolution imaging with localized plasmonic structured illumination microscopy”. In: *ACS nano* 12.8 (2018), pp. 8248–8254.

[157] Nicolae C Panoiu et al. “Nonlinear optics in plasmonic nanostructures”. In: *Journal of Optics* 20.8 (2018), p. 083001.

[158] Gitanjal Deka et al. “Nonlinear plasmonic imaging techniques and their biological applications”. In: *Nanophotonics* 6.1 (2017), pp. 31–49.

[159] Mikko J Huttunen et al. “Using surface lattice resonances to engineer nonlinear optical processes in metal nanoparticle arrays”. In: *Physical Review A* 97.5 (2018), p. 053817.

[160] Daniel A Dombeck et al. “Uniform polarity microtubule assemblies imaged in native brain tissue by second-harmonic generation microscopy”. In: *Proceedings of the National Academy of Sciences* 100.12 (2003), pp. 7081–7086.

[161] Hannu Husu et al. “Metamaterials with tailored nonlinear optical response”. In: *Nano letters* 12.2 (2012), pp. 673–677.

[162] Robert Czaplicki et al. “Enhancement of second-harmonic generation from metal nanoparticles by passive elements”. In: *Physical review letters* 110.9 (2013), p. 093902.

[163] Feng Li et al. “Interparticle gap geometry effects on chiroptical properties of plasmonic nanoparticle assemblies”. In: *Nanotechnology* 33.12 (2021), p. 125203.

[164] Cristian Ciracı et al. “Origin of second-harmonic generation enhancement in optical split-ring resonators”. In: *Physical Review B—Condensed Matter and Materials Physics* 85.20 (2012), p. 201403.

[165] Nikola Bralović, Uli Lemmer, and Mohamed Hussein. “Asymmetric L-shaped resonant optical antennas with plasmon length tuning and

high-electric field enhancement". In: *Optical and Quantum Electronics* 55.9 (2023), p. 824.

[166] Asad A Tahir et al. "Design principles for wave plate metasurfaces using plasmonic L-shaped nanoantennas". In: *Journal of Optics* 19.3 (2017), p. 035001.

[167] Aydin Amini, Saeed Golmohammadi, and Sina Aghili. "Plasmonic response of graphene-like metallic-molecular nanocluster for optical applications". In: *Optical Engineering* 57.7 (2018), pp. 077104–077104.

[168] Mikko J Huttunen, Robert Czaplicki, and Martti Kauranen. "Nonlinear plasmonic metasurfaces". In: *Journal of Nonlinear Optical Physics & Materials* 28.01 (2019), p. 1950001.

[169] Periklis Pantazis et al. "Second harmonic generating (SHG) nanoprobes for in vivo imaging". In: *Proceedings of the National Academy of Sciences* 107.33 (2010), pp. 14535–14540.

[170] Peter W Baas et al. "Polarity orientation of microtubules in hippocampal neurons: uniformity in the axon and nonuniformity in the dendrite." In: *Proceedings of the National Academy of Sciences* 85.21 (1988), pp. 8335–8339.

[171] Arash Aghigh et al. "Second harmonic generation microscopy: a powerful tool for bio-imaging". In: *Biophysical Reviews* 15.1 (2023), pp. 43–70.

[172] Sina Aghili, Saeed Golmohammadi, and Aydin Amini. "Proposing an on/off optical router in telecom wavelength using plasmonic tweezer". In: *Optics Communications* 427 (2018), pp. 95–100.

[173] Jérémy Butet, Pierre-Francois Brevet, and Olivier JF Martin. "Optical second harmonic generation in plasmonic nanostructures: from fundamental principles to advanced applications". In: *ACS nano* 9.11 (2015), pp. 10545–10562.

[174] Alexandre Bouhelier et al. "Near-field second-harmonic generation induced by local field enhancement". In: *Physical review letters* 90.1 (2003), p. 013903.

[175] Binglin Shen et al. "Nonlinear Spectral-Imaging Study of Second-and Third-Harmonic Enhancements by Surface-Lattice Resonances". In: *Advanced Optical Materials* 8.8 (2020), p. 1901981.

[176] Yizhuo Chu, Mohamad G Banaee, and Kenneth B Crozier. "Double-resonance plasmon substrates for surface-enhanced Raman scattering with enhancement at excitation and stokes frequencies". In: *ACS nano* 4.5 (2010), pp. 2804–2810.

[177] S Linden et al. “Collective effects in second-harmonic generation from split-ring-resonator arrays”. In: *Physical review letters* 109.1 (2012), p. 015502.

[178] Brian K Canfield et al. “Local field asymmetry drives second-harmonic generation in noncentrosymmetric nanodimers”. In: *Nano Letters* 7.5 (2007), pp. 1251–1255.

[179] M Saad Bin-Alam et al. “Hyperpolarizability of plasmonic meta-atoms in metasurfaces”. In: *Nano Letters* 21.1 (2020), pp. 51–59.

[180] Yisheng Gao et al. “Nonlinear holographic all-dielectric metasurfaces”. In: *Nano letters* 18.12 (2018), pp. 8054–8061.

[181] Maxim R Shcherbakov et al. “Enhanced third-harmonic generation in silicon nanoparticles driven by magnetic response”. In: *Nano letters* 14.11 (2014), pp. 6488–6492.

[182] Yuri Kivshar. “All-dielectric meta-optics and non-linear nanophotonics”. In: *National Science Review* 5.2 (2018), pp. 144–158.

[183] Wenjie Tang et al. “Realizing high-efficiency third harmonic generation via accidental bound states in the continuum”. In: *Optics Letters* 49.5 (2024), pp. 1169–1172.

[184] Kirill Koshelev et al. “Nonradiating photonics with resonant dielectric nanostructures”. In: *Nanophotonics* 8.5 (2019), pp. 725–745.

[185] Martín Caldarola et al. “Non-plasmonic nanoantennas for surface enhanced spectroscopies with ultra-low heat conversion”. In: *Nature communications* 6.1 (2015), p. 7915.

[186] J Van de Groep and A Polman. “Designing dielectric resonators on substrates: Combining magnetic and electric resonances”. In: *Optics express* 21.22 (2013), pp. 26285–26302.

[187] Mikko J Huttunen et al. “Efficient nonlinear metasurfaces by using multiresonant high-Q plasmonic arrays”. In: *Journal of the Optical Society of America B* 36.7 (2019), E30–E35.

[188] M Saad Bin-Alam et al. “Cross-polarized surface lattice resonances in a rectangular lattice plasmonic metasurface”. In: *Optics Letters* 47.8 (2022), pp. 2105–2108.

[189] David C Hooper et al. “Second harmonic spectroscopy of surface lattice resonances”. In: *Nano letters* 19.1 (2018), pp. 165–172.

[190] Krishnan Thyagarajan et al. “Enhanced second-harmonic generation from double resonant plasmonic antennae”. In: *Optics express* 20.12 (2012), pp. 12860–12865.

[191] Kuang-Yu Yang et al. "Enhancement mechanisms of the second harmonic generation from double resonant aluminum nanostructures". In: *Acs Photonics* 4.6 (2017), pp. 1522–1530.

[192] Jan Sperrhake et al. "Analyzing the polarization response of a chiral metasurface stack by semi-analytic modeling". In: *Optics Express* 27.2 (2019), pp. 1236–1248.

[193] Jan Sperrhake et al. "Experimental validation of the fundamental mode approximation for stacked metasurfaces and its application to the treatment of arbitrary period ratios". In: *APL photonics* 6.9 (2021).

[194] C Menzel et al. "Asymmetric transmission of linearly polarized light at optical metamaterials". In: *Physical review letters* 104.25 (2010), p. 253902.

[195] Timo Stolt et al. "Backward phase-matched second-harmonic generation from stacked metasurfaces". In: *Physical Review Letters* 126.3 (2021), p. 033901.

[196] Karim Achouri, Yousef Vahabzadeh, and Christophe Caloz. "Mathematical synthesis and analysis of nonlinear metasurfaces". In: *arXiv preprint arXiv:1703.09082* (2017).

[197] Sohail A Jalil et al. "Spectroscopic Signatures of Plasmonic Near-Fields on High-Harmonic Emission". In: *Laser & Photonics Reviews* 17.12 (2023), p. 2300448.

[198] Joshua Baxter, Antonio Calà Lesina, and Lora Ramunno. "Hyperpolarizability of Plasmonic Nanostructures: A Method to Quantify". In: *Light-Matter Interactions Towards the Nanoscale* (2022), p. 243.

[199] J Sebastian Gomez-Diaz et al. "Nonlinear processes in multi-quantum-well plasmonic metasurfaces: electromagnetic response, saturation effects, limits, and potentials". In: *Physical Review B* 92.12 (2015), p. 125429.

[200] Jongwon Lee. "Nonlinear and wavelength-tunable plasmonic metasurfaces and devices". PhD thesis. 2014.

[201] Constantine A Balanis. *Balanis' Advanced Engineering Electromagnetics*. John Wiley & Sons Hoboken, NJ, USA, 2024.

[202] *COMSOL Multiphysics® v6.2*. `https://www.comsol.com`. 2024.

[203] Debra Krause, Charles W Teplin, and Charles T Rogers. "Optical surface second harmonic measurements of isotropic thin-film metals: Gold, silver, copper, aluminum, and tantalum". In: *Journal of applied physics* 96.7 (2004), pp. 3626–3634.

[204] Augustin Verneuil et al. "Far-field mapping and efficient beaming of second harmonic by a plasmonic metagrating". In: *Nanophotonics* 13.18 (2024), pp. 3609–3614.

[205] Kirill Koshelev et al. "Nonlinear metasurfaces governed by bound states in the continuum". In: *Acs Photonics* 6.7 (2019), pp. 1639–1644.

[206] Yuan Zeng et al. "Enhanced second harmonic generation in double-resonance colloidal metasurfaces". In: *Advanced Functional Materials* 28.51 (2018), p. 1803019.

[207] Zhuo Wang et al. "Selectively plasmon-enhanced second-harmonic generation from monolayer tungsten diselenide on flexible substrates". In: *ACS nano* 12.2 (2018), pp. 1859–1867.

[208] Nils Bernhardt et al. "Quasi-BIC resonant enhancement of second-harmonic generation in WS2 monolayers". In: *Nano Letters* 20.7 (2020), pp. 5309–5314.

[209] Robert Czaplicki et al. "Surface lattice resonances in second-harmonic generation from metasurfaces". In: *Optics letters* 41.12 (2016), pp. 2684–2687.

[210] John E Carroll, James Whiteaway, Dick Plumb, et al. "Distributed feedback semiconductor lasers". In: IET. 1998.

[211] Hooshang Ghafouri-Shiraz. *Distributed feedback laser diodes and optical tunable filters*. John Wiley & Sons, 2003.

[212] Torgil Kjellberg and Richard Schatz. "The effect of stitching errors on the spectral characteristics of DFB lasers fabricated using electron beam lithography". In: *Journal of lightwave technology* 10.9 (2002), pp. 1256–1266.

[213] Junichi Kinoshita. "Analysis of radiation mode effects on oscillating properties of DFB lasers". In: *IEEE journal of quantum electronics* 35.11 (2002), pp. 1569–1583.

[214] A Yariv and A Gover. "Equivalence of the coupled-mode and Floquet-Bloch formalisms in periodic optical waveguides". In: *Applied Physics Letters* 26.9 (1975), p. 537.

[215] Tuhin Paul. "Photonic Integration with III-V Semiconductor Technologies". PhD thesis. Université d'Ottawa/University of Ottawa, 2022.

[216] Shayan Saeidi et al. "Finite-difference coupled-mode analysis of waveguide gratings and their optimization for single-mode DFB lasers". In: *Journal of the Optical Society of America B* 42.2 (2025), pp. 438–445.

[217] William Streifer, R Burnham, and D Scifres. "Effect of external reflectors on longitudinal modes of distributed feedback lasers". In: *IEEE Journal of Quantum Electronics* 11.4 (1975), pp. 154–161.

[218] Sina Aghili et al. "Short-cavity single-mode on-chip DFBL source for monolithic PICs in the telecom range". In: *Journal of Physics D: Applied Physics* (2026).